Modélisation physique et mécanique pour les procédés de transformation de la matière végétale

Xavier Frank

Synthèse des travaux
présentée à l'Université de Montpellier
pour obtenir le
Diplôme d'Habilitation à Diriger des Recherches

par

Xavier FRANK

Modélisation physique et mécanique pour les procédés de transformation de la matière végétale

Soutenue publiquement le 17/06/2022 devant le jury composé de :

Pr. Mohammed GUESSASMA	Université de Picardie Jules Verne	Rapporteur
Pr. Pascale AUSSILOUS	Aix-Marseille Université	Rapportrice
Dr. Jean-Noël ROUX,	IFSTTAR	Rapporteur
Pr. Gaël COMBE	Université Grenoble Alpes	Examinateur
Pr. Huai Zhi LI	Université de Lorraine	Examinateur
Dr. Farhang RADJAÏ	CNRS	Examinateur

Je déclare avoir respecté, dans la conception et la rédaction de ce mémoire d'HDR, les valeurs et principes d'intégrité scientifique destinés à garantir le caractère honnête et scientifiquement rigoureux de tout travail de recherche, visés à l'article L.211-2 du Code de la recherche et énoncés par la Charte nationale de déontologie des métiers de la recherche et la Charte d'intégrité scientifique de l'Université de Montpellier. Je m'engage à les promouvoir dans le cadre de mes activités futures d'encadrement de recherche.

Table des Matières

Introduction

Dans un contexte marqué par le réchauffement climatique et la raréfaction prochaine des ressources fossiles, la diversification des voies de valorisation des ressources végétales est un enjeu crucial. Pour le moment, nos circuits industriels sont encore très largement fondés sur l'exploitation du pétrole. Une première approche de la transition vers une industrie basée sur les agroressources consiste à utiliser et adapter des procédés issus de l'industrie pétro-centrée aux matières premières d'origine végétale. Il s'agira, par exemple, d'opérer des réactions chimiques sur un substrat divisé et mis en suspension, par exemple sous forme de boues. Les questions de physique et de mécanique posées par ces procédés relèvent alors de la mécanique des fluides non newtoniens, notamment concernant les écoulements polyphasiques (Section 2.1).

L'étape première des voies de transformation du pétrole est la raffinerie, une séparation des constituants du pétrole en d'autres phases fluides. Par analogie, l'idée maîtresse du concept de bioraffinerie est de mettre au point l'étape de première transformation des agroressources végétales. Toutefois, cet objectif implique des obstacles et des opportunités spécifiques. L'obstacle le plus évident et le plus contraignant réside dans le fait que, contrairement au pétrole, les agroressources végétales brutes se présentent sous forme solide, alors que le pétrole est une phase liquide. L'obtention de molécules à partir de cette ressource va donc nécessiter une ou, le plus souvent, plusieurs étapes de broyage. Or, les matériaux d'origine végétales présentent une structuration à différentes échelles (Section 2.2), des interactions complexes avec l'eau (Section 2.3), ainsi que des propriétés mécaniques le plus souvent inhomogènes et anisotropes. Une approche du problème pourrait consister à se ramener systématiquement à l'échelle moléculaire, c'est-à-dire pousser la séparation des constituants du végétal jusqu'à l'échelle la plus fine, et utliliser les briques moléculaires ainsi obtenues dans des opérations de synthèse, calquant ainsi le modèle de la pétrochimie.

Si la complexité et la variabilité des structures du végétal implique de toute évidence des obstacles à surmonter, ce n'est pas systématique. Rappelons que beaucoup d'usages traditionnels des agroressources végétales s'appuient largement sur la diversité des microstructures plutôt que sur la seule composition moléculaire. Le cas du bois est emblématique ; les usages variés des essences disponibles s'appuient sur des critères de densité, d'anisotropie et de comportement hygroscopiques liées, au moins en partie, à la microstructure du bois. Pour prendre un exemple caricatural, appliquer le modèle pétrochimique de manière stricte consisterait à décomposer le bois en molécules, à utiliser ces molécules pour synthétiser un équivalent biosourcé du PVC, et à utiliser ce bio-plastique dans des applications relevant de la menuiserie. Au lieu de fabriquer tout simplement des fenêtres en bois... Parmi les activités de recherche finalisée de l'UMR IATE, on peut trouver un exemple à priori moins caricatural, mais tout aussi convainquant, celui du moteur à poudre de biomasse. Les voies "classiques" de transformation de végétaux en carburant consiste à faire subir au substrat un certain nombre de réaction chimiques afin d'obtenir un liquide inflammable : éthanol ou biodiesel. On peut également citer la méthanisation. Ces voies

ont en commun d'être coûteuses et d'impliquer des pertes de rendement à chaque étape. Une voie alternative consiste à utiliser la biomasse combustible directement sous forme solide [110]. Cette approche alternative pose des questions de recherche fondamentale, concernant le broyage fin de la matière végétale (Section 2.4), la coulabilité des poudres dans les moteurs, etc...

Qu'il s'agisse d'optimiser des procédés de traitement de la matière végétale, d'adapter un procédé à la variabilité des agroressources ou de développer un usage innovant des produits de ces procédés, il est essentiel de comprendre finement, à différentes échelles, les phénomènes impliqués. Les paramètres à considérer pourront être les caractéristiques structurales d'un tissu végétal à broyer, la rhéologie de la matière à transformer, qu'il s'agisse d'une poudre, d'une suspension ou d'une émulsion, etc... Les approches purement empiriques ou statistiques présentent des limites pour aborder des problématiques aussi complexes. Celles-ci requièrent des démarches de type "bottom-up", visant à dégager les causalités physiques permettant de mettre en relation des caractéristiques et paramètres d'une échelle donnée aux comportements observés à l'échelle immédiatement supérieure. Pour relever ces défis, la simulation numérique présente des avantages significatifs :

— L'intégralité des informations constituant la description du problème est accesible
— Il est possible de découpler les phénomènes ordinairement couplés dans les systèmes réels
— Les valeurs accessibles des paramètres sont limités par la méthode numérique, et non pas par des contraintes de préparation d'échantillon, ce qui permet potentiellement d'étendre les blayages paramétriques
— La préparation des échantillons est numérique, et donc, le plus souvent, très rapide si le processus est automatisé. L'expérimentation sur échantillon réel peut nécessiter de longues préparations, en particulier lorsque le matériau concerné doit être extrait d'un végétal

Le projet de recherche que je développe au sein de l'UMR IATE, à Montpellier (Chapitre 3), s'appuie sur ce type de méthodologie en vue d'apporter une contribution à la compréhension des phénomènes physiques et mécaniques impliqués dans les procédés de transformation des ressources d'origine végétales. La simulation numérique de la fragmentation des matériaux hétérogènes (Section 3.1), du mouillage (Section 3.2), ainsi que de l'écoulement des milieux granulaires (Section 3.1.4) seront mises en œuvre de façon à comprendre l'impact de la microstructure sur ces phénomènes, et, à terme, sur les procédés de transformation de la matière végétale.

Dans la suite du manuscrit, je présenterai un rapide résumé de mon parcours (Chapitre 1), ainsi qu'un bilan de mes activités (Chapitre 2), mettant en évidence les compétences acquises au long de ce parcours. Ce bilan comporte une partie relative à la dynamique des bulles en fluide non newtonien (Section 2.1), présentant les travaux effectués dans le prolongement de ma thèse, une partie concernant la modélisation moléculaire de polymères de la paroi du bois (Section 2.1)

Enfin, je présenterai, dans mon projet de recherche (Chapitre 3), comment ces compétences permettront de répondre aux problématiques posées ici.

Chapitre 1

Aperçu de mon parcours

J'ai débuté mes activités de recherche au Centre de Génie Chimique des Milieux Rhéologiquement Complexes (GEMICO), laboratoire aujourd'hui fusionné avec trois autres au sein du Laboratoire Réactions et Génie des Procédés (LRGP), UMR 7274 CNRS/Université de Lorraine. Ces travaux portaient sur la dynamique des bulles en fluide non Newtonien, il s'agissait en particulier d'étudier l'impact des coalescences entre bulles issues d'un orifice immergé dans une solution de polymère en régime semi-dilué. Ce choix a été dicté par le fait que le train de bulles ainsi formé est chaotique... la théorie du chaos faisait alors partie de mes principaux centres d'intérêt. Ce sujet avait alors fait l'objet de nombreuses investigations expérimentales au sein du GEMICO, et s'il était admis que la clé de l'explication des phénomènes observés résidait dans les interactions entre bulles successives, les approches de modélisation expérimentale et numérique proposées restaient assez globales. Disposant d'un corpus de données expérimentales conséquent, accumulé, organisé et analysé par les étudiants qui m'avaient précédés sur ce sujet, je me suis orienté vers la modélisation et la simulation numérique. J'ai donc couplé un modèle d'accumulation d'effets de mémoire au sein du fluide cisaillé par le passage des bulles successives à un modèle de rétroaction de ces effets de mémoire sur la dynamique individuelle des bulles. Cette approche 1D a permis de simuler numériquement la dynamique du train de bulles, et de reproduire les phénomènes émergents remarquables qu'elle engendre : transition vers le chaos par doublement de période [1], diminution du nombre de bulles du fait des coalescences, diversification des tailles de bulles et saturation de l'évolution loin de l'orifice d'injection du gaz [68].

A l'issue du DEA, j'ai enseigné à plein temps dans le secondaire en tant qu'agrégé de physique et j'ai préparé ma thèse. Celle-ci, encadrée par Huai Zhi Li, aujourd'hui professeur à l'Ecole Nationale Supérieur des Industries Chimiques (ENSIC) et rattaché au LRGP, s'est donc déroulée à distance, mes établissements scolaires d'affectation successifs (Académies d'Orléans-Tours, Caen, Le Mans...) étant éloignés du LRGP. D'autre part, j'ai été recruté deux ans après ma soutenance de thèse. Habituellement, cet intervalle est passé en ATER ou stage post-doctoral. Etant donnée ma situation particulière, j'ai conservé mon poste d'enseignant et poursuivi en parallèle mes activités de recherche sur la dynamique des bulles. Cette thématique a donc été au centre de mes activités de recherche bien au-delà de ma thèse, c'est pourquoi elle est détaillée dans le manuscrit.

1. Un système animé d'une dynamique périodique de période T présente une transition vers le chaos par doublement de période lorsque, par variation du paramètre de contrôle, des modes de période $2T$, $4T$, etc... se superposent successivement à la dynamique périodique initiale jusqu'à produire une dynamique résultante apériodique.

J'ai d'abord affiné le modèle d'interaction entre bulles, validé expérimentalement dans le cas d'un train de bulles périodique [30], puis appliqué au train de bulles chaotique [33]. Une analyse plus fine des résultats bruts obtenus par simulation numérique a également permis d'identifier la cause du doublement de période [38]. La dynamique chaotique n'était pas le seul aspect remarquable du système, les bulles présentent individuellement des particularités contre-intuitives dans ce type de fluide. Tout d'abord, sous les bulles, dans l'axe d'ascension, le fluide est animé d'un mouvement descendant au lieu d'être entraîné par la bulle dans un mouvement ascendant. Ce phénomène, appelé sillage négatif, avait fait l'objet de plusieurs études divergentes quant à leurs hypothèses explicatives. Ce sillage négatif est entouré d'une zone en forme de cône où le fluide présente un mouvement ascendant. L'angle d'ouverture de ce cône dépend de la taille de la bulle. Enfin, les bulles en ascension dans ces fluides présentent une forme allongée comportant une queue. Une part importante de mon travail de thèse a été consacrée à l'expérimentation numérique au sujet de la dynamique d'ascension d'une bulle. Une première approche a consisté à coupler un modèle lattice Boltzmann diphasique, afin de tenir compte de la déformabilité de l'interface gaz/liquide, avec un modèle rhéologique relativement complet pour la phase liquide, tenant compte de la viscoélasticité, de la rhéofluidifiance, ainsi que de la thixotropie. Si cette approche a permis de prédire les caractéristiques du champ de vitesse, ainsi que la forme des bulles [36], il a été indispensable de découpler les différentes phénoménologies pour identifier les causalités à l'œuvre. Une étude à la fois numérique et expérimentale a mis en évidence l'analogie très forte entre champ de vitesse autour de bulles en ascension et autour de particules en sédimentation dans ces fluides [64]. Les phénomènes liées à l'interface gaz/liquide ont donc pu être exclus comme déterminants du champ de vitesse, sillage négatif comme cône ascendant. Une autre série d'expériences numériques a consisté à translater une sphère solide dans un fluide viscoélastique linéaire simple. Malgré la grande simplification du problème, l'essentiel des charactéristiques du champ de vitesse sont prédites par ce modèle [37]. Cette approche purement linéaire du problème a permis de dégager des causalités claires quant aux caractéristiques du champ de vitesse, en reliant quantitativement le nombre de Mach viscoélastique à l'angle d'ouverture du cône et aux oscillations dans le silage négatif derrière une sphère en translation, en bon accord avec les résultats expérimentaux [28].

J'ai ensuite été recruté comme chargé de recherche INRA dans l'équipe de Patrick PERRE au Laboratoire d'Etude et de Recherche sur le Matériau Bois (LERMAB), unité qui n'est aujourd'hui plus associée à l'INRAE. Il s'agissait d'un poste fléché, dont la thématique était "Modélisation moléculaire appliquée à la paroi du bois". Si, du fait de ma formation initiale de physicien, les principes généraux de ces approches m'étaient connus, je ne disposais d'aucun savoir-faire en la matière. Il m'a donc fallu acquérir cette compétence. Dans l'intervalle, j'ai cherché à utiliser les compétences acquises durant ma thèse dans le contexte de la recherche finalisée sur le matériau bois.

Celui-ci présente de fortes interactions avec l'eau, ce qui implique de nombreuses conséquences pratiques dans tous les domaines d'application du matériau bois. De nombreux travaux avaient déjà été menés sur ce sujet au LERMAB avant mon arrivée [3, 88, 99], et je me suis investi dans l'expérimentation numérique à l'échelle du pore, ce qui m'a permis d'apporter des éléments nouveau dans cette thématique de fond du laboratoire. J'ai donc développé des outils pour la simulation numérique de phénomènes de capillarité au sein du bois par approche lattice Boltzmann [39]. Or, étant donnée la structure de ce matériau, ce type d'étude ne peut être réalisée qu'à l'aide de simulations 3D. Le principal obstacle résidait dans la puissance de calcul nécessaire. Alors que les calculs 2D de ma thèse ont pu être exécutés sur des ordinateurs de bureau grand public, des ressources bien plus conséquentes étaient nécessaires pour exécuter des simula-

tions 3D haute résolution. J'ai donc appris la programmation parallèle par échange de messages (MPI) sur cluster de calcul. Le cours de l'IDRIS (Institut du développement et des ressources en informatique scientifique, affilié au CNRS), particulièrement bien fait et disponible en ligne gratuitement, m'a permis d'acquérir cette compétence. En collaboration avec les collègues du LERMAB, disposant d'une expertise forte aussi bien concernant le matériau bois que le traitement d'images, j'ai pu simuler l'imbibition capillaire d'un échantillon de bois réel, numérisé par coupes successives [27]. L'interaction entre la surface d'un échantillon de bois et un liquide concerne aussi bien la finition d'une pièce de bois à l'aide d'un spray ou les conditions de service en extérieur. Faire interagir une structure 3D similaire à l'anatomie locale d'une surface d'un échantillon de bois avec une goutte de liquide mouillant est donc apparu comme une application pertinente de l'approche LB. J'ai initié ce champ de recherche avec un cas particulier simple : le bois est assimilé à un assemblage régulier de fibres creuses de section carrée et la surface considérée est générée par une section orthogonale à l'axe des fibres. Un tel modèle est générique et sa portée dépasse le seul domaine des sciences du bois [31, 32].

Les propriétés mécaniques de la paroi du bois ne découlent pas de l'échelle strictement moléculaire, mais plutôt d'une échelle supramoléculaire. La paroi est un composite renforcé par des microfibrilles de cellulose, en interaction avec une matrice amorphe. Or, les approches de simulation moléculaire sont particulièrement lourdes numériquement, à la fois du fait du grand nombre de degrés de liberté impliqués, mais aussi du fait de la très fabile valeur de pas de temps imposée par les vibrations haute fréquence des liaisons covalentes. Il n'est pas possible de simuler un système d'une taille suffisante pour être représentatif en s'appuyant uniquement sur la force brute d'un supercalculateur. Rappelons par ailleurs que cette partie de mon parcours se déroule entre 2008 et 2011, la puissance de calcul des ordinateurs n'était pas celle des machines de 2020. Il a donc fallu mettre au point une méthode d'approximation de type approche gros grain ou Coarse Grain (CG). Celle-ci consiste à réduire le nombre de degrés de libertés en regroupant les atomes en "grains" représentant, par exemple, des monomères, des groupes chimiques, etc... Dans le cadre de la thèse de Liang Li, financée par l'ANR ANALOGS, un modèle gros grain de composite cellulose cristalline/xylane a été mis au point [71] à l'aide de simulations atomistiques réalisées par Karim Mazeau, DR CNRS au Centre de Recherches sur les Macromolécules Végétales (CERMAV). Avant que ce modèle aie pu faire l'objet d'applications, l'équipe a été supprimée pour des raisons de restructuration interne de l'INRA et les personnels ont dû changer de laboratoire.

Les possibilités de poursuivre mes travaux antérieurs au sein du département CEPIA étant très limitées j'ai été contraint de m'investir une autre thématique. J'ai choisi de rejoindre l'équipe de Valérie LULLIEN-PELLERIN au laboratoire Ingénierie des Agroplymères et Technologies Emergentes (IATE) où je me suis investi dans l'étude de la modélisation de la fragmentation de la biomasse. Suite à la restructuration de l'UMR IATE, j'ai intégré l'équipe PhyProDiv, animée par Jean-Yves DELENNE, afin de poursuivre mes travaux sur ce sujet. J'ai cherché une approche numérique capable de simuler la fissuration et la fragmentation de structures complexes, y compris en régime dynamique. Parmi les diverses méthodologies exposées dans la littérature, la péridynamique s'est avérée être un choix pertinent, en particulier du fait de sa capacité à simuler la formation de patterns de fissuration très complexe sans de lourdes procédures de remaillage. J'ai développé un code péridynamique 2D parallélisé via MPI. Celui-ci est générique concernant aussi bien la façon de définir l'échantillon que les paramètres mécaniques. Ce code a été utilisé par deux étudiants et a généré une grande quantité de données, encore en cours de valorisation [56, 87]. A ce stade de mon parcours, j'ai adopté une méthodologie qui consiste à mener des expérimences numériques de taille moyenne, mais en très grand nombre. Cette

approche est pratiquable à l'aide du cluster de calcul installé à IATE lors de mon arrivée, mais s'avère bien plus adaptée encore sur les moyens de calculs mutualisés extérieurs : clusters INRAE de bioinformatique GENOTOUL (Toulouse) et MIGALE (Jouy-en-Josas), mésocentre Occitanie, calculateur national du CINES OCCIGEN. Il est ainsi possible de réaliser des balayages massifs concernant les paramètres structuraux des matériaux, mais également d'exécuter des répétitions de grande ampleur pour chaque jeu de paramètre, et d'étudier en détail la statistique, notamment concernant la contrainte à la rupture (loi de Weibull...).

Chapitre 2

Bilan des activités

2.1 Dynamique des bulles

A l'issue de ma thèse, j'ai connu une période de deux ans durant laquelle j'étais toujours enseignant du secondaire à plein temps. En parallèle, j'ai poursuivi mes activités de recherche concernant la dynamique des bulles en fluide non Newtonien, dans le prolongement de mes travaux de thèse. C'est pouquoi cette thématique représente une part importante de mes activités de recherche et de ma production scientifique passées, raison pour laquelle je la détaille ici.

2.1.1 Contexte

Une voie classique de la transformation de matières issues du végétal consiste à traiter les ressources en phase liquide saturée, par exemple sous la forme d'une suspension. les réacteurs utilisés sont alors très proches de dispositifs classiques de l'industrie pétro-centrée. Parmi ceux-ci, on trouve des contacteurs gaz-liquide, notamment des colonnes à bulles, souvent utilisés pour leur faible coût d'installation et d'exploitation. Une colonne à bulles est un contacteur gaz-liquide de construction à priori simple. Il s'agit d'un réservoir contenant la phase liquide dans laquelle du gaz est injecté par un distributeur, par exemple, un plateau percé de nombreux trous. La phase gaz forme des bulles et la mise en contact des espèces chimiques a lieu à l'interface des ces bulles au cours de leur ascension (Fig. 2.1).

Si le principe de la colonne à bulles est très simple, son comportement hydrodynamique peut être extrêmement complexe. D'une part, la trajectoire des bulles n'est pas nécéssairement rectiligne, en particulier dans les cas où la viscosité de la phase liquide est faible. Les interactions hydrodynamiques entre bulles peuvent donner lieu à l'émergence de structures globales impactant l'homogénéité à grande échelle. D'autre part, les bulles peuvent interagir à courte portée lors de coalescences. Dans ce cas, la distribution de tailles de bulles n'est plus seulement fonction du régime de bullage au niveau du distributeur, mais aussi de l'hydrodynamique globale de la colonne. Ce point est particulièrement important, dans la mesure où les coalescences vont donner naissance à des bulles plus grosses, impactant négativement le transfert de matière à l'interface.

L'approche classique du génie des procédés consiste à décrire l'état de la colonne de manière globale (taux de gaz, aire interfaciale par mètre de colonne...), définir plusieurs nombres sans dimension et à rechercher empiriquement des corélations entre eux, de façon à caractériser le fonctionnement du réacteur. La généricité de cette approche n'est pas garantie en soi, et il peut être nécessaire de recommencer la détermination des paramètres empiriques de la corélation ainsi obtenue suite à une modification du réacteur. D'autre part, cette approche ne permet pas

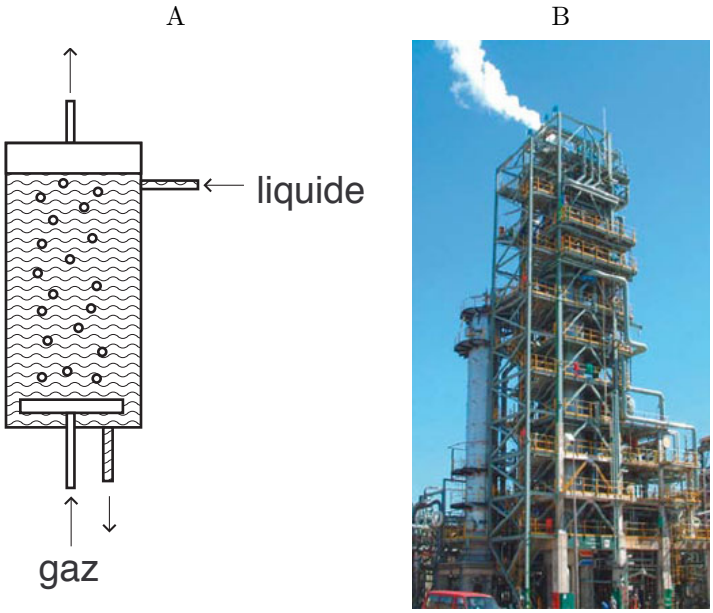

FIGURE 2.1 – Colonnes à bulles. A : schéma de principe d'une colonne à bulles. B : exemple de colonne à bulle industrielle.

de comprendre les phénomènes de base desquels découle le comportement global du réacteur.

Ces difficultés sont grandement accrues dans les cas où la phase liquide ne présente pas un comportement newtonien. Ce peut être le cas de solutions de polymère, des émulsions et des suspensions. En particulier, de tels fluides peuvent être viscoélastiques, être le siège d'effets de mémoire, ou encore avoir une viscosité croissante avec l'intensité de déformation. Or, les phases liquides impliquées dans la transformation des matières végétales présentent souvent une rhéologie non newtoniennes. C'est le cas, par exemple, dans la production de biogaz en colonnes par micro-algues [2]. Les approches classiques du génie des procédés sont alors inopérantes la plupart du temps. Il est donc nécessaire de recourrir à une approche bottom-up, partant des petites échelles et des phénomènes mécaniques pour comprendre comment émerge le comportement global aux grandes échelles.

L'approche précédemment décrite a d'abord été mise en œuvre expérimentalement par Huai-Zhi LI et ceux qui m'ont précédés parmi ses étudiants. Il s'agit en premier lieu de décomposer le système en éléments plus simples, puis d'étudier les interactions entre ces éléments. L'injection de gaz est faite à l'aide d'un distributeur, généralement un simple plateau percé de trous. Des bulles se forment au niveau de chaque trou et l'ensemble des bulles issues d'un trou donnée est appelé train de bulles. Les trains de bulles issus de trous voisins interagissent entre eux. Une première décomposition du problème consiste à étudier d'abord la dynamique d'un train de bulle isolé [42]. Le gaz est injecté à travers un orifice unique (Fig. 2.2 :A), d'une part, et, d'autre part, deux types d'injection de gaz ont été utilisés : l'injection en continu à un débit fixé, et, grâce à une électrovanne, l'injection de bulles à une période contrôlés (Fig. 2.2 :A), la pression d'injection permettant de contrôler indirectement le volume des bulles.

A la limite des grandes périodes, le train de bulles dans son ensemble reste périodique, les bulles atteignent une vitesse d'ascension stationnaire rapidement, et aucune coalescence n'a lieu dans la colonne [70]. En revanche, la limite des courtes périodes de formation de bulle (notamment

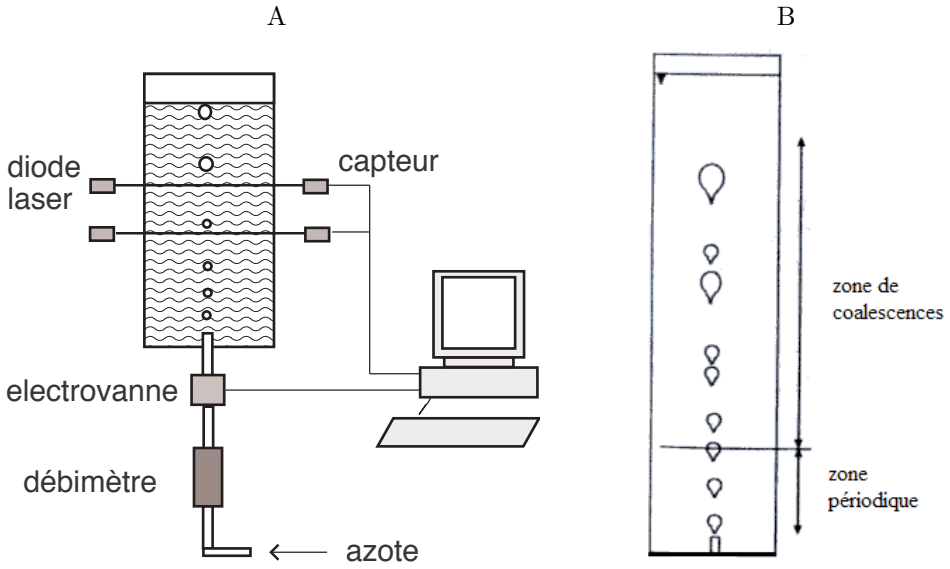

FIGURE 2.2 – Etude expérimentale d'un train de bulles dans un fluide non newtonien. A : dispositif expérimental. B :

en injection de gaz à débit fixé) génère une dynamique beaucoup plus complexe [69]. On observe dans ce cas deux régimes différents chacun dans une zone distincte . Près de l'orifice, le train de bulles est périodique et ne comporte qu'une seule taille de bulle, qui s'identifie à la taille des bulles générées au niveau de l'orifice. En revanche, un peu plus haut dans la colonne, des bulles se rapprochent les unes des autres, coalescent en donnent naissance à des bulles plus volumineuses, qui à leur tour, subissent des coalescences, etc... Il résulte de ces multiples interactions une dynamique très complexe, qu'on qualifiera de chaotique, dans le reste de la colonne (Fig. 2.2 :B). On peut donc assimiler la hauteur dans la colonne à laquelle on observe la dynamique de passage des bulles à un pseudo-paramètre de contrôle secondaire.

A une échelle plus locale, l'écoulement autour des bulles a été caractérisé grâce à un dispositif de vélocimétrie par image de particules (P.I.V.) [42]. Les captures de champ de vitesse ont révélé un champ de vitesse complexe [43] dont l'élément le plus contre-intuitif est le sillage négatif, une zone à l'arrière de la bulle où le fluide descend au lieu d'être entraîné vers le haut par l'ascension de la bulle (Fig. 2.3).

Ce sillage négatif est par ailleurs entouré d'un cône ascendant (Fig. 2.3). L'existence du sillage négatif est connue depuis longtemps [53], mais la structure complète du champ de vitesse n'a été révélée que grâce au PIV.

Ces travaux sont essentiellement expérimentaux. Ma contribution a consisté à mettre en place des démarches de modélisation et de simulation numérique à différentes échelles afin de comprendre la dynamique de train de bulles en fluide non newtonien.

2.1.2 Train de bulles périodique : approche analytique

En régime périodique, la dynamique du train de bulles dépend de la période de formation de bulles en ceci que la vitesse d'ascension stationnaire est décroissante avec la période [70]. On peut donc attribuer l'accélération des bulles à une interaction entre bulles, dont l'intensité

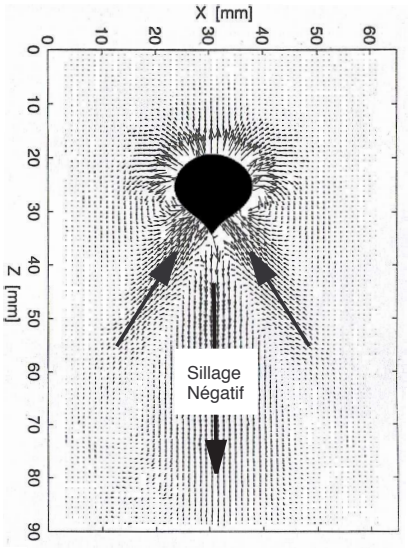

FIGURE 2.3 – Champ de vitesse autour d'une bulle de volume $V_0 = 1200mm^3$ en ascension dans une solution aqueuse de PAAm à $0,75\%$ en masse. On distingue le sillage négatif, ainsi que le cône ascendant entourant le sillage négatif et indiqué par deux flèches.

décroit avec la distance entre deux bulles successives. Un tel phénomène n'est pas propre aux fluides non newtoniens et peut s'observer en fluide newtonien [98]. Dans ce cas, on peut attribuer l'accélération des bulles aux effets intertiels du sillage des bulles [10, 62], ou à la recirculation globale du liquide, si la colonne est suffisamment étroite. Mais le cas des fluides non newtonien viscoélastiques est très différent. D'une part, le sillage négatif imposerait plutôt un ralentissement global du train de bulles plutôt qu'une accélération [68], d'autre part, les interactions entre bulles successives ont une portée très grande, à priori incompatible avec un effet direct des recirculations dans le sillage. En effet, suivant la rhéologie du fluide utilisé, une bulle peut subir un effet d'accélération alors même que la bulle précédente, avec laquelle elle "interagit", a atteint la surface du liquide bien avant que la bulle qui la suit ne soit formée [69]. On attribue donc ces interactions à très longue portée à un effet de mémoire au sein du liquide : le cisaillement imposé par le passage d'une bulle ne disparaît pas immédiatement et relaxe progressivement [70]. Le phénomène peut donc être décrit ainsi : le passage d'une bulle provoque localement un cisaillement, dont la conséquence est l'apparition d'une contrainte locale. Cette contrainte relaxe lentement, et n'est donc pas entièrement relaxée lorsque la bulle suivante arrive au point considéré. Cette contrainte locale est liée à une fludification transitoire du fluide (désenchevêtrement des chaînes de polymère, etc...), la bulle suivante rencontre donc un fluide localement moins visqeux et accélère. Le fluide subit donc un cisaillement plus intense, ce qui aura pour conséquence d'engendrer une plus grande fluidification locale du liquide pour la bulle suivante, etc... En régime permanent, toutes les bulles rencontrent la même viscosité effective et montent à la même vitesse.

Un modèle ayant pour finalité d'expliquer ce phénomène et de prédire la vitesse d'ascension des bulles dans un train de bulles périodique en fluide non newtonien devra donc impérativement tenir compte de la dynamique d'un champ de contrainte résiduel sur toute la hauteur de la colonne. Il ne s'agit donc pas d'interactions de paire entre bulles successives, mais d'interactions indirectes à travers les contraintes résiduelles du liquide. Dans le cadre de ma thèse, j'ai eu à

développer un tel modèle [30].

Etant donné que les bulles, dans les conditions qui sont celles de cette étude, adoptent une trajectoire strictement rectiligne verticale, le modèle analytique pourra être décrit selon une seule dimension. Les champs utilisés dépendront donc uniquement de la coordonnée z et du temps t. Dans la mesure où, dans le cas présent, le régime est périodique, on fixe un point d'observation et on ignore la dépendance en z, formellement équivalente à la dépendance en t.

La contrainte résiduelle au point z, notée τ, obéit à une équation relaxationnelle

$$\frac{d\tau}{dt} + \alpha\tau = \beta\dot{\gamma} \tag{2.1}$$

où α et β sont des paramètres dépendant de la période de passage des bulles T, qui s'identifie avec la période de formation des bulles au niveau de la buse d'injection et imposé par les conditions de bullage contrôlées par électrovanne au niveau de la buse d'injection du gaz. On détermine α et β à l'aide de la simulation rhéologique, une démarche de simulation expérimentale sur rhéomètre du passage successif de bulles dans un fluide non Newtonien [67, 70]. Le cisaillement $\gamma(t)$ est le cisaillement imposé par le passage d'une bulle. Son ordre de grandeur est $\gamma_b = u_b/D_b$ où u_b est la vitesse de bulle, l'inconnue du problème et D_b le diamètre de bulle, un paramètre lui aussi imposé par les conditions de bullage. On déduit de ce modèle une expression de la contrainte résiduelle rencontrée par chaque bulle τ_b, et dépendant de $\gamma_b = u_b/D_b$ et de T.

Reste à formuler un modèle hydrodynamique prédisant la vitesse d'ascension des bulles u_b à partir du diamètre des bulles D_b, des propriétés rhéologiques du fluide, mais aussi de la contrainte résiduelle τ_b. On s'appuie sur une corrélation de Rodrigue [97], initiallement conçue pour prédire la vitesse d'ascension de bulles isolées en fluide visqueux Newtonien. Cette corrélation devra donc être modifiée. Le fluide étant rhéofluidifiant, la viscosité constante du modèle initial de Rodrigue est remplacé par une vicosité η dépendant du cisaillement, prédite par le modèle de Carreau

$$\frac{\eta - \eta_\infty}{\eta_0 - \eta_\infty} = \left[1 + (\lambda\dot{\gamma}_b)^2\right]^{\frac{n-1}{2}} \tag{2.2}$$

où η_0, η_∞, λ et n sont des paramètres du modèle de Carreau directement ajustés sur rhéomètre. Le couplage avec la contrainte résiduelle s'effectue simplement en modifiant le cisaillement utilisé pour calculer la viscosité : $\dot{\gamma}_b$ est remplacé par $\dot{\gamma}_b + \dot{\gamma}_{eq}$, où $\dot{\gamma}_{eq}$ est relié à $\tau - b$ à l'aide d'un modèle rhéologique plus simple que le modèle de Carreau, le modèle d'Oswald

$$\tau_b = K\dot{\gamma}_{eq}^{n'} \tag{2.3}$$

où K et n' sont des paramètres du modèle d'Oswald, dit "en loi de puissance", ajustés directement au rhéomètre.

La vitesse u_b dépend de la contrainte résiduelle τ_b et τ_b dépend de u_b. Le système d'équations couplées a été résolu numériquement pour un large échantillon de diamètres de bulles D_b pour chaque période de bullage T utilisée durant les expérimentations [30, 42]. Un bon accord entre le modèle et les résultats expérimentaux a été obtenu (Fig. 2.4).

2.1.3 D'où vient le sillage négatif ?

Faits expérimentaux

L'existence d'un sillage négatif derrière une bulle en fluide viscoélastique est connue depuis longtemps [53], mais une capture complète du champ de vitesse n'a été possible que grâce au PIV [43]. L'analyse du champ de vitesse autour d'une bulle en ascension dans un fluide viscoélastique implique donc plusieurs questions :

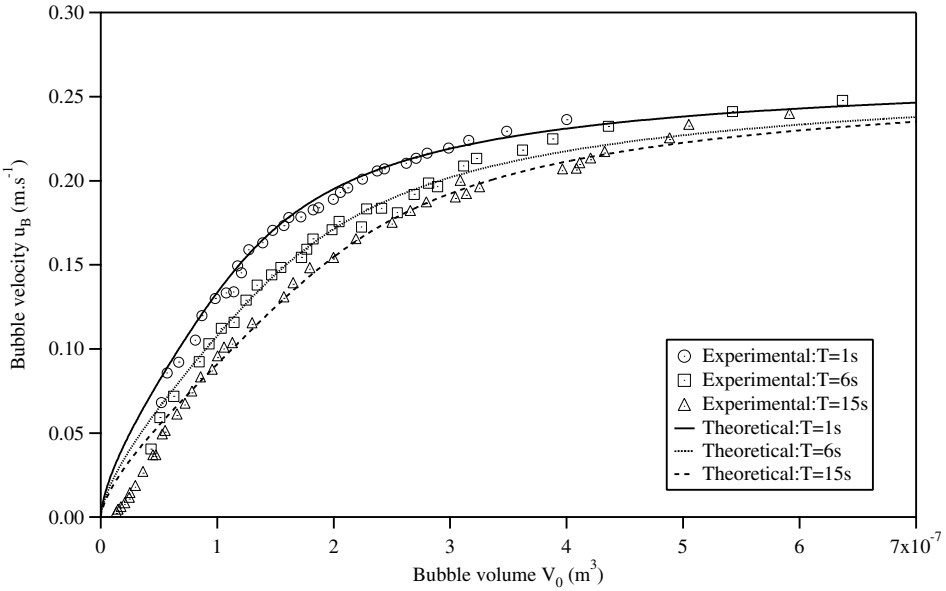

FIGURE 2.4 – Vitesse d'ascension d'un train de bulles périodique dans une solution de PAAm de concentration $0,50\%$ en poids en fonction du volume de bulle individuel et pour différentes périodes d'injection des bulles. Points : valeurs expérimentales, courbes : prédictions du modèle.

1. Quelle est l'origine du sillage négatif ?
2. Comment évolue l'angle d'ouverture du cône ascendant et pourquoi ?
3. Quel est le rôle de l'interface gaz-liquide ?

Les étudiants qui m'ont précédés sur cette thématique ont apporté des éléments de réponse expérimentaux.

J'ai utilisé, pour répondre à ces questions, des outils d'expérimentation numérique. La démarche a consisté en l'élaboration de modèles de plus en plus simples et épurés, afin d'isoler les causalités physiques essentielles.

Modèle lattice Boltzmann diphasique

Le modèle rhéologique n'est certainement pas l'élément le plus complexe d'une démarche de modélisation et de simulation numérique de l'ascension d'une bulle dans un fluide non newtonien. En effet, la prise en charge de l'interface gaz-liquide est déjà en soi un défi. Intuitivement, l'interface d'une bulle relèverait plutôt d'une approche lagrangienne, alors que le champ de vitesse, de pression, etc... relèvent plutôt d'une approche eulerienne. Dans ce cas, toute la difficulté réside dans la gestion du couplage de ces deux types de description. Si de telles approches couplées existent, une approche mettant en œuvre un unique schéma de description sera plus simple et plus robuste. En l'occurence, l'approche Lattice Boltzmann relève d'une desciption Eulerienne.

La plupart des méthodes numériques Euleriennes en mécanique des fluides s'appuient sur une description continue de la matière. Au contraire, l'approche Lattice Boltzmann (LB) est issue de la physique statistique des sytèmes hors équilibre et prédit l'évolution d'une distribution de probabilité de présence de particules de fluide en un point donné et à une vitesze donnée. Par

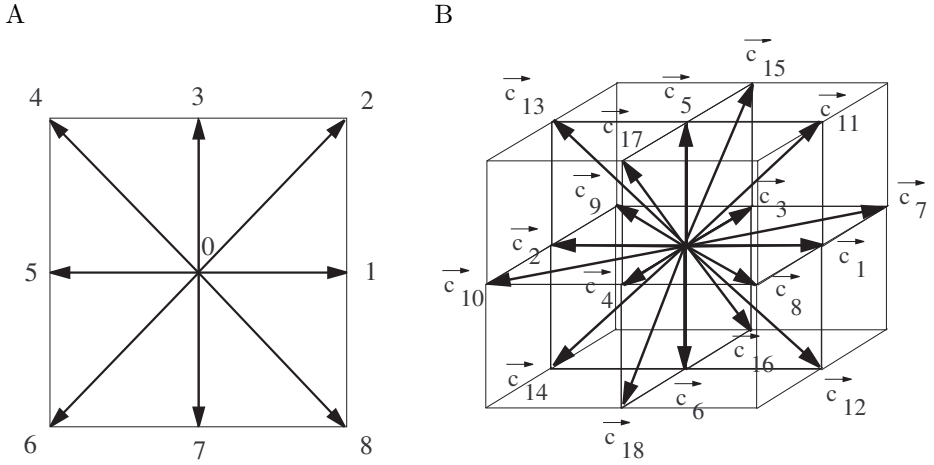

FIGURE 2.5 – Exemples de réseaux LB très utilisés. A : D2Q9, B : D3Q19.

conséquent, l'implémentation de l'approche nécéssite une discrétisation particulière, qui n'est pas seulement une discrétisation de l'espace et du temps, mais aussi une discrétisation de l'espace des vitesses de particule de fluide, appelée réseau (lattice), constitué d'un ensemble de vitesses de particules possibles $\vec{e}_i$. Le réseau doit obéir à certaines contraintes d'isotropie, aussi les réseaux habituellement utilisés sont peu nombreux. On peut citer deux réseaux très populaires (Fig. 2.5), le réseaux D2Q9 (réseau 2D comportant 9 vitesses de particule, vitesse nulle incluse) et le réseau D3Q19 (réseau 3D comportant 19 vitesses de particule, vitesse nulle incluse). Seul le réseau D2Q9 a été utilisé lors de mes travaux relatifs à la dynamique des bulles. L'état physique est décrit par une distribution $f_i\left(\vec{r},t\right)$ proportionnelle à la probabilité de trouver en $\vec{r}$ à l'instant t une particule de vitesse $\vec{e}_i$. Les grandeurs macroscopiques sont déduites des f_i sous la forme de moments, par exemple $\rho\vec{u} = \sum_i f_i\vec{e}_i$ où ρ est la densité du fluide et $\vec{u}$ sa vitesse.

La dynamique du système est prédite via une équation impliquant les f_i et non avec des équations portant directement sur les grandeurs macroscopiques.

$$f_i\left(\vec{r}+\delta t\vec{e}_i, t+\delta t\right) - f_i\left(\vec{r},t\right) = -\frac{1}{\tau_f}\left(f_i - f_i^{eq}\right) \tag{2.4}$$

Les distributions d'équilibre f_i^{eq} sont déduites des grandeurs macroscopiques, moyennant un tenseur de contrainte d'équilibre $P\delta_a, b$. Dans le cas monophasique Newtonien, celui-ci se réduit au tenseur de pression des gaz parfaits $P = \rho c_s^2$, où c_s est la vitese du son sur le réseau, ou, dit autrement, la vitesse maximale de propagation de l'information sur le réseau. Les grandeurs macroscopiques obéissent alors à l'équation de Navier-Stokes.

Les approches LB s'appuient donc sur une discrétisation particulière de l'équation de Boltzmann. Le modèle présenté ici est un modèle simplifié, dit Bhatnagar-Gross-Krook (BGK), dans lequel le terme de collision (Eq. 2.4 : membre de droite) s'identifie à un terme de relaxation linéaire simple vers l'état d'équilibre f_i^{eq}. Ce type d'approche très simple n'est utilisable que pour des bas nombre de Reynolds Re. Les approches à temps de relaxations multiples (MRT) permettent d'atteindre des nombres de Reynolds plus élevés [24].

Mettre en œuvre des écoulement diphasiques requiert d'introduire une thermodynamique plus complexe. Parmi les nombreux modèles LB diphasique disponibles, l'approche dite "à énergie libre" consiste à définir une densité d'énergie libre et à modifier en consquence l'état d'équilibre.

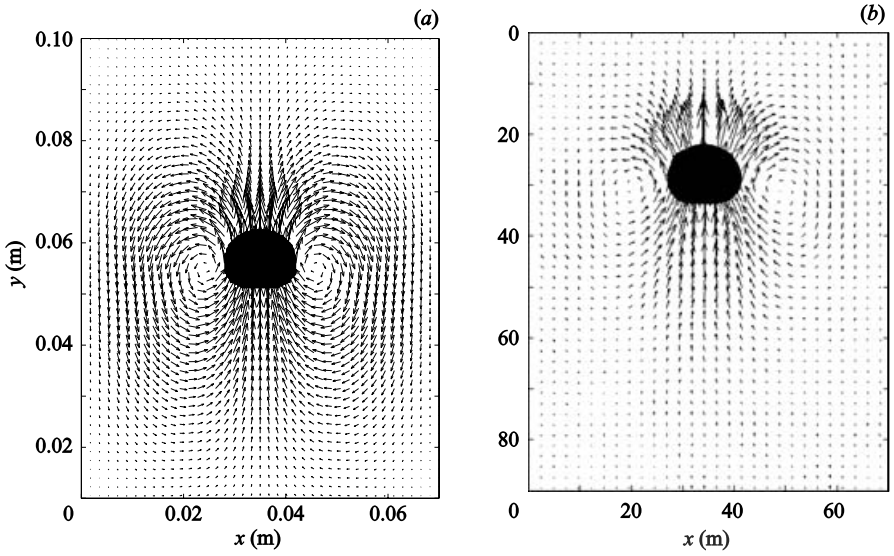

FIGURE 2.6 – Champ de vitesse autour d'une bulle et forme de bulle dans un fluide newtonien visqueux (glycérol 95%). a : Simulation numérique LB, b : Champ expérimental obtenu par P.I.V.. Volume de bulle $V_0 = 1100mm^3$.

Dans mes travaux de simulation, j'ai utilisé un modèle bi-constituant. La densité devient alors la somme des densités des constituants A et B : $\rho = \rho_A + \rho_B$, et on définit une différence de densités $\Delta\rho = \rho_A - \rho_B$. On définit deux distributions f_i et g_i, desquelles on déduit les grandeurs macroscopiques. On a donc deux équations LB, et il faut définir deux distributions d'équilibre f_i^{eq} et g_i^{eq}, à partir de ρ, $\Delta\rho$, $\vec{u}$, un tenseur de constrainte d'équilibre $P\delta_a, b$ (qui, cette fois, ne se réduit plus à la pression isotrope des gaz parfaits), ainsi qu'une différence de potentiel chimique $\Delta\mu$.

A titre de validation, l'approche LB $2D$ à énergie libre a été appliquée à l'ascension d'une bulle isolée dans un fluide newtonien visqueux [29]. Un fluide newtonien peut être considéré comme visqueux si son nombre de Morton $Mo = \frac{g\eta^4}{\rho\sigma^3}$ est grand. Ici, g est la pesanteur, η est la viscosité, σ le coefficient de tension interfciale. Le glycerol est un bon exemple de fluide visqeux, puisque $Mo = 67,7$. Par ailleurs, des mesures de vitesse d'ascension, des captures de forme de bulle, ainsi que des captures de champ de vitesse autour de bulles en ascension dans le glycerol ont été réalisées par Denis Fünfschilling [42], les résultats numériques ont donc pu être comparés systématiquement aux champs de vitesse mesurés par PIV (Fig. 2.6). Dans ces simulations LB sont imposés le volume des bulles, la poussée d'Archimèdes ainsi que la viscosité du liquide. La forme et la vitesse d'ascension sont prédites par les simulations.

Etant donnée la viscosité du fluide, le champ de vitesse est assez simple, et finalement pas très éloigné de ce qu'on pourrait observer en régime de Stokes. Le courant au voisinage de l'axe d'ascension est ascendant, et loin de l'axe, le courant est descendant, du fait de la recirculation globale. De même, la forme des bulles a été relevée pour différents volumes de bulle [42]. Comme constaté expérimentalement [9, 42], la forme prédite numériquement des bulles de faible volume est sphérique, alors que les bulles plus volumineuses présentent une forme légèrement applatie à l'arrière (Fig. 2.6). On constate par ailleurs, au vu des valeurs expérimentales et numériques de Re, que les vitesses d'ascension issues des simulations numériques sont en bon accord avec

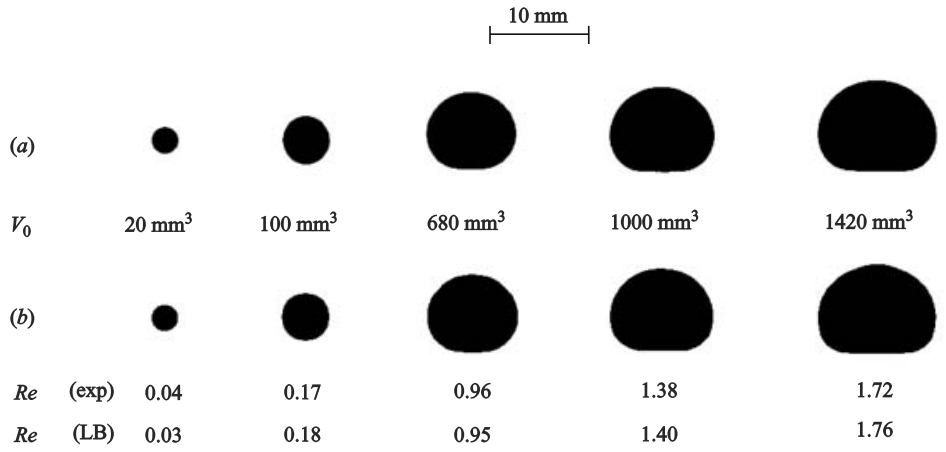

FIGURE 2.7 – Forme de bulle dans un fluide newtonien visqueux (glycérol 95%) en fonction du volume de bulle V_0. a : Simulation numérique Lattice Boltzmann, b : Forme obtenue expérimentalement. Valeurs expérimentales de Re, valeurs de Re prédites par les simulations LB.

l'expérience.

Comme le montre cette étude de validation, l'approche LB à énergie libre est capable de simuler l'ascension d'une bulle dans un fluide visqueux. Moyennant un couplage avec un modèle rhéologique, elle servira de base à la construction d'une approche LB diphasique dédiée aux fluides non newtoniens.

Couplage avec un modèle rhéologique

Plusieurs voies sont possibles pour réaliser un couplage entre un modèle LB diphasique et un modèle rhéologique. La plus directe consiste à calculer la force exercée localement par la composante non newtonienne de la rhéologie du liquide et à introduire cette force dans le modèle LB par les voies classiques [59]. Une approche plus sophistiquée consiste à s'appuyer sur un réseau LB étendu ainsi que sur un schéma du type MRT [46]. La question du couplage d'une approche LB avec un modèle rhéologique fait encore l'objet de recherches actives [51, 60, 86]. L'approche mise en œuvre durant ma thèse a consisté à ajouter au tenseur de pression d'origine thermodynamique lié au modèle diphasique à énergie libre P_{ij} un tenseur τ_{ij} lié aux contraintes mécaniques issues du modèle rhéologique [36].

Modèle non linéaire

Les fluides utilisés lors des travaux expérimentaux sur lesquels je me suis appuyé sont à la fois viscoélastiques, rhéofluidifiants et présentent des effets de mémoire assimilables à de la thixotropie. Ces comportments ont été caractérisés par des rhéogrammes (viscosité en régime permanent en fonction du taux de cisaillement), des essais en régime oscillant (viscoélasticité linéaire) et des tests de relaxation successifs (effets de mémoire). Un modèle a été conçu de façon à être en accord avec toutes les caractérisations disponibles. La base du modèle est un modèle

de Maxwell généralisé d'ordre 6

$$\tau_{ij} = \sum_{1}^{6} {\tau^k}_{ij} \tag{2.5}$$

$$\frac{d{\tau^k}_{ij}}{dt} + \lambda_k {\tau^k}_{ij} = G_k \epsilon_{ij} \tag{2.6}$$

où les (G_k, λ_k) sont les paramètres des ordres successifs du modèles de Maxwell, ajustés directement à partir des essais en régime oscillatoie linéaire, et ϵ_{ij} est le tenseur de cisaillement. Afin d'obtenir un comportement en régime de cisaillement permanent conforme aux rhéogrammes expérimentaux, on remplace les temps de relaxation λ_k du modèle de Maxwell par des temps de relaxation modifiés ${\lambda_k}'$ tels que

$${\lambda_k}' = \lambda_k \frac{\eta(\phi)}{\sum G_k \lambda_k} \tag{2.7}$$

où $\eta(\phi)$ est la viscosité prédite par le modèle de Carreau (2.2), le cisaillement étant remplacé par ϕ. L'expression au dénominateur de (2.7) s'ientifie à la viscosité de régime permanent prédite par le modèle de Maxwell d'ordre 6. Les effets de mémoire sont pris en compte dans le modèle à travers ϕ, qui obéit à une équation de relaxation phénoménologique dont le terme source est le cisaillement scalaire déduit de ϵ_{ij}. Les paramètres du modèle rhéologique non linéaire ont été ajustés grâce aux expériences de relaxations successives, réalisées par Denis Fünfschilling [36].

A partir de ce modèle couplé rhéologie/LB, plusieurs expriences numriques ont été réalisées. Celles-ci consistent à forcer verticalement une bulle dans le fluide non Newtonien, le champ de vitesse, le champ de contrainte et la forme de la bulle étant les sorties de la simulation. Comme on peut le constater au vu de mla Figure 2.8, un bon accord entre les simulations et les résultats expérimentaux est atteint. Une comparaison un peu plus quantitative concerne l'évolution de l'angle d'ouverture du cône ascendant entourant le sillage négatif avec le volume de bulle. Là encore, un bon acord avec l'expérience est constaté (Fig. 2.9). Ces résultats metent en évidence que l'origine du sillage négatif est à chercher dans les phénomènes pris en compte dans le modèle. A ce stade, on peut déjà formuler l'hypothèse que le sillage négatif est causé par la viscoslasticité. En effet, le sillage négatif n'apparaît pas derrière les bulles en fluide rhéofluidifiant non viscoélastique [42]. D'autre part, les effets de mémoire induisent à priori plutôt les interactions à longue distance entre bulles.

Viscoélasticité linéaire

Pour valider l'hypothèse de l'origine purement viscoélastique du sillage négatif, il faut drastiquement simplifier le modèle. D'une part, on va éliminer la déformabilité de l'inclusion en translation dans le fluide, et déplacer une particule sphérique plutôt qu'une bulle. D'autre part, le modèle rhéologique sera un modèle de Maxwell simple

$$\frac{d\tau_{ij}}{dt} = -\frac{1}{De}\left(\tau_{ij} - \tau_{ij}^{eq}\right) \tag{2.8}$$

$$\tau_{ij}^{eq} = \frac{1}{Re}\epsilon_{ij} \tag{2.9}$$

où De est le nombre de Deborah et Re est le nombre de Reynolds, l'équation (2.8) étant sous forme adimensionnée. Le nombre de Deborah est le ratio entre le temps de relaxation du fluide et le temps caractéristique de l'écoulement, ce qui peut s'exprimer à l'aide du taux de cisaillement $\dot{\gamma}$ sous la forme

$$De = \lambda \dot{\gamma} \tag{2.10}$$

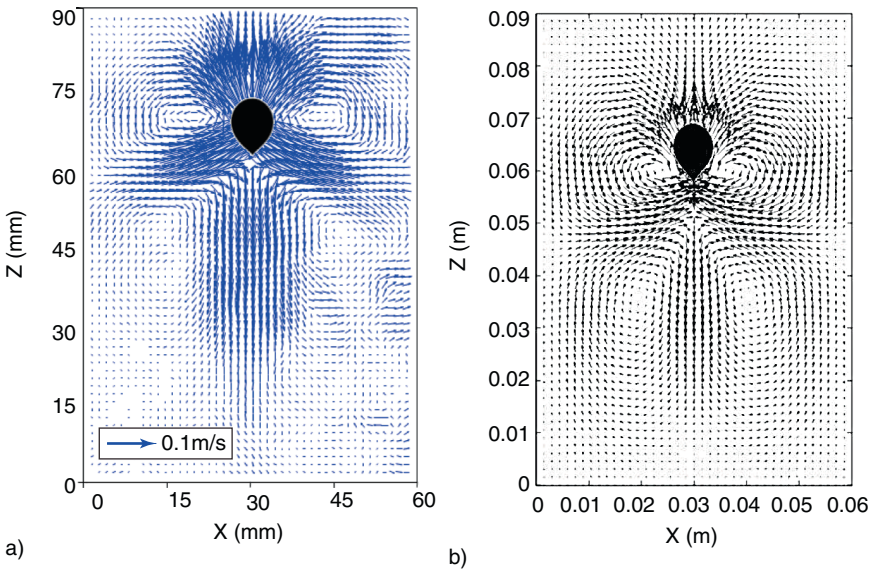

FIGURE 2.8 – Champ de vitesse autour d'une bulle et forme de bulle (volume de bulle $V_0 = 190mm^3$) dans un fluide non newtonien viscoélastique et rhéofluidifiant (solution aqueuse de PAAm 0, 75% en masse). a : Champ expérimental obtenu par P.I.V. et forme de bulle expérimentale, b : Champ de vitesse et forme de bulle prédite par simulation numérique LB.

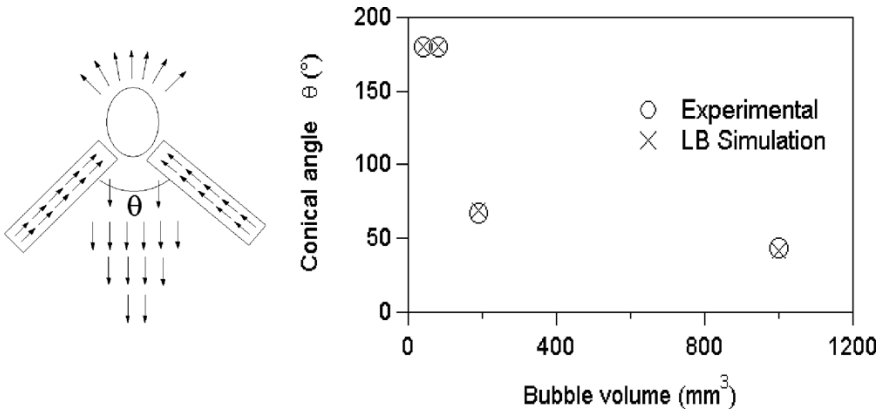

FIGURE 2.9 – Angle d'ouverture du cône ascendant autour du sillage négatif derrière une bulle en ascension dans un fluide non newtonien viscoslélastique. A gauche : représentation schématique du champ de vitesse autour de la bulle, définition de l'angle d'ouverture du cône ascendant θ. A droite : valeur de θ en fonction du volume de bulle, valeurs expérimentales obtenues par P.I.V. et valeurs prédites par simulation numérique LB.

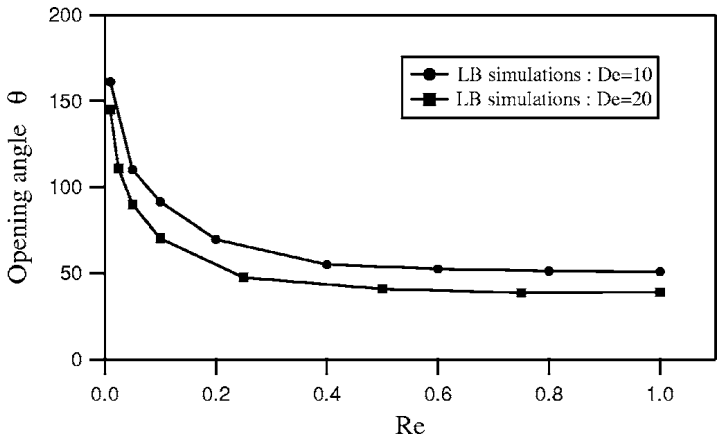

FIGURE 2.10 – Angle d'ouverture du cône ascendant en fonction du nombre de Reynolds Re pour différentes valeurs du nombre de Deborah De. Modèle rhéologique linéaire et inclusion rigide.

où λ est le temps de relaxation du fluide. Comme λ est une grandeur caractéristique intrinsèque du fluide, De caractérise un régime dépendant de $\dot{\gamma}$. Si le fluide est sollicité trop vite pour pouvoir relaxer vers l'équilibre ($\dot{\gamma} \gg 1/\lambda$), la valeur de De est grande et le fluide se comporte de manière élastique. A l'inverse, si le fluide est sollicité assez lentement pour pouvoir relaxer vers l'équilibre ($\dot{\gamma} \ll 1/\lambda$), la valeur de De est faible et le fluide se comporte de manière visqueuse. Dans ce dernier cas, le tenseur de contrainte τ_{ij} est alors très proche de τ_{ij}^{eq}.

Le modèle LB est, dans le cas présent, lui aussi beaucoup plus simple, puisqu'il s'agit d'un écoulement monophasique sollicité par une inclusion solide (la sphère qui remplace la bulle).

Un balayage paramétrique avec différentes valeurs de De et de Re a été réalisé. On observe encore une fois un champ de vitesse conforme aux constatations expérimentales [37]. Par ailleurs, l'angle d'ouverture du cône θ est également décroissant avec Re, mais aussi avec De (Fig. 2.10).

Si ces expériences numériques permettent d'attribuer le sillage négatif et le cône ascendant à la viscoélasticité, elles ne permettent pas d'expliciter clairement les causalités.

Oscillations dans le sillage

Une interprétation physique complète de l'apparition du sillage négatif comme conséquence de la viscoélasticité linéaire a été rendue possible grâce à un phénomène découvert indépendamment par l'expérimentation et la simulation numérique. Il s'agit des oscillations dans le sillage. On considère la translation d'une particule en sédimentation pour simplifier. Si on se place en un point fixé du fluide, après le passage de la particule, on observe le sillage négatif ascendant, puis, le fluide reprend un mouvement descendant, comme en fluide Newtonien, puis encore le sillage négatif, etc... [28].

Un tel comportement évoque un oscillateur amorti par frottement fluide. En capturant, à l'aide de la P.I.V., non plus un champ de vitesse, mais la vitesse locale du fluide en un point fixe, on peut adopter un point de vue plus quantitatif. Ici, seule la composante verticale sur l'axe de sédimentation de la particule est intéressante. Les oscillations ainsi observées sont bien représentées par un modèle d'oscillateur linéaire amorti (Fig. 2.11).

On peut donc formuler l'hypothèse que le sillage négatif est lié à un comportement essentiellement élastique du fluide. Le passage de l'inclusion, qu'il s'agisse d'une bulle en ascension

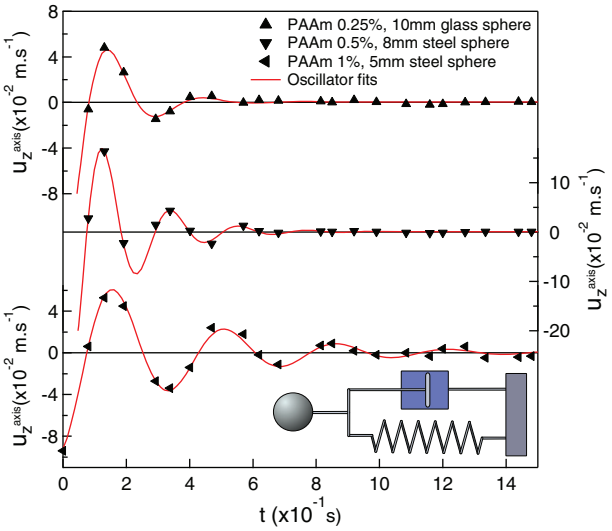

FIGURE 2.11 – Exemples de dynamique de la composante verticale de la vitesse sur l'axe de sédimentation après le pasage d'une sphère dans un fluide viscoélastique, prédictions d'un modèle d'oscillateur linéaire amorti.

ou d'une particule en sédimentation, déplace une masse de fluide. Du fait du comportement élastique, celle-ci revient à sa position initiale sous l'effet des forces de rappel élastiques et des processus dissipatifs au sein du fluide. Ce retour à l'équilibre a lieu selon une dynamique d'oscillateur amorti. Si cet oscillateur est sous-critique, des oscillations apparaissent et se traduisent dans le sillage sous la forme de zones alternées de flot ascendant et de flot descendant.

Dans ce contexte, il est plus judicieux de raisonner en termes de cisaillement plutôt que de vitese de cisaillement. Si on définit δ comme un déplacement local du fluide, on peut définir un cisaillement $\frac{\delta}{r_s}$ où r_s est le rayon de la sphère en sédimentation. Moyennant un bilan de forces sur la portion de fluide initialement déplacée par le passage de l'inclusion [28], et en négligeant la dissipation visqueuse, le déplacement δ obéit à une équation diférentielle du second ordre

$$\frac{d^2\delta}{d\delta^2} + \frac{G}{\rho {r_s}^2}\delta = 0 \tag{2.11}$$

où G est le module de cisaillement et ρ la masse volumique. Il s'agit bien de l'équation d'un oscillateur et on identifie une fréquence d'oscillation propre $\omega_0 = \sqrt{\frac{G}{\rho {r_s}^2}}$. Relier la fréquence d'oscillation à un module de cisaillement représente un avantage important. La valeur de G effective dans le cas présent est une valeur transitoire, et s'il est difficile de l'obtenir à l'aide d'un rhéomètre, il est en revanche aisé de mesurer la fréquence d'oscillation dans le sillage négatif. Celui-ci jour donc le rôle de rhéomètre local.

La forme du cône entourant le sillage négatif évoque spontanément celle d'une onde de choc. De plus, l'angle du cône θ diminue lorsque la vitesse de la source augmente, ce qui tendrait à corroborer cette idée. Ce type de structure dépend de la valeur du nombre de Mach M, qui est le ratio entre entre la vitesse de la source d'ondes, qui n'est autre que la vitesse de sédimentation de la sphère et la vitesse de propagation des ondes. Ici, il s'agit d'ondes de cisaillement, et on

peut exprimer leur célérité sous la forme $c = \sqrt{\frac{G}{\rho}}$, et donc, le nombre de Mach est donné par

$$M = \frac{v_s}{c} = \frac{v_s}{\omega_0 r_s} \tag{2.12}$$

où v_s est la vitesse de sédimentation de la sphère. Le nombre de Mach peut également être calculé à partir des paramètres du modèle rhéologique sous la forme $M = \sqrt{DeRe}$. Etant donné que θ dépend à la fois de Re et de De (Fig. 2.10), on peut vérifier numériquement l'hypothèse selon laquelle le cône entourant le sillage négatif trouve son origine dans un phénomène de propagation d'ondes. Deux jeux de simulations LB ont été réalisés, chacun à M constant, et cette hypothèse a été confirmée, θ étant constant à M constant [28].

Cependant, les simulations numériques ne prédisent pas un changement qualitatif lorsque $M < 1$, ce qui est en contradiction avec l'hypothèse d'une onde de choc. Dans ces situations, le cône est simplement très plat, mais il existe toujours. Sans renoncer à l'hypothèse de la propagation d'ondes, sur la base de résultats expérimentaux de la littérature [112], on peut avancer une hypothèse légèrement différente selon laquelle le passage de l'inclusion génère une onde de cisaillement se propageant horizontalement. Dans ce cas, le cône existe quel que soit M, et son angle est prédit par la relation

$$\tan\left(\frac{\theta}{2}\right) = \frac{1}{M} \tag{2.13}$$

On peut mesurer θ à partir des simulations numériques et à partir des champs de vitesse obtenus expérimentalement. Le nombre de mach M peut être déduit de De et de Re dans le cas des simulations numériques. Enfin, les valeurs expérimentales de M peuvent être déduites de la fréquence d'oscillation à l'aide de la relation (2.12). Les simulations numériques et les résultats expérimentaux peuvent donc être comparés aux deux hypothèses concernant l'origine du cône : celle d'une onde de choc, et celle d'une propagation latérale (Fig. 2.12).

On constate clairement que l'hypothèse de l'onde de choc n'est pas valide. En revanche, celle de la propagation latérale d'une onde de cisaillement au passage de l'inclusion est en bon accord avec les simulations numériques et avec les résultats expérimentaux. Il est donc posible d'expliquer la géométrie du sillage à l'aide de la viscoélasticité linéaire.

2.1.4 Modèle multi-agents

Lorsque le gaz est injecté en continu, ou, d'une manière plus générale, lorsque la période de bullage T est suffisamment faible, le train de bulles ne reste pas périodique et des coalescences ont lieu entre bulles successives, donnant lieu à une dynamique globale très complexe. Une coalescence entre bulles implique différentes échelles, le film liquide séparant les bulles étant progresivement aminci jusqu'à l'échelle moléculaire. Prendre en compte tous les détails de la dynamique d'un train de bulles chaotique en fluide non Newtonien demeure une tâche irréaliste, en particulier lorsque l'objectif est de dégager la statistique du système. Non seulement le système requiert d'être décrit à des échelles très différentes, mais doit surtout être simulé sur des durées importantes, de façon à obtenir un échantillonnage suffisant.

Etant donné qu'une coalescence est un phénomène très rapide à l'échelle de la dynamique globale du système, une description détaillée est non seulement d'une difficulté extrême, elle est aussi dépourvue de pertinence. Malgré tout, il faut bien prendre en compte les coalescences. Une expérience fortuite a inspiré une approche radicale, proposée par le professeur Huai Zhi Li, et que j'ai pu mettre en œuvre dans mes travaux. Initialement, l'expérience consistait à injecter du colorant au voisinage d'un train de bulle, afin de visualiser les écoulements locaux. Celle-ci a eu

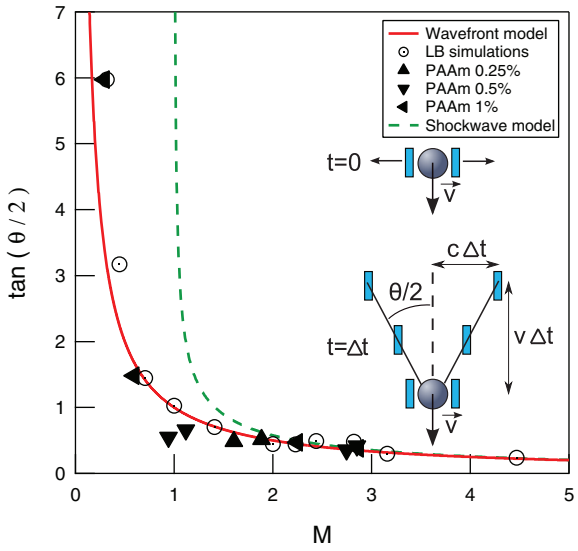

FIGURE 2.12 – Ouverture du cône autour du sillage négatif derrière une sphère sédimentant dans un fluide viscoélastique. Résultats expérimentaux, simulations numériques, modèle de propagation d'ondes latérales (représentation schématique incluse), modèle de l'onde de choc, pour comparaison.

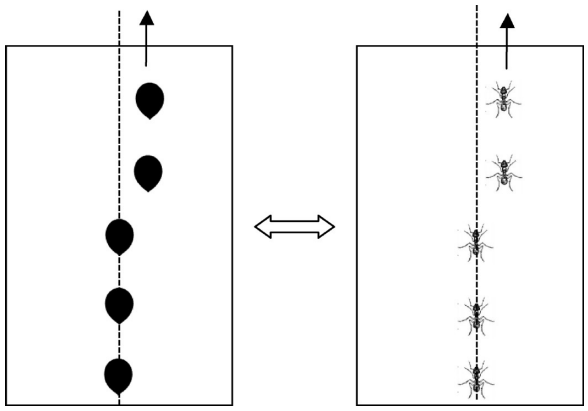

FIGURE 2.13 – Analogie entre un train de bulles en fluide Newtonien en interaction avec les contraintes résiduelles liées aux passages successifs de bulle et une colonne de fourmis en interaction avec les phéromones déposées sur le sol lors des passages successifs de fourmi.

un effet inattendu : le train de bulles a été dévié au voisinage de la zone d'injection du colorant, et ce, durablement (Fig. 2.13).

Ce comportement rappelle celui d'une colonne de fourmis en quête de nourriture. Une fourmi dépose des phéromones sur le sol au cours de ses déplacements, et les fourmis suivantes ont tendance à suivre le même chemin de phéromones. Ce mécanisme permet à une fourmillière d'exploiter en priorité les sources de nourriture les plus proches du nid [17]. Cette expérience suggère une analogie entre les bulles et les fourmis, entre les contraintes résiduelles créées par le passage des bulles et les phéromones. Les phénomènes d'intelligence collective en société d'insectes, en robotique, etc... sont habituellement modélisés à l'aide de systèmes multi-agents : les individus ont un comportement obéissant à des règles simples et sont en interaction les uns avec les autres [17]. Le comportement global du système émerge des ces règles locales.

Plutôt que de décrire précisément toute la complexité des coalescences, il s'agit ici de modéliser celles-ci à l'aide d'une règle très simple : une fois que deux bulles sont en contact, elles coalescent et sont remplacées par la bulle résultante. Cette transition a lieu en un pas de temps de la simulation numérique, on considère donc que le temps caractéristique d'une coalescence est négligeable vis-à-vis des temps impliqués dans les interactions à distance.

Concernant les bulles, etant donnée la visosité du fluide, on fait l'approximation du régime quasi-statique, ce qui signifie que la vitesse d'ascension de chaque bulle ne dépend que d'un seul paramètre extrinsèque : la contrainte résiduelle locale rencontrée par la bulle. On utilise donc le modèle dynamique développé dans le cas du train de bulles périodique (2.1.2), la contrainte résiduelle n'étant plus une constante, mais un champ dependant de la hauteur z dans la colonne à bulle. Le champ de contrainte résiduelle obéit à l'équation 2.1 en chaque point, le cisaillement $\dot{\gamma}$ étant lui aussi un champ, résultant de la superposition linéaire de chaque champ de cisaillement moyenné sur une section de colonne imposé par chaque bulle.

La hauteur de la colonne est discrétisée par 20000 cellules afin de résoudre numériquement l'équation 2.1, les bulles sont introduites en bas de la colonne à la fréquence de bullage observée expérimentalement et les bulles ayant atteint le haut de la colonne sont simplement éliminées de la simulation. Les simulations numériques prédisent un comportement tout aussi complexe que celui qui est observé expérimentlement (2.14).

La comparaison simulation/expérience nécessite une caractérisation quantitative. Du fait de la légèreté numérique du modèle, celui-ci permet de simuler des temps très longs, ce qui donne accès à un échntillonnage en terme de nombre de bulles comparable aux données expérimentales.

Un premier niveau de comparaison porte sur les signaux de détection de bulle eux-même. Ils sont reconstitués à partir des simulations numérique moyennant l'hypothèse que les pics de détection sont des gaussiennes dont la largeur temporelle corespond au temps de pasage d'une bulle en un point donné, et dont l'amplitude est fixée. Le spectre du signal ainsi généré est calculé, et comparé aux spectres issus des expérimentations (2.15).

L'accord entre simulation et expérience est correct [68]. Près de la buse d'injection de gaz, le signal est périodique, on observe une fréquence fondamentale et une ou plusieurs harmoniques. Plus haut dans la colonne, la dynamique est chaotique et le spectre devient continu. Un raisonnement théorique simple suggère que cette transition vers le chaos relève d'un doublement de période [38]. Cependant, expérimentalement, la transition vers le chaos en fonction de la hauteur de détection des bulles est extrêmement rapide, ce qui signifie qu'il est difficile d'observer concrètement le doublement de période. Réaliser cette observation est bien plus facile dans le cadre des simulations numériques. L'hypothèse d'un doublement de période est ainsi coroboré par la simulation numérique [38].

Du point de vue des application industrielles, l'information la plus essentielle est la surface de bulle disponible pour les transferts de matière entre la phase liquide et la phase gaz. La conséquence directe des coalescences est la diminution du nombre de bulles comptées à hauteur

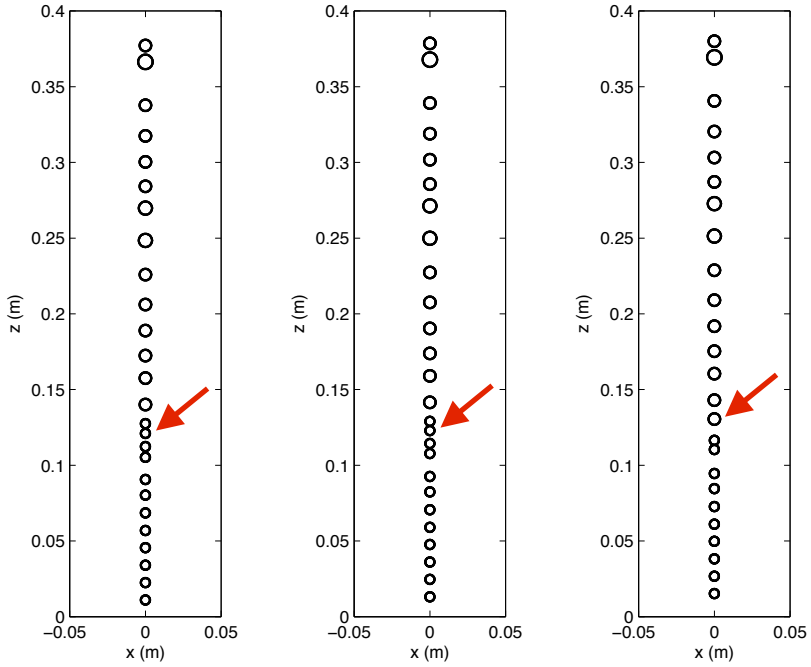

FIGURE 2.14 – Extrait de la dynamique d'un train de bulles chaotique modélisé et simulé par approche multi-agents. La flèche indique une coalescence.

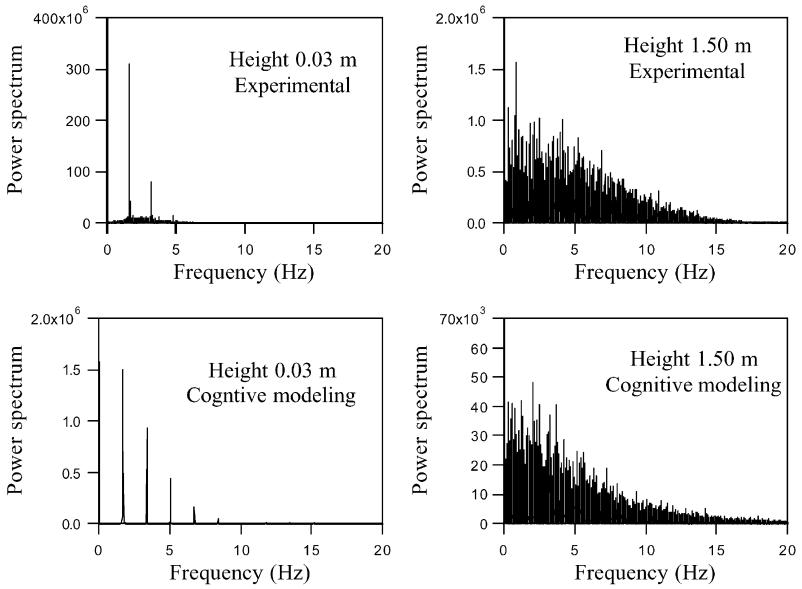

FIGURE 2.15 – Spectres des signaux de détection du passage des bulles prélevés à une hauteur de $3cm$ et à une hauteur de $1,5m$ dans le cas d'une solution à $0,75\%$ de PAAm. Comparaison modèle multi-agents/expérimental.

de détection croissante, ainsi que la diversification des diamètres de bulle. Par conséquent, les coalescences ont pour effet de faire chuter la surface d'interface gaz-liquide disponible. L'évolution du nombre de bulles avec la hauteur de détection (2.16 :A), ainsi que la distribution de tailles de bulles (2.16 :B) prédites par les simulations numériques sont en bon accord avec les résultats expérimentaux [33, 41, 68].

Ces effets ne sont pas sytématiquement négatifs, dans certains cas, il peut être intéresant de faire apparaître de grosses bulles. Par exemple, la dévolatilisation des polymères permet d'évacuer le solvant et les monomères n'ayant pas réagi après polymérisation. Si les coalescences génèrent des bulles plus grosses, celles-ci se déplacent plus vite et évacuent la phase volatile avec une efficacité accrue.

Les succès de l'approche multi-agents permettent de valider les hypothèses faites quant aux interactions entre bulles à l'origine de la dynamique complexe observée, et corroborent l'idée d'une transition vers le chaos par doublement de période.

2.2 Modélisation moléculaire

A certaines échelles, les propriétés globales des systèmes considérés ne peuvent être prédites et comprises que en tenant compte de la structure moléculaire ou supra-moléculaire. Dans ce cas, les seules approches numériques bottom-up viables relèvent de la simulation moléculaire. En toute rigueur, seules les approches quantiques mettent en œuvre une description réaliste des systèmes moléculaires, mais en pratique, si le système n'est pas le siège de réactions chimiques, il est possible de l'assimiler à un ensemble d'atomes ponctuels en interaction. Tout l'enjeu est alors de définir et paramétrer les interactions entre atomes. Un jeu de potentiels dûement paramétré

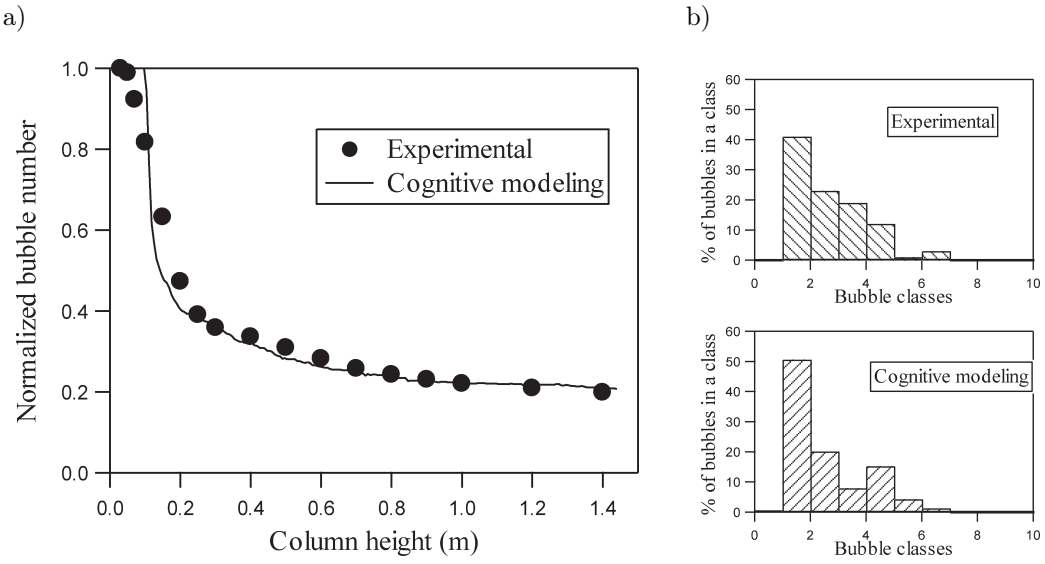

FIGURE 2.16 – Statistique des populations de bulles, comparaison modèle multi-agents/expérimental : a) Evolution du nombre de bulles détectées avec la hauteur de détection dans la colonne dans le cas d'une solution à $0,5\%$ de PAAm, b) classes de bulles détectées à une hauteur de $0,4m$ dans le cas d'une solution à $0,75\%$ de PAAm.

est appelé un champ de forces.

Les champs de forces constituent un ensemble particulièrement vaste et varié [20,21,61,96]. Il existe des champs de force à vocation universelle [94], spécialisés dans les matériaux métalliques [111] ou certains types de molécules [47,73]. Si un certain nombre de champs de force sont en partie paramétrés grâce à des simulations par approche quantique, il est toujours nécessaire d'ajuster les paramètres à posteriori, en particulier pour être en mesure de prédire correctement certaines constantes thermodynamiques. Du fait de leur caractère souvent empirique ou semi-empirique, les champs de force ont une précision croissante avec le degré de spécialisation.

On peut distinguer deux types de potentiel d'interaction dans un champ de forces :

— Les potentiels liées, représentant des interactions de forte intensité, dûes aux liaisons covalentes

— Les potentiels non liés, représentant des interactions de faible intensité, indépendantes des liaisons covalentes

Les potentiels liés (Fig. 2.17 :a) peuvent impliquer deux corps (élongation des liaisons), trois corps (flexion entre deux liaisons covalentes), quatre corps (torsion d'une liaison covalente). La plupart des interactions non liées (Fig. 2.17 :b) impliquent deux corps, il s'agit par exemple des interactions de type Van der Waals ou électrostatiques.

Une caractéristique importante des interactions non liées est qu'elles ont une portée bien plus importante que les interactions liées. C'est pourquoi le nombre de termes à calculer dans cette catégorie est bien plus grand que dans l'autre. Une conséquence capitale est que, en général, 95% du temps de calcul est consacré au calcul des termes d'interaction non liés. Le volume de calcul à exécuter est très important, ce qui limite en pratique les durées de phénomène simulé à quelques dizaines de nanosecondes. Une durée de cet ordre peut être suffisant pour déterminer

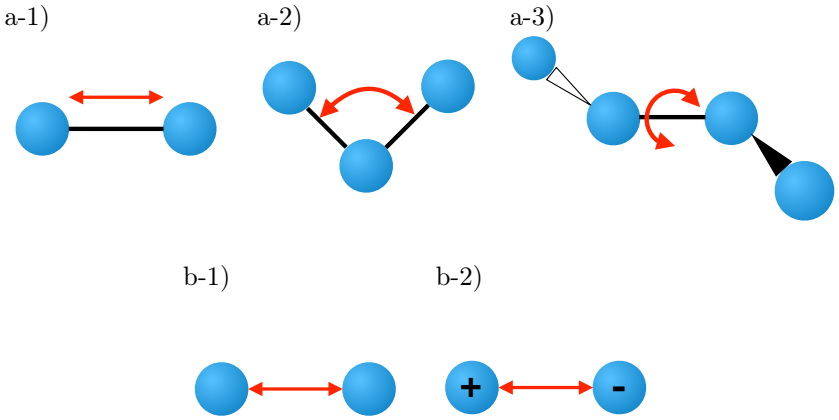

FIGURE 2.17 – Exemples d'interactions impliquées en dynamique moléculaire. a) interactions liées : 1) liaisons, 2) angles, 3) angles dièdres. b) interactions non liées : 1) forces de Van der Waals, 2) forces électrostatiques.

la dynamique de phénomènes impliquant de petits systèmes. En revanche, lorsque les systèmes impliqués sont plus volumineux, il peut être nécessaire de simuler des phénomènes aux temps plus long, comme par exemple, dans le cas des repliements de protéine.

2.2.1 Modèle gros grain (Coarse Grain)

Afin de réduire la durée des calculs nécéssaires à la simulation numérique d'un système moléculaire donné, il peut être efficace de réduire le nombre de degrés de liberté. Un modèle gros grain a pour objectif de réduire le nombre de degrés le liberté, d'une part, et de réduire le nombre de termes d'interaction à calculer, d'autre part. Il s'agit d'une approximation, par conséquent, la réduction du nombre de degrés de liberté implique une perte d'information. Le nombre de modèles et champs de force gros grain disponibles dans la littérature est en constante croissance. Certains sont dédiés à des ensembles de molécule, comme le champ de force MARTINI, dédié aux biomolécules [75, 80, 109] et d'autres sont plus spécialisés [25, 84, 93].

En pratique, la définition d'un modèle gros grain consiste à

— Regrouper des atomes voisins en " grains ".

— Déterminer les potentiels d'interaction entre ces grains.

La définition des grains est nécessairement entachée d'une part d'arbitraire. On peut tout de même noter que cette étape va être déterminante pour l'accélération attendue, mais aussi la perte d'information concernant la forme effective des molécules simulées, leur déformabilité, leur orientation... Un modèle gros grain sera d'autant plus rapide que la définition du système s'appuie sur un nombre de grains faible, mais les informations qui pourront en être tirées seront d'autant plus parcellaires et imprécises.

Les champs de force gros grains peuvent également être construits de différentes manière. Cependant, une approche très fréquente consiste à passer par l'intermédiaire d'une trajectoire à l'échelle atomistique. Dans ce cas, le champ de force gros grain est dépendant du champ de force atomistique utilisé pour produire la trajectoire tout atomes.

a) 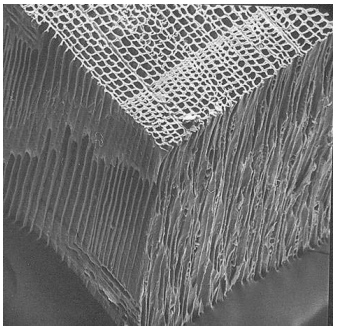 b) 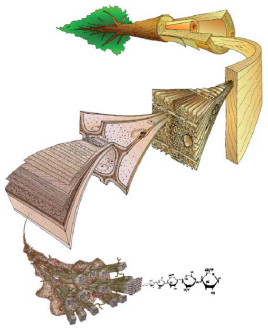

FIGURE 2.18 – Composition du bois : a) agencement cellulaire à l'échelle micrométrique visualisée par microscope électronique à balayage (pin maritime, image issue de [89]), b) représentation schématique de la structure moléculaire des parois des cellules (représentation de Mark Harrington, University of Canterbury, 1996).

Une méthode simple consiste à déduire chaque terme d'interaction par inversion de Boltzmann. Dans l'ensemble canonique de la physique statistique (c.a.d. à volume et températures fixées), la probabilité d'une configuration du système d'énergie U est proportionnelle au facteur de Boltzmann e^{-U/k_BT}, où k_B est la constante de Boltzmann et T la température. A partir de la trajectoire atomistique, il est possible de déduire la trajectoire du système gros grain correspondant, et donc, les probabilités de configuration p. Un potentiel tabulé se déduit enfin du facteur de Boltzmann (eq. 2.14) et peut faire l'objet d'une modélisation mathématique.

$$U = -k_B T \ln p \tag{2.14}$$

Une autre approche consiste à calculer la force exercée entre grains par sommation des forces s'exerçant entre les atomes qui les composent pour un nombre suffisant d'états de la trajectoire atomistique. A partir du nuage de points obtenu, les paramètres d'un modèle de force peuvent être ajustés.

Pour chacune de ces méthodes il peut être nécessaire d'affiner les paramètres du modèle de potentiel obtenu. Pour ce faire, on se donne comme référence une distribution de probabilité g_{ref}, par exemple celle d'une distance entre deux grains, issue de la trajectoire atomistique. L'optimisation du modèle consiste à exécuter des simulations numériques gros grain, en déduire la distribution de probabilité g_{CG}, et à ajuster les paramètres en fonction de la différence entre g_{CG} et g_{ref}.

2.2.2 Application : composite xylane-cellulose

Le bois est un matériau composite à la fois anisotrope, hétérogène et poreux [63]. Il est composé des parois lignifiées produites par les cellules de l'arbre (Fig. 2.18 :a). Les propriétés mécaniques du bois dépendent à la fois de son agencement cellulaire et des propriétés mécaniques intrinsèques des parois [87]. Les parois sont elles-même des matériaux composites, constitués d'une matrice amorphe d'hémicelluloses et de lignines renforcées par des microfibrilles de cellulose (Fig. 2.18 :b).

Le projet ANR *ANALOGS* (2009-2013) a consisté en la mise en œuvre de deux démarches de modélisation de la paroi du bois : une démarche de modélisation expérimentale, s'appuyant sur la construction d'analogues de la paroi à partir des polymères pariétaux et une démarche de modélisation numérique par dynamique moléculaire.

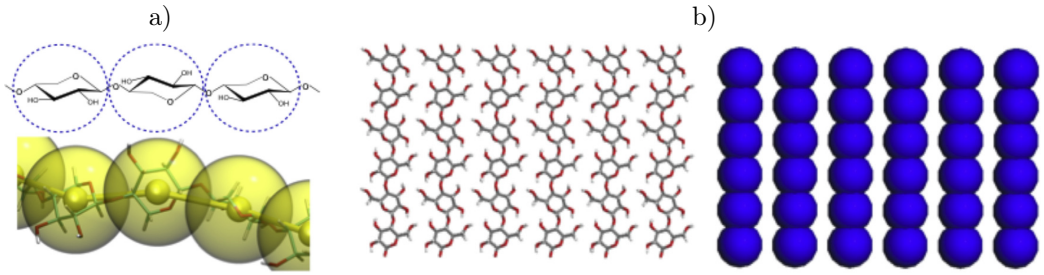

FIGURE 2.19 – Définition des grains dans le modèle cellulose-xylane. Un monomère définit un grain. a) définition des grains pour le xylane. b) définition des grains pour la surface de cellulose cristalline.

Un modèle numérique minimal d'un tel matériau devrait comporter plusieurs microfibrilles de cellulose et représenterait un poids numérique considérable en tout atomes. Pour exemple, on peut citer une simulation atomistique réalisée en 2009 (c.a.d. à peu près contemporaine des travaux présentés ici), impliquant 52 polymères de lignine comportant chacun 61 monomères, 36 polymères de cellulose comportant chacun 80 monomères, ainsi qu'un solvant explicite (de l'eau), pour un total de 3 300 000 atomes [100]. En dépit de la modeste taille de ce système au regard de la paroi végétale, les 30 000 processeurs dévolus au calcul n'ont pu simuler que $28ns$ de dynamique par jour. Bien qu'il ne s'agisse pas, en toute rigueur, d'un modèle de paroi du bois, cet exemple démontre clairement l'intérêt des approches gros grain pour ce type de problématique.

L'approche la plus simple pour définir des grains à partir de la structure moléculaire d'un polymère consiste à attribuer un grain à chaque monomère. Dans le cas des polymères de la paroi du bois, il s'agit donc de définir un grain par ose (Fig. 2.19). En procédant ainsi, on perd toute information concernant l'orientation des monomères, ce qui consistue une approximation assez forte. C'est le choix qui a été fait, en partie en raison du faible poids numérique impliqué.

On se limite ici à des applications impliquant uniquement du xylane non branché et de la cellulose cristalline [71]. Le champ de forces gros grain a été paramétré grâce à des simulations atomistiques, réalisées par Karim MAZEAU, du CERMAV à Grenoble.

Les potentiels intramoléculaires ont été déduits par inversion de Boltzmann à partir de trajectoires atomistiques de chaines de xylane isolées (Fig. 2.20). Une distribution de probabilité des valeurs de distance grain-grain, d'angle ou d'angle dièdre est générée à partir des trajectoires atomistiques, puis les paramètres d'un modèle de potentiel gros-grain sont ajustés de façon à ce que la distribution de probabilité calculée à l'aide du facteur de Boltzmann soit le plus proche possible de la distribution initiale, issue des simulations atomistiques. Cette approche simple est particulièrement efficace dans le cas des interactions intramoléculaires, du fait que les positions relatives des grains soient très contraintes en intramoléculaire, il est par conséquent assez facile d'obtenir un échantillonnage atomistique de qualité.

Le potentiel contraignant les liaisons xylane-xylane est un potentiel quadratique très simple

$$U_{stretching}\left(r\right) = \frac{1}{2} k_{stretching} (r - r_{stretching})^2 \tag{2.15}$$

où r est la distance entre les grains, $r_{stretching}$ la distance d'équilibre et $k_{stretching}$ une constante. Le potentiel contraignant l'angle entre deux liaisons xylane-xylane sucessives est un potentiel quadratique sur les cosinus

$$U_{bending}\left(\theta\right) = k_{angle} (\cos\theta - \cos\theta_0)^2 \tag{2.16}$$

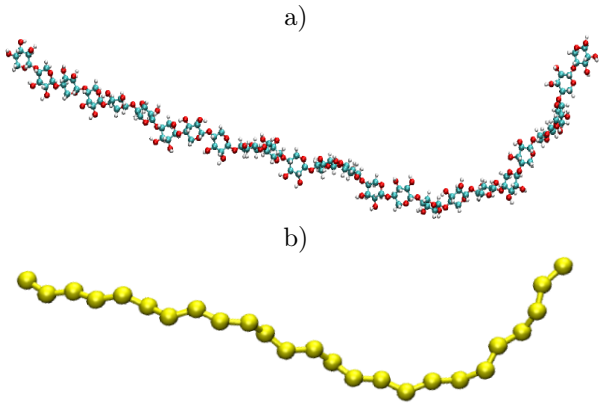

FIGURE 2.20 – Chaîne de xylane utilisée pour déterminer les potentiels d'interaction intramoléculaire : a) en atomistique b) en gros grain.

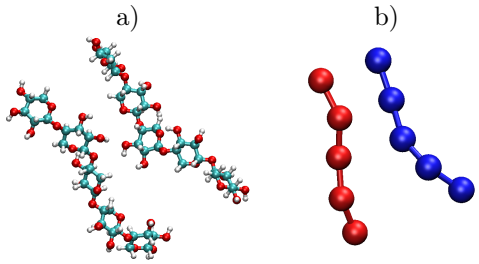

FIGURE 2.21 – Oligomères de xylane utilisés pour déterminer le potentiel d'interaction intermoléculaire xylane-xylane : a) en atomistique b) en gros grain.

où θ est l'angle entre deux liaisons, θ_0 l'angle d'équilibre et k_{angle} une constante. Le potentiel contraignant les angles dièdres s'exprime comme les premiers termes d'une série de Fourier

$$U_{dihedral}(\phi) = \sum_{n=1}^{n=3} \frac{1}{2} k_n \left(1 - \cos\left(n\left(\phi - \phi_n\right)\right)\right) \tag{2.17}$$

où ϕ est l'angle dièdre entre trois liaisons successives, les k_n et les ϕ_n sont des constantes.

Le potentiel d'interaction intermoléculaire xylane-xylane a été obtenu à partir de trajectoires atomistiques d'une paire d'oligomères de xylane (Fig. 2.21).

L'échantillonnage utilisé dans le cas de cette interaction était de moindre qualité, aussi le potentiel a-t-il été obtenu en deux étapes. En premier lieu, un premier paramétrage a été obtenu de la même façon que celui des modèles de potentiels intramoléculaires : une distribution de probabilité de la distance entre grains de xylane a été déduite des trajectoires atomistiques et les paramètres d'un modèle de potentiel d'interaction ont été ajustés de façon à faire coïncider le facteur de Boltzmann gros grain avec la distribution issue des simulations atomistiques. Le potentiel gros grain obtenu a été utilisé afin de reproduire la distribution initiale. L'écart observé étant non négligeable, les paramètres du potentiel gros grain ont été ajustés à posteriori de façon à le minimiser. Le potentiel définitifg est un potentiel de Morse :

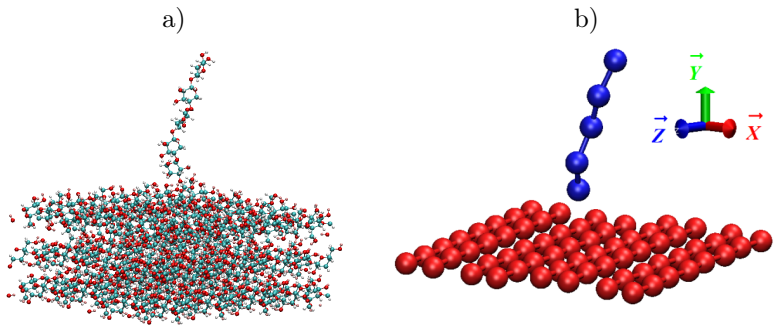

FIGURE 2.22 – Système xylane-cellulose cristalline utilisé pour déterminer le potentiel d'interaction intermoléculaire xylane-cellulose : a) en atomistique b) en gros grain.

$$U_{xylan-xylan}\left(r\right) = D_e\left(1 - e^{-\alpha(r - r_{xylan-xylan})^2}\right) \tag{2.18}$$

où r est la distance entre deux grains de xylane, $r_{xylan-xylan}$ la distance d'équilibre, D_e et α sont des constantes.

Le potentiel d'interaction intermoléculaire xylane-cellulose est déduit de la trajectoire atomistique d'un oligomère de xylane en interaction avec une surface (110) de cellulose cristalline (Fig. 2.22).

Un paramétrage initial du potentiel gros grain est déduit par force-matching : l'intensité des forces exercées entre un grain de xylane et les grains de cellulose de surface est calculée à chaque pas de temps à partir des forces atomistiques. On génère ainsi un nuage de points liant une duistance inter-grains à une intensité de force. Les paramètres d'un modèle de force gros grain sont ensuite ajustés à l'aide de ce nuage de points. Encore une fois, il est nécessaire d'optimiser ces paramètres à l'aide de simulations gros grain successives. On cherche à prédire la distribution de distances grain de xylane-surface de cellulose. Le modèle utilisé est le classique potentiel de Lennard-Jones

$$U_{xylan-cellulose}\left(r\right) = 4\epsilon\left[\left(\frac{\sigma}{r}\right)^{12} - \left(\frac{\sigma}{r}\right)^{6}\right] \tag{2.19}$$

où r est la distance entre un grain de xylane et un grain de cellulose, σ est la distance d'équilibre et ϵ une constante.

Plusieurs faces différentes peuvent être identifiées sur la cellulose cristalline, et pour chaque face, les periodicités spaciales et les groupes exposées ne sont pas les mêmes. Par conséquent, on définit un paramétrage pour chaque surface de cellulose. On tient compte ici des principales surfaces : (110) , $(1-10)$ et (100). Les potentiels d'interaction xylane-cellulose pour les surfaces $(1-10)$ et (100) sont déduits du potentiel d'interaction xylane-cellulose pour les surfaces (110) moyennant l'application au potentiel d'interaction d'un facteur multiplicatif identique aux ratios d'énergie d'absorption du xylane obtenus par dynamique moléculaire tout-atomes.

Ce modèle gros grain a été appliqué à différentes situations [71], notamment l'adsorption d'une chaine de xylane sur une surface de cellulose infinie, et la formation d'un composite xylane-cellulose à partir d'un monocristal de cellulose et d'un grand nombre de chaines de xylane (Fig. 2.23 :a).

On peut constater un effet de structuration au voisinage des surfaces : des couches successives se forment sur le cristal, couches matérialisées dans la distribution de probabilité du xylane

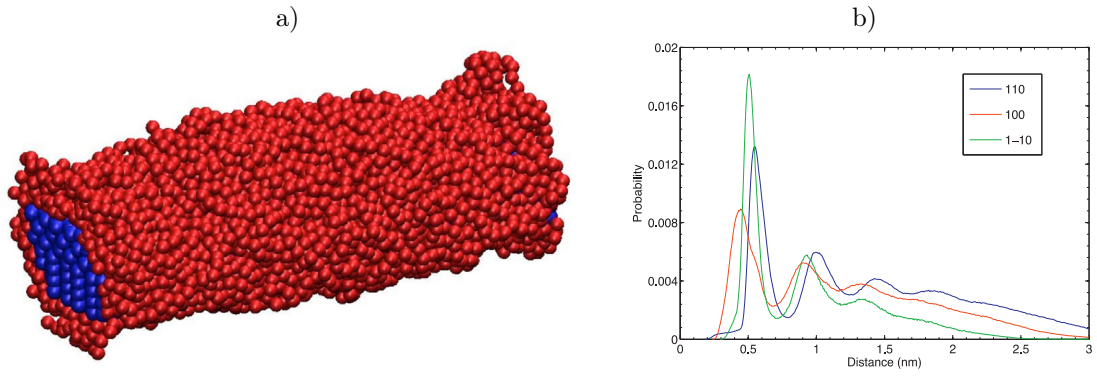

FIGURE 2.23 – Simulation gros grain de l'adsorption de 200 chaines de xylane sur un monocristal de cellulose : a) état d'équilibre, les grains de cellulose étant représentés en bleus et les grains de xylane en rouge, b) Distributions de probabilité du xylane en fonction de la distance aux surfaces de cellulose cristalline. En bleu : surface (110), en vert : surface $(1-10)$, en rouge : surface (100).

sous forme de pics (Fig. 2.23 :b). Cette structuration s'atténue avec la distance pour disparaître aux environs de $2nm$. Au vu de ces résultats, il a été constaté que l'épaisseur des couches varie avec l'énergie d'interaction. Plus l'énergie d'interaction xylane-surface est élevée, plus l'épaisseur de couche est faible. Par ailleurs, la densité locale de xylane est croissante avec l'énergie d'interaction.

Cette thématique reste aujourd'hui importante, comme en témoignent les citations de notre article (par exemple [7, 48, 58, 103, 106]). Par ailleurs, les développements méthodologiques liés à la mise en œuvre de ce modèle m'ont amenés à acquérir une expertise en implémentation de méthodes numériques lagrangiennes, indispensable dans le cadre des approches par éléments discrets dédiées aux milieux granulaires.

2.3 Phénomènes capillaires

Pour beaucoup de matériaux, qu'ils soient naturels ou synthétiques, des interactions avec une phase liquide interviennent au cours de leur transformation ou de leur usage. L'interaction d'un matériau avec l'eau peut avoir de multiples conséquences, recherchées ou préjudiciables selon les applications, comme des effets de cohésion dans un milieu granulaire, de la viscoélasticité, de la corrosion dans le cas du béton armé, une modification de la durabilité d'un biomatériau ou de la digestibilité d'un aliment, etc... Dans de nombreux cas, la phase liquide n'est pas saturée, et se présente sous une forme divisée. Par exemple, un bois d'œuvre destiné à un usage en extérieur pourra avoir reçu un traitement de finition en phase liquide pulvérisée, et sera mis en contact avec des gouttes d'eau du fait de son utilisation. Des forces de capillarité interviennent alors au niveau des lignes triples solide/liquide/gaz et, en fonction de l'échelle pertinente du problème, peuvent contribuer à déterminer le régime de comportement du système. L'étude de ces phénomènes s'avère complexe. Les détails des surfaces à petite échelle peuvent avoir des conséquences importantes à grande échelle. D'autre part, il est souvent difficile de contrôler parfaitement l'homogénéité des états de surface. Du fait des difficultés expérimentales, la simulation numérique est une approche complémentaire permettant de dégager des causalités dans des situations idéalisées.

2.3.1 Approche lattice Boltzmann pour les phénomènes de capillarité

La prise en charge d'une interface gaz-liquide dans une approche numérique est en soi un défi. Intuitivement, l'interface d'une bulle relèverait plutôt d'une approche lagrangienne, alors que le champ de vitesse, de pression, etc... relèvent plutôt d'une approche eulerienne. Dans ce cas, toute la difficulté réside dans la gestion du couplage de ces deux types de description. Si de telles approches couplées existent, une approche mettant en œuvre un unique schéma de description sera plus simple et plus robuste. En l'occurence, l'approche Lattice Boltzmann relève d'une desciption Eulerienne.

Parmi les modèles LB les plus simples dans le domaine des écoulements polyphasiques, les modèles du type "pseudo-potentiel" ou "Shan et Chen" [101] présentent l'avantage d'être très versatiles et de pouvoir être utilisés directement avec des géométries d'interface fluide-solide de forme complexe. Ces modèles peuvent être construits sur deux constituants (ou plus...) ou un seul. Dans ce dernier cas, une goutte est par exemple une inclusion de phase liquide baignant dans sa phase vapeur, ce qui permet de réduire le poids numérique et d'avoir un contraste de densité entre les deux phases. Les approches à deux constituants seront plus appropriés pour des systèmes liquide-liquide.

Ces modèles LB reposent sur une modification du calcul de la vitesse du fluide lors du calcul des distributions d'équilibre f_i^{eq}. La vitesse locale $\vec{u}'$ est déduite de la vitesse $\vec{u}$ calculée à partir des distributions f_i et d'une force d'interaction $\vec{F}$ selon

$$\rho\vec{u}' = \rho\vec{u} + \tau_f\vec{F} \tag{2.20}$$

où τ est le temps de relaxation liée à la viscosité dans le schéma lattice Boltzmann LBGK. Cette force est la somme d'une force d'interaction fluide-fluide $\vec{F}_{FF}$ et d'une force d'interaction fluide-solide $\vec{F}_{FS}$

$$\vec{F} = \vec{F}_{FF} + \vec{F}_{FS}. \tag{2.21}$$

Les interactions fluide-fluide ont lieu entre particules de fluide situées sur des noeuds de réseau voisins. La force $\vec{F}_{FF}$ est la somme pondérée (pour des raisons d'isotropie de réseau) de ces interactions avec les proches voisins, selon l'expression

$$\vec{F}_{FF}\left(\vec{r}\right) = \psi\left(\vec{r}\right)\sum_i G_i^{FF}\psi\left(\vec{r} + \delta t\vec{e}_i\right) \tag{2.22}$$

où les G_i^{FF} sont des poids dépendant de la direction de réseau i et où $\psi\left(\vec{r}\right) = 1 - e^{-\rho(\vec{r})}$ est une densité effective. Ce modèle minimaliste permet déjà de simuler la transition de phase liquide-vapeur et de simuler des gouttes présentant une tension interfaciale fixée en fonction de l'intensité de l'interaction [27, 101].

Les interactions fluide-solide sont modélisées de la même façon, les noeuds voisins impliqués dans l'interaction n'étant plus des noeuds fluide, mais des noeuds solide, l'expression devient

$$\vec{F}_{FS}\left(\vec{r}\right) = \psi\left(\vec{r}\right)\sum_i G_i^{FS}S\left(\vec{r} + \delta t\vec{e}_i\right) \tag{2.23}$$

où les G_i^{FS} sont des poids dépendant de la direction de réseau i et où $\S\left(\vec{r}\right)$ est un index prenant la valeur $S = 0$ sur les noeuds fluide et la valeur $S = 0$ sur les noeuds solide.

Cette approche permet de modéliser les phénomènes de mouillage, l'angle de contact à l'équilibre θ^{eq} dépendant à la fois de l'intensité de l'interaction fluide-fluide et de l'intensité de l'interaction fluide-solide [27, 76, 92].

D'autres approches lattice Boltzmann permettent de réaliser des simulations numériques de phénomènes de mouillage, notamment l'approche de He *et al.* [54] modifiée par Yiotis *et al.* [120].

2.3.2 Etalement d'une gouttelette sur une surface poreuse

L'étalement d'une goutte sur une surface solide est un phénomène complexe. Les surfaces réelles n'étant pas exemptes de défauts ou d'impuretés, obtenir expérimentalement des conditions parfaitement contrôlées n'est pas aisé. Par ailleurs, dès que le système étudié est d'échelle plus que millimétrique, la gravité intervient et modifie la phénoménologie. C'est pourquoi la simulation numérique présente des avantages significatifs. D'une part, il est possible de découpler des phénomènes qui, expérimentalement sont couplés, par exemple en imposant une gravité nulle au cours des simulations. D'autre part, imposer un état de surface est infiniment plus facile numériquement qu'expérimentalement. Il peut s'agir de patterns de composition chimique, d'une surface texturée ou encore de porosité homogène ou hétérogène. On peut noter ici que la versatilité des approches LB à "pseudo-potentiel", du type Shan et Chen, facilite grandement de telles éxpérimentations virtuelles.

La dynamique du mouillage d'une surface lisse par une goutte est un phénomène étudié depuis longtemps et a fait l'objet de nombreux travaux expérimentaux et théoriques [11, 12, 22, 74, 108, 113]. A priori, la dynamique de ce phénomène dépend de l'angle de contact à l'équilibre entre la surface et le liquide, mais aussi de la tension interfaciale gaz/liquide, de la masse volumique du liquide et de sa viscosité. Le nombre de Laplace $La = \frac{\rho_L \gamma R}{{\mu_L}^2}$, ρ_L étant la masse volumique du liquide, γ étant la tension interfaciale, μ_L la viscosité du liquie, est intrinsèque a la goutte et n'implique pas le propriétés de la surface solide. Dans les cas où $La \gg 1$, on peut considérer que la goutte est peu visqueuse. En revanche, pour des valeurs modérées ou faibles de La, il ne sera pas possible d'ignorer la viscosité dans les modèles prédisant le comportement de la goutte lors du mouillage. Tous les résultats présentés ici concernent des gouttes peu visqueuses.

Le cas d'une surface lisse a été abordé dans le cadre de mes travaux afin de fournir un point de comparaison expérimental via les données de la littérature [12] et de valider l'approche (Fig. 2.24 :a). Les premiers instants du contact entre la phase liquide et la surface solide mettent en jeu des phénomènes très rapides impliquant un nombre restreint de molécules. Ces étapes précoces du mouillage ne sont pas compatibles avec l'utilisation de l'approche LB mais peuvent faire l'objet de simulations par dynamique moléculaire [118]. Par contre, les simulations LB pourront rendre compte de la compétition entre forces macroscopiques, par exemple, entre l'inertie du liquide formant la goutte et les forces capillaires tendant à étaler la phase liquide sur la surface [12]. J'ai mis en oeuvre un modèle LB de type Shan et Chen mono-constituant afin de vérifier la capacité de ce modèle simple à prédire la dynamique d'étalement d'une goutte [32], en bon accord avec les résultats expérimentaux de la littérature (Fig. 2.24b). En particulier, on contstate que l'évolution temporelle du rayon r de la zone mouillée du solide obéit à une loi de puissance :

$$\frac{r}{R} = C\left(\frac{t}{\tau}\right)^{\alpha} \tag{2.24}$$

où C est le préfacteur, α l'exposant et $\tau = \sqrt{\rho_L R^3/\gamma}$ le temps capillaire.

Lors de l'étalement d'une goutte sur une surface poreuse, la forme de la ligne triple gaz / liquide / solide est beaucoup plus complexe (Fig. 2.25), et la dynamique d'étalement devrait en être affectée. Il faut souligner ici un détail important : un coefficient de porosité ne suffit pas à définir une surface poreuse. Il peut s'agir de pores de grande taille largement espacés les uns des autres ou des pores petits mais densément répartis. Par ailleurs, la forme des pores peut varier. La grande versatilité de l'approche de Shan et Chen m'a permis de réaliser des simulations numériques d'étalement de goutte sur des surfaces perforées en faisant varier la forme et la taille des pores, ainsi que la période spatiale du réseau de pores (Fig. 2.25a). Grâce à ces données, il a été possible de vérifier une hypothèse simple. Si on attribue une mouillabilité nulle aux pores, c'est-à-dire un angle de contact à l'équilibre de 90°, la loi de Cassie-Baxter permet de déduire

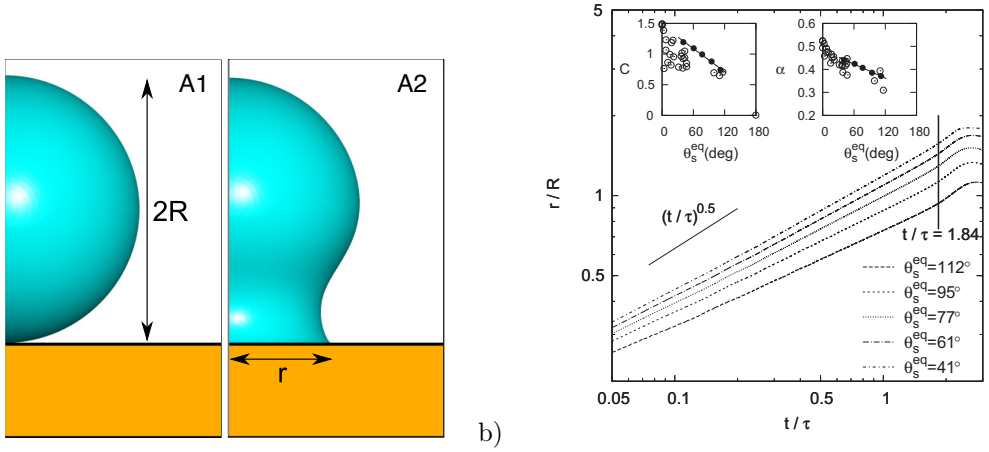

FIGURE 2.24 – Etalement d'une goutte sur une surface solide lisse. a) Représentation schématique du problème. b) Evolution temporelle du rayon r de la zone mouillée du solide. Distance normalisée par le rayon R de la goutte, temps normalisé la la constante de temps capillaire τ. Insertions : préfacteur et exposant de la loi de puissance.

un angle de contact effectif à l'équilibre :

$$\cos\theta^{eq}_{eff} = (1-\epsilon)\cos\theta^{eq} \tag{2.25}$$

Si on fait l'hypothèse que la surface équivalente se comporte comme une surface lisse d'angle de contact à l'équilibre θ^{eq}_{eff}, il est possible de déterminer un préfacteur C_{eff} et un exposant α_{eff} de loi de puissance à partir des résultats obtenus pour le cas d'une surface lisse (Fig. 2.24b). Ce modèle a été comparé favorablement aux simulations (Fig. 2.25b).

Ce résultat est limité au cas des gouttes peu visqueuses, pour lesquelles le mécanisme essentiel est la conservation de l'énergie entre l'énergie cinétique dans la goutte et l'énergie capillaire liée au mouillage. Le détail de la surface n'intervient donc pas.

Ce type d'approche pourrait aisément s'appliquer à d'autres situations plus complexes, présentant, par exemple, des contrastes de mouillabilité ou des communications entre pores voisins.

2.3.3 Imbibition capillaire

Une fois qu'un liquide pénètre à l'intérieur d'un milieu poreux à l'issue d'une phase de mouillage, en l'absence de forçage externe le liquide progresse dans le matériau par imbibition capillaire. Sauf conditions exceptionnelles ou purement théoriques, le mécanisme dominant sera une compétition entre les forces capillaires liées au mouillage des parois des pores et la dissipation visqueuse dans les pores déjà remplis de liquide. La dynamique du phénomène va dépendre de la mouillabilité de phase solide et de la viscosité du liquide. Dans le cas idéalisé d'un tube de section uniforme et en négligeant la viscosité de la phase gaz, l'avancée du ménisque est prédite par la loi de Washburn [116] :

$$h = \sqrt{\frac{\gamma d \cos\theta^{s}_{eq}}{4\eta_L} t} \tag{2.26}$$

a) 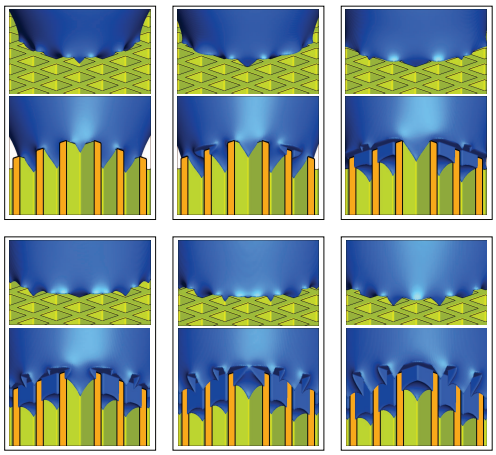

b) 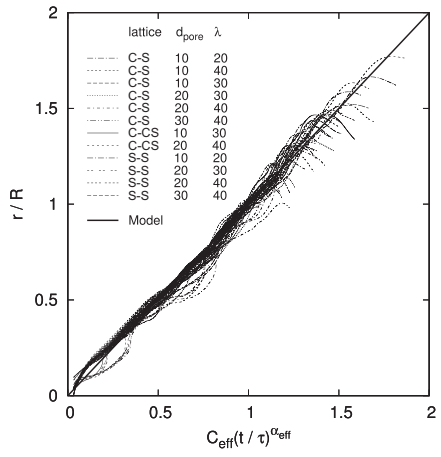

FIGURE 2.25 – Etalement d'une goutte sur une surface poreuse. a) Exemple de simulation LB. b) Comparaison entre les dynamiques d'étalement prédites par simulation et l'équation 2.25 pour diverses surfaces poreuses. C-S : pores circulaires en réseau carré, C-CS : pores circulaires en réseau carré centré. S-S : pores carrés en réseau carré. d_{pore} : taille des pores en unités LB, λ : période spatiale du réseau de pore en unités LB.

où γ est la capillarité, d est le diamètre du tube, θ^s_{eq} l'angle de contact à l'équilibre du solide et η_L la viscosité du liquide. Dans un milieu poreux plus complexe, la géométrie de la porosité aura un impact majeur sur la dynamique d'imbibition et pourra donner lieu à des phénomènes plus complexes comme l'apparition de chemins préférenciels ou l'emprisonnement de bulles de gaz. Dans ce cas, la simulation numérique est un outil d'expérimentation pertinent.

On peut trouver dans la littérature de nombreux exemples d'applications de l'approche lattice Boltzmann aux écoulement monophasiques et polyphasiques dans les milieux poreux [5, 16, 50, 72, 85, 115]. En particulier, les approches du type Shan et Chen permettent de mettre en œuvre très facilement des phases solides d'une grande complexité géométrique. Par conséquent, c'est dans ce cadre que j'ai réalisé des simulations numériques de l'imbibition d'échantillons virtuels de bois construits à partir d'échantillons réels. A titre d'exemple, je citerai une étude numérique de l'imbibition d'un réseau vasculaire, réalisé en collaboration avec Giana ALMEIDA et Patrick PERRE [27]. Des coupes successives d'un échantillon de bois ont été réalisées au microtome, transversalement aux vaisseaux et à intervalles identiques. Après chaque coupe, une image a été réalisée à l'aide d'un microscope optique et a fait l'objet d'une analyse permettant d'extraire les contours des vaisseaux. L'échantillon 3D est construit à partir de ces coupes successives à l'aide d'une méthode d'interpolation spécifique. Celle-ci a été développée afin de générer les bifurcations de vaisseaux. Il en résulte une grille 3D où un index, défini en chaque noeud, prends la valeur 0 pour la porosité et la valeur 1 pour le solide. Etant donnée la taile de la grile, celle-ci a été mise en œuvre dans un code LB parallélisé via MPI et exécuté sur un cluster. La phase liquide envahit spontanément le réseau de vaisseaux (Fig. 2.26). On remarque que après la première bifurcation, l'imbibition est plus rapide dans le vaisseau-fils le plus étroit que dans le vaisseau-fils le plus large, ce qui est en contradiction avec la loi de Washburn.

Le paradoxe n'est bien-sûr qu'apparent, puisque la loi de Washburn porte sur un régime asymptotique d'équilibre entre les forces capillaires et les forces visqueuses. Ce qui est observé ici relève d'un phénomène transitoire dans l'intervalle de temps où la colonne de liquide dans le

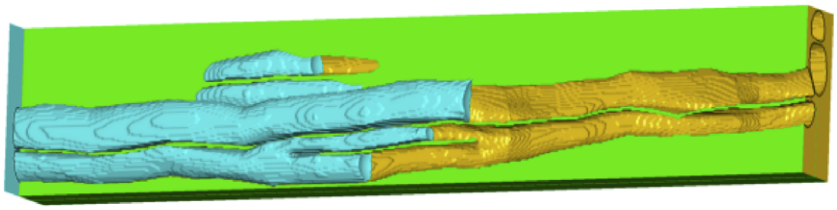

FIGURE 2.26 – Imbibition capillaire du réseau vasculaire de l'échantillon de bois virtuel.

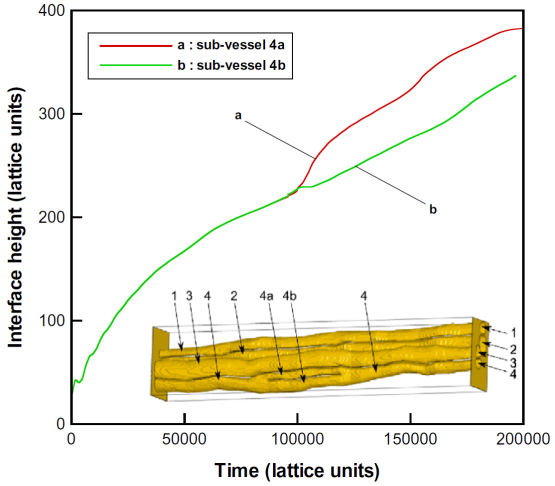

FIGURE 2.27 – Evolution temporelle de la distance d'imbibition (abscisse curviligne) dans un vaisseau présentant deux bifurcation. Les vaisseaux sont identifiés sur l'image insérée.

vaisseau-fils étroit est très courte et où la dissipation visqueuse globale est faible. Lorsque ce n'est plus le cas, la vitesse d'imbibition dans le vaisseau-fils décroit (Fig. 2.27) et, si les deux vaisseaux-fils sont suffisamment longs, devient inférieure à la vitesse d'imbibition dans le vaisseau-fils large.

De telles situations peuvent donner lieu à l'emprisonnement d'une bulle de gaz. Cependant, il n'est pas certain qu'il soit possible de former une telle bulle avec un modèle LB mono-constituant. La bulle de vapeur sera plus vraisemblablement condensée pour finir par disparaître après sa formation. En revanche, un modèle à deux constituants permettrait à la pression interne de la bulle de s'établir et de stabiliser celle-ci.

Ce genre d'étude peut être réalisé à l'aide d'autres techniques d'imagerie, notamment la micro-tomographie à rayons X, et ce dans de nombreux champs thématiques : matériaux, géosciences, etc...

2.4 Fragmentation

La fissuration, la rupture et la fragmentation sont des phénomènes omniprésents dans bien des processus naturels comme la formation de roches [107], la mastication [4] ou encore la formation de planètes [18]. Ces phénomènes sont également très présents dans les procédés industriels.

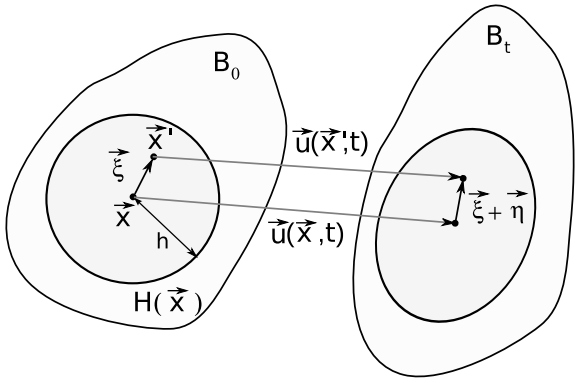

FIGURE 2.28 – Schéma de principe de la peridynamique.

Il est souvent nécessaire de mettre un matériau solide sous forme divisée pour pouvoir le traiter, ou encore de modifier la granulométrie d'une matière première initialement sous la forme d'une poudre ou d'un matériau granulaire. Il peut s'agir d'optimiser l'étape de transformation suivante, la cinétique des réactions chimiques transformant des solides étant d'autant plus rapide que la surface spécifique du solide est grande. Les opérations de broyage sont particulièrement énergivores [77, 81] et s'avèrent être peu contrôlés, ce qui implique d'avoir recourt à posteriori à des procédés de séparation, eux-même fortement consommateurs d'énergie et de rendement souvent médiocre. Il existe donc un besoin crucial de compréhension fine des phénomènes ayant lieu au cours de ce type de procédé industriel.

La granulométrie résultant d'une opération de fragmentation, tout comme la nature des surfaces créées, dépendent des chemins de fissure.

C'est pourquoi il est crucial de comprendre le rôle joué par la microstructure dans l'apparition de ces fissures. De manière générale, les fissures apparaissent et croissent dans les matériaux au voisinage des concentrations de contrainte. Or, les concentrations de contrainte dépendent directement de la microstructure. Afin de comprendre le comportement à la rupture d'un matériau donné, il est essentiel que les démarches de modélisation mises en place le soient à l'échelle de la microstructure. Mettre en œuvre ce type de démarche implique d'être capable de construire et caractériser une microstructure numérique, d'une part, et, d'autre part, de s'appuyer sur une approche numérique qui soit à même de prendre en charge ce niveau de détail. On privilégiera donc des méthodologies dont l'échelle de discrétisation est inférieure à celle des hétérogénéités. La construction des échantillons numériques peut, en revanche, s'appuyer sur des méthodes numériques relevant d'échelles légèrement supérieures.

2.4.1 Approche peridynamique

L'approche péridynamique constitue un cadre alternatif de la mécanique des milieux continus [104]. Elle repose sur l'idée que chaque point matériel $\vec{x}$ constituant le système est en interaction avec les points matériels $\vec{x'}$ dans un voisinage $H(\vec{x})$ de taille finie (Fig. 2.28) caractérisée par un cutoff h habituellement nommé horizon.

On peut donc dire que la peridynamique est une approche non locale, reposant sur des interactions à distance.

Au cours de l'évolution temporelle du système de l'état B_0, à l'instant initial, à l'état B_t, à l'instant t, les liaisons $\vec{\xi}$ entre points voisins évoluent vers un état déformé $\vec{\xi} + \vec{\eta}$ (Fig. 2.28). Les

forces exercées sur les points matériels dépendent des déformations des liaisons et l'équation du mouvement en tout point $\vec{x}$ est

$$\rho(\vec{x})\ \ddot{\vec{u}}(\vec{x},t) = \int_{H(\vec{x})} \vec{f}\left(\vec{u}(\vec{x'},t) - \vec{u}(\vec{x},t), \vec{x'} - \vec{x}, \vec{x}\right)\ \mathrm{d}V_{\vec{x'}} + \vec{b}(\vec{x},t)\ , \tag{2.27}$$

où ρ est la masse volumique, $\vec{u}(\vec{x},t)$ est le déplacement (Fig. 2.28), $\vec{f}$ représente une force par unité de volume au carré exercée par le point matériel $\vec{x'}$ sur $\vec{x}$ et $\vec{b}$ une densité de force extérieure.

La peridynamique permet de décrire des comportements mécaniques variés [], mais si on se limite aux solides élastiques fragiles, il est possible de s'appuyer sur une approche peridynamique simplifiée, dite "bond-based" [105]. Dans ce cas, seules des interactions de paire s'exercent entre points matériels voisins, et la force exercée à travers une liaison a la même direction que la liaison :

$$\vec{f}\left(\vec{\xi},\vec{\eta},\vec{x}\right) = f\left(\vec{\xi},\vec{\eta},\vec{x}\right)\frac{\vec{\xi}+\vec{\eta}}{\left\|\vec{\xi}+\vec{\eta}\right\|}\ , \tag{2.28}$$

Dans le cadre d'un modèle structement linéaire, l'intensité de la force $f\left(\vec{\xi},\vec{\eta},\vec{x}\right)$ s'exprime très simplement :

$$f\left(\vec{\xi},\vec{\eta},\vec{x}\right) = cs\left(\vec{\xi},\vec{\eta}\right) \tag{2.29}$$

où c est le micro-module élastique et $s\left(\vec{\xi},\vec{\eta}\right) = \frac{\|\vec{\xi}+\vec{\eta}\|-\|\vec{\xi}\|}{\|\vec{\xi}\|}$ est l'élongation de la liaison $\vec{\xi}$. Le micro-module c se déduit directement [52] du module élastique macroscopique E, de l'horizon h et du coefficient de Poisson ν (dans le cas de la péridynamique bond-based, $\nu = 1/3$ en $2D$ et $\nu = 1/4$ en $3D$) selon la relation $E = \frac{c\pi h^3(1-\nu)}{6}$. Une liaison est définie par deux points $\vec{x}$ et $\vec{x'}$ qui, dans le cas de matériaux hétérogènes, n'appartiennent pas nécessairement à la même phase. On définit pour cette liaison un module d'Young $E_{\vec{x},\vec{x'}}$ et on en déduit le micro-module élastique $c_{\vec{x'},\vec{x'}}$. Les paramètres mécaniques peuvent être uniformes dans chque phase ou dépendre explicitement de la position et, par exemple, présenter des gradients.

L'endommagement est introduit à l'échelle des liaisons. Quand l'élongation s d'une liaison atteint une élongation critique s_0, elle est définitivement rompue et n'exerce plus aucune force. La valeur de s_0 peut être déduite [52] d'une énergie de fracture G, du module d'Young E du matériau et du coefficent de Poisson ν selon la relation $G = \frac{9Ehs_0^2}{4\pi}$. A partir de ces paramètres, on définit, pour chaque liaison, une ténacité $K = \sqrt{EG}$, et on en déduit l'élongation critique s_0.

Après discrétisation, un modèle peridynamique bond-based s'identifie à un système masse-ressort de voisinage d'ordre supérieur à 1. La péridynamique permet de décrire des chemins de fissure très complexes sans faire usage d'une description explicite de ceux-ci. D'autre part, du fait de son caractère non local, la péridynamique permet de réduire significativement l'impact des anisotropies locales de maillage.

Un modèle péridynamique discrétisé sur une grille de points régulière est bien adapté à la parallélisation par décomposition de domaine. J'ai développé un code péridynamique parallélisé via MPI et testé ses performances sur le cluster de la plateforme INRAE Genotoul à Toulouse. La raison principale du choix de cette machine réside dans le fait qu'il est construit sur un réseau à faible latence de type Infiniband. Le code s'est révélé scalable jusqu'à 200 processeurs (Fig. 2.29). Les règles d'attribution des ressources sur cette machine n'ont pas permis de tester le code sur un nombre de processeur plus important.

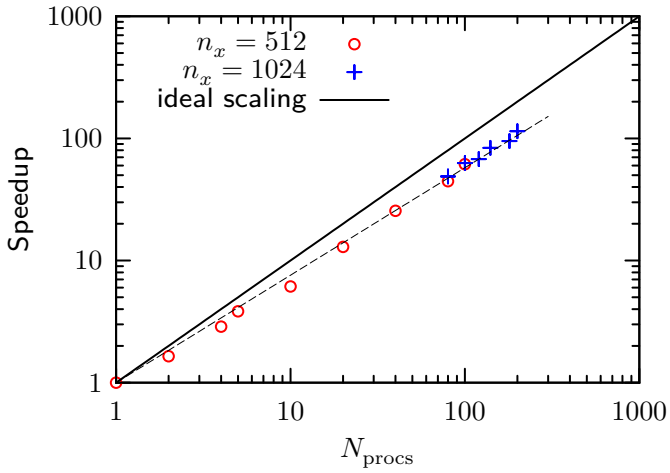

FIGURE 2.29 – Accélération de l'exécution du code péridynamique ($h/\delta x = 3$) en fonction du nombre de processeurs pour deux grilles de dimensions, respectivement : 512×1024 et 1024×2048.

2.4.2 Rupture des matériaux granulaires cimentés

Les matériaux granulaires cimentés sont constitués de particules collées entre elles par une matrice cohésive. Celle-ci peut être une phase continue, le matériau s'apprentant à un composite plus ou moins dilué, mais peut aussi se présenter sous la forme de ponts, le matériau présentant dans ce cas de la porosité. On peut citer de nombreux exemples de matériaux granulaires cimentés, qu'ils soient naturels ou synthétiques. Certaines roches sont assimilables à des granulaires cimentés [26], ainsi que certains tissus végétaux [114], le béton [6], et beaucoup de matériaux composites [117].

Le comportement mécanique d'un matériau granulaire cimenté dépend de paramètres microstructuraux, comme la distribution granulométrique des grains, la fraction de matrice, mais aussi des paramètres mécaniques intrinsèques des phases et de l'adhésion entre les phases solides en contact. Le balayage systématique de toutes les situations possible nécéssiterait un nombre colossal de simulations numériques, aussi est-il nécessaire de fixer certains paramètres.

Il est possible de construire un échantillon virtuel de granulaire cimenté à partir d'un échantillon granulaire issu d'une simulation par éléments discrets (DEM), Monte Carlo (MC) ou toute autre approche déterministe ou stochastique capable de produire des assemblages de grains sans recouvrements. Si la matrice cohésive est continue, la construction est directe. En revanche, des ponts ne peuvent être mis en place qu'entre grains proches, mais pas nécessairement en contact. Moyennant un critère portant sur la distance entre grains, les ponts peuvent être mis en place sous forme de polygones en 2D [19] ou de cônes tronqués en 3D [1]. En modulant l'épaisseur des ponts cohésifs, diverses porosités peuvent être obtenues.

Avec l'augmentation de l'épaisseur des ponts, la fraction de solide de l'espace inter-grains S augmente, la porosité diminue, la taille des pores diminue, ainsi que leur nombre [40]. En fixant les paramètres mécaniques et la granulométrie et en faisant varier l'épaisseur des ponts, on étudie l'impact de la porosité. En choisissant des grains plus tenaces que la matrice (ratio de ténacités et d'élasticités de 4) et une polydispersité modérée (ratio de 2 entre le plus diamètre de la plus grande particule et le diamètre de la plus petites particule), on se place dans une situation commune à de nombreux matériaux. Cependant, il faut souligner ici que d'autres situations sont

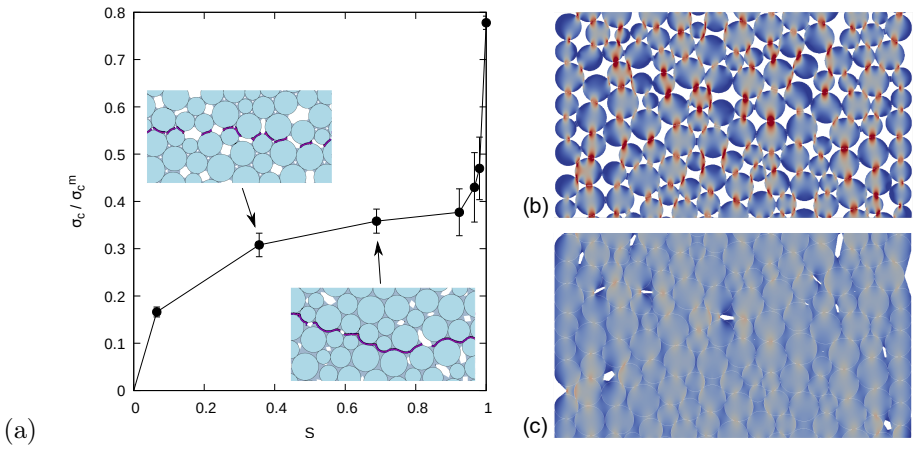

FIGURE 2.30 – Fissuration d'un granulaire cimenté. (a) Contrainte à la rupture en fonction de la fraction de matrice dans l'espace inter-grains S. La contrainte à la rupture est normalisée par la contrainte critique de la matrice. Exemples de chemins de fissure pour $S = 0.34$ et $S = 0.67$. Champ de contrainte avant rupture pour (b) $S = 0.064$ et (c) $S = 0.91$. La contrainte est normalisée par la contrainte de traction (positive) moyenne $\langle \sigma_{zz}^+ \rangle$. L'échelle de couleurs va du bleu pour les contraintes nulles au rouge pour les fortes contraintes ($\sigma_{zz} > 3\langle \sigma_{zz}^+ \rangle$).

possibles et présentent un intérêt, tant académique qu'applicatif, notamment les cas de forte polydispersité.

Dans ces conditions, en traction, le matériau a un comportement fragile [40]. Les chemins de fissure et la contrainte à la rupture dépendent de la fraction de matrice de l'espace poral S (Fig. 2.30a). Pour les faibles fractions, la fissure est discontinue et résulte de la rupture successive de ponts isolés (Fig. 2.30a) ; pour les fractions élevées, la fissure est continue sur de plus grandes distances et parcours la matériau d'un pore à un autre (Fig. 2.30a). Dans les deux cas, la fissure ne traverse que la matrice et les grains ne sont pas endommagés, comme on peut s'y attendre au vu du ratio de ténacités entre les deux phases. La contrainte à la rupture suit une évolution nettement non linéaire en fonction de S (Fig. 2.30a) : σ_c augmente rapidement pour les faibles valeurs de S, puis atteint un plateau où σ_c évolue très lentement. Enfin, à partir de $S = 0.9$, σ_c évolue très rapidement pour finalement atteindre sa valeur maximale, dans le cas saturé. Un tel comportement peut s'interpréter au vu de l'évolution des champs de contrainte en fonction de S (Fig. 2.30bc). Pour les faibles valeurs de S, les concentrations de contrainte sont localisées au niveau des ponts (Fig. 2.30b) et la croissance rapide de σ_c résulte de l'épaississement de ces ponts. Pour les grandes valeurs de S, la matrice est quasiement continue et la porosité y apparaît sous la forme de pores isolés (Fig. 2.30c). Les concentrations de contrainte apparaissent au niveau de ces pores et la seconde croissance rapide de σ_c résulte de la décroissance du nombre et de la taille des pores.

Dans cette exemple, la simulation numérique permet d'isoler un paramètre structural, et de relier le champ de contrainte et le comportement à la rupture de la microstructure résultante. Les paramètres mécaniques des différentes phases constituant le matériau sont également déterminants pour le comportement mécanique. J'ai mené une étude préliminaire dans le cas particulier d'un composite constitué des grains dilués dans une matrice sans porosité [35]. Pour différentes fractions de grains, la variation du ratio de ténacités $\Psi = K_G/K_M$ entre les grains et la matrice donne lieu à des comportements à la rupture différents. Pour des ratios de ténacité faibles, la

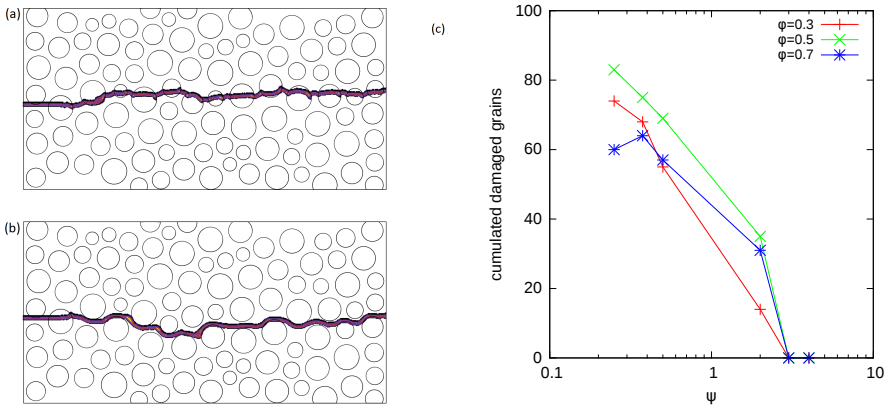

FIGURE 2.31 – Fissuration d'un matériau comportant des inclusions. Chemin de fissure pour une fraction de grains $\varphi = 0.5$ et une ratio de ténacités (a) $\Psi = 0.5$, (b) $\Psi = 4.0$. (c) Nombre de grains cassés sur l'ensemble des répétitions en fonction du ratio de ténacités Ψ pour différentes fractions de grains.

fissure traverse à la fois la matrice et les grains ; ces derniers sont donc endommagés (Fig. 2.31a). Pour des ratios de ténacité élevés, la fissure ne traverse que la matrice et les grains sont intacts (Fig. 2.31b). De manière plus quantitative, pour chaque couple de paramètres, le nombre de grains cassé a été déterminé sur 10 répétitions (Fig. 2.31c). On constate que la transition entre les deux régimes de fissuration a lieu entre $\Psi = 2.0$ et $\Psi = 3.0$, indépendamment de la fraction de grains.

Parmi les procédés mécaniques utilisés dans le traitement des matériaux d'origine végétale, certains ont pour fonction de séparer les phases pures constitutives du matériau. Dans le cas de l'albumen des céréales, il s'agirait de séparer les grains d'amidon de la matrice protéique qui assure leur cohésion. Savoir dans quelles conditions il est possible de le faire sans casser les grains est alors d'une importance capitale pour la qualité du produit fini.

2.4.3 Fragmentation d'un disque comportant des défauts

Comme le montre l'exemple des granulaires cimentés, les hétérogénéités des matériaux polyphasiques génèrent des concentrations de contrainte, raison pour laquelle le comportement à la rupture dépend de la micro-structure. Cependant, les phases pures comportent elles aussi des défauts sans lesquels leur contrainte à la rupture serait bien plus élevée [49]. L'impact de ces défauts sur l'efficacité énergétique des procédés est évidemment très important, en particulier lors des dernières opérations de broyage s'appliquant à des phases pures déjà séparées. Si on s'affranchit de la forme des particules en ne considérant que des sphères (des disques en $2D$), le problème posé s'identifie à celui de l'essai brésilien, qui consiste à soumettre un disque à une compression entre deux plans.

Considérons donc un disque d'un matériau comportant des défauts soumis à une compression entre deux plateaux [14]. Les défauts sont modélisé sous la forme d'une micro-fissure partielle linéaire. On génère alors une population de défauts d'une densité numérique donnée, d'une longueur donnée et d'orientation aléatoire (Fig. 2.32a). La rigidité de chaque liaison péridynamique traversant le segment représentatif d'un défaut est réduite d'un facteur compris entre 0 et 1. Par conséquent, les défauts introduits dans l'échantillon génèrent des concentrations de contrainte

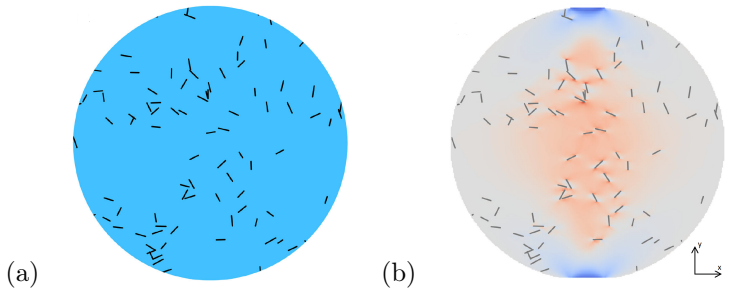

(a) (b)

FIGURE 2.32 – Particule comportant une population de défauts (représentés par des segments noirs). (a) Position des défauts (b) champ de contrainte σ_{xx}.

(Fig. 2.32b).

Une première conséquence de la présence de ces concentrations de contrainte est que les fissures vont apparaître préférentiellement au voisinage de défauts (2.33a). Une autre conséquence importante est que d'un échantillon à l'autre, la contrainte à la rupture varie. D'une part, la répartition des défauts dans l'échantillon et leur orientation sont aléatoires, d'autre part, que les défauts soient présents ou non, les contraintes sont inhomogènes dans le disque (Fig. 2.32b), du fait que les forces sont appliquées à travers deux zones de contact de très faible étendue. Un défaut ne va donc pas avoir la même efficacité de fragilisation de l'échantillon selon sa position [14], et la contrainte à la rupture va donc dépendre de l'orientation des défauts situés dans les zones les plus contraintes. La caractérisation du comportement à la rupture d'un matériau comportant des défauts ne peut donc qu'être statistique, ce qui implique, pour un jeu de paramètres structuraux donné, de réaliser un grand nombre de simulations avec des tirages aléatoires de population de défauts. Classiquement, la probabilité de survie P_S d'un échantillon soumis à une contrainte σ donnée dépend de la valeur de la contrainte selon une loi de Weibull

$$P_S = e^{-\left(\frac{\sigma}{\sigma_w}\right)^m} \tag{2.30}$$

où σ_w est la contrainte à laquelle 63% des particules sont cassées et m est le module de Weibull, qui dépend du matériau. Les résultats des simulation peridynamique réalisées dans le cadre de la thèse de Nicolas BLANC sont en accord avec cette loi (2.33b).

En s'appuyant sur ce type de simulations numériques, il est possible d'analyser la distribution de tailles de fragments [14], ainsi que leur forme, et d'en déduire l'efficacité du broyage en fonction des différents paramètres matériaux ou opératoires.

2.4.4 Fissuration des matériaux d'origine végétale

Etudier l'influence des paramètres mécaniques et structuraux sur le comportement à la rupture des matériaux permet de fournir des éléments de compréhension au sujet des procédés de traitement de la matière végétale solide. La mise en œuvre de modèles dans des situations idéalisées permet d'identifier les phénomènes impliqués et de les étudier isolément. A l'opposé de cette démarche, une méthodologie complémentaire consiste à partir d'un échantillon végétal et à l'utiliser dans le cadre d'expérimentations virtuelles. Cette approche permet de réaliser des tests destructifs sur un même échantillon avec différents paramètres, ce qui n'est pas possible dans une expérience réelle. Tout l'enjeu est de construire un échantillon virtuel à partir d'un échantillon réel. Comme évoqué dans le cas de l'imbibition de réseau vasculaire d'un échantillon

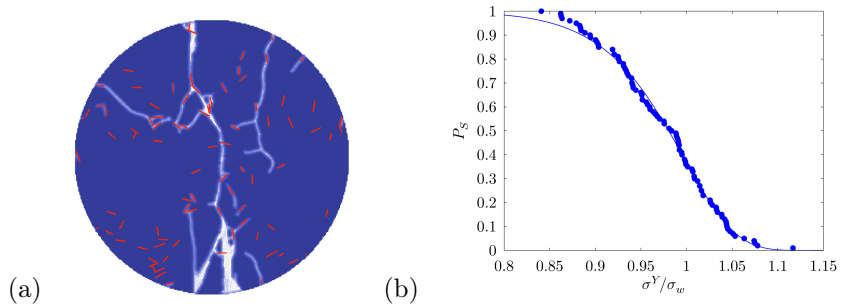

FIGURE 2.33 – Rupture de particules comportant une population de défauts. (a) Exemple de pattern de fissuration. Les zones de degré d'endommagement nul apparaissent en bleu et les zones endommagées à 100% apparaissent en blanc. La position initiale des défauts apparaît sous la forme de segments noirs. (b) Probabilité de survie d'un échantillon en fonction de la contrainte appliquée. La contrainte est normalisée par σ_w.

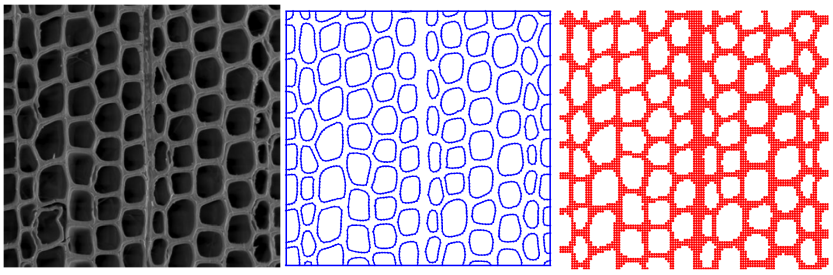

FIGURE 2.34 – Traitement vectoriel d'image utilisé pour construire une grille de points matériels à partir d'une image de bois à l'échelle cellulaire. De gauche à droite : image de microscopie électronique environnemental, contours vectoriels des lumens et grille de points.

de bois (2.3.3), la structure du matériau réel peut être obtenue à l'aide de techniques d'imagerie : microscopie, tomographie, etc...

Dans l'exemple du bois, la discrétisation d'un tissu végétal sous la forme d'une grille de points peut faire l'objet d'applications dans des approches numériques variées afin de modéliser des phénomènes très différents, comme la déformation en compression, la diffusion de matière ou la fissuration sous traction [87]. Dans le cadre d'approches $2D$, il est possible de partir d'une image, d'identifier les structures essentielles de l'anatomie, et d'en déduire une grille de points (Fig. 2.34).

Idéalement, ce type de procédure permet d'extraire de l'image l'intégralité des éléments nécessaires aux simulations numériques. Cependant, cela n'est pas toujours possible, en raison d'un manque de contraste entre deux phases solides, ou d'une résolution insuffisante de la technique d'imagerie utilisée ou encore de l'échelle des détails anatomiques requis. Dans le cas du bois, si le modèle à mettre en œuvre dépend de contrastes de propriétés entre les parois des cellules et la lamelle mitoyenne cimentant deux cellules voisines, l'identification des seuls lumens des cellules n'est pas suffisante. Il est alors nécessaire de re-construire l'information manquane, en l'occurence, la lamelle mitoyenne [87]. Une telle reconstruction s'appuie nécessairement du des paramètres ayant une part d'arbitraire. La seule façon de réduire cet arbitraire consiste à

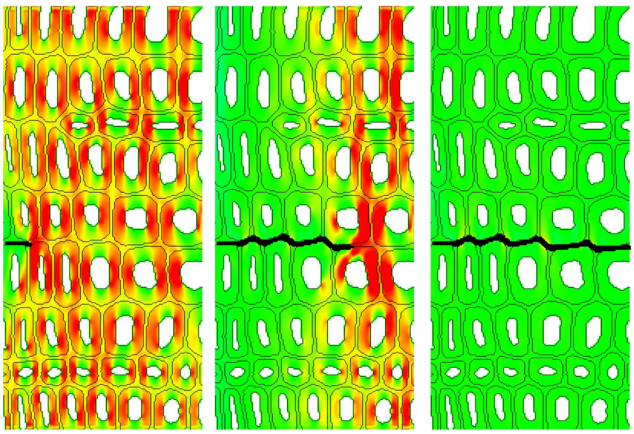

FIGURE 2.35 – Etapes successives de la simulation péridynamique de la rupture d'un échantillon de bois d'épicéa en tension. La fissure est en noir, les couleurs sont reliées à la contrainte σ_{zz} : vert pour les vlauers proches de 0, bleu pour les valeurs négatives et rouge pour les valeurs positives.

s'appuyer sur d'autres techniques de caractérisation anatomique afin de faire des hypothèses.

Dans le cas de la matière ligno-cellulosique comme dans le cas de l'albumen du grain de blé, la détermination des chemins de fissure, et donc de la nature des surfaces créées, est un enjeu important pour les applications. Si on prends l'exemple d'une biomasse destinée à faire l'objet d'un traitement chimique en vue de la production de molécules d'intérêt, un facteur fortement limitant est l'accessibilité du substrat pour les réactifs. Or, cette accessibilité ne sera pas la même si les parois cellulaires sont fissurées ou si la fissure ne traverse que la lamelle mitoyenne. Un autre exemple est la fabrication de matériaux composites composés de fibres et d'une matrice cohésive. La densité, l'élasticité et la cohésion du matériau dépendront également du niveau d'endommagement des fibres. Pour déterminer un pattern de fissuration d'un matérieu complexe, la péridynamique est bien adaptée. C'est l'approche que j'ai mise en œuvre pour simuler la fisuration d'un échantillon de bois (Fig. 2.35).

Il s'agit de résultats préliminaires mettant uniquement en évidence la faisabilité de la méthode. Il est évidemment possible de transposer ce type d'approche à bien d'autres exemples de matériaux d'origine végétale.

2.4.5 Conclusion

Cette partie de mon activité a consisté pour l'essentiel à construire des microstructures virtuelles de matériaux et a déterminer numériquement leur comportement mécanique, en particulier à la rupture. La construction des microstructures est la plupart du temps un problème physique en soi et fait intervenir des approches numériques et des algorithmes variés, telles que les approches par éléments discrets ou du type Monte Carlo. L'usage de microstructures virtuelles plutôt que réelles permet de réaliser des balayages paramétriques rigoureux. Les paramètres de génération sont dans ce cas bien identifiés, porteurs d'un sens physique clair et modifiable indépendamment les uns des autres. Les changements de comportement macroscopique observés, une fois interprétés et expliqués en lien avec les paramètres de génération des microstructures, permettent la compréhension du comportement complexe des matériaux réels, et donc d'orienter les démarches expérimentales implisquant des matériaux réels.

Chapitre 3

Projet de recherche

Les procédés de transformation de la matière végétale impliquent en grandes parties des phases solides, essentiellement sous forme divisée, et reposent donc sur la physique des milieux granulaires. Ce constat est d'ailleurs indépendant de la destination applicative des produits, qu'elle soit alimentaire, comme pour le couscous [8] ou non alimentaire, comme pour les poudres combustibles [110]. La réactivité et le comportement mécanique de ces ressources en cours de transformation dépendent donc fortement de la taille des fragments qui les constituent, mais aussi de leur forme et de la nature de leurs surfaces. Un enjeu majeur est donc de comprendre la physique des procédés de traitement de la matière végétale solide afin de maîtriser ces paramètres et de comprendre leur influence.

Il s'agira de caractériser la structure du matériau à différentes échelles aux différentes étapes de transformation et de relier les modifications structurales aux phénomènes impliqués dans les procédés. Un des attendus est la réduction de la consommation d'énergie des procédés de broyage, particulièrement consommateurs. D'autre part, les produits obtenus à l'issue des premières opérations de broyage sont des mélanges de fragments issus de tissus différents présentant par conséquent une polydispersité, une variété de formes et de compositions chimiques. La plupart du temps, ces complexités sont préjudiciables aux applications. Afin d'y remédier, on peut envisager de s'appuyer sur les procédés de broyage eux-même ainsi que sur l'utilisation de procédés de séparation.

Les objectifs de cette démarche ne résident pas uniquement dans une simple optimisation des procédés. Au-delà de la seule composition moléculaire de la biomasse, les caractéristiques structurales des matières premières d'origine végétales peuvent donner lieu à des fonctionnalités spécifiques. Par exemple, le broyage d'une biomasse lignocellulosique produit d'abord des fragments sous forme de fibres, et la longueur de ces fibres a une grande importance si elles sont mises en œuvre comme charge d'un matériau composite. Dans un contexte radicalement différent, la réactivité des poudres d'origine végétale au cours de procédés de transformation chimiques, enzymatiques ou biologiques, dépend de la nature des surfaces accessibles aux réactifs ou aux organismes impliqués. Or, la nature de ces surfaces dépend à la fois du procédé, de l'organisation histologique de la biomasse et de la microstructure cellulaire.

D'un point de vue méthodologique, mon approche de ces problématiques consiste à adopter une démarche bottom-up et hypothético-déductive. En l'occurence, le choix d'une approche bottom-up relève d'un réductionnisme visant à comprendre des phénomènes relevant d'une échelle donnée à partir de prémisses relevant de l'échelle immédiatement inférieure. Par exemple, le comportement à la rupture des matériaux hétérogènes s'explique par leur microstructure et par le comportement à la rupture des phases pures qui les constituent. A une échelle plus grande, la

micromécanique des milieux granulaires consiste à comprendre le comportement mécanique d'un matériau granulaire à partir de sa texture, elle-même grandement déterminée par la géométrie des particules. Du point de vue de la physique, il ne s'agit pas de champs thématiques clos dont on pourrait appliquer tels quels les résultats aux procédés. Ces thématiques sont ouvertes et relèvent de la recherche fondamentale. C'est pourquoi je couplerai des études fondamentales, relevant de la physique de la rupture, des milieux granulaires et des phénomènes capillaires, et des études plus appliquées, s'appuyant par exemple, sur la microstructure spécifique d'une biomasse donnée.

Le comportement des poudres et milieux granulaires découle de phénoménologies diverses et potentiellement couplées : fissuration, écoulement, interaction avec des fluides, capillarité. La diversité des phénomènes impose une diversité d'approches numériques, et ce depuis longtemps pour certains membres de PhyProDiv. A ce stade de mon parcours scientifique, il apparaît donc essentiel de poursuivre la mise en œuvre d'approches numériques diversifiées afin de réaliser les expérimentations numériques nécessaires à la résolution des questions génériques posées par les procédés. Pour ce faire, je pourrai m'appuyer sur l'expertise que j'ai acquise concernant différentes approches numériques du fait de l'historique de mes affiliations thématiques : lattice Boltzmann, Monte Carlo, Dynamique Moléculaire, Eléments Discrets, Péridynamique...

Par ailleurs, la nécéssaire prise en compte du désordre structural en général, et de la matière d'origine végétale en particulier, implique d'utiliser des échantillons numériques de grande taille, de réaliser des répétitions et d'explorer de grands espaces paramétriques. Ces contraintes imposent à la fois le développement de codes de calcul massivement parallèles, leur exécution sur des plateformes de calcul haute performance et l'automatisation de toutes les étapes de la chaîne de calcul, depuis la génération des échantillons jusqu'à l'analyse physique des résultats.

Mes activités de recherche consisteront donc, les prochaines années, à mettre en œuvre des expérimentations numériques relatives à la physique de la rupture des matériaux hétérogènes, à la rhéophysique des milieux granulaires et aux phénomènes capillaires. Le développement de codes de calcul parallèles et leur mise en œuvre sur des architectures de calcul haute performance (HPC) sont une part importante de ce projet.

3.1 Fragmentation

3.1.1 Désordre et anisotropie

Comme exposé dans ce document, les hétérogénéités et les défauts déterminent le comportement à la rupture des matériaux. Des paramètres comme la porosité, les contrastes de propriétés mécaniques, la densité de défauts ou encore la fraction d'inclusions ont un fort impact sur ce phénomène. Cependant, deux aspects importants qui caractérisent la microstructure d'un matériau en général ne figurent pas dans le bilan de mes activités. Il s'agit du degré de désordre et de l'anisotropie. D'une part, les matériaux virtuels que j'ai pu mettre en œuvre ont été construits de façon à être le plus isotropes possible. D'autre part, le degré de désordre n'est pas étudié systématiquement en tant que tel dans mes travaux, à quelques rares exceptions près.

A titre d'exemple, j'ai étudié la statistique de rupture d'un milieu poreux aléatoire dans deux cas, celui d'un milieu poreux monodisperse et celui d'un matériau poreux polydisperse (Fig. 3.1a). L'objectif de cette étude était de déterminer l'impact du désordre granulométrique de la porosité sur la statistique des contraintes à la ruptures d'un ensemble d'échantillons de chacun de ces matériaux. Pour obtenir une statistique correcte, 200 simulations ont été réalisées dans chaque cas, les échantillons ayant une résolution 512×1024. La probabilité de rupture prédite par la loi de Weibull se déduit facilement de la probabilité de survie (2.30) :

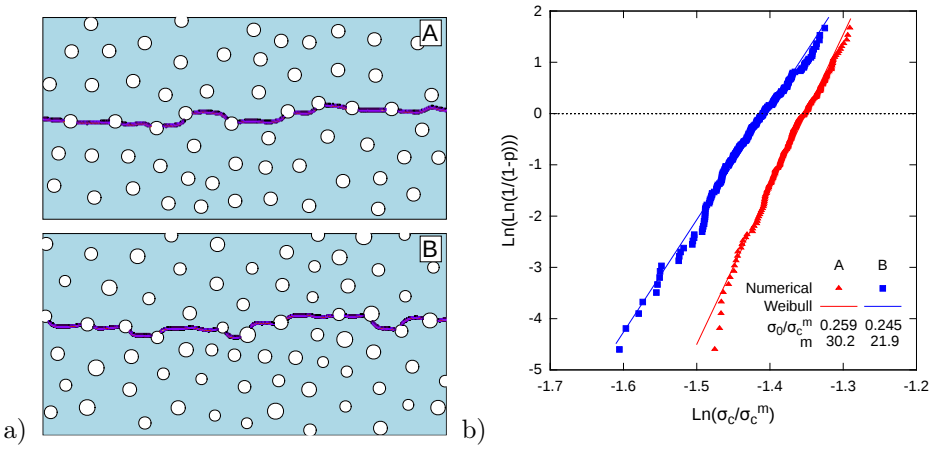

FIGURE 3.1 – Rupture d'un milieu poreux. a) Exemples de patterns de fissuration. A : cas monodisperse, B : cas polydisperse. b) Distribution de probabilité de rupture d'un matériau poreux en fonction de la contrainte σ A : dans le cas d'un matériau poreux monodisperse, B : dans le cas d'un matériau poreux polydisperse. La contrainte σ est normalisée par la conctrainte à la rupture du matériau sans porosité ${\sigma_c}^m$. Symboles : simulations péridynamiques, lignes : lois de Weibull. La valeur normalisée de la contrainte d'échelle σ_0 et le module de Weibull m sont donnés dans les deux cas.

$$P_F \propto 1 - e^{-\left(\frac{\sigma}{\sigma_0}\right)^m} \tag{3.1}$$

Les simulations numériques prédisent un comportement conforme à cette loi (Fig. 3.1b). Comme attendu, le désordre granulométrique amplifie la variabilité de la contrainte à la rupture. Cependant, si à ce stade le comportement observé est cohérente, on ne peut encore dégager et expliquer une tendance au sens quantitatif du terme.

Cette question du désordre granulométrique est large, et concerne aussi bien les milieux poreux que les granulaires cimentés [57]. Un cas particulier de milieu poreux est celui des matériaux cellulaires. De telles structures sont bien-sûr omniprésentes dans les matériaux d'origine végétale, mais sont aussi à l'origine de la texture de certains aliments [55]. Dans le cadre d'un projet AIC (MiDiDAM) impliquant IATE et BIA, j'ai réalisé une étude numérique $2D$ de la fissuration de matériaux cellulaires bidisperses. Bien que les matériaux cellulaires en général soient étudiés depuis longtemps [44, 45], cette problématique particulière des conséquences mécanique de la polydispersité a été peu abordée. Un grand nombre d'échantillons ont été générés à partir d'empilements granulaires bidisperses, et ont fait l'objet de simulations de traction jusqu'à la rupture (Fig. 3.2). Un article à ce sujet est en cours de rédaction et sera soumis sous peu.

Beaucoup d'aspects du problème restent à aborder. Dans cet exemple, l'épaisseur des paroi est fixe. Or, le procédé de fabrication des cellulaires polydisperses implique généralement que l'épaisseur de paroi soit variable, et éventuelement correlée aux volumes de cellule. Nul doute que la règle d'attribution de l'épaisseur des paroi aie un impact important sur les propriétés mécanique du matériau. D'autre part, des simulations $3D$ permettraient d'étudier l'influence de paramètres structuraux come le rapport d'aspect des cellules, ou encore de comparer le cas des cellules fermées et des cellules ouvertes.

L'étude de l'influence du désordre sur le comportement à la rupture des matériaux est un

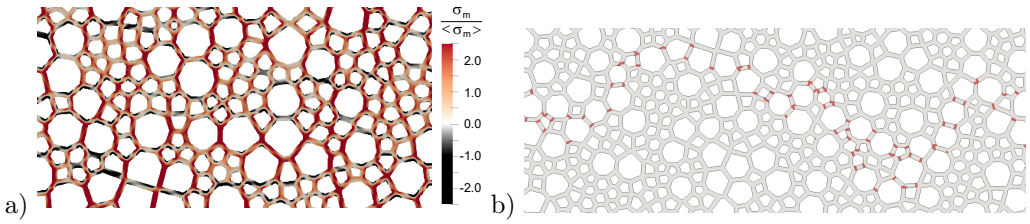

FIGURE 3.2 – Simulation peridynamique de la rupture d'un matériau cellulaire bidisperse. Le ratio de taille entre les plus grandes cellules et les plus petites est de 2. a) champ de contrainte $\sigma_m = \frac{1}{2}(\sigma_1 + \sigma_2)$, où les σ_i sont les contraintes principales. La contrainte est normalisée par sa valeur moyenne. b) chemin de fissure typique. Le ratio de taille entre les plus grandes cellules et les plus petites est de 2.

champ thématique immense, qui est loin de se limiter au seul cas de la granulométrie, de pore ou d'inclusion. En particulier, on peut envisager des situation dans lesquels un système partiellement ordonné génère au moins autant de complexité qu'un système totalement désordonné. Si on prends l'exemple d'une particuler comportant des défauts assimilable à des pré-fissures (Sec. 2.4.3), le matériau est désordonné dans la mesure où l'orientation des défauts est aléatoire. Si ce n'est pas le cas, les défauts vont présenter une ou plusieurs directions privilégiées, et le matériau sera anisotrope.

S'il existe des approches péridynamiques dédiées aux matériaux anisotropes [78, 102], leur vocation n'est pas d'établir un lien de causalité entre l'anisotropie et la microstructure qui l'engendre. Il s'agit plutôt d'approches de champ moyen, parfaitement applicables à l'étude de structures de plus grande échelle. On peut citer comme application potentielle l'étude d'un matériau lignocellulosique à l'échelle de la cellule et prenant en compte l'anisotropie mécanique des parois cellulaires lignifiées.

La versatilité de la péridynamique permet de mettre en place des expériences numériques liant anisotropie de microstructure et anisotropie mécanique. Il peut s'agir d'anisotropies liées à la croissance végétale et à l'orthotropie des tiges en général, mais aussi d'anisotropies liées aux procédés de transformation ou de mise en forme de matériaux. Ce type d'investigation numérique s'appuie nécessairement sur des balayages paramétriques massifs.

3.1.2 Fragmentation dynamique

La fissuration quasi-statique représente une situation-limite. L'intérêt de ce type d'expérimentation réside dans le fait que l'information qui en est obtenue est intrinsèque au matériau et ne dépend pas de la vitesse de sollicitation. Concrètement, on peut qualifier une fissuration de quasi-statique lorque la propagation des ondes élastiques n'a pas d'influence sur le pattern de fissuration. Dans bien des cas, il n'est pas possible de négliger ces phénomènes, on parle alors de fissuration dynamique. L'approche péridynamique est parfaitement adaptée à ce type d'expérimentation numérique, et a été appliquée à des cas très dynamiques, comme des impacts [119].

Les simulations péridynamiques quasi-statiques que j'ai réalisées relèvent, en toute rigueur, de la fissuration dynamique fortement amortie. La mise en œuvre de simulations dynamiques à partir des outils existants est donc immédiates. En fait, chronologiquement, j'ai commencé par mettre au points des approches dynamiques, le passage ultérieur au quasi-statique s'étant avéré fastidieux, sans doute du fait du nombre important de modes à amortir. On peut ici citer un exemple qui a été présenté au Congrès Français de Mécanique, en 2013 [34]. Il s'agit de la fissuration d'un

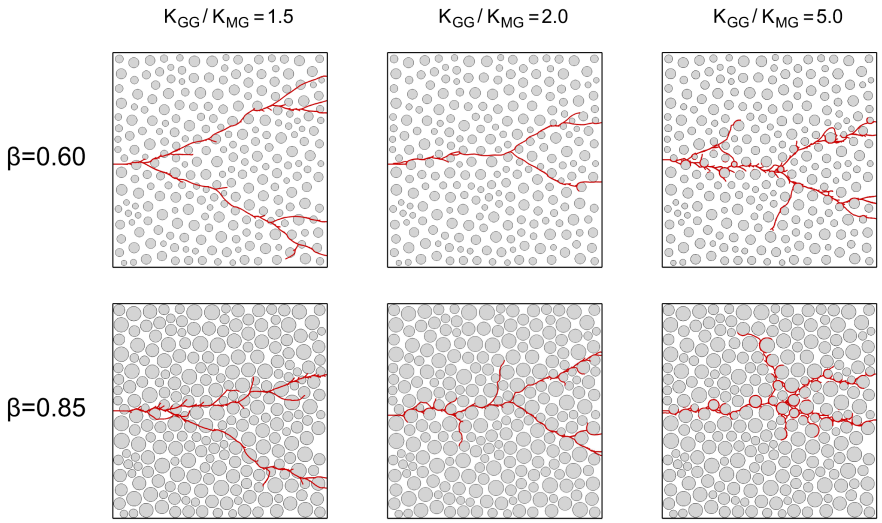

FIGURE 3.3 – Fissuration dynamique de matériaux composites pour deux valeurs du facteur de réduction des grains β et trois valeurs du ratio entre ténacité des grains K_{GG} et ténacité de l'interface matrice-grain K_{MG}.

matériau composite $2D$ constitués de particules réparties dans une matrice (Fig. 3.3). A partir d'un milieu granulaire ayant fait l'objet d'une compression isotrope, les diamètres des particules sont réduits d'un facteur β variable et le ratio de ténacités entre les grains et l'interface est également varié (la ténacité de la matrice est choisie identique à la ténacité d'interface). Comme attendu, l'endommagement des grains est nul pour les forts ratios de ténacité et non nul pour les ratios faibles.

L'objectif de cette étude était de tester la péridynamique comme outil de simulation numérique de la fissuration dynamique de matériaux hétérogènes. La principale difficulté de ce genre d'étude ne réside évidemment pas dans l'aspect strictement numérique, mais dans l'interprétation physique des résultats. Pour autant, il semble essentiel d'explorer cet aspect du problème, en particulier du fait de son importance dans les procédés de broyage. Quelques tests de fragmentation dynamique $2D$ de particules polygonales ont été réalisés durant le thèse de Nicolas BLANC et ont été présentés lors du Congrès Français de Mécanique de 2015 [13]. Des résultats préliminaires intéressants ont pu être obtenus, notamment au sujet de l'influence de l'énergie d'impact et de la forme des particules sur l'aire des surfaces créees et le volume des fragments. Il s'agit d'un champ particulièrement riche et encore peu exploré.

3.1.3 Péridynamique 3D

En physique et mécanique numériques, le passage à la $3D$ est toujours souhaitable, mais le prix à payer est important. Non seulement, la péridynamique ne fait pas exception, mais implique une augmentation de coût numérique explosive, et ce, pour des raisons très simples. Dans le cas général, si N_x est la résolution caractéristique, passer de la $2D$ à la $3D$ revient, en première approximation, à passer d'un poids numérique en ${N_x}^2$ à un poids numérique en ${N_x}^3$. Mais dans le cas de la péridynamique, il ne faut pas oublier que celle-ci repose sur une double discrétisation : celle du domaine de simulation et celle du voisinage. L'approche étant non locale, le nombre

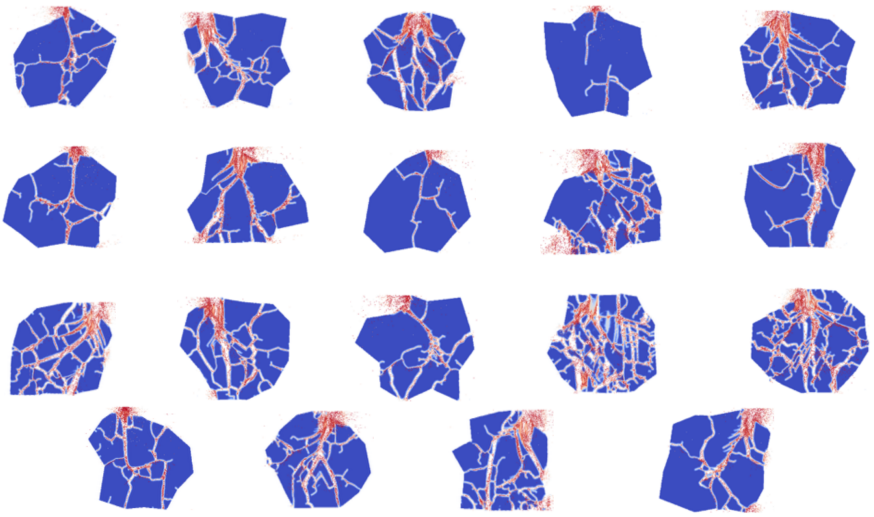

FIGURE 3.4 – Exemples de simulations péridynamiques $2D$ de fragmentation dynamique de particules polygonales (thèse de Nicolas BLANC).

de voisins de chaque point matériel est très supérieur au nombre de voisins impliqués dans des approches locales, comme les différences finie d'ordre 1 par exemple. C'est le cas en $2D$, mais c'est bien plus le cas encore en $3D$. Par exemple, si l'horizon est de 4 pas, le voisinage comporte 48 voisins en $2D$ et 256 voisins en $3D$, soit presque 5 fois plus. Un autre point concerne les simulations parallèles reposant sur le MPI. Du fait du caractère non local de la péridynamique, le voisinage est d'ordre supérieur à 1, ce qui implique un volume de communications entre processeurs plus important qu'avec des approches s'appuyant sur un voisinage d'ordre 1. Cet effet est plus important en $3D$ qu'en $2D$.

Au début de mes travaux en péridynamique, j'ai exécuté, à titre de test, une simulation $3D$ de fissuration dynamique (Fig. 3.5). L'échantillon, un cube comportant une seule inclusion, était discrétisé sur une grille $256 \times 256 \times 256$, et comportait donc presque 17×10^6 points matériels. Le modèle péridynamique bond-based comportait plus de 2×10^9 termes d'interaction à calculer à chaque itération. Pour exécuter cette simulation, il a fallu mobiliser 16 noeuds du cluster infiniband qui avait été déménagé du LERFOB à IATE. C'était il y a 10 ans, et l'adressage des voisins était explicite, comme en dynamique moléculaire. Aujourd'hui, mes codes reposent sur un adressage implicite des voisins, ce qui est bien plus efficace, et sont optimisés en accès mémoire. Par ailleurs, la puissance de calcul des machines est bien supérieure qu'à l'époque. Enfin, j'ai aujourd'hui l'opportunité de soumettre ce type de calcul sur des supercalculateurs régionaux ou nationaux, ainsi que les compétences pour le faire. Même s'il est clair que la $3D$ imposera des limites à la taille des échantillons, la mise en œuvre de ce type d'expériences numériques fait partie de mes projets pour les prochaines années.

Etant donné le poids numérique des simulations $3D$, je prilvilégierai sans doute les expériences relatives à la fissuration et la fragmentation dynamiques, beaucoup plus rapides que les expériences en régime quasi-statique.

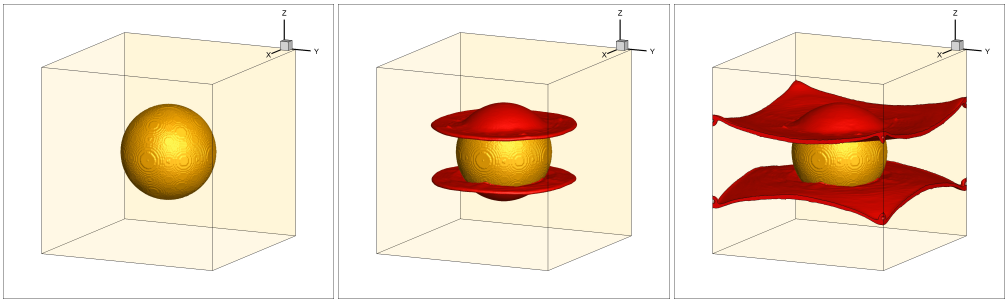

FIGURE 3.5 – Simulation péridynamique $3D$ de fissuration dynamique d'un échantillon comportant une inclusion. Résolution de la grille de points matériels : $256 \times 256 \times 256$.

a) 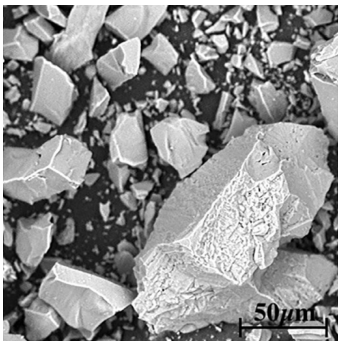

b) 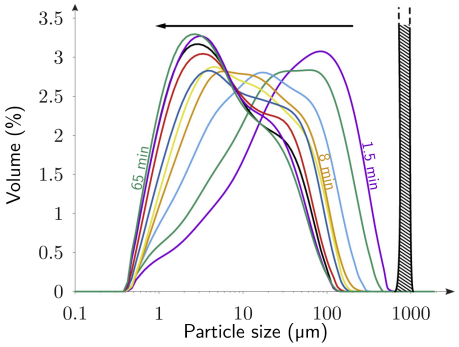

FIGURE 3.6 – Broyage d'un sable de silice [15]. a) Image par microscopie électronique en début de broyage ($30s$). b) Evolution de la distribution de tailles de particules avec la durée de broyage (de $1.5min$ à $65min$). La distribution granulométrique avant broyage est représentée par la surface hachurée.

3.1.4 Milieux granulaires

Lors d'un broyage en conditions réelles, les particules ne sont évidemment pas isolées et broyées l'une après l'autre. Sauf exception, les procédés de broyage consistent à imposer des contraintes mécaniques à un milieu granulaire dense. Si la microstructure interne des particules est source de complexité, le réseau de contacts entre grains l'est tout autant. La transmission des contraintes imposées via les conditions aux limites jusqu'à chaque grain passe par les chaînes de force du milieu granulaire [90]. Or, ce réseau est particulièrement hétérogène, certaines chaînes de force transmettant l'essentiel des contraintes [91]. La dispersion de la contrainte à la rupture individuelle des particules et la dispersion des intensités des forces de contact entre grains impliquent une distribution hétérogène des évènements de rupture. Ces phénomènes ont un impact majeur sur la granulométrie du matériau en cours de broyage. Outre la diminution de la taille moyenne des particules, la dispersion des diamètres de grain va augmenter, en particulier au début du broyage (Fig. 3.6). Par ailleurs, transmettre les contraintes à travers un réseau de contacts implique une dissipation par frottement, qui va impacter le bilan énergétique du procédé.

Pour ces raisons, la compréhension du broyage à grande échelle s'appuie nécessairement sur la physique des milieux granulaires. Etablir une relation de causalité entre la sollicitation mé-

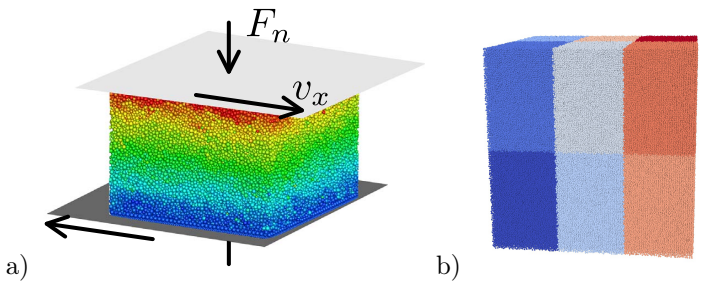

FIGURE 3.7 – Tests du code DEM $3D$ parallélisé par MPI. a) Exemple de cisaillement d'un échantillon de 10^5 particules. La couleur indique la composante selon x de la vitesse des particules : rouge pour les valeurs positives, vert pour les valeurs proches de 0 et bleu pour les valeurs négatives. b) Exemple de simulation impliquant 10^6 particules. La couleur indique le numéro de processeur.

canique du milieu granulaire et les évènements de rupture nécessite d'avoir accès à la fois à des informations globales et à des informations très locales. La simulation numérique est donc une approche d'expérimentation particulièrement utile. De récents progrès ont été accomplis en ce sens à l'aide d'une approche numérique $2D$ [83] au cours de la thèse de Luisa OROZCO, effectuée dans le cadre d'une collaboration entre le LMGC, le CEA et IATE.

La plupart des approches numériques en physique des milieux granulaires relèvent de la dynamique moléculaire. La trajectoire des particules, ainsi que leur mouvement de rotation, sont déterminés à l'aide des forces auxquelles elles sont soumises. Outre les forces imposées de l'exterieur au système, comme la gravité, ces forces sont essentiellement des forces de contact, en général avec frottement. Il faut donc déterminer, pour chaque particule, les voisins suceptibles d'entrer en contact avec elle. Cette recherche doit par ailleurs être effectuée fréquemment au cours de la simulation, dans la mesure où les contacts sont créés et rompus en permanence du fait des mouvements des particules. Une des difficultés de l'adaptation de ce type d'approche à la $3D$ réside évidemment dans les temps de calcul impliqués. Or, l'équipe PhyProDiv ne dispose pas de code DEM $3D$ parallélisé. Parmi les opérations réalisées par un code DEM, la recherche de voisins peut s'avérer chronophage dans le cas des milieux de forte polydispersité. Il s'agit de systèmes peu étudiés numériquement en $3D$, et qui sont pourtant d'une grande importance pour les procédés. C'est pourquoi j'ai commencé à développer un code DEM $3D$ parallélisé par MPI (Fig. 3.7) et optimisé pour les fortes polydispersités. Il s'agit d'un code reposant sur un algorithme de type dynamique moléculaire et parallélisé par décomposition de domaine. D'une part, la topologie de décomposition est non régulière, d'autre part, le code est dynamiquement équilibré en charge, et enfin, les communications sont asynchrones. La scalabilité du code doit encore être évaluée, mais ces caractéristiques devraient permettre un fonctionnement efficace. Pour gérer les fortes polydispersités, une hiérarchie de grilles de cellules [82] sur tables de hachage est en cours de développement.

Cet outil trouvera évidemment d'autres applications. A titre d'exemple, Komlanvi LAMPOH, de l'équipe PhyProDiv, étudie le tri électrostatique de particules aussi bien expérimentalement que numériquement. Les simulations doivent bien-sûr être réalisées en $3D$, et impliquent des calculs longs, même avec un nombre modeste de particules. L'intégration de l'électrostatique dans mon code DEM sera réalisé en collaboration avec Komlanvi LAMPOH et permettra de mettre en œuvre des simulations de plus grande ampleur. Par ailleurs, les numériciens de l'équipe PhyProDiv sont impliqués dans un réseau de collaborations régulières autour des questions de simulation

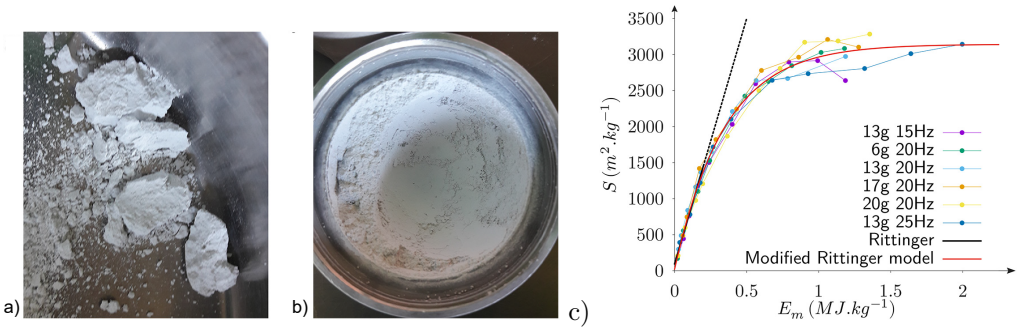

FIGURE 3.8 – Phénomène d'agglomération au cours du broyage d'un sable de silice à l'aide d'un broyeur à boulet [15]. a) Agglomérats, observés en cours de broyage. b) Collematage du broyeur. c) Evolution de la surface spécifique des particules en fonction de l'énergie de broyage spécifique. Comparaison avec le modèle de Rittinger et un modèle de Rittinger modifié prenant en compte l'agglomération.

numérique pour la physique des milieux granulaires, notamment avec Farhang RADJAI (LMGC, Montpellier) et Vincent RICHEFEU (3SR, Grenoble). Disposer d'une architecture massivement parallèle dédiée à la simulation de milieux granulaires polydisperses de grande taille nous permet d'envisager une grande variété d'applications. La rhéologie de milieux composés de fibres présente un intérêt fondamental, mais aussi applicatif, en particulier dans le cadre de la bioraffinerie. Cette application particulière a l'avantage de nécessiter des modifications peu invasives du code. En effet, si on considère des fibres rigides, les particules peuvent être assimilées à des sphéro-cylindres, et restent donc convexes. Dans ce cas, deux particules ne peuvent avoir qu'un seul point de contact et la structure du code n'est pas modifiée. Par ailleurs, les empilements de fibre ainsi produits pourront être utilisés dans le cadre d'expériences numériques de mouillage ou de filtration.

3.2 Capillarité

Les interactions avec l'eau ont un impact majeur sur le comportement mécanique d'un milieu granulaire. Même à des taux d'humidité de l'ordre de 1%, des ponts capillaires se forment entre les grains en contact et donnent lieu à des phénomènes de cohésion [95]. La rhéologie du milieu est alors modifiée, et des aggrégats peuvent se former. Certains procédés de broyage reposent sur un mode de sollicitation mécanique peu efficace pour briser ces agrégats. C'est le cas des broyeurs à boulet, utilisés pour produire des particules très fines. Or, l'intensité relative des interactions capillaires vis-à-vis des autres forces est d'autant plus grande que les particules sont petites. Des agrégats stables se forment (Fig. 3.8a) et sont, aux temps longs, susceptibles de s'assembler et de colmater l'intégralité de la surface intérieure du broyeur (Fig. 3.8b). Cette épaisse couche de poudre cohésive amortit les chocs du boulet contre les parois et inhibe les évènements de rupture. Par conséquent, le rendement énergétique du procédé s'effondre et la taille minimale de particule pouvant être obtenue est limitée (Fig. 3.8c).

La présence de ponts capillaires entre particules est préjudiciable au rendement des procédés de broyage, mais beaucoup de procédés de mise en forme ou de traitement de solides d'origine végétale reposent sur la mise en contact d'un milieu granulaire avec une phase liquide. Ces procédés sont utilisés aussi bien en agro-alimentaire [8] que dans la production de matériaux [121]. Com-

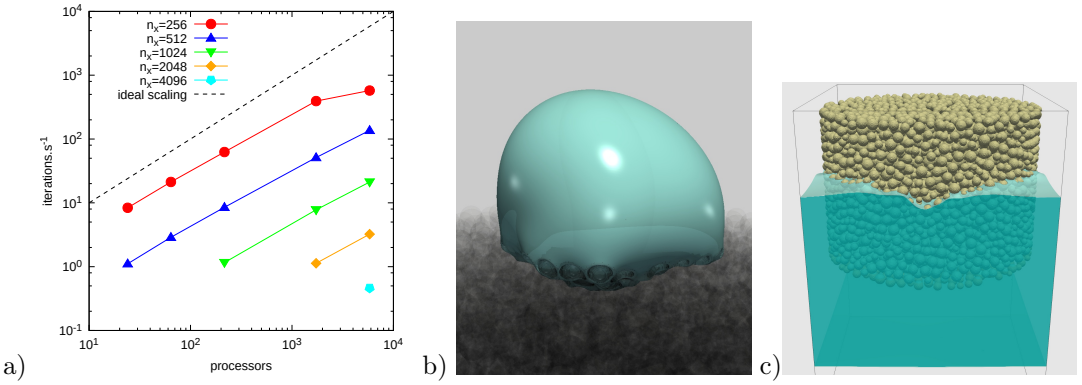

FIGURE 3.9 – a) Vitesse d'exécution du code LB sur le super-calculateur Occigen en fonction du nombre de processeurs pour différentes résolution ($n_x = n_y = n_z$). b) Etalement d'une goutte sur un milieu granulaire simulé par LB c) Imbibition d'un milieu granulaire simulé par LB.

prendre la cinétique de mouillage d'une poudre est un enjeu majeur dans la mesure où l'efficacité du procédé et les qualités du produit final dépendent souvent fortement de cette étape [8]. Or, il s'agit d'un processus complexe, qui va dépendre non seulement de l'intensité des interactions entre la surface des grains et la phase liquide, mais aussi de la microstructure du milieu granulaire. Qu'il s'agisse d'optimiser le contact entre les particules et la phase liquide, de générer une cohésion ou encore de produire des agregats d'une taille fixée, la topologie de la phase liquide est particulièrement importante. Si la teneur en eau de l'espace poral est faible, à l'équilibre, le liquide se présente sous forme de ponts isolés. Pour des teneurs en eau plus importantes, des ponts voisins coalescent, et la phase liquide se présente sous forme de clusters englobant plusieurs grains, tout en restant discontinue. Enfin, pour les fortes valeurs de taux d'humidité, les clusters coalescent et la phase liquide devient continue. Ces régimes sont, respectivement, le régime pendulaire, le régime funiculaire et le régime capillaire [79].

Etant données les difficultés inhérentes à cette thématique de recherche, l'expérimentation numérique est une voie privilégiée d'obtention d'informations à l'échelle du pore. Des résultats consistants peuvent être obtenus avec des approches $2D$, notamment concernant les états d'équilibre [23]. Cependant, il est clair que la topologie de la phase porale n'est pas du tout la même en $2D$ et en $3D$, ce qui est rédhibitoire pour la simulation des phénomènes dynamiques. Il est donc indispensable de développer des approches $3D$ efficaces. L'approche LB est bien adaptée à l'éxécution en parallèle, elle constitue donc un choix pertinent pour mener des expériences numériques impliquant des systèmes de grande taille, comme des milieux poreux complexes décrits à l'échelle du pore en $3D$. J'ai donc développé un code LB basé sur l'approche de Kupershtokh [65, 66] et parallélisé via MPI. Ce code a été porté sur le supercalculateur Occigen du CINES afin de tester sa scalabilité. Les tests n'ont pu être menés qu'avec 5832 processeurs au maximum (Fig. 3.9a). Le code s'est avéré très scalable jusqu'à 5832 processeurs pour des résolutions $512 \times 512 \times 512$ et au-delà.

L'approche de Kupershtokh est tout aussi versatile que l'approche Shan et Chen ; la mouillabilité de la phase solide est fixée en lui attribuant une densité virtuelle. Un index, défini sur l'intégralité de la grille, prends une valeur entière dépendant de la phase, par exemple, 0 pour les phases fluides, et 1 pour la phase solide, voire une valeur supérieure à 1 si le système comprends plusieurs phases solides de mouillabilités différentes. Reste alors à construire le milieu granulaire. Celui-ci peut être issu d'une tomographie 3D, mais la voie la plus immédiate pour étudier

l'influence de paramètres microstructuraux consiste à générer la phase solide numériquement, à l'aide d'une simulation par éléments discrets, par Monte Carlo...

A partir de cette structure, diverses expériences numériques peuvent être mises en œuvre en fonction de l'état initial de la phase liquide et de la phase gaz et en fonction d'un éventuel terme source affectant la densité ou la quantité de mouvement. On peut réaliser une expérience d'imbibition capillaire, d'imbibition forcée, de drainage, d'étalement d'une goutte. Il est également possible de provoquer une condensation quasi-statique sur les grains afin de déterminer les états d'équilibre non saturés. Quelques tests prélimnaires ont été réalisés avec mon code (Fig. 3.9 :b,c). Toute la méthodologie nécessaire est donc en place pour étudier l'impact de la microstructure sur le comportement d'un milieu granulaire vis-à-vis de l'eau : influence de la compacité de l'empilement, de la polydispersité, de la forme des particules, etc... En particulier, il serait possible de réaliser ce type d'étude sur un empilement de particules non sphériques en collaboration avec Vincent RICHEFEU (3SR, Grenoble), qui a développé un code DEM $3D$ dédié aux granulaires constitués de polyèdres.

Conclusion

De manière générale, mes activités de recherche relèvent de la physique numérique et prennent place dans un contexte applicatif relevant du génie des procédés. Dans un premier temps, je me suis intéressé à des phénomènes observés dans les colonnes à bulles. Si ce type de réacteur permet de traiter des matières premières d'origine végétale, il s'agit encore du génie des procédés hérité de la pétrochimie, centré sur les transformations à l'échelle moléculaire. Les enjeux scientifiques visent essentiellement à s'appuyer sur la mécanique des fluides pour optimiser la mise en contact des espèces chimiques. Après mon recrutement à l'INRA, j'ai été affecté dans des unités de recherche majoritairement tournées vers les ressources d'origine végétales. j'ai donc été amené à m'intéresser davantage à la matière à l'état solide.

Cette évolution constitue une opportunité de mettre en accord mes activités avec un changement d'orientation industrielle rendu nécessaire pas les enjeux environnementaux. Il s'agit alors de substituer les ressources végétales au pétrole dans divers secteurs, énergie et matériaux, notamment. Les circuits industriels de transformation du pétrole commencent par la raffinerie, une étape de séparation et de fractionnement des constituants de la matière première fossile. De même, une condition nécessaire de la transition vers une industrie fondée sur la transformation de ressources d'origine végétale est le développement de procédés de bioraffinerie. Ceux-ci consistent à diviser la matière végétale et à en séparer les différents tissus. Le fractionnement passe alors par des procédés de broyage et des procédés de séparation qui s'avèrent à la fois plus complexes, plus énergivores et moins sélectifs que leurs homologues en phase liquide. Pour comprendre les phénomènes impliqués dans ces procédés et être en mesure de les optimiser, il faut s'appuyer à la fois sur la rhéophysique des milieux granulaires et la mécanique de la fissuration des matériaux hétérogènes.

Depuis mon arrivée à l'UMR IATE, mes activités relèvent pleinement de ce cadre. Mes recheches sur la fragmentation des matériaux hétérogènes contibuent à comprendre les processus de division de la matière végétale à partir de la microstructure complexe de ces matériaux. Les poudres ainsi obtenues sont soumises à des écoulements granulaires dans tous les procédés voie sèche, qu'il s'agisse de broyage ou de séparation. Les simulations DEM massivement parallèles qui font partie de mon projet constitueront une voie d'expérimentation dans cette thématique. Enfin, l'interaction des granulaires produits avec l'eau influe fortement leur rhéologie. Par ailleurs, dans le cadre d'applications relevant de la chimie, l'imprégnation d'un lit granulaire est une étape limitante potentielle. C'est pourquoi j'ai inclus dans mon projet l'étude des phénomènes capillaires dans les granulaires à l'aide de simulations Lattice Boltzmann massivement parallèles.

Bibliographie

[1] R. Affes, J. Y. Delenne, Y. Monerie, F. Radjaï, and V. Topin. Tensile strength and fracture of cemented granular aggregates. *The European Physical Journal E*, 35(11) :117, November 2012.

[2] Sikandar Almani, Walid Blel, Emilie Gadoin, and Caroline Gentric. Investigation of single bubbles rising in Newtonian and non-Newtonian fluids inside a thin-gap bubble column intended for microalgae cultivation. *Chemical Engineering Research and Design*, 167 :218–230, March 2021.

[3] G. Almeida, S. Leclerc, and P. Perre. Nmr imaging of fluid pathways during drainage of softwood in a pressure membrane chamber. *International Journal of Multiphase Flow*, 34(3) :312 – 321, 2008.

[4] M. Assad-Bustillos, C. Tournier, G. Feron, S. Guessasma, A.L. Reguerre, and G. Della Valle. Fragmentation of two soft cereal products during oral processing in the elderly : Impact of product properties and oral health status. *Food Hydrocolloids*, 91 :153–165, June 2019.

[5] Sahar Bakhshian, Seyyed A. Hosseini, and Nima Shokri. Pore-scale characteristics of multiphase flow in heterogeneous porous media using the lattice Boltzmann method. *Scientific Reports*, 9(1) :3377, December 2019.

[6] György L. Balázs, Éva Lublóy, and Tamás Földes. Evaluation of concrete elements with x-ray computed tomography. *Journal of Materials in Civil Engineering*, 30(9) :06018010, 2018.

[7] F. Barthelat, Z. Yin, and M.J. Buehler. Structure and mechanics of interfaces in biological materials. *Nature Reviews Materials*, 1, 2016. cited By 265.

[8] Bettina Bellocq, Bernard Cuq, Thierry Ruiz, Agnès Duri, Kevin Cronin, and Denis Ring. Impact of fluidized bed granulation on structure and functional properties of the agglomerates based on the durum wheat semolina. *Innovative Food Science & Emerging Technologies*, 45 :73–83, February 2018.

[9] D. Bhaga and M. E. Weber. Bubbles in viscous liquids : shapes, wakes and velocities. *Journal of Fluid Mechanics*, 105 :61–85, 1981.

[10] D. Bhaga and M.E. Weber. In-line interaction of a pair of bubbles in a viscous liquid. *Chemical Engineering Science*, 35(12) :2467 – 2474, 1980.

[11] Anne-Laure Biance, Christophe Clanet, and David Quéré. First steps in the spreading of a liquid droplet. *Physical Review E*, 69 :016301, Jan 2004.

[12] James C. Bird, Shreyas Mandre, and Howard A. Stone. Short-time dynamics of partial wetting. *Physical Review Letters*, 100 :234501, Jun 2008.

[13] Nicolas Blanc, Xavier Frank, Jean-Yves Delenne, Claire Mayer-Laigle, and Farhang Radjai. Etude peridynamique de la rupture de particules sous impact. In *22ème Congrès Français de Mécanique*, Lyon, France, Août 2015.

[14] Nicolas Blanc, Xavier Frank, Farhang Radjai, Claire Mayer-Laigle, and Jean-Yves Delenne. Breakage of flawed particles by peridynamic simulations. *Computational Particle Mechanics*, February 2021.

[15] Nicolas Blanc, Claire Mayer-Laigle, Xavier Frank, Farhang Radjai, and Jean-Yves Delenne. Evolution of grinding energy and particle size during dry ball-milling of silica. *Powder Technology*, 376 :661–667, 2020.

[16] Edo S. Boek and Maddalena Venturoli. Lattice-Boltzmann studies of fluid flow in porous media with realistic rock geometries. *Computers & Mathematics with Applications*, 59(7) :2305–2314, April 2010.

[17] Eric Bonabeau and Guy Theraulaz. *Intelligence collective*. Hermes Science Publications, 1994.

[18] F. Brauer, C. P. Dullemond, and Th. Henning. Coagulation, fragmentation and radial motion of solid particles in protoplanetary disks. *Astronomy & Astrophysics*, 480(3) :859–877, March 2008.

[19] Emna Chichti, Valérie Lullien-Pellerin, Matthieu George, Farhang Radjai, Rafik Affès, and Jean-Yves Delenne. Bottom-up model for understanding the effects of wheat endosperm microstructure on its mechanical strength. *Journal of Food Engineering*, 190 :40–47, December 2016.

[20] Stefan Chmiela, Huziel E. Sauceda, Klaus-Robert Müller, and Alexandre Tkatchenko. Towards exact molecular dynamics simulations with machine-learned force fields. *Nature Communications*, 9(1) :3887, December 2018.

[21] Kirsten Claridge and Alessandro Troisi. Developing Consistent Molecular Dynamics Force Fields for Biological Chromophores via Force Matching. *The Journal of Physical Chemistry B*, 123(2) :428–438, January 2019.

[22] P. G. de Gennes. Wetting : statics and dynamics. *Reviews of Modern Physics*, 57(3) :827–863, July 1985.

[23] Jean-Yves Delenne, Vincent Richefeu, and Farhang Radjai. Liquid clustering and capillary pressure in granular media. *Journal of Fluid Mechanics*, 762 :R5, January 2015.

[24] Dominique d'Humières. Multiple–relaxation–time lattice boltzmann models in three dimensions. *Philosophical Transactions of the Royal Society of London A : Mathematical, Physical and Engineering Sciences*, 360(1792) :437–451, 2002.

[25] Agustí Emperador, Pedro Sfriso, Marcos Ariel Villarreal, Josep Lluis Gelpí, and Modesto Orozco. PACSAB : Coarse-Grained Force Field for the Study of Protein–Protein Interactions and Conformational Sampling in Multiprotein Systems. *Journal of Chemical Theory and Computation*, 11(12) :5929–5938, December 2015.

[26] S. Esna Ashari, G. Buscarnera, and G. Cusatis. A lattice discrete particle model for pressure-dependent inelasticity in granular rocks. *International Journal of Rock Mechanics and Mining Sciences*, 91 :49–58, January 2017.

[27] X. Frank, G. Almeida, and P. Perré. Multiphase flow in the vascular system of wood : From microscopic exploration to 3-d lattice boltzmann experiments. *International Journal of Multiphase Flow*, 36(8) :599–607, 2010.

[28] X. Frank, N. Dietrich, and Huai Z. Li. A damping phenomenon in viscoelastic fluids. *Europhysics Letters*, 105(5) :54006, 2014.

[29] X. Frank, D. Funfschilling, N. Midoux, and H.-Z. Li. Bubbles in a viscous liquid : lattice boltzmann simulation and experimental validation. *Journal of Fluid Mechanics*, 546 :113–122, 2006.

[30] X. Frank, H.Z. Li, and D. Funfschilling. An analytical approach to the rise velocity of periodic bubble trains in non-newtonian fluids. *The European Physical Journal E*, 16(1) :29–35, 2005.

[31] X. Frank and P. Perré. Droplet spreading on a porous surface : A lattice boltzmann study. *Physics of Fluids*, 24(4) :042101, 2012.

[32] X. Frank, P. Perré, and H.Z. Li. Lattice boltzmann investigation of droplet inertial spreading on various porous surfaces. *Physical Review E*, 91 :052405, May 2015.

[33] Xavier Frank, Jean-Claude Charpentier, Youguang Ma, Noël Midoux, and Huai Zhi Li. A multiscale approach for modeling bubbles rising in non-newtonian fluids. *Industrial & Engineering Chemistry Research*, 51(4) :2084–2093, 2012.

[34] Xavier Frank and Jean-Yves Delenne. Simulation numérique de la fissuration d'un matériau granulaire cimenté par une approche peridynamique. In *21ème Congrès Français de Mécanique*, Bordeaux, France, Août 2013.

[35] Xavier Frank, Jean-Yves Delenne, and Farhang Radjai. Numerical study of the failure of materials embedding soft to hard particles. *EPJ Web of Conferences*, 140 :02029, 2017.

[36] Xavier Frank and Huai Z. Li. Complex flow around a bubble rising in a non-newtonian fluid. *Physical Review E*, 71 :036309, Mar 2005.

[37] Xavier Frank and Huai-Zhi Li. Negative wake behind a sphere rising in viscoelastic fluids : A lattice boltzmann investigation. *Physical Review E*, 74 :056307, Nov 2006.

[38] Xavier Frank and Huai-Zhi Li. Route to chaos in the rising dynamics of a bubble chain in a polymeric fluid. *Physics Letters A*, 372(40) :6155–6160, 2008.

[39] Xavier Frank and Patrick Perré. The potential of meshless methods to address physical and mechanical phenomena involved during drying at the pore level. *Drying Technology*, 28(8) :932–943, 2010.

[40] Xavier Frank, Farhang Radjaï, Saied Nezamabadi, and Jean-Yves Delenne. Tensile strength of granular aggregates : Stress chains across particle phase versus stress concentration by pores. *Physical Review E*, 102(2) :022906, August 2020.

[41] Frank, X., Charpentier, J.-C., Cannevière, F., Midoux, N., and Li, H.Z. Bubbles in non-newtonian fluids : A multiscale modeling. *Oil & Gas Science and Technology – Rev. IFP Energies Nouvelles*, 68(6) :1059–1072, 2013.

[42] D. Fünfschilling. *Dynamique des bulles dans les fluides rhéologiquement complexes*. Thèse de doctorat, Institut National Polytechnique de Lorraine, Nancy, 1999.

[43] D. Funfschilling and H.Z. Li. Flow of non-newtonian fluids around bubbles : {PIV} measurements and birefringence visualisation. *Chemical Engineering Science*, 56(3) :1137 – 1141, 2001. 16th International Conference on Chemical Reactor Engineering.

[44] L. J. Gibson and M. F. Ashby. The mechanics of three-dimensional cellular materials. *Proceedings of the Royal Society of London. A. Mathematical and Physical Sciences*, 382(1782) :43–59, July 1982.

[45] L. J. Gibson, M. F. Ashby, G. S. Schajer, and C. I. Robertson. The mechanics of two-dimensional cellular materials. *Proceedings of the Royal Society of London. A. Mathematical and Physical Sciences*, 382(1782) :25–42, July 1982.

[46] L. Giraud, D. d'Humières, and P. Lallemand. A lattice boltzmann model for jeffreys viscoelastic fluid. *Europhysics Letters*, 42(6) :625, 1998.

[47] Timothy M. Glennon, Ya-Jun Zheng, Scott M. Le Grand, Brad A. Shutzberg, and Kenneth M. Merz. A force field for monosaccharides and (1 ? 4) linked polysaccharides. *Journal of Computational Chemistry*, 15(9) :1019–1040, September 1994.

[48] N.J. Grantham, J. Wurman-Rodrich, O.M. Terrett, J.J. Lyczakowski, K. Stott, D. Iuga, T.J. Simmons, M. Durand-Tardif, S.P. Brown, R. Dupree, M. Busse-Wicher, and P. Dupree. An even pattern of xylan substitution is critical for interaction with cellulose in plant cell walls. *Nature Plants*, 3(11) :859–865, 2017. cited By 89.

[49] Alan Arnold Griffith. The phenomena of rupture and flow in solids. *Philosophical Transactions of the Royal Society of London. Series A, Containing Papers of a Mathematical or Physical Character*, 221(582-593) :163–198, January 1921.

[50] Andrew K. Gunstensen and Daniel H. Rothman. Lattice-Boltzmann studies of immiscible two-phase flow through porous media. *Journal of Geophysical Research : Solid Earth*, 98(B4) :6431–6441, April 1993.

[51] A. Gupta, M. Sbragaglia, and A. Scagliarini. Hybrid lattice boltzmann/finite difference simulations of viscoelastic multicomponent flows in confined geometries. *Journal of Computational Physics*, 291 :177 – 197, 2015.

[52] Youn Doh Ha and Florin Bobaru. Characteristics of dynamic brittle fracture captured with peridynamics. *Engineering Fracture Mechanics*, 78 :1156–1168, 2011.

[53] O. Hassager. Negative wake behind bubbles in non-newtonian liquids. *Nature*, 279 :402 – 403, 1979.

[54] Xiaoyi He, Shiyi Chen, and Raoyang Zhang. A lattice boltzmann scheme for incompressible multiphase flow and its application in simulation of rayleigh-taylor instability. *Journal of Computational Physics*, 152(2) :642 – 663, 1999.

[55] L. Hedjazi, C.L. Martin, S. Guessasma, G. Della Valle, and R. Dendievel. Experimental investigation and discrete simulation of fragmentation in expanded breakfast cereals. *Food Research International*, 55 :28–36, January 2014.

[56] K. Heinze, X. Frank, V. Lullien-Pellerin, M. George, F. Radjai, and J.-Y. Delenne. Stress transmission in cemented bidisperse granular materials. *Phys. Rev. E*, 101 :052901, May 2020.

[57] K. Heinze, X. Frank, V. Lullien-Pellerin, M. George, F. Radjai, and J.-Y. Delenne. Stress transmission in cemented bidisperse granular materials. *Physical Review E*, 101(5) :052901, May 2020.

[58] R. Hu, J. Li, X. Wang, X. Zhao, X. Yang, Q. Tang, G. He, G. Zhou, and Y. Kong. Xylan synthesized by irregular xylem 14 (irx14) maintains the structure of seed coat mucilage in arabidopsis. *Journal of Experimental Botany*, 67(5) :1243–1257, 2016. cited By 31.

[59] Ispolatov Iaroslav and Grant Martin. Lattice boltzmann method for viscoelastic fluids. *Physical Review E*, 65 :056704, May 2002.

[60] Su Jin, Ouyang Jie, Wang Xiaodong, and Yang Binxin. Lattice boltzmann method coupled with the oldroyd-b constitutive model for a viscoelastic fluid. *Physical Review E*, 88 :053304, Nov 2013.

[61] Zhifeng Jing, Chengwen Liu, Sara Y. Cheng, Rui Qi, Brandon D. Walker, Jean-Philip Piquemal, and Pengyu Ren. Polarizable Force Fields for Biomolecular Simulations : Recent Advances and Applications. *Annual Review of Biophysics*, 48(1) :371–394, May 2019.

[62] J. Katz and C. Meneveau. Wake-induced relative motion of bubbles rising in line. *International Journal of Multiphase Flow*, 22(2) :239 – 258, 1996.

[63] R. Keller. Structure composition formation du bois, 1991.

[64] M. Kemiha, X. Frank, S. Poncin, and H.Z. Li. Origin of the negative wake behind a bubble rising in non-newtonian fluids. *Chemical Engineering Science*, 61(12) :4041 – 4047, 2006.

[65] A L Kupershtokh. Three-dimensional LBE simulations of a decay of liquid dielectrics with a solute gas into the system of gas–vapor channels under the action of strong electric fields. page 10, 2014.

[66] A.L. Kupershtokh, D.A. Medvedev, and D.I. Karpov. On equations of state in a lattice Boltzmann method. *Computers & Mathematics with Applications*, 58(5) :965–974, September 2009.

[67] Huai Z. Li, Youssef Mouline, Lionel Choplin, and Noël Midoux. Rheological simulation of in-line bubble interactions. *AIChE Journal*, 43(1) :265–267, 1997.

[68] H.Z. Li, X. Frank, D. Funfschilling, and Y. Mouline. Towards the understanding of bubble interactions and coalescence in non-newtonian fluids : a cognitive approach. *Chemical Engineering Science*, 56(21–22) :6419 – 6425, 2001. Proceedings of the 5th International Conference on Gas-Liquid and Gas-Liquid-Solid Reactor Engineering.

[69] H.Z. Li, Y. Mouline, L. Choplin, and N. Midoux. Chaotic bubble coalescence in non-newtonian fluids. *International Journal of Multiphase Flow*, 23(4) :713 – 723, 1997.

[70] H.Z. Li, Y. Mouline, D. Funfschilling, P. Marchal, L. Choplin, and N. Midoux. Evidence for in-line bubble interactions in non-newtonian fluids. *Chemical Engineering Science*, 53(12) :2219 – 2230, 1998.

[71] Liang Li, Patrick Perré, Xavier Frank, and Karim Mazeau. A coarse-grain force-field for xylan and its interaction with cellulose. *Carbohydrate Polymers*, 127 :438–450, 2015.

[72] Wei Lin, Shengchun Xiong, Yang Liu, Ying He, Shasha Chu, and Siyu Liu. Spontaneous imbibition in tight porous media with different wettability : Pore-scale simulation. *Physics of Fluids*, 33(3) :032013, 2021.

[73] Roberto D. Lins and Philippe H. Hünenberger. A new GROMOS force field for hexopyranose-based carbohydrates. *Journal of Computational Chemistry*, 26(13) :1400–1412, October 2005.

[74] Jaime Lopez, Clarence A Miller, and Eli Ruckenstein. Spreading kinetics of liquid drops on solids. *Journal of Colloid and Interface Science*, 56(3) :460–468, September 1976.

[75] Siewert J. Marrink, H. Jelger Risselada, Serge Yefimov, D. Peter Tieleman, and Alex H. de Vries. The MARTINI Force Field : Coarse Grained Model for Biomolecular Simulations. *The Journal of Physical Chemistry B*, 111(27) :7812–7824, July 2007.

[76] Nicos S. Martys and Hudong Chen. Simulation of multicomponent fluids in complex three-dimensional geometries by the lattice boltzmann method. *Phys. Rev. E*, 53 :743–750, Jan 1996.

[77] Z. Miao, T.E. Grift, A.C. Hansen, and K.C. Ting. Energy requirement for comminution of biomass in relation to particle physical properties. *Industrial Crops and Products*, 33(2) :504–513, March 2011.

[78] Yozo Mikata. Linear peridynamics for isotropic and anisotropic materials. *International Journal of Solids and Structures*, 158 :116–127, February 2019.

[79] Namiko Mitarai and Franco Nori. Wet Granular Materials. *Advances in Physics*, 55(1-2) :1–45, January 2006. arXiv : cond-mat/0601660.

[80] Luca Monticelli, Senthil K. Kandasamy, Xavier Periole, Ronald G. Larson, D. Peter Tieleman, and Siewert-Jan Marrink. The MARTINI Coarse-Grained Force Field : Extension to Proteins. *Journal of Chemical Theory and Computation*, 4(5) :819–834, May 2008.

[81] Tim Napier-Munn. Is progress in energy-efficient comminution doomed ? *Minerals Engineering*, 73 :1–6, March 2015.

[82] V. Ogarko and S. Luding. A fast multilevel algorithm for contact detection of arbitrarily polydisperse objects. *Computer Physics Communications*, 183(4) :931–936, April 2012.

[83] Luisa Fernanda Orozco, Duc-Hanh Nguyen, Jean-Yves Delenne, Philippe Sornay, and Farhang Radjai. Discrete-element simulations of comminution in rotating drums : Effects of grinding media. *Powder Technology*, 362 :157–167, February 2020.

[84] Mario Orsi and Jonathan W. Essex. The ELBA Force Field for Coarse-Grain Modeling of Lipid Membranes. *PLoS ONE*, 6(12) :e28637, December 2011.

[85] C. Pan, M. Hilpert, and C. T. Miller. Lattice-Boltzmann simulation of two-phase flow in porous media : LB SIMULATION OF TWO-PHASE FLOW. *Water Resources Research*, 40(1), January 2004.

[86] S. Papenkort and Th. Voigtmann. Lattice boltzmann simulations of a viscoelastic shear-thinning fluid. *The Journal of Chemical Physics*, 143(4) :044512, 2015.

[87] Patrick Perré, Giana Almeida, Mehdi Ayouz, and Xavier Frank. New modelling approaches to predict wood properties from its cellular structure : image-based representation and meshless methods. *Ann. Forest Sci.*, 73(1) :147–162, 2016.

[88] P. Perré and J. Passard. A physical and mechanical model able to predict the stress field in wood over a wide range of drying conditions. *Drying Technology*, 22(1-2) :27–44, 2004.

[89] Jérôme Peydecastaing. Chemical modification of wood by mixed anhydrides. page 234.

[90] Farhang Radjai, Michel Jean, Jean-Jacques Moreau, and Stéphane Roux. Force Distributions in Dense Two-Dimensional Granular Systems. *Physical Review Letters*, 77(2) :274–277, July 1996.

[91] Farhang Radjai, Dietrich E. Wolf, Michel Jean, and Jean-Jacques Moreau. Bimodal character of stress transmission in granular packings. *Phys. Rev. Lett.*, 80 :61–64, Jan 1998.

[92] P. Raiskinmäki, A. Shakib-Manesh, A. Jäsberg, A. Koponen, J. Merikoski, and J. Timonen. Lattice-boltzmann simulation of capillary rise dynamics. *Journal of Statistical Physics*, 107(1) :143–158, Apr 2002.

[93] Shuling Rao, Xuejin Li, and Haojun Liang. Developing coarse-grained force fields for polystyrene with different chain lengths from atomistic simulation. *Macromolecular Research*, 15(7) :610–616, December 2007.

[94] A. K. Rappe, C. J. Casewit, K. S. Colwell, W. A. Goddard, and W. M. Skiff. UFF, a full periodic table force field for molecular mechanics and molecular dynamics simulations. *Journal of the American Chemical Society*, 114(25) :10024–10035, December 1992.

[95] Vincent Richefeu, Moulay Saïd El Youssoufi, and Farhang Radjaï. Shear strength properties of wet granular materials. *Physical Review E*, 73(5) :051304, May 2006.

[96] Paul Robustelli, Stefano Piana, and David E. Shaw. Developing a molecular dynamics force field for both folded and disordered protein states. *Proceedings of the National Academy of Sciences*, 115(21) :E4758–E4766, May 2018.

[97] D. Rodrigue. Generalized correlation for bubble motion. *AIChE Journal*, 47(1) :39–44, 2001.

[98] M.C. Ruzicka. On bubbles rising in line. *International Journal of Multiphase Flow*, 26(7) :1141 – 1181, 2000.

[99] R. Rémond, J. Passard, and P. Perré. The effect of temperature and moisture content on the mechanical behaviour of wood : a comprehensive model applied to drying and bending. *European Journal of Mechanics - A/Solids*, 26(3) :558 – 572, 2007.

[100] R. Schulz, B. Lindner, L. Petridis, and J.C. Smith. Scaling of multimillion-atom biological molecular dynamics simulation on a petascale supercomputer. *Journal of Chemical Theory and Computation*, 5 :–, 2009.

[101] Xiaowen Shan and Hudong Chen. Lattice boltzmann model for simulating flows with multiple phases and components. *Physical Review E*, 47 :1815–1819, Mar 1993.

[102] Rulin Shen, Rui Xiong, and Yanling Gong. Analysis of Damage and Crack Propagation in Unidirectional Composite Laminates with a Peridynamic Model. *Journal of Physics : Conference Series*, 1549 :032088, June 2020.

[103] M. Shishehbor and P.D. Zavattieri. Effects of interface properties on the mechanical properties of bio-inspired cellulose nanocrystal (cnc)-based materials. *Journal of the Mechanics and Physics of Solids*, 124 :871–896, 2019. cited By 25.

[104] S.A. Silling. Reformulation of elasticity theory for discontinuities and long-range forces. *J. Mech. Phys. Solids*, 48 :175–209, 2000.

[105] Stewart A Silling, Michael J Epton, Olaf Weckner, Jiadi Xu, and Ebrahim Askari. Peridynamic states and constitutive modeling. *Journal of Elasticity*, 88 :151–184, 2007.

[106] T.J. Simmons, J.C. Mortimer, O.D. Bernardinelli, A.-C. Pöppler, S.P. Brown, E.R. DeAzevedo, R. Dupree, and P. Dupree. Folding of xylan onto cellulose fibrils in plant cell walls revealed by solid-state nmr. *Nature Communications*, 7, 2016. cited By 166.

[107] I. J. Smalley. Formation of Quartz Sand. *Nature*, 211(5048) :476–479, July 1966.

[108] Stuart H. Smith. On initial value problems for the flow in a thin sheet of viscous liquid. *Zeitschrift für angewandte Mathematik und Physik ZAMP*, 20(4) :556–560, July 1969.

[109] Paulo C. T. Souza, Riccardo Alessandri, Jonathan Barnoud, Sebastian Thallmair, Ignacio Faustino, Fabian Grünewald, Ilias Patmanidis, Haleh Abdizadeh, Bart M. H. Bruininks, Tsjerk A. Wassenaar, Peter C. Kroon, Josef Melcr, Vincent Nieto, Valentina Corradi, Hanif M. Khan, Jan Domański, Matti Javanainen, Hector Martinez-Seara, Nathalie Reuter, Robert B. Best, Ilpo Vattulainen, Luca Monticelli, Xavier Periole, D. Peter Tieleman, Alex H. de Vries, and Siewert J. Marrink. Martini 3 : a general purpose force field for coarse-grained molecular dynamics. *Nature Methods*, 18(4) :382–388, April 2021.

[110] L. Stover, B. Piriou, C. Caillol, P. Higelin, C. Proust, X. Rouau, and G. Vaïtilingom. Direct use of biomass powder in internal combustion engines. *Sustainable Energy Fuels*, 3 :2763–2770, 2019.

[111] Alejandro Strachan, Tahir Ça in, O uz Gülseren, Sonali Mukherjee, Ronald E Cohen, and William A GoddardIII. First principles force field for metallic tantalum. *Modelling and Simulation in Materials Science and Engineering*, 12(4) :S445–S459, July 2004.

[112] Hervé Tabuteau, Darek Sikorski, and John R. de Bruyn. Shear waves and shocks in soft solids. *Physical Review E*, 75 :012201, Jan 2007.

[113] L H Tanner. The spreading of silicone oil drops on horizontal surfaces. *Journal of Physics D : Applied Physics*, 12(9) :1473–1484, sep 1979.

[114] Vincent Topin, Farhang Radjaï, Jean-Yves Delenne, Abdelkrim Sadoudi, and Frédéric Mabille. Wheat endosperm as a cohesive granular material. *Journal of Cereal Science*, 47(2) :347–356, March 2008.

[115] Jonas Tölke. Lattice Boltzmann simulations of binary fluid flow through porous media. *Philosophical Transactions of the Royal Society of London. Series A : Mathematical, Physical and Engineering Sciences*, 360(1792) :535–545, March 2002.

[116] Edward W. Washburn. The dynamics of capillary flow. *Phys. Rev.*, 17 :273–283, Mar 1921.

[117] J.J. Williams, Z. Flom, A.A. Amell, N. Chawla, X. Xiao, and F. De Carlo. Damage evolution in SiC particle reinforced Al alloy matrix composites by X-ray synchrotron tomography. *Acta Materialia*, 58(18) :6194–6205, October 2010.

[118] Koen G. Winkels, Joost H. Weijs, Antonin Eddi, and Jacco H. Snoeijer. Initial spreading of low-viscosity drops on partially wetting surfaces. *Physical Review E*, 85(5) :055301, May 2012.

[119] Jifeng Xu, Abe Askari, Olaf Weckner, and Stewart Silling. Peridynamic analysis of impact damage in composite laminates. *Journal of Aerospace Engineering*, 21(3) :187–194, 2008.

[120] Andreas G. Yiotis, John Psihogios, Michael E. Kainourgiakis, Aggelos Papaioannou, and Athanassios K. Stubos. A lattice boltzmann study of viscous coupling effects in immiscible two-phase flow in porous media. *Colloids and Surfaces A : Physicochemical and Engineering Aspects*, 300(1) :35 – 49, 2007. Proceedings of the Fourth International TRI/Princeton Workshop «Characterization of Porous Materials : from Angstroms to Millimeters».

[121] Tingtao Zhou, Katerina Ioannidou, Franz-Josef Ulm, Martin Z. Bazant, and R. J.-M. Pellenq. Multiscale poromechanics of wet cement paste. *Proceedings of the National Academy of Sciences*, 116(22) :10652–10657, May 2019.

Curriculum Vitae

Informations générales

Xavier FRANK
Né le 23 / 06 / 1975
Adresse professionnelle : UMR IATE, 2 place Pierre Viala, 34060 MONTPELLIER
Téléphone : 04 99 61 23 88
Adresse mail : xavier.frank@inrae.fr

Situation actuelle

Depuis 2011	Chargé de recherche INRAE **(UMR INRAE 1208 IATE, Montpellier)**

Situations passées

2007-2011	Chargé de recherche INRA **(UMR INRA 1092 LERFOB, Nancy)**
2000-2007	Professeur agrégé de l'enseignement secondaire "*Physique-Chimie*", temps plein. Niveaux collège, lycée. Vacations IUT et L3.
2000–2005	Thèse, "*Approche multiéchelle de la dynamique des bulles en fluide non Newtonien*", directeur : Huai Zhi Li **(Laboratoire des Sciences du Génie Chimique, UPR CNRS 6811, ENSIC, INPL, Nancy)**
1996-2000	Scolarité département "*Physique*" **(Ecole Normale Supérieure de Cachan)**. Magistère "*Physique Fondamentale*" **(Université Paris XI, Orsay)**

Diplômes, formation

2005	Doctorat, "*Approche multiéchelle de la dynamique des bulles en fluide non Newtonien*", directeur : Huai Zhi Li **(Laboratoire des Sciences du Génie Chimique, UPR CNRS 6811, ENSIC, INPL, Nancy)**
2000	DEA "*Génie des procédés*" **(ENSIC, INPL, Nancy)**
1999	Agrégation de Physique **(Ecole Normale Supérieure de Cachan)**
1998	Maîtrise de Physique Fondamentale **(Université Paris XI, Orsay)**
1997	Licence de Physique Fondamentale **(Université Paris XI, Orsay)**

Stages

1999-2000	Stage de DEA "*Modèles mésoéchelles de trains de bulles en fluide non Newtonien : théorie et simulation numérique*" **(centre de Génie Chimique des Milieux Rhéologiquement Complexes, Nancy)**
1998	Stage de maîtrise "*Etude bibliographique et discussion de la théorie de Malkus, une théorie variationnelle de la turbulence*" **(GeoHydrodynamics and Environment Research, Université de Liège, Belgique)**

1997 Stage de licence "*Caractérisation expérimentale de pigments naturels, élaboration et utilisation d'un critère d'évaluation de leur pouvoir colorant*" **(Laboratoire de Recherche des Musées de France, Musée du Louvres, Paris)**, travaux publiés sous la forme d'un guide sur les pigments naturels édité par l'association "*Terres et Couleurs*"

Participation à l'encadrement de thèses

Depuis 2020 **Emile Collignon** Directeur de thèse : Huai Zhi Li (Pr ENSIC), co-encadrant : Xavier Frank. "*Coalescence ou étalement d'une goutte liquide sur une surface liquide ou solide : approche expérimentale multi-échelle et modélisation*". Ecole doctorale Ressources Procédés Produits Environnement, Nancy. Financement : MESR.

2015-2018 **Nicolas Blanc** Directeur de thèse : Jean-Yves Delenne (DR INRA), co-encadrants : Claire Mayer (IR INRA), Xavier Frank. "*Etude expérimentale et modélisation de la fragmentation des milieux granulaires : application au cobroyage de matières minérales et lignocellulosiques*". Ecole doctorale Information Structures Systèmes, Montpellier. Financement : BPI France.

2009-2012 **Liang Li** Directeur de thèse : Patrick Perré (Pr AgroParisTech), co-encadrant : Xavier Frank. "*Modélisation gros grain de macromolécules végétales : champ de force paramétré par dynamique moléculaire est application à des assemblages cellulose-xylane.*". Ecole doctorale Ressources Procédés Produits Environnement, Nancy. Financement : ANR.

Participation à des comités de suivi de thèse

2021 Membre du comité de suivi de thèse de **William JENKINSON** Directeurs de thèse : Olivier VITRAC (INRAE, Saclay), Denis FLICK. "*The application of novel and multiscale computational methods to oral processing*".

2020, 2021 Membre du comité de suivi de thèse de **Hao LI** Directeur de thèse : Huai Zhi LI (Université de Lorraine, Nancy). "*Initial Coalescence and Spreading of drops of non newtonian fluids*".

2017, 2018 Membre du comité de suivi de thèse de **Valério SORICHETTI** Directeur de thèse : Walter KOB (Université de Montpellier, Montpellier). "*Dynamique de nanoparticules dans des solutions et gels de polymères, approche par simulation*".

2014 Membre du comité de suivi de thèse de **Jeff NGOMA** Directeur de thèse : Pierre PHILIPPE (IRSTEA, Aix-en-Provence). " *Modélisation de la fluidisation dans les milieux granulaires immergés par couplage DEM/LB*".

Participation à des jury de thèses

2017 Membre du jury de thèse de **Xiaofeng JIANG** "*Interfacial phenomena involved in the manipulation of drops and bubbles*". LRGP, Nancy (14 Novembre)

2013 Membre du jury de thèse de **Liang LI** "*Modélisation gros grain de macromolécules végétales : champ de force paramétré par dynamique moléculaire est application à des assemblages cellulose-xylane*". LERFOB, Nancy (20 Décembre).

2011 Membre du jury de thèse de **Anh Tuan DINH** "*Comportement élastique linéaire et non-linéaire du bois en relation avec sa structure*". LERFOB, Nancy (21 Novembre)

2008 Membre du jury de thèse de **Nicolas DIETRICH** "*Étude locale et expérimentale des phénomènes interfaciaux*". LSGC, Nancy (13 Novembre).

Participation à des commissions de recrutement

2012 Membre de la commission de recrutement d'un maître de conférences à l'École Centrale de Paris (laboratoire : **LGPM**) "*Modelisation numerique des transferts de chaleur et de matiere dans le milieux poreux*".

Formation continue des chercheurs

2015 Formation théorique et pratique au calcul parallèle via MPI. Public : étudiants (thèse, post-doc) et collègues de l'UMR IATE et du LMGC.

Enseignements

2015-2020 Cours/TD annuels niveau M1 "*Bases de physique et de mathématiques appliquées*" **(Master Sciences & Procédés des Agroressources pour l'Alimentation et l'Environnement, Université de Montpellier)**. Volume annuel : 7H équivalent-TD

2015-2018 Cours annuel niveau PhD ouvert aux étudiants étrangers "*Modelling and numerical simulation for agro-resources dry biorefinery*" **(Ecole Doctorale Sciences des Procédés-Sciences des Aliments, Montpellier)**. Volume annuel : 1,5H équivalent-TD

2000-2007 Enseignement secondaire "*Physique-Chimie*", temps plein. Niveaux collège, lycée.

2006-2007 Cours/TD niveau L3 "*Transfert de chaleur*" **(Filière EEA, Université de Bretagne Occientale, Brest)**. Volume : 31H équivalent-TD

2005-2006 TP niveau IUT 1ère année "*Technologie/mécanique des fluides*" **(IUT, département chimie, Université du Mans)**. Volume : 90H équivalent-TD

2005-2006 TP niveau IUT 2ème année "*Optique*" **(IUT, département chimie, Université du Mans)**. Volume : 48H équivalent-TD

2004-2005 TP niveau IUT 1ème année "*Automatique*" **(IUT, département mesures physiques, Université du Mans)**. Volume : 17,5H équivalent-TD

Activités d'intérêt collectif

2020,2021 Membre du Comité Scientifique des Utilisateurs du cluster INRAE *MIGALE* (Jouy-en-Josas).

2010-2020 Relecture d'article pour divers journaux : *Physics of Fluids*, *International Journal of Heat and Mas Transfer*, *Chemical Engineering Science*, *Drying Technology Journal*, *International Journal for Numerical and Analytical Methods in Geomechanics*, *Microfluidics Nanofluidics*...

Evaluation de projets scientifiques

2020 Expertise de 2 projets de recherche pour le compte du Fond National de la Recherche Scientifique (**FNRS**, Belgique)

2019 Expertise de 2 projets de recherche pour le compte du Fond National de la Recherche Scientifique (**FNRS**, Belgique)

2016 Expertise de 1 projet de recherche pour le compte du Fond National de la Recherche Scientifique (**FNRS**, Belgique)

Gestion d'infrastructures scientifiques collectives

Depuis 2011 Responsable de l'infrastructure de calcul intensif à l'UMR **IATE**

2014 Dimensionnement d'un cluster de calcul implanté à l'UMR **IATE**

2008-2011 Responsable de l'infrastructure de calcul intensif à l'UMR **LERMAB/LERFOB**

2008 Dimensionnement d'un cluster de calcul implanté à l'UMR **LERMAB**

Développements informatiques pour la communauté

2013-2016 Participation au développement du site web de l'UMR IATE

2015 Jean-Yves Delenne, Vincent Richefeu, Xavier Frank, Farhang Radjaï, "*FLOWbox*", Code de calcul basé sur l'approche Lattice Boltzmann permettant, à partir d'une tomographie ou d'une modélisation de la microstructure, de calculer l'écoulement d'un gaz ou d'un liquide à travers l'échantillon (milieu poreux, milieu granulaire, etc.) et d'évaluer la perméabilité et les pertes de charge.
Dépôt APP : IDDN.FR.001.210008.000.R.A.2015.000.41000

Projets de recherche

2018-2019 Coordinateur du projet **AIC MiDiDAM** "*Approches de modélisation des Milieux Divisés appliquées à la Déconstruction d'Aliments lors de la Mastication*". Partenaires : BIA (Nantes), LMGC (Montpellier), 3SR (Grenoble). L'objectif de l'AIC MiDiDAM est d'établir une relation entre la microstructure d'un aliment de type mousse solide et son comportement mécanique en vue d'applications au lien texture-mastication. Cette démarche repose sur le développement et l'utilisation de méthodes de simulation numérique du type éléments discrets et approches sur réseau.

2014-2019 Partenaire du projet **Oséo ACA** "*Nouvelle génération de produits pour l'industrie de la construction issus de matières premières alternatives – Cobroyage minéral-lignocellulosique en vue d'optimiser la réactivité des produits*" (Coordinateur du projet : Claire Mayer-Laigle), une étude comparative du broyage de matières minérales et ligno-cellulosiques afin de quantifier les régimes en fonction de la nature de la matière première et des paramètres procédés. Deux partenaires industriels, l'entreprise Kerneos et l'entreprise Fabemi, étaient associés à ce projet. A l'échelle de la particule, des simulations numériques ont été réalisées par Nicolas BLANC, l'étudiant en thèse recruté dans le cadre du projet. Le code utilisé était le code péridynamique parallèle que j'ai développé, et j'ai co-encadré Nicolas BLANC sur ces aspects.

2012-2013 Coordinateur du projet **AIC** "*Modélisation et simulation numérique de la fragmentation des matériaux ligno-cellulosiques*". L'objectif de ce projet est de mettre au point une approche de simulation numérique dédiée aux phénomènes de fragmentation, notamment des matériaux ligno-cellulosiques. Au cours de ce projet, j'ai développé une approche de modélisation reposant sur la péridynamique.

2009-2013 Partenaire du projet **ANR ANALOGS** Coordinateur du projet : Patrick PERRE. Partenaires du projet : LERFOB (Nancy), FARE (Reims), CERMAV (Grenoble), BIA (Nantes). L'objectif ce projet est de développer deux voies parallèles de modélisation de la paroi du bois : une bois expérimentale, via la synthèse de films composites à partir des polymères pariétaux isolés, et une voie numérique. Mon implication dans le projet concerne le développement d'un modèle de dynamique moléculaire gros grain à partir de simulations atomistiques réalisées par Karim MAZEAU (CERMAV). Développement réalisé dans le cadre de la thèse de Liang LI, financée par l'ANR.

Collaborations scientifiques

2018-2021 (1 article en rédaction, **2 posters**) Application de l'approche péridynamique à la simulation numérique de la rupture de mousses solides. Collaboration avec Jean-Yves Delenne (INRAE, **IATE**, Montpellier), Sofiane Guessassma (INRAE, **BIA**, Nantes), Guy Della Valle (INRAE, **BIA**, Nantes) et Vincent Richefeu (Université Grenoble, **3SR**, Grenoble). Financement AIC MiDiDAM.

2018-2020 (**1 article, 1 communication orale, 1 séminaire**) Application de l'approche péridynamique à la modélisation du transfert des contraintes mécaniques dans l'albumen du grainde blé. Travaux dans le cadre de la thèse de Karsta HEINZE. Collaboration avec Karsta Heinze (INRAE, **IATE**, Montpellier), Jean-Yves Delenne (INRAE, **IATE**, Montpellier), Valérie Lullien-Péllerin (INRAE, **IATE**, Montpellier) et Mathieu George (Université de Montpellier, **L2C**, Montpellier).

2018-2020 (**1 article, 1 communication orale, 1 séminaire**) Application de l'approche péridynamique à la simulation numérique de la rupture d'agrégats granulaire cimentés. Collaboration avec Jean-Yves Delenne

(INRAE, **IATE**, Montpellier), Saeid Nezamabadi (Université de Montpellier, **LMGC**, Montpellier), Farhang Radjaï (CNRS, **LMGC**, Montpellier).

2018-2020 (**2 articles, 5 communications orales, 1 poster**) Développement d'une approche numérique parallélisée, basées sur la MPM et la dynamique des contacts, pour la rhéologie des matériaux constitués de grains mous, applications. Collaboration avec Saeid Nezamabadi (Université de Montpellier, **LMGC**, Montpellier), Julien Averseng (Université de Montpellier, **LMGC**, Montpellier), Jean-Yves Delenne (INRAE, **IATE**, Montpellier), Farhang Radjaï (CNRS, **LMGC**, Montpellier).

2016-2019 (**1 article, 1 poster, 3 communications orales**) Application de l'approche péridynamique à la rupture d'une particule sous compression diamétrale. Statistique de la contrainte à la rupture et des tailles de fragments. Travaux dans le cadre de la thèse de Nicolas BLANC et du projet ACA. Collaboration avec Nicolas Blanc (**IATE**, Montpellier), Jean-Yves Delenne (INRAE, **IATE**, Montpellier), Claire Mayer-Laigle (INRAE, **IATE**, Montpellier).

2015-2016 (**1 article**) Simulation peridynamique de la fissuration d'un matériau ligno-cellulosique reconstruit numériquement à partir de l'image d'une coupe d'un échantillon réel de bois et moyennant un algorithme de reconstruction de la lamelle mitoyenne. Collaboration avec Giana ALMEIDA (Agroparistech, **GENIAL**, Massy) et Patrick PERRE (École Centrale Paris, **LGPM**, Châtenay-Malabry).

2012-2015 (**2 articles, 1 communication orale**) Simulation Lattice Boltzmann de l'étalement d'une goutte sur une surface poreuse. Analyse physique de la dynamique d'imbibition capillaire, mise au point et validation numérique d'une loi effective d'étalement, universelle vis-à-vis de la forme et de la densité des pores. Collaboration avec Patrick PERRE (École Centrale Paris, **LGPM**, Châtenay-Malabry) et Huai-Zhi Li (Université de Lorraine, **LRGP**, Nancy).

2013-2014 (**3 communications orales**) Mise au point d'une démarche de modélisation et de simulation numérique de la fissuration quasi-statique d'un matériau hétérogène par une approche peridynamique. Collaboration avec Jean-Yves DELENNE (INRAE, **IATE**, Montpellier).

2012-2013 (**2 communications orales**) Mise au point d'une démarche de modélisation et de simulation numérique de la fissuration dynamique d'un matériau hétérogène par une approche peridynamique. Collaboration avec Jean-Yves DELENNE (INRAE, **IATE**, Montpellier). Financement AIC.

2010-2013 (**1 article, 2 communications orales**) Développement d'un champ de force coarse grain (CG) pour la simulation moléculaire des polymères pariétaux. Les paramètres sont déduits de simulations moléculaires atomistiques réalisées par Karim Mazeau. Application à un composite cellulose-xylane. Travaux dans le cadre le l'ANR ANALOGS et de la thèse de Liang LI. Collaboration avec Liang Li (**LERFOB**, Nancy), Karim Mazeau (CNRS, **CERMAV**, Grenoble) et Patrick Perré (École Centrale Paris, **LGPM**, Châtenay-Malabry).

2011-2012 (**1 poster**) Etude expérimentale de la dynamique d'étalement d'une goutte sur une surface de bois. Comparaison du bois natif et du bois traité. Collaboration avec Giana ALMEIDA (**LERFOB**, Nancy), Philippe JACQUIN (INRA, **LERFOB**, Nancy) et Patrick PERRE (AgroParisTech, **LERFOB**, Nancy).

2009-2010 (**1 article, 1 communication orale**) Simulation Lattice Boltzmann de l'imbibition capillaire d'un réseau vasculaire de bois reconstruit numériquement à partir des images de coupes sériées d'un échantillon de bois réel. Observation d'une dynamique contre-intuitive au niveau des bifurcations et interprétation physique. Collaboration avec Giana ALMEIDA (**LERFOB**, Nancy) et Patrick PERRE (AgroParisTech, **LERFOB**, Nancy).

Participations à l'organisations de congrès

2019 Membre du comité d'organisation des journées "*Workshop on Powders and Granular Materials, Challenges and Future Trends*", Montpellier, France.

2017 Membre du comité d'organisation du congrès "*International Conference on Micromechanics of Granular Media (Powders & Grains)*", Montpellier, France.

Participation à des réseaux thématiques

2012-2021 Membre du réseau "*Milieux Divisés*" (MiDi), groupe de recherche régional pluridisciplinaire s'intéressant à la modélisation des milieux granulaires.

Contribution organisationnelle

2018-2020 Participation au "*Groupe Chantier*", dont la mission a été de réformer l'organisation de l'UMR IATE, aussi bien en termes de gouvernance que de structure.

Production scientifique

Articles dans des revues internationales à comité de lecture

Nicolas Blanc, Xavier Frank, Farhang Radjaï, Claire Mayer-Laigle and Jean-Yves Delenne, "*Breakage of flawed particles by peridynamic simulations*", **Computational Particle Mechanics**, (2021) 2196-4386

Nicolas Blanc, Claire Mayer-Laigle, Xavier Frank, Farhang Radjaï and Jean-Yves Delenne, "*Evolution of grinding energy and particle size during dry ball-milling of silica*", **Powder Technology**, 376 (2020) 661-667

Xavier Frank, Farhang Radjaï, Saeid Nezamabadi and Jean-Yves Delenne, "*Tensile strength of granular aggregates : stress chains across particle phase vs. stress concentration by pores*", **Physical Review E**, 102, 2 (2020) 022906

Karsta Heinze, Xavier Frank, Valérie Lullien-Péllerin, Mathieu George, Farhang Radjaï and Jean-Yves Delenne, "*Stress transmission in cemented bi-disperse granular materials*", **Physical Review E**, 101, 5 (2020) 052901

Saeid Nezamabadi, Xavier Frank, Jean-Yves Delenne, Julien Averseng and Farhang Radjaï, "*Parallel implicit contact algorithm for soft particle systems*", **Computer Physics Communications**, 237 (2019) 17-25

Marc Barnabé, Nicolas Blanc, Thomas Chabin, Jean-Yves Delenne, Agnès Duri, Xavier Frank, Virginie Hugouvieux, Evelyne Lutton, Frédéric Mabille, Saeid Nezamabadi, Nathalie Perrot, Farhang Radjaï, Thierry Ruiz and Alberto Tonda, "*Multiscale modelling for bioresources and bioproducts*", **Innovative Food Science and Emerging Technologies**, 46 (2018) 41-53

Claire Mayer-Laigle, Abdellatif Barakat, Cécile Barron, Jean-Yves Delenne, Xavier Frank, Frédéric Mabille, Xavier Rouau, Abdelkrim Sadoudi, Marie-Françoise Samson, Valérie Lullien-Pellerin, "*Dry Bio-refinery : Multiscale modelling studies and innovative processing*", **Innovative Food Science and Emerging Technologies**, 46 (2018) 131-139

Saeid Nezamabadi, Thanh H. Nguyen, Jean-Yves Delenne, Julien Averseng, Xavier Frank and Farhang Radjaï, "*MPM with Frictional Contact for Application to Soft Particulate Materials*", **Procedia Engineering**, 175 (2017) 141-147

Patrick Perré, Giana Almeida, Mehdi Ayouz and Xavier Frank, "*New modelling approaches to predict wood properties from its cellular structure : image-based representation and meshless methods*", **Annals of Forest Science**, 73, 1 (2016) 147-162

Xavier Frank, Patrick Perré and Huai-Zhi Li, "*Lattice Boltzmann investigation of droplet inertial spreading on various porous surfaces*", **Physical Review E**, 91, 5 (2015) 052405

Liang Li, Patrick Perré, Xavier Frank and Karim Mazeau, "*A coarse-grain force field for xylan and its interaction with cellulose*", **Carbohydrate Polymers**, 127 (2015) 438-450

Xavier Frank, Nicolas Dietrich and Huai-Zhi Li, "*A damping phenomenon in viscoelastic fluids*", **Europhysics Letters**, 105, 5 (2014) 54006

Xavier Frank, Jean-Claude Charpentier, Frédéric Cannevière, Noël Midoux and Huai-Zhi Li, "*Bubbles in non-Newtonian fluids : a multiscale modeling*", **Oil & Gas Science and Technology**, 68, 6 (2013) 1059-1072

Patrick Perré, Anh Tuan Dinh, Carole Assor, Xavier Frank and Gilles Pilte, "*Stiffness of normal, opposite and tension poplar wood determined using micro-samples in the*

three material directions", **Wood Science and Technology**, 47, 3 (2013) 481-498

Xavier Frank and Patrick Perré, "*Droplet Spreading on a porous surface : A lattice Boltzmann study*", **Physics of Fluids**, 24, 4 (2012) 042101

Xavier Frank, Jean-Claude Charpentier, Youguang Ma, Noël Midoux and Huai-Zhi Li, "*A Multiscale Approach for Modeling Bubbles Rising in Non-Newtonian Fluids*", **Industrial and Engineering Chemistry Research**, 51, 4 (2012) 2084-2093

Xavier Frank, Giana Almeida and Patrick Perré, "*Multiphase flow in the vascular system of wood : from microscopic exploration to 3-D Lattice Boltzmann experiments*", **International Journal of Multiphase Flow**, 36, 8 (2010) 599-607

Xavier Frank and Patrick Perré, "*The potential of meshless methods to address physical and mechanical phenomena involved during drying at the pore level*", **Drying Technology Journal**, 28, 8 (2010) 932-943

Xavier Frank and Huai-Zhi Li, "*Route to chaos in the rising dynamics of a bubble chain in a polymeric fluid*", **Physics Letters A**, 372, 40 (2008) 6155-6160

Xavier Frank, Nicolas Dietrich, Jing Wu, Renaud Barraud and Huai-Zhi Li, "*Bubble nucleation and growth in fluids*", **Chemical Engineering Science**, 62, 24 (2007) 7090-7097

Xavier Frank and Huai-Zhi Li, "*Negative wake behind a sphere rising in viscoelastic fluids : A lattice Boltzmann investigation*", **Physical Review E**, 74, 5 (2006) 056307

Mohammed Kemiha, Xavier Frank, Souhila Poncin and Huai-Zhi Li, "*Origin of the negative wake behind a bubble rising in non Newtonian fluids*", **Chemical Engineering Science**, 61, 12 (2006) 4041-4047

Xavier Frank, Denis Fünfschilling, Noël Midoux and Huai-Zhi Li, "*Bubbles in viscous liquid : Lattice Boltzmann simulation and experimental validation*", **Journal of Fluid Mechanics**, 546 (2006) 113-122

Xavier Frank and Huai-Zhi Li, "*Complex flow around a bubble rising in a non Newtonian fluid*", **Physical Review E**, 71, 3 (2005) 036309

Xavier Frank, Denis Fünfschilling and Huai-Zhi Li, "*An analytical approach of the rise velocity of periodic bubble trains in non-Newtonian fluids*", **European Physical Journal E**, 16, 1 (2005) 29-35

Huai-Zhi Li and Xavier Frank, "*Bubbles' rising dynamics in polymeric solutions*", **Physics Letters A**, 325, 1 (2004) 43-50

Xavier Frank, Huai-Zhi Li, Denis Fünfschilling, Florence Burdin and Youguang Ma, "*Bubble Motion in non Newtonian Fluids and Suspensions*", **Canadian Journal of Chemical Engineering**, 81, 3-4 (2003) 483-490

Huai-Zhi Li, Xavier Frank, Denis Fünfschilling and Youssef Mouline, "*Towards the understanding of bubble interactions and coalescence in non-Newtonian fluids : a cognitive approach*", **Chemical Engineering Science**, 56, 21-22 (2001) 6419-6425

Documents techniques

Notice du logiciel FLOWbox : J.Y. Delenne, V. Richefeu, X. Frank, F. Radjai, FLOWbox user guide, 2014

Documents video

Karsta Heinze, Xavier Frank, Valerie Lullien-Pellerin, Matthieu George, Farhang Radjai, "*Numerical modeling of the tensile strength of a biological granular aggregate : Effect of the particle size distribution*", In International workshop on Powders and Grains, Jul 2017, Montpellier, France.

Publications destinées à des professionnels

Cecile Barron, Claire Mayer-Laigle, Xavier Rouau, Marie-Françoise Samson, Frédéric Mabille, Abdelkrim Sadoudi, Jean-Yves Delenne, Xavier Frank, et Valerie Lullien-Pellerin., "*Quelles avancées de la recherche sur le fractionnement du blé tendre ?*", **Industries Agricoles et Alimentaires**, 11/12 (2016) 16-19

Communications orales : congrès internationaux

Xavier Frank, Jean-Yves Delenne, Saeid Nezamabadi, Farhang Radjai, "*Numerical simulation of the fracture of heterogeneous materials by a peridynamic approach*", **MiDi Day, Workshop on Granular Materials**, Montpellier, France, September (2021)

Nicolas Blanc, Xavier Frank, Claire Mayer-Laigle, Farhang Radjai, Jean-Yves Delenne, "*Fracturation of particle embodying defects using Peridynamics simulation*", **Joint GeoMech-M2UN Workshop on Upscaling for Strategic Materials**, Montpellier, France, September 2-4 (2019)

Karsta Heinze, Xavier Frank, Valérie Lullien-Pellerin, Matthieu George, Farhang Radjaï, Jean-Yves Delenne, "*Breaking the grains : Fragmentation of a cemented granular bio-material*", **Joint GeoMech-M2UN Workshop on Upscaling for Strategic Materials**, Montpellier, France, September 2-4 (2019)

Saeid Nezamabadi, Farhang Radjai, Xavier Frank, Jean-Yves Delenne, "*Modelling soft granular materials : Compaction behaviour*", **Joint GeoMech-M2UN Workshop on Upscaling for Strategic Materials**, Montpellier, France, September 2-4 (2019)

Xavier Frank, Jean-Yves Delenne, Saeid Nezamabadi, Farhang Radjai, "*Strength and fracture of porous, granular and cellular materials by peridynamic simulations*", **8$^{\mathbf{th}}$ International Conference on Discrete Element Methods**, Enschede, Netherlands, July 21-26 (2019)

Nicolas Blanc, Xavier Frank, Claire Mayer-Laigle, Farhang Radjai, Jean-Yves Delenne, "*Peridynamics simulation of particle crushing*", **8th International Conference on Discrete Element Methods**, Enschede, Netherlands, July 21-26 (2019)

Saeid Nezamabadi, Thanh Hai Nguyen, Xavier Frank, Jean-Yves Delenne, Farhang Radjai, "*Modelling and rheology of soft granular materials*", **8th International Conference on Discrete Element Methods**, Enschede, Netherlands, July 21-26 (2019)

Nicolas Blanc, Jean-Yves Delenne, Xavier Rouau, Farhang Radjai, Xavier Frank, Claire Mayer-Laigle, "*How the device and the process parameters influence milling efficiency and agglomeration ?*", **Workshop on Powders and Granular Materials, Challenges and Future Trends**, Montpellier, France, June (2019)

Xavier Frank, Jean-Yves Delenne, Saeid Nezamabadi, Farhang Radjai, "*Strength and fracture of heterogeneous materials by peridynamic simulations*", **Workshop on Powders and Granular Materials, Challenges and Future Trends**, Montpellier, France, June (2019)

Nicolas Blanc, Xavier Frank, Claire Mayer-Laigle, Farhang Radjaï and Jean-Yves Delenne, "*Peridynamics simulation of the comminution of particles containing microcraks*", **8th International Conference on Micromechanics on Granular Media**, Montpellier, France, July 3-7 (2017)

Saeid Nezamabadi, Thanh Hai Nguyen, Jean-Yves Delenne, Julien Averseng, Xavier Frank, and Farhang Radjai, "*MPM with frictional contact for application to soft particulate materials*", **1st International Conference on the Material Point Method**, Delft, Netherlands , January 10-13 (2017)

Nicolas Blanc, Xavier Frank, Jean-Yves Delenne, Claire Mayer-Laigle and Farhang Radjaï, "*Peridynamic study of particle fracture under impact loading*", **IVth International Conference on Particle-Based Methods. Fundamentals and Applications**, Barcelona, Spain, September 28-30 (2015)

Karim Mazeau, Liang Li, Patrick Perré and Xavier Frank, "*The interface in biomimetic xylan/cellulose nanocomposites probed by multiscale modelling*", **IAWPS, International Symposium on Wood Science and Technology**, Tokyo, Japan, March 15-17 (2015)

Xavier Frank and Jean-Yves Delenne, "*Failure of materials embedding inclusions : a numerical study using a peridynamic approach*", **Modeling Granular Media Across Scales**, Montpellier, France, July 9-11 (2014)

Karim Mazeau, Patrick Perré, Liang Li and Xavier Frank, "*Multiscale modelling of the interfacial structure in xylan/cellulose nanocomposites*", **245th ACS National Meeting & Exposition**, Denver, Colorado, USA, March 22-26 (2013)

Patrick Perré, Giana Almeida and Xavier Frank, "*Spreading and penetration of a*

water droplet on native and heat treated wood", **18th International Drying Symposium**, Xiamen, China, November 11-15 (2012)

Xavier Frank, Jean-Claude Charpentier, Noël Midoux and Huai-Zhi Li, "*A Multiscale Approach for Modeling Bubbles Rising in Non-Newtonian Fluids*", **International Conference on Multiscale Approaches for Process Innovation**, Lyon, France, January 25-27 (2012)

Xavier Frank and Patrick Perré, "*Lattice Boltzmann approach of wood surface wetting at the pore level*", **3rd International Conference on Porous Media**, Bordeaux, France, March 29-31 (2011)

Xavier Frank, Nicolas Dietrich, Jing Wu, Renaud Barraud and Huai-Zhi Li, "*Bubble nucleation and growth in fluids*", **8th International Conference on Gas-Liquid and Gas-Liquid-Solid Reactor Engineering**, New Delhi, India, December 16-19 (2007)

Mohammed Kemiha, Xavier Frank, Souhila Poncin and Huai-Zhi Li, "*Origin of the negative wake behind a bubble rising in non Newtonian fluids*", **7th International Conference on Gas-Liquid and Gas-Liquid-Solid Reactor Engineering**, Strasbourg, France, August 21-24 (2005)

Mohammed Kemiha, Xavier Frank, Souhila Poncin and Huai-Zhi Li, "*Flow fields around rigid spheres in a non-Newtonian fluid : PIV measurements and simulations*", **7th World Congress of Chemical Engineering**, Glasgow, Scotland, July 10-14 (2005)

Xavier Frank, Huai-Zhi Li, Denis Fünfschilling, Florence Burdin and Youguang Ma, "*Bubble Motion in Non-Newtonian Fluids and Suspensions*", **6th International Conference on Gas-Liquid and Gas-Liquid-Solid Reactor Engineering**, Vancouver, BC, Canada, August 17-20 (2003)

Posters : congrès internationaux

Karsta Heinze, Xavier Frank, Valérie Lullien-Pellerin, Matthieu George, Farhang Radjaï and Jean-Yves Delenne, "*Numerical modeling of the tensile strength of a biological granular aggregate : Effect of the particle size distribution*", **8th International Conference on Micromechanics on Granular Media**, Montpellier, France, July 3-7 (2017)

Xavier Frank, Jean-Yves Delenne and Farhang Radjaï, "*Numerical study of the failure of materials embedding soft to hard particles*", **8th International Conference on Micromechanics on Granular Media**, Montpellier, France, July 3-7 (2017)

Saeid Nezamabadi, Thanh Hai Nguyen, Jean-Yves Delenne, Julien Averseng, Xavier Frank, and Farhang Radjai, "*Textural analysis of soft granular materials*", **Gordon Research Conference session Granular Matter**, Easton, MA, United States, July (2016)

Nicolas Blanc, Xavier Frank, Claire Mayer, Farhang Radjai and Jean-Yves Delenne, "*Peridynamic study of the fracture of particles embedding microcracks*", **EMI International Conference**, Metz, France, October 25-27 (2016)

Patrick Perré, Giana Almeida, Philippe Jacquin and Xavier Frank, "*Spreading and penetration of a water droplet on native and heat treated wood*", **12$^{\text{th}}$ International IUFRO Wood Drying Conference**, Belém, Para, Brazil, July 30-August 03 (2012)

Patrick Perré, Xavier Frank and Giana Almeida, "*MPM modeling of the wood/water relations at the cellular level : shrinkage and collapse*", **3$^{\text{rd}}$ International Conference on Porous Media**, Bordeaux, France, March 29-31 (2011)

Communications orales : congrès nationaux

Saeid Nezamabadi, Farhang Radjai, Xavier Frank, Jean-Yves Delenne et Julien Averseng, "*Modélisation parallèle des milieux granulaires à particules déformables*", **14$^{\text{ème}}$ Colloque National en Calcul des Structures**, Giens, Mai (2019)

Xavier Frank, Jean-Yves Delenne, et Farhang Radjaï, "*Approche peridynamique de la fissuration quasi-statique d'un matériau comportant des inclusions*", **22$^{\text{ème}}$ Congrès Français de Mécanique**, Lyon, 24-28 Août (2015)

Nicolas Blanc, Xavier Frank, Jean-Yves Delenne, Claire Mayer-Laigle et Farhang Radjaï, "*Etude peridynamique de la rupture de particules sous impact*", **22$^{\text{ème}}$ Congrès Français de Mécanique**, Lyon, 24-28 Août (2015)

Xavier Frank et Jean-Yves Delenne, "*Simulation numérique de la fissuration d'un matériau granulaire cimenté par une approche peridynamique*", **21$^{\text{ème}}$ Congrès Français de Mécanique**, Bordeaux, 26-30 Août (2013)

Xavier Frank, Giana Almeida et Patrick Perré, "*Imbibition capillaire d'un échantillon de bois : reconstitution 3D de l'anatomie et simulation Lattice Boltzmann*", **19$^{\text{ème}}$ Congrès Français de Mécanique**, Marseille, 24-28 Août (2009)

Patrick Perré et Xavier Frank, "*Modélisation par MPM du comportement de l'agencement cellulaire du bois en grandes déformations*", **19$^{\text{ème}}$ Congrès Français de Mécanique**, Marseille, 24-28 Août (2009)

Xavier Frank, Mohammed Kemiha et Huai-Zhi Li, "*Interaction entre deux sphères sédimentant en fluide non Newtonien : PIV et simulation Lattice Boltzmann*", **18$^{\text{ème}}$ Congrès Français de Mécanique**, Grenoble, 27-31 Août (2007)

Nicolas Dietrich, C Zhao, Xavier Frank, Souhila Poncin, Noël Midoux et Huai-Zhi Li, "*Etude de l'effet Weissenberg microscopique par micro-PIV*", **18$^{\text{ème}}$ Congrès Français de Mécanique**, Grenoble, 27-31 Août (2007)

Xavier Frank, Anne-Laure Bonnier, Renaud Barraud, Youguang Ma et Huai-Zhi Li, "*Nucléation homogène et croissance des bulles en fluide non Newtonien*", **9$^{\text{ème}}$**

Congrès de la Société Française de Génie des Procédés, Saint-Nazaire, 9-11 Septembre (2003)

Xavier Frank et Huai-Zhi Li, "*Coalescence des bulles : dynamique chaotique et comportement cognitif*", **8ème Congrès de la Société Française de Génie des Procédés**, Nancy, 17-19 Octobre (2001)

Xavier Frank et Huai-Zhi Li, "*Cognition collective des bulles dans les fluides rhéologiquement complexes*", **VIIIèmes Journées Théorie du chaos et Science de la cognition**, Aix-en-Provence, 29-30 Juin (2000)

Posters : congrès nationaux

Saied Nezamabadi, T.-H. Nguyen, Xavier Frank, Jean-Yves Delenne, Farhang Radjaï, "*Compaction rheology of soft granular materials*", **54ème Congrès du Groupe Français de Rhéologie**, Montpellier, France, 23-25 Octobre (2019)

Xavier Frank, Sofiane Guessasma, Guy Della Valle, Saied Nezamabadi, Vincent Richefeu, Farhang Radjaï, Jean-Yves Delenne, "*Modélisation péridynamique du comportement à la rupture de mousses solides*", **54ème Congrès du Groupe Français de Rhéologie**, Montpellier, France, 23-25 Octobre (2019)

Séminaires

Xavier Frank, Farhang Radjai, Saeid Nezamabadi, and Jean-Yves Delenne, "*Tensile strength of granular aggregates : Stress chains across particle phase versus stress concentration by pores*", **PMMD team Seminars**(online), June (2020)

Xavier Frank, Jean-Yves Delenne, Komlanvi Lampoh, Saeid Nezamabadi, Farhang Radjai, Sofiane Guessasma, Guy Della Valle, Magdalena Kristiawan, Anne-Laure Reguerre, Imen Jebalia, Vincent Richefeu, "*Modélisation discrète de la déconstruction d'aliments - projet AIC MiDiDAM*", **In Métaséminaire CEPIA**, Paris, France, Mars (2018)

Xavier Frank, "*Modélisation physique discrète, des systèmes moléculaires aux matériaux granulaires*", **Journées InCom**, Maison des industries agricoles et alimentaires, Cité Internationale Universitaire, Paris, France, Novembre (2017)

Jean-Yves Delenne, Xavier Frank, Saeid Nezamabadi, Farhang Radjaï, Vincent Richefeu, "*Dynamic simulations of granular materials*", **Séminaire MIT/IATE**, Montpellier, France, Septembre (2015)

Xavier Frank, Jean-Yves Delenne, Abdellatif Barakat, Abdelkrim Sadoudi, Frederic Mabille, and Cecile Barron, "*Modélisation et simulation numérique de la fragmentation des matériaux lignocellulosiques*", **Séminaire Bioraffinerie des Lignocelluloses (BILI)**, AgroParisTech, Paris, France, Mai (2014)

Xavier Frank, "*Simulation numérique de la fissuration de matériaux hétérogènes par approche péridynamique*", **Séminaire de IATE**, Montpellier, France, Avril (2013)

Xavier Frank, "*Modélisation : contours, méthodologies, usages, enjeux*", **Séminaire de IATE**, Montpellier, France, Février (2012)

Xavier Frank, "*Ecoulements polyphasiques complexes : expérimentation, simulation Lattice Boltzmann et approche multiéchelle appliquées à des exemples issus du génie chimique*", **Séminaire du LEPTIAB**, Université de La Rochelle, France, 8 Novembre (2007)

Xavier Frank, "*Bulles et sphères en fluide non Newtonien : approche Lattice Boltzmann et validation expérimentale*", **Séminaire du Laboratoire de Modélisation en Mécanique**, Université Pierre et Marie Curie, Paris, France, 2 Avril (2007)

Xavier Frank, "*Sédimentation d'une sphère dans un fluide non Netonien : approche Lattice Boltzmann et validation expérimentale*", **Séminaire du Pôle Mécanique Brestois**, Université de Bretagne Occientale, Brest, France, 18 Janvier (2007)

Principaux articles

PERGAMON

Chemical Engineering Science 56 (2001) 6419–6425

Chemical Engineering Science

www.elsevier.com/locate/ces

Towards the understanding of bubble interactions and coalescence in non-Newtonian fluids: a cognitive approach

Huai Z. Li*, Xavier Frank, Denis Funfschilling, Youssef Mouline

Centre de Génie Chimique des Milieux Complexes, CNRS-ENSIC-INPL, 1 rue Grandville, BP 451, 54001 Nancy, Cedex, France

Abstract

The present work provides new insights into the behavior of air bubbles in non-Newtonian fluids. The interactions and coalescence between bubbles rising in non-Newtonian fluids were simultaneously investigated by means of birefringence measurements and particle image velocimetry for a chain of bubbles formed from a submerged orifice. Two aspects are identified for the first time as central to interactions and coalescence: (i) the stress creation by the passage of bubbles, and (ii) their relaxation due to the fluid's memory. This competition displays complex nonlinear dynamics, from periodic phenomena to deterministic chaos. From these fundamental mechanisms, a cognitive model based on behavioral rules has been developed to describe collective behaviors of a group of bubbles. By simulating bubbles as adaptive agents with their fluid via residual stresses, model predictions for consecutive coalescence between a great number of bubbles compare very satisfactorily with the experimental investigation.

Keywords: Bubbles; Interactions; Coalescence; Non-Newtonian fluids; Cognitive approach; Adaptive agent

1. Introduction

The understanding of bubble behavior in non-Newtonian fluids is useful in such diverse fields as bubble columns, fermentation, air-lift reactors, polymer devolatilization, composites processing, boiling, plastic foam processing, and bubble absorption. There is also a strong motivation from a theoretical standpoint towards satisfactorily describing the influence of the fluid's rheology on the bubble flow pattern.

Compared to bubbles in Newtonian fluids (e.g. Clift, Grace, & Weber, 1978; Sadhal, Ayyaswamy, & Chung, 1997), much less is known about the bubble behavior in non-Newtonian fluids. Due to the inherent complex nature of bubble phenomena and the influence of the fluid's rheology, a complete theoretical and analytical analysis is still impossible at present. In particular, one often encounters ensembles of bubbles under industrial conditions rather than individual ones (Chhabra, 1992).

An adequate understanding of the bubbles formed from a single submerged orifice is then a prerequisite for studying the interactions and coalescence between bubbles stemming from many orifices. The first major work was reported by Astarita and Apuzzo (1965) on the motion of single bubbles. The investigation in this field has been followed by other authors: e.g. Calderbank, Johnson, and Loudon (1970), Carreau, Devic, and Kapellas (1974), Zana and Leal (1978), and Rodrigue, De Kee, and Chan Man Fong (1996). The results available in the literature provide essentially experimental information on the rise velocity of a single bubble. To date, there is very little published information about the interactions in non-Newtonian fluids. Only two experimental investigations on the coalescence, in such media have so far been reported in the literature: measurements of coalescence time (Acharya & Ulbrecht, 1978) and visual observations by injecting two or three bubbles (De Kee, Chhabra, & Dajan, 1990). In this paper we investigate a comprehensive understanding of the in-line bubble interactions and coalescence in non-Newtonian fluids, in particular with the help of a cognitive approach.

* Corresponding author. Tel.: +33-383-175-109; fax: +33-383-175-319.

E-mail address: li@ensic.inpl-nancy.fr (H. Z. Li).

0009-2509/01/$ - see front matter
PII: S0009-2509(01)00269-X

2. Experimental

The experiments were conducted in a Plexiglas cylindrical tank (0.24 m diameter and 1.60 m height) enveloped by a square duct (0.33 m). The square outer duct eliminated optical distortions and acted as a heat exchanger to control the liquid temperature inside the cylindrical tank. Air bubble generation was through an orifice of varying diameters ($1–5 \times 10^{-3}$ m), submerged in the liquid in the center of the bottom section of the tank. A reservoir was used to avoid any fluctuations due to bubble formation and detachment. Besides the continuous injection of a constant gas flowrate, an electronic valve of rapid response controlled by a personal computer allowed bubbles of known volume to be injected with a known injection period T—interval between successive bubbles (Li, Mouline, Choplin, & Midoux, 1997b, c). The bubble rise velocity and the frequency of passage were measured by two optical probes of laser and photodiodes placed at different heights. All experiments were carried out at a constant temperature (293 K).

The three non-Newtonian fluids used in this work were 0.25, 0.50 and 0.75 wt% polyacrylamide (PAAm, AN913SH, SNF Floerger) in demineralized water. A Rheometrics Fluid Spectrometer RFS II (Rheometric Scientific) was employed to measure the rheological properties. All three fluids behaved as shear-thinning and viscoelastic fluids. In the range of the shear rates corresponding to the motion of bubbles, the viscosity could be fitted by the power law model

$$\eta = 1.22\dot{\gamma}^{-0.69}, \quad 0.25\% \text{ PAAm},$$

$$\eta = 2.67\dot{\gamma}^{-0.70}, \quad 0.50\% \text{ PAAm},$$

$$\eta = 6.04\dot{\gamma}^{-0.73}, \quad 0.75\% \text{ PAAm}. \qquad (1)$$

Their elasticity was characterized by the first normal stress difference, and by the slow relaxation of the stresses after shear (Li et al., 1998). The elasticity increased with the PAAm concentration in these fluids.

3. Results and discussion

3.1. In-line interactions and coalescence between bubbles

The evidence for in-line interactions between bubbles in non-Newtonian fluids has been highlighted previously (Li, Mouline, Choplin, & Midoux, 1997a–c; Li et al., 1998; Li, 1999), where it was found that the rise velocity decreases with the increase of the injection period for a given bubble volume. In the present study, the interaction between bubbles was much stronger than in the previously used Carboxymethylcellulose and Separan polyacrylamide fluids. An injection period of order of 40, 60, and 90 s was necessary to prevent the interactions between bubbles, respectively, for the 0.25%, 0.50%, and 0.75% PAAm fluids. When the injection period became short enough (< 0.5 s), coalescence occurred.

In PAAm fluids, bubbles were perfectly axisymmetric, and displayed neither shape nor trajectory oscillations within the range of bubble volumes studied. Hence, the measurements of the flow field in a plan crossing the axis of symmetry of the bubble gave a complete knowledge of the flow field around the bubble. We carried out the flow field measurements in these fluids by means of a particle image velocimetry (PIV, Dantec Measurement Technology) system. The fluid was inseminated with fluorescent polymer beads of 75 μm as seeding particles. An orange filter placed in front of the camera eliminated the reflections of the lasers on the bubbles and let only the fluorescent light of the particles pass. The laser sheets of the two laser sets crossed the vertical symmetry axis of the bubble. The camera, placed perpendicular to the laser sheet, took two successive images, each at the maximum intensity of the laser impulse. These images were divided into a few thousands small interrogation areas of 16×16 pixels. A cross correlation was then performed on the two corresponding interrogation areas. This cross correlation gave the instantaneous flow field. In non-Newtonian, the flow fields around an individual bubble have very peculiar features: the flow in the front of the bubble is very similar to that the Newtonian case; in the central wake, the movement of the fluid is surprisingly downward; finally, a hollow cone of upward flow surrounds this negative wake. This conical upward flow zone begins on the sides of the bubble, and is extended backward (Funfschilling & Li, 2001). However, the negative wake does not prevent interactions and coalescence taking place between bubbles rising in a chain. The flow field around two coalescing bubbles is shown in Fig. 1. These results suggest clearly that a new mechanism should be discovered for interactions and coalescence in non-Newtonian fluids.

Based on the polarization modulation method, flow birefringence measurements were also performed for the fluids. This method does not allow a numerical measure of stress distribution due to the small magnitude of stresses induced by the passage of bubbles, but can provide useful qualitative information about the transient evolution of stress relaxation after the passage of a bubble. The non-Newtonian fluids used did not exhibit noticeable birefringent behavior; therefore another birefringent product (0.2% hydroxypropylcellulose) was used to improve visualization quality. The birefringence device began with a cold polarized light source through a polarizer. As the light passed through the fluid whose molecular chains were oriented under stresses, the angle of polarization of the light was changed. Having passed through the fluid, the light passed through another polarizer oriented at 90° with respect to the first. The resulting images were visualized by the video camera

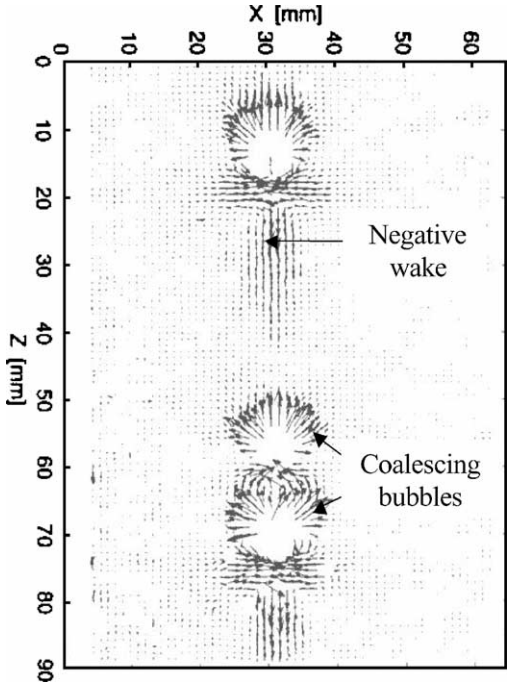

Fig. 1. Flow field around a train of bubbles rising in 0.75% PAAm by means of PIV (gas flowrate $Q = 0.1 \times 10^{-6}$ m^3/s).

Fig. 2. Birefringence visualization: bubble volume $V_B = 0.56 \times 10^{-6}$ m^3/s; injection period $T = 0.2$ s; 0.25% PAAm.

(Fig. 2). Typically, stresses can be visualized by white zones. Black zones correspond to the extinction of the polarized light due to the absence of stress. Despite of the negative wake, the trailing bubble can enter in the large field of dominant residual stresses behind the leading one. The memory effect of these residual stresses holds the shear-thinning process during a certain time so that the local viscosity decreases and provokes either interactions, through pure acceleration of rise velocity, or coalescence at shorter injection periods between bubbles. After coalescence, the bigger bubble will shear strongly the fluid, induce a more extended field of residual stresses and facilitate the rise of trailing bubbles. In brief, there is a dynamical competition between the creation and relaxation of stresses due to the consecutive passage of bubbles, which was highlighted by our previous rheological simulation (Li et al., 1997a) which shows a gradual accumulation of residual stresses towards a stationary value with the increase of the passage number of bubbles.

Above a certain threshold ($T < 0.5$ s in the case of a constant flowrate for example), the interactions are no longer linear as a result of coalescence, and the regular bubble chain is broken up. The regularity of the bubble formation at the orifice and the dynamical competition between the creation and relaxation of stresses lead naturally to the theory of chaos. From time series data (bubble passage) recorded at different heights in the bubble column, the calculation of several parameters: the largest Lyapunov exponent, the correlation dimension, the power spectrum and the phase portraits, indicates that the coalescence between bubbles is chaotic. These results are quite similar to that obtained in other fluids (Li et al., 1997b, 1998).

Experimentally, the chaos appearance can also be described by the period-doubling sequences. It is worth noting that the variation of the correlation dimension with the embedding dimension shows that the chaos is deterministic with a limited number of degrees of freedom. This is also confirmed by the evolution of the bubble number at different heights in the column. As shown in Fig. 3, the bubble number normalized by the total number of bubbles generated at the orifice for a fixed duration (typically about 2000 bubbles) levels off a plateau before falling due to coalescence of consecutive bubbles. The plateau corresponding to the constant bubble number in the inertial rise stage increases inversely with the fluid viscosity. The decrease of the bubble number in the higher column section is bounded by an asymptotic value due to the limited capacity of bubble generation at the orifice. This result shows explicitly that the complexity of the in-line bubble coalescence in non-Newtonian fluids cannot degenerate into an arbitrary nature. Intuitively, the collective behaviors of bubbles in such media obey underlying fundamental laws.

3.2. Cognitive approach: bubbles as adaptive agents

Recently, researchers (Gell-Mann, 1994; Holland 1992) have developed new methods to describe the complex adaptive systems such as an anthill, a central nervous system or ecosystems. Even though these complex systems differ in detail, the question of coherence under change is the central enigma for each. General principles usually rule the behavior of these complex

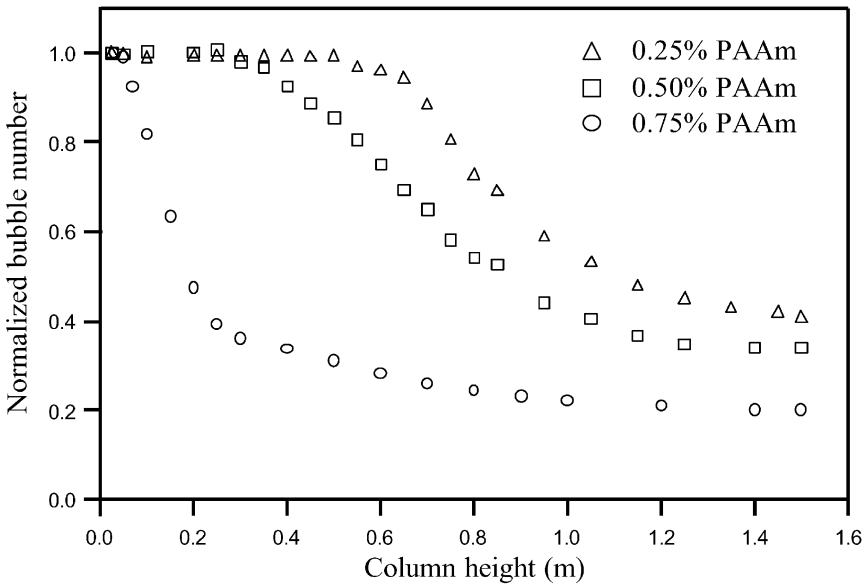

Fig. 3. Variation of the normalized bubble number with the column height in three fluids (gas flowrate $Q = 0.2 \times 10^{-6}$ m^3/s).

adaptive systems (CAS), principles that point to ways of solving the attendant problems. The task of formulating theory for these systems is more than difficult as the collective behavior of such a system is more than a simple sum of the behaviors of its parts. Nonlinearities governing these systems imply that our most useful tools for generalizing observations into theory—trend analysis, determination of equilibrium, sample means, and so on—are not appropriate. The main quest is to extract these general principles and to shape them into building blocks for a new scientific approach.

If we are to understand the interactions of large numbers of agents, we must first be able to describe the capabilities of individual agents. It is quite logic to suppose that an agent's behavior is determined by a collection of rules. Stimulus–response rules are typical and simple: IF stimulus S occurs THEN gives response R. In an anthill, the stimuli could be pheromones deposed by other ants in search of foods, the response could be the movement in a given direction according to the magnitude of pheromones. The collective behavior of the whole anthill would privilege the shortest way to go to the food source with progressive increase on the pheromones' intensity as each ant passing through this way would drop new pheromones. Therefore, we can establish qualitatively an ethnological analogy between bubbles and ants. They interact both between them through the interactions with their environment: pheromones for ants and residual stresses in fluid for bubbles.

The clusters of rules can generate sufficiently complex behaviors that can be computationally described. Of course, the definition of rules is difficult in the real agents as an anthill or industrial firms in practice. In the case of bubbles, these rules are essentially based on the fundamental physical mechanisms as described above. Our immediate objective is to find a simple syntax for IF/THEN rules that depend critically on the way an agent (a bubble) interacts with its environment (fluid) and other agents (bubbles).

Starting from the knowledge of the interactions and coalescence between bubbles, we adopt the following strategy as the cognitive approach that specifies the bubble's capacities at a fixed point in fluid in time. The three basic elements of this approach are a set of detectors, a set of IF/THEN rules, and a set of effectors. The detectors represent the bubble's capacities for extracting information from its environment (residual stresses in fluid, presence of other bubbles); the IF/THEN rules describes its capacities for processing that information (accelerating or not the rise velocity, coalescence or not); and the effectors are its ability to act on the environment (leaving its own residual stresses according to its size).

The total fluid height is divided into 20,000 cells, in which the stresses are continuously computed according to the passage of consecutive bubbles. Each cell represents a height of 75 μm and is supposed to display homogenous stresses whose evolution is estimated by the following dynamical competition between the creation (passage of bubbles) and relaxation of stresses (memory effects) of the first order:

$$\frac{\mathrm{d}\tau_m}{\mathrm{d}t} = -\alpha\tau_m + \beta\dot{\gamma}_B, \tag{2}$$

α and β are determined by the rheological simulation under different conditions of fluid and bubble volume (Li et al., 1997a, 1998).

As a first approximation, the bubble is considered to be spherical with an equivalent diameter d_{eq}. Including

added-mass (Milne-Thomson, 1960), the motion equation of a bubble is described by a balance of different forces: inertial, buoyancy and drag forces:

$$\left(\rho_G + \frac{11}{16}\rho_L\right) V_B \frac{\mathrm{d}U}{\mathrm{d}t} \approx \frac{11}{16}\rho_L V_B \frac{\mathrm{d}U}{\mathrm{d}t} = F_b - F_t, \quad (3)$$

where the buoyancy force

$$F_b = (\rho_L - \rho_G) V_B g \quad (4)$$

and the drag force

$$F_t = \tfrac{1}{2} A C_D \rho_L U^2 \quad \text{with } A = \frac{\pi d_{\mathrm{eq}}^2}{4}. \quad (5)$$

After the passage of a preceding bubble, the memory effect of the fluid holds the shear-thinning process for a certain time so that the local viscosity decreases and induces the acceleration of the rise velocity of the trailing bubble. The increase of the rise velocity is estimated using the drag coefficient expression (Funfschilling, 1999)

$$C_D = \frac{16}{Re_e}, \quad (6)$$

where the local effective Reynolds number Re_e is based on the local effective fluid viscosity that takes into account the residual stresses

$$Re_e = \frac{\rho_L U d_{\mathrm{eq}}}{\eta_e}. \quad (7)$$

The estimation of the local effective viscosity is made through a virtually additional shear rate corresponding to the residual stresses

$$\dot{\gamma}_m = (\tau_m / K)^{1/n}. \quad (8)$$

The passage of a bubble of rising velocity U induces a shear rate to the fluid that may have symmetrically distributed forms like hyperbolic cosine function for a spherical geometry (Li et al., 1997a). In the present study, we use simply, as a first approximation, the maximum shear rate

$$\dot{\gamma}_B = U / d_{\mathrm{eq}}. \quad (9)$$

It is clear that the sum of these two shear rates leads to an effective viscosity in a cell,

$$\eta_e = K\dot{\gamma}^{n-1} = K(\dot{\gamma}_B + \dot{\gamma}_m)^{n-1}. \quad (10)$$

For a bubble rising initially at U, the main rules have then the form:

- IF (there are residual stresses in a cell τ_m) THEN (compute the new increased velocity U' via η_e).
- IF (two bubbles enter in contact) THEN (coalescence takes place to form a new bigger bubble $V_B = V_{B1} + V_{B2}$ and compute the new rise velocity U').

The evolutions of bubble rise velocity and size affect the stresses in fluid that are computed by Eqs. (2) and (10). The computation is performed on a PC, following 2000 bubbles consecutively generated at the orifice with a constant formation frequency and their ascension through the fluid of 1.50 m height represented by 20,000 cells. For each bubble, the rise velocity, the position, the value of stresses are computed cell by cell. As the spherical form is used, it is possible to determine the contact between a leading bubble and a following one which encounters less drag due to residual stresses. Any contact between two bubbles leads to coalescence as well as to a size increase which modifies then the above-mentioned parameters. The count of bubble number can be made for each height. We make use of a normalized bubble number which is defined as the ratio of the bubble number at a given height over the total number of bubbles initially generated at the orifice. Fig. 4 shows a comparison of the such normalized bubble number at different heights between the experiments and the cognitive modelling. The global tendency is well described by this approach even though the local curve details are not perfect. The small difference results essentially in the mean values used for α and β, determined by the rheological simulation, for bubbles of different size instead of more accurate values for each size. Fig. 5 shows the comparison of the power spectrum of bubble passage at, respectively, 0.03 cm and 1.50 m above the orifice in 0.75% PAAm solution. Near the orifice, the principal frequency followed by a set of harmonics demonstrates that the formation of bubbles is perfectly periodic. However, this regularity is progressively lost once coalescence occurs. The experimental power spectrum at 1.50 m is typically that of a chaotic phenomenon, since it exhibits broadened spectral lines that are mostly located at low frequencies with no dominant frequencies (Schuster, 1988). Both periodic and chaotic behaviors predicted by this cognitive modelling are particularly noteworthy as they emerge naturally without special fitting. In addition, a close analysis shows that the present cognitive modeling generates a period doubling bifurcation sequence, this route to chaos is experimentally confirmed. In the chaotic regime, we observe that both of the model and experiments display a power spectrum of exponentially decaying envelope until it levels off at a certain frequency, a signature of deterministic chaos. Obviously, this new approach captures important qualitative features of the collective behaviors of bubbles.

4. Conclusions

By means of the rheological simulation, birefringence visualization and PIV measurements, a coherent physical picture begins to emerge for the rise of a chain of bubbles in non-Newtonian fluids. The dynamical competition between the creation of stresses after the passage of bubbles and their relaxation forming temporarily

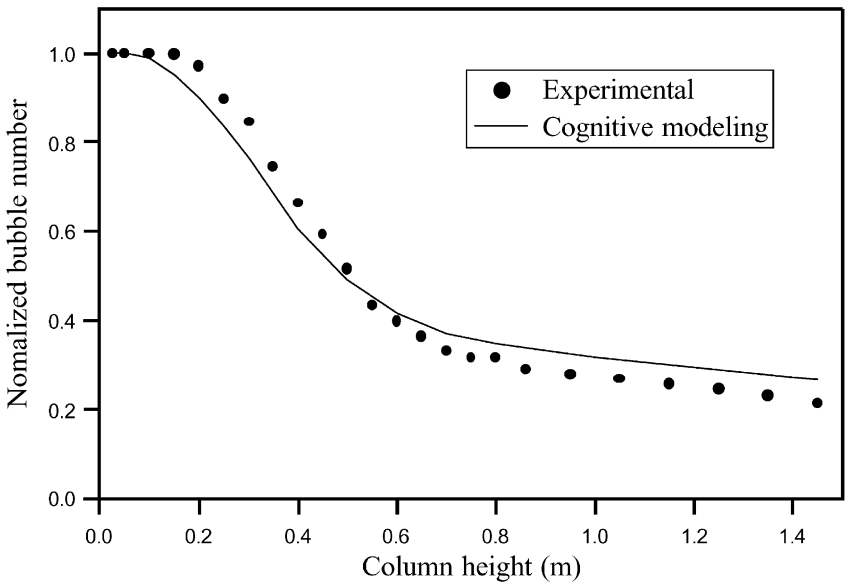

Fig. 4. Comparison of the variation of the normalized bubble number with the column height in 0.5% PAAm between the experiments and cognitive approach (gas flowrate $Q = 0.5 \times 10^{-6}$ m^3/s).

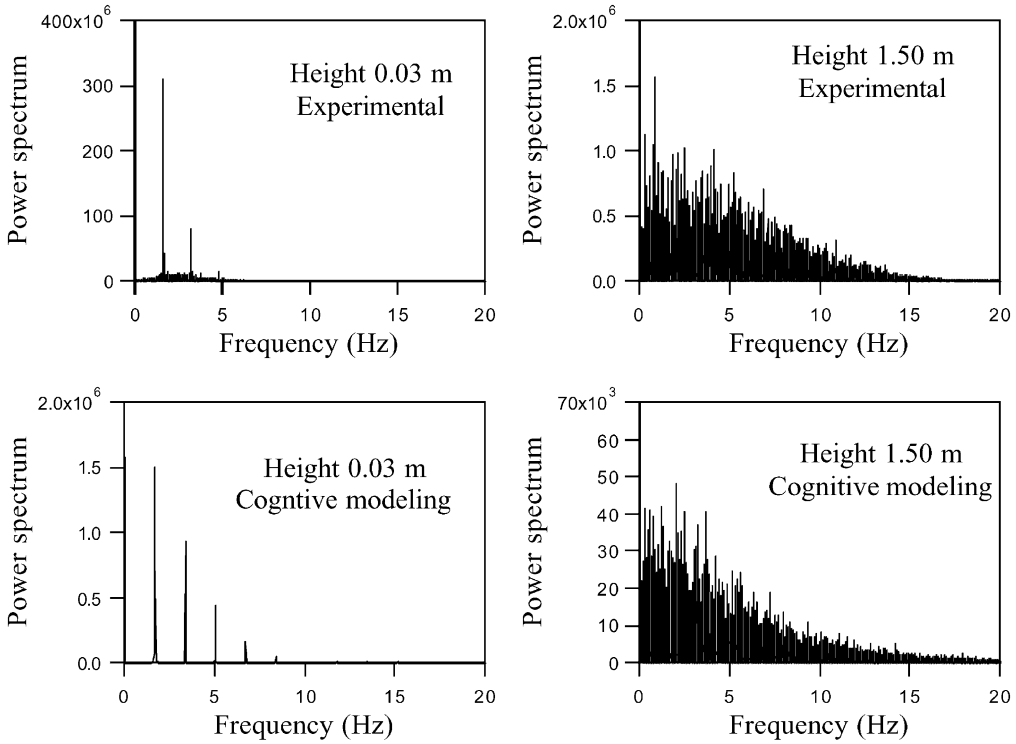

Fig. 5. Comparison of the power spectrum of the bubble passages at 0.03 and 1.50 m in 0.75% PAAM between the experiments and cognitive approach ($Q = 0.2 \times 10^{-6}$ m^3/s).

a corridor of reduced viscosity is clearly identified as the mechanism governing the in-line interactions and coalescence. We have developed a cognitive modeling based on fundamental physical understanding to model the collective behaviors of a bubble chain in non-Newtonian fluids. Without arbitrary assumption nor numerical fitting, this approach is composed of interacting bubbles between them and with their fluid environment via residual stresses described in terms of IF/THEN rules. These bubbles adapt by changing their behaviors to generate complex

temporal patterns such as interactions and coalescence. Good agreement of the simulation results with experimental data has been achieved, including the period doubling bifurcation sequence to chaotic coalescence. The cognitive approach allows also studying the interactions and coalescence not only in-line but also in parallel between bubbles formed from several orifices. This is an avenue we are currently exploring.

Notation

A	bubble surface, m^2
C_D	drag coefficient
d_{eq}	equivalent bubble diameter, m
F_b	buoyancy force, Pa
F_t	drag force, Pa
Re	Reynolds number
U	bubble rise velocity, m/s
V_B	bubble volume, m^3

Greek letters

$\dot{\gamma}_B$	shear rate due to the passage of a bubble, 1/s
$\dot{\gamma}_m$	shear rate due to residual stresses, 1/s
η	viscosity, Pa.s
ρ_L	fluid density, kg/m^3
ρ_G	gas density, kg/m^3
τ_m	mean stress in a cell, Pa

Subscript

e	effective

Acknowledgements

The authors gratefully acknowledge the financial support provided by the French Ministère de la Recherche et de la Technologie.

References

Acharya, A., & Ulbrecht, J. (1978). Note on the influence of viscoelasticity on the coalescence rate of bubbles and drops. *A.I.Ch.E. Journal*, *24*, 348–351.

Astarita, G., & Apuzzo, G. (1965). Motion of gas bubbles in non-Newtonian liquids. *A.I.Ch.E. Journal*, *11*, 815–820.

Calderbank, P. H., Johnson, D. S. L., & Loudon, J. (1970). Mechanics and mass transfer of single bubbles in free rise through some Newtonian and non-Newtonian liquids. *Chemical Engineering Science*, *25*, 235–256.

Carreau, P. J., Devic, M., & Kapellas, M. (1974). Dynamique des bulles en milieu viscoélastique. *Rheologica Acta*, *13*, 477–489.

Chhabra, R. P. (1992). *Bubbles, drops & particles in non-Newtonian fluids*. Boca Raton, FL: CRC Press.

Clift, R., Grace, J. R., & Weber, M. E. (1978). *Bubbles, drops and particles*. New York: Academic Press.

De Kee, D., Chhabra, R. P., & Dajan, A. (1990). Motion and coalescence of gas bubbles in non-Newtonian polymer solutions. *Journal of Non-Newtonian Fluid Mechanics*, *37*, 1–18.

Funfschilling, D. (1999). *Dynamique de bulles dans des fluides rhéologiquement complexes*. Ph.D. Thesis, Institut National Polytechnique de Lorraine.

Funfschilling, D., & Li, H. Z. (2001). Flow of non-Newtonian fluids around bubbles: PIV measurements and birefringence. *Chemical Engineering Science*, *56*, 1137–1141.

Gell-Mann, M. (1994). *The quark and the jaguar: Adventures in the simple and the complex*. New York: Wiley.

Holland, J. H. (1992). *Adaptation in natural and artificial systems: An introductory analysis with applications to biology, control and artificial intelligence* (2nd ed.). Cambridge, MA: MIT Press.

Li, H. Z., Mouline, Y., Choplin, L., & Midoux, N. (1997a). Rheological simulation of in-line bubble interactions. *A.I.Ch.E. Journal*, *43*, 265–267.

Li, H. Z., Mouline, Y., Choplin, L., & Midoux, N. (1997b). Chaotic bubble coalescence in non-Newtonian fluids. *International Journal of Multiphase Flow*, *23*, 713–723.

Li, H. Z., Mouline, Y., Choplin, L., & Midoux, N. (1997c). Interactions et coalescence des bulles dans les fluides rhèologiquement complexes. *Comptes Rendus des l' Academie des Science Paris*, *324*, 491–500.

Li, H. Z., Mouline, Y., Funfschilling, D., Marchal, P., Choplin, L., & Midoux, N. (1998). Evidence for in-line bubble interactions in non-Newtonian fluids. *Chemical Engineering Science*, *53*, 2219–2230.

Li, H. Z. (1999). Bubbles in non-Newtonian fluids: Formation, interactions and coalescence. *Chemical Engineering Science*, *54*, 2247–2254.

Milne-Thomson, L. M. (1960). *Theoretical hydrodynamics*. New York: Macmillan.

Rodrigue, D., De Kee, D., & Chan Man Fong, C. F. (1996). An experimental study of the effect of surfactants on the free rise velocity of gas bubbles. *Journal of Non-Newtonian Fluid Mechanics*, *66*, 213–232.

Sadhal, S. S., Ayyaswamy, P. S., & Chung, J. N. (1997). *Transport phenomena with drops and bubbles*. Berlin: Springer.

Schuster, H. G. (1988). *Deterministic chaos*. Weinheim: VCH.

Zana, E., & Leal, L. G. (1978). The dynamics and dissolution of gas bubbles in a viscoelastic fluid. *International Journal of Multiphase Flow*, *4*, 237–262.

Complex flow around a bubble rising in a non-Newtonian fluid

Xavier Frank and Huai Z. Li*
Laboratoire des Sciences du Génie Chimique (CNRS, UPR 6811), ENSIC-INPL, 1, rue Grandville, BP 451, 54001 Nancy Cedex, France
(Received 31 March 2004; revised manuscript received 18 January 2005; published 22 March 2005)

Our experimental investigation by both particle image velocimetry and birefringence modulation method shows very complex flow features around a bubble rising in a non-Newtonian fluid. We model this two-phase flow by coupling the free-energy-based lattice Boltzmann scheme and the fluid rheology in the framework of the sixth-order Maxwell model with shear thinning effects. A Newtonian low viscosity drop is used to simulate the rising bubble. Numerical results including noticeably negative wake behind the bubble, stress field, as well as the bubble's teardrop shape are obtained, and compare satisfactorily with our experiments.

DOI: 10.1103/PhysRevE.71.036309 PACS number(s): 47.50.+d, 47.55.Dz

I. INTRODUCTION

Bubble dynamics in non-Newtonian fluids is of great academic interest and industrial relevance in such diverse domains as polymer devolatilization, volcanic eruption, decompression sickness, fermentation, glass manufacture, wastewater treatment, and metallurgy. Since the pioneer works [1,2], considerable efforts have been directed at elucidating a number of particular phenomena not observed in Newtonian fluids such as the negative wake behind a bubble revealed by the laser Doppler anemometer (LDA) measurements at a point in fluid [3] and the memory effects in stress relaxation [4,5]. Recently, the lattice Boltzmann (LB) method as a mesoscopic approach to the simulation of fluid dynamics has been shown to give convincing results for Newtonian one-component flows [6]. It has also been applied to Newtonian two-phase flows with promising perspectives [7–9]. However, there are still few studies towards the inclusion of viscoelastic properties in the lattice Boltzmann method even for one-component flows [10–12]. Therefore it is our aim here to elaborate a suitable lattice Boltzmann model for a gas bubble rising in non-Newtonian fluids.

II. EXPERIMENT

Experiments were conducted in a Plexiglas cylindrical column of 0.3 m diameter surrounded by a square duct and filled with a solution of 0.50 wt % polyacrylamide (PAAm, average molecular weight of 6.96×10^6 g mol^{-1}) in water to a depth of 0.5 m. This fluid was shear thinning and viscoelastic. Air bubbles were individually generated by a computer-controlled electronic valve through a submerged orifice of 1 mm diameter at the bottom section. The bubble shape was always axisymmetric for considered volumes up to 1100 mm^3 [13,14]. Both the experimental and theoretical results presented below correspond to a steady flow where the bubble's terminal rise velocity was reached.

A particle image velocimetry (PIV) three-dimensional (3D) system with two YAG lasers and two cameras (Dantec Dynamics) was used to measure the fluid flow field around a bubble with the help of fluorescent seeding particles. Owing to the axisymmetry of the bubble, our measurements were performed for two-dimensional (2D) flow fields in a plane containing the axis of symmetry of the bubble. The flow field around a bubble in the PAAm solution has a very peculiar shape (Fig. 1), compared with the one in a viscous Newtonian fluid. In the central wake, the movement of the fluid is surprisingly downward to form a so called negative wake. A cone of upward flow surrounds this negative wake. This zone begins on the sides of the bubble and is developed backward.

Under shearing, a polymer solution may exhibit birefringent behavior as a consequence of stretching of polymeric chains. To provide evidence of the stresses around bubbles in our fluid, flow birefringence measurements were performed based on polarization modulation method. This method provides mainly useful information about the localization of stresses. In Fig. 2, typical examples of butterflylike spatial distribution of stresses around a bubble are shown in 0.50% PAAm solution for a bubble volume of respectively 80 and 190 mm^3. White zones illustrate the existence of axisymmetric stresses, in front of the bubble due to the fluid compression and especially behind the bubble at the border of the negative wake due to the relative movement of fluid, while black zones owing to the extinction of the polarized light characterize the absence of stress.

III. SIMULATION METHOD

To simulate a bubble rising in a non-Newtonian fluid, we chose the free-energy-based model developed initially in Oxford [15,16] for a binary fluid. Macroscopic quantities ρ, $\vec{u}$ and $\Delta\rho$ are deduced from functions f_i and g_i [15]. The bubble was assimilated as a drop where $\Delta\rho>0$. If external forces are imposed to the fluid, these forces result in an acceleration $\vec{a}$. Functions f_i obey the lattice Boltzmann equation (1) and (2), where the parameter t_f is a dimensionless time, linked to fluid's kinematic viscosity as $\nu_{LB}=t_f\delta t c_s^2$, t_g is another dimensionless time parameter that is chosen equal to 1 according to the literature [8,17],

*Electronic address: li@ensic.inpl-nancy.fr

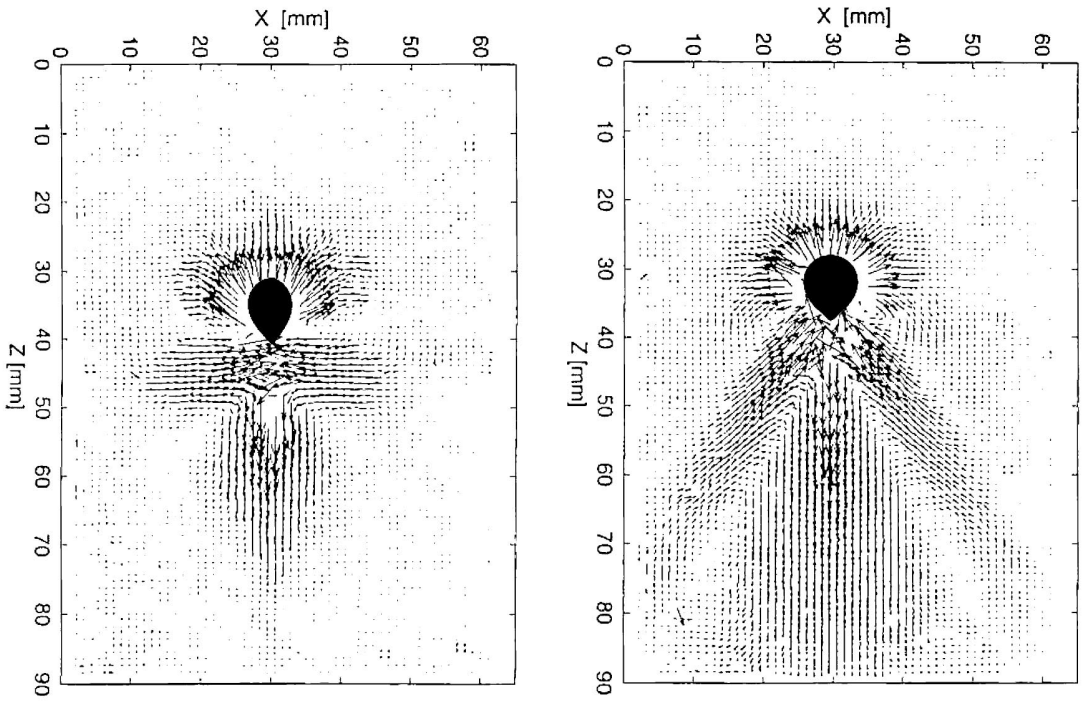

FIG. 1. Flow field obtained by PIV measurements around a bubble in 0.50% PAAm solution. The bubble volume $V_0=80$ mm^3 on the left; $V_0=190$ mm^3 on the right. The real bubble shape is artificially added.

$$f_i(\vec{r}+\delta t\vec{c}_i,t+\delta t)-f_i(\vec{r},t)=-\frac{[f_i(\vec{r},t)-f_i^{eq}(\vec{r},t)]}{t_f}+\frac{\vec{a}\cdot(\vec{c}_i-\vec{u})}{c_s^{\,2}}f_i^{eq}(\vec{r},t), \quad (1)$$

$$g_i(\vec{r}+\delta t\vec{c}_i,t+\delta t)-g_i(\vec{r},t)=-\frac{[g_i(\vec{r},t)-g_i^{eq}(\vec{r},t)]}{t_g}. \quad (2)$$

The functions f_i^{eq} and g_i^{eq} are equilibrium ones. Well-known thermodynamic quantities used to compute them, pressure tensor $P_{\alpha\beta}$ and chemical potential difference $\Delta\mu$, are derived from conserved quantities [16]. Interfacial tension is controlled by the parameter κ, involved in $P_{\alpha\beta}$ and $\Delta\mu$ definition; we chose $\kappa=0.05$, a classical value for air-aqueous systems.

IV. RHEOLOGICAL MODEL

A suitable rheological model is required to allow both the description of main viscoelasticity features. We used a modified sixth-order Maxwell fluid. The model finds its physical

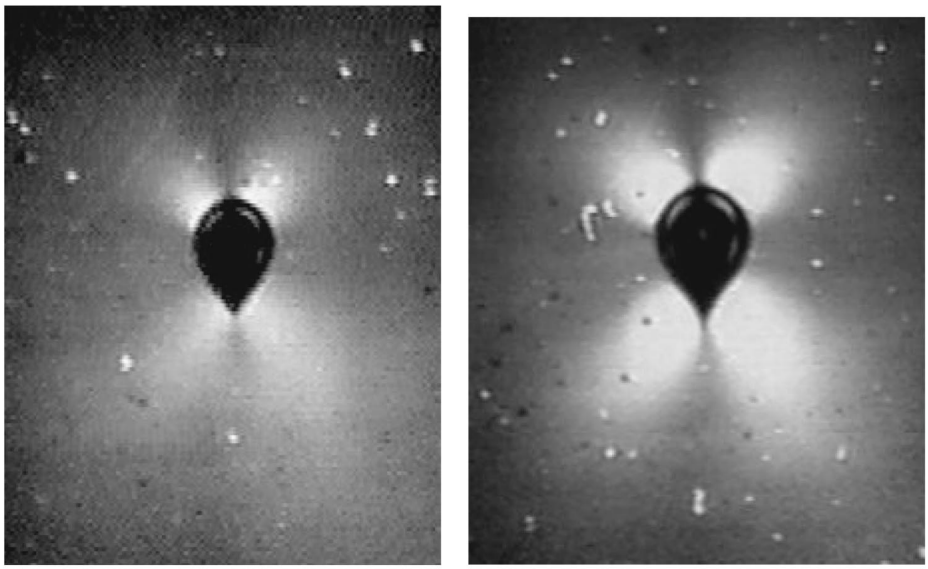

FIG. 2. Stress around a bubble rising in 0.50% PAAm solution visualized by birefringence measurement. On the left: bubble volume 80 mm^3; on the right: bubble volume 190 mm^3.

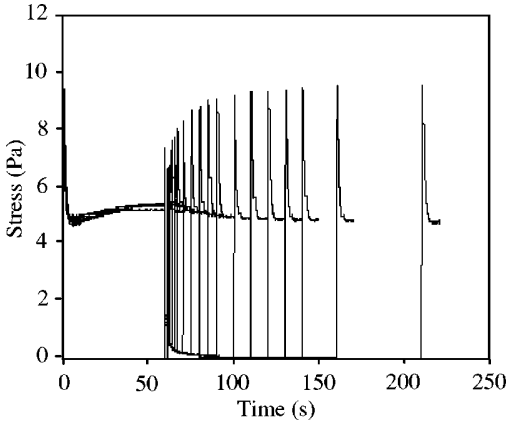

FIG. 3. Successive relaxation experiments, time delay, respectively: 1, 2, 3, 5, 7, 10, 15, 20, 25, 30, 40, 50, 60, 70, 90, 120, 150 s.

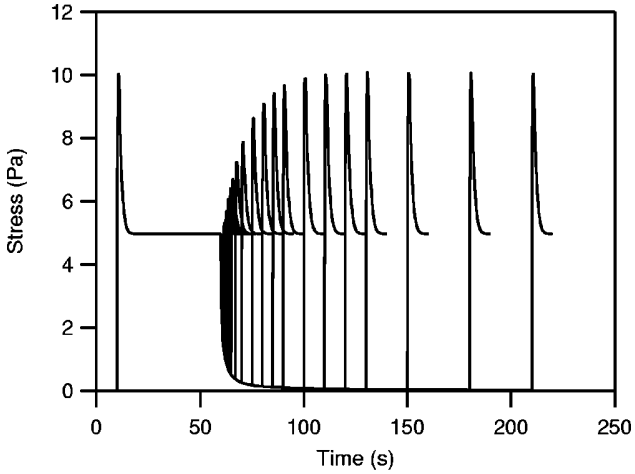

FIG. 4. Computation of the stress exhibited in same conditions as successive relaxation experiments.

justification by our previous studies concerning the linear superposition of accumulated stresses in fluid due to consecutive passages of a regular train of identical bubbles [4,5,14]. We then used a linear viscoelasticity model of Maxwell composed of six stress tensors whose sum leads to the total stress tensor (3)–(5), where (G_k, λ_k) are the coefficients of the sixth-order Maxwell fluid, obtained experimentally by rheological characterization,

$$\sum_{k=1}^{6} \tau_{i,j}^{k} = \tau_{i,j}, \tag{3}$$

$$\frac{\partial \tau_{i,j}^{k}}{\partial t} = G_k D_{i,j} - \frac{1}{\lambda_k} \tau_{i,j}^{k}, \tag{4}$$

$$D_{i,j} = \partial_i u_j + \partial_j u_i. \tag{5}$$

In order to satisfy the dynamical behavior experimentally observed in successive relaxation tests (Fig. 3), we introduce a physical quantity $\phi(\vec{r},t)$ that is a phenomenological parameter of fluid's viscosity evolution, obeying a relaxation equation (8) and (9),

$$\lambda_k' = \lambda_k \frac{\eta(\phi)}{\sum_k \lambda_k G_k}, \tag{6}$$

$$\frac{\eta - \eta_\infty}{\eta_0 - \eta_\infty} = [1 + (\lambda \phi)^2]^{(n-1)/2}. \tag{7}$$

The quantity $I_D^{(2)}$ is the second invariant of the tensor $D_{i,j}$. Relaxation times λ_k' depend on ϕ (6) and (7) so that asymptotical viscosity reaches the correct value described by an experimentally fitted Carreau model (7),

$$\frac{\partial \phi}{\partial t} = -\frac{\phi - \sqrt{|I_D^{(2)}|}}{t_r}, \tag{8}$$

$$t_r = \frac{t_{r0}}{1 + \dfrac{\phi}{\phi_0}}. \tag{9}$$

To validate this model, we performed consecutive relaxation experiments. The fluid was sheared during 50 s followed by a time interval during which the fluid was remained at rest, another steady shearing was then imposed to the fluid with the same shear rate. The fluid's stress was monitored (Fig. 3). It is worth noting that the parameters G_k and λ_k and as well as that in the Carreau model were determined by the standard rheological characterization. Consecutive relaxation experiments allowed us only to choose $t_{r0} = 12$ s and $\phi_0 = 0.50\ \mathrm{s}^{-1}$, in comparison to the computation of the fluids stress response by Eqs. (3)–(7). As shown in Figs. 3 and 4, this model describes correctly the relaxation behavior, a central phenomena governing the passage of a bubble in fluid.

V. NUMERICAL RESULTS

We integrated the above numerical scheme by means of a classical D2Q9 lattice 200 nodes large and 400 nodes high, and solid walls for borders of the simulation box, to discretize the phase space. In order to implement the Newtonian behavior inside the drop, we let parameters (G_k, λ_k) depend on $\Delta\rho$ in such a way that inside the bubble, $G_k = 0$ and the tensors $\tau_{i,j}^{k}$ are forced to relax quickly as relaxation times λ_k are 100 times shorter than in the bulk liquid. As $c_{i\alpha}$ is the α component of the ith direction velocity $\vec{c}_i$ of the lattice, the total stress tensor $\tau_{i,j}$ is used as follows:

$$\sum_i f_i^{eq} c_{i\alpha} c_{i\beta} = \rho u_\alpha u_\beta + P_{\alpha\beta} - \tau_{\alpha\beta}. \tag{10}$$

As shown in Fig. 5, the flow field was successfully simulated: a central negative wake does appear behind the bubble and the upward flow has a cone shape surrounding this downward wake. With respect to the birefringence method, we plotted computed shear stresses around a bubble (Fig. 6). A butterflylike shape, mainly due to the strong velocity gradients located at the interface between the upward flow and

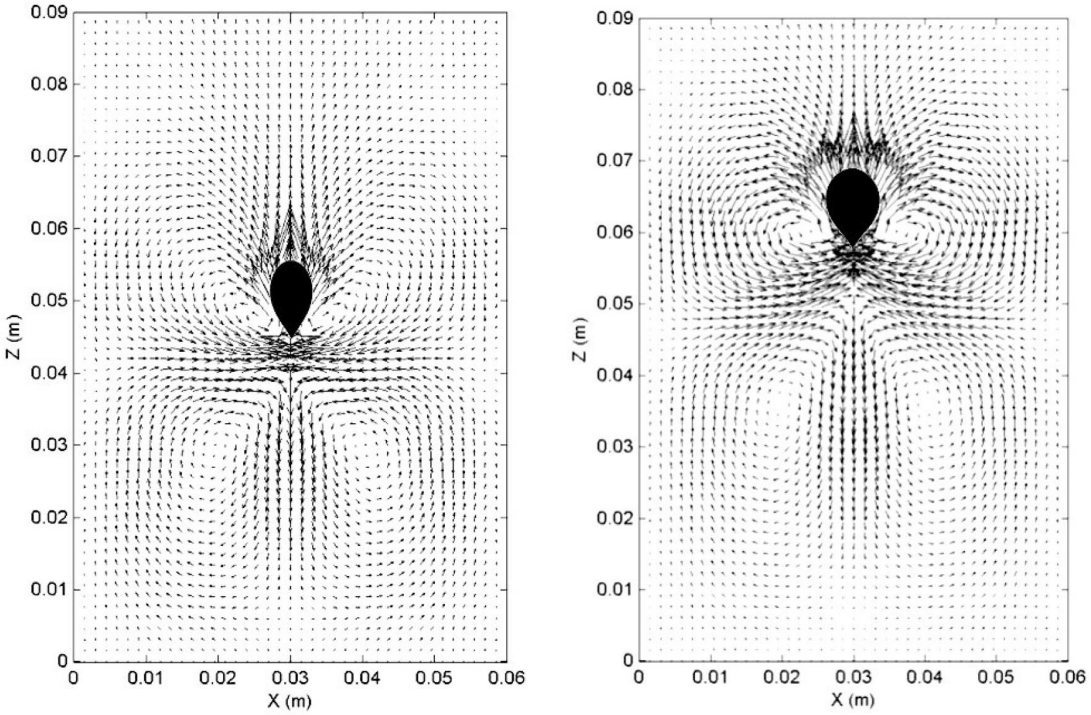

FIG. 5. Simulation results: flow field and bubble shape for a bubble rising in a 0.50% PAAm solution, on the left: bubble volume 80 mm^3; on the right: bubble volume 190 mm^3.

the negative wake, is also in good agreement with experiments (Fig. 2). Finally, our simulation produces correctly the teardrop shape of the bubble, even the emphasis was given to the computation of flow field.

Both the negative wake and bubble's teardrop shape predicted by the lattice Boltzmann approach are particularly noteworthy as they emerge naturally without special fitting within the LB scheme. In addition, a close analysis shows that the bubble's teardrop shape stems from a dual action of the negative wake drawing down the vertical axis of bubble and the lateral stresses stretching the bottom of the bubble, this phenomenon is experimentally confirmed. Obviously, this approach captures main features of the bubble rising in non-Newtonian fluid.

VI. CONCLUSION

In summary, we have developed a lattice Boltzmann scheme interfaced with a linear viscoelastic model that successfully captures the negative wake, the bubble's teardrop

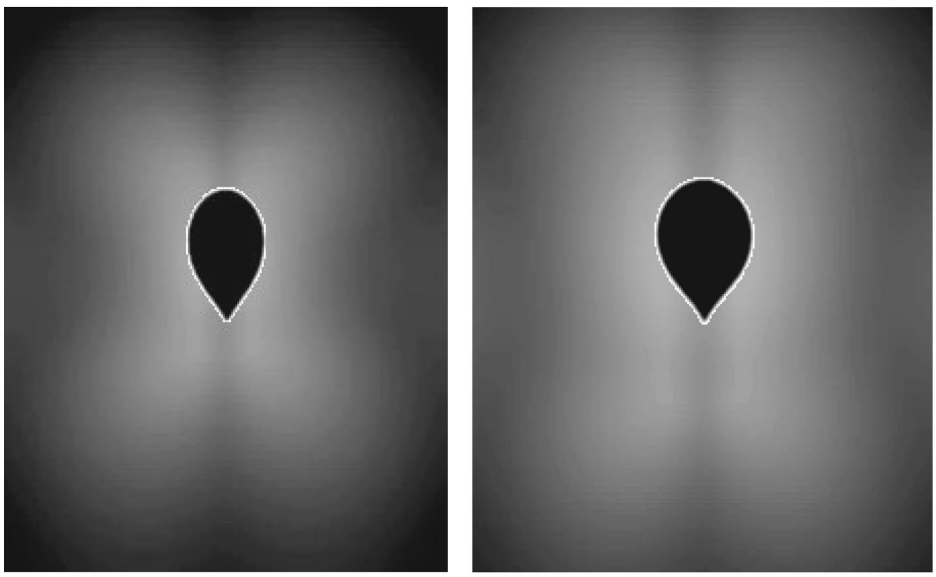

FIG. 6. Simulation results: simulated stress field around a bubble rising in a 0.50% PAAm solution, bubble volume on the left: 80 mm^3; on the right: 190 mm^3.

shape and the spatial stress distribution around the bubble rising in a non-Newtonian fluid. We are currently exploring the possibilities of complete measurements of largely extended flow field by PIV and 3D LB implementation. It is also envisaged that the present study could provide the basis for the further studies on long-range interactions and coalescence between bubbles through both velocity and stress fields as well as the bubble-fluid mass transfer.

[1] G. Astarita and G. Apuzzo, AIChE J. **11**, 815 (1965).
[2] G. F. Tiefenbruck and L. G. Leal, J. Non-Newtonian Fluid Mech. **7**, 257 (1980).
[3] O. Hassager, Nature (London) **279**, 402 (1979).
[4] H. Z. Li, Y. Mouline, L. Choplin, and N. Midoux, C. R. Acad. Sci., Ser. IIb: Mec., Phys., Chim., Astron. **324**, 491 (1997).
[5] H. Z. Li, X. Frank, D. Funfscilling, and Y. Mouline, Chem. Eng. Sci. **56**, 6419 (2001).
[6] S. Succi, *The Lattice Boltzmann Equation for Fluid Dynamics and Beyond* (Clarendon Press, Oxford, 2001).
[7] L. S. Luo and S. S. Girimaji, Phys. Rev. E **67**, 036302 (2003).
[8] N. Takada, M. Misawa, A. Tomiyama, and S. Fujiwara, Comput. Phys. Commun. **129**, 233 (2000).
[9] S. Chen and G. D. Doolen, Annu. Rev. Fluid Mech. **30**, 329 (1998).
[10] P. Lallemand, D. d'Humières, L. S. Luo, and R. Rubinstein, Phys. Rev. E **67**, 021203 (2003).
[11] I. Ispolatov and M. Grant, Phys. Rev. E **65**, 056704 (2002).
[12] A. J. Wagner, L. Giraud, and C. E. Scott, Comput. Phys. Commun. **129**, 227 (2000).
[13] D. Funfschilling and H. Z. Li, Chem. Eng. Sci. **56**, 1137 (2001).
[14] X. Frank, H. Z. Li, D. Funfscilling, F. Burdin, and Y. Ma, Can. J. Chem. **81**, 483 (2003).
[15] M. R. Swift, W. R. Osborn, and J. M. Yeomans, Phys. Rev. Lett. **75**, 830 (1995).
[16] M. R. Swift, E. Orlandini, W. R. Osborn, and J. M. Yeomans, Phys. Rev. E **54**, 5041 (1996).
[17] K. Langaas and J. M. Yeomans, Eur. Phys. J. B **15**, 133 (2000).

J. Fluid Mech. (2006), *vol.* 546, *pp.* 113–122.
doi:10.1017/S0022112005007135 Printed in the United Kingdom

Bubbles in a viscous liquid: lattice Boltzmann simulation and experimental validation

By XAVIER FRANK, DENIS FUNFSCHILLING, NOËL MIDOUX AND HUAI Z. LI

Laboratoire des Sciences du Génie Chimique (UPR 6811 CNRS), ENSIC-INPL, 1, rue Grandville, BP 451, 54001 Nancy Cedex, France

(Received 20 May 2005 and in revised form 9 September 2005)

The dynamics of a single bubble rising in a viscous Newtonian fluid was investigated both experimentally by a particle image velocimetry (PIV) device and numerically using the free-energy-based lattice Boltzmann (LB) model. The rise velocity, bubble shape and flow field were considered for various bubble volumes in axisymmetric flow conditions. Experimentally, the flow measurements by the PIV device revealed the wake increasing with the bubble volume. Such an evolution is linked to the deformation of bubble shape from spherical for small bubbles to flattened at the bottom for large bubbles. The LB simulations compare satisfactorily with our experimental data for both the bubble shape and drag coefficient over the range of Reynolds number ($0.033 \leqslant Re \leqslant 1.8$). With a more extended flow structure around the bubble compared to experiments, the two-dimensional approach shows some limitations in its quantitative description. Fully three-dimensional simulations are necessary, especially for bigger bubbles with $Re > 1.8$.

1. Introduction

The motion of bubbles in a liquid has been the focus of both academic and practical interest for a long time. A huge literature has been generated (Clift, Grace & Weber 1978; Sadhal, Ayyaswamy & Chung 1997). The central problem is the relationship between the rise velocity, bubble shape due to the interface deformation and flow field. For example, the deformation of a bubble rising in an inviscid or viscous liquid has been experimentally studied by Hnat & Buckmaster (1976), Bhaga & Weber (1981) and Maxworthy *et al.* (1996). Approximate theoretical solutions have been developed in the limit of very small deformation of bubbles for either high (Moore 1959) or low (Taylor & Acrivos 1964) Reynolds numbers.

In the case of very viscous fluids, there are also numerous applications that require knowledge of the rise of bubbles either individually or in an interacting cloud, such as volcanic eruption (Morrissey & Chouet 1997; Rust, Manga & Cashman 2003), metallurgy (Xie & Oeters 1994), wastewater treatment (Cui, Chang & Fane 2003) and fermentation (Kilonzo & Margaritis 2004). Aside from the terminal velocity usually estimated by empirical correlations (Rodrigue 2001), we know little about the flow field around a bubble in such fluids.

The lattice Boltzmann (LB) method, emerging from theoretical physics studies on lattice gas automata, has recently become an interesting alternative to the classical computational fluid dynamics. In a multiphase flow context, LB has been successfully applied to various classical problems, like bubbly flows in narrow channel (Yang,

Palm & Sehgal 2002), phase transition (Martys & Douglas 2001) and bubbles rising in non-Newtonian fluids (Frank & Li 2005). Sankaranarayanan *et al.* (2002) focused on the computation of drag and virtual mass forces in a regular array of uniformly sized bubbles with a Reynolds number ranging from 50 to 400, and observed no difference between two- and three-dimensional simulations. In this paper, we present an investigation of axisymmetric bubble motion in a viscous Newtonian fluid both by the LB scheme and experimentally. For small Reynolds number, both the axisymmetric bubble shape and flow structure are particularly suitable for experimental investigation and validation of the LB method. To our best knowledge, there exist neither LB simulation nor flow field measurements by particle image velocimetry (PIV) around a rising bubble for small Reynolds number except for the qualitative visualization by Bhaga & Weber (1981) through the hydrogen bubble tracer technique.

2. Lattice Boltzmann approach

Fluids are described statistically at the microscopic level within the framework of the lattice Boltzmann scheme. Particle probability density functions (PPDF) $f_i(\boldsymbol{r}, t)$ represent the number of particles having velocity $\boldsymbol{c}_i$ at point $\boldsymbol{r}$ and time t. The LB approach consists of computing the evolution of $f_i(\boldsymbol{r}, t)$, due to advection and collisions of particles. Particles can move only on the nodes of a lattice, the classical D2Q9 lattice is used in the present work, which is a two-dimensional lattice involving nine particle velocities $\boldsymbol{c}_i$. The main macroscopic quantities are deduced from the PPDF.

Several LB approaches have been proposed in the literature for modelling multiphase flows (Yang *et al.* 2002; Nourgaliev *et al.* 2003), but there is no consensus. The pseudo-potential approach developed by Shan & Chen (1994) stems from pairwise molecular interactions. The physical meaning is that at each lattice site, the net force experienced by a particle of a species is the sum of the momentum exchanges with particles of all other species in the neighbourhood. The attractive features of this model are the ease implementation and the spontaneous separation between phases. Unfortunately, some numerical fluctuations such as spurious velocities arise near the interface due to the lack of local momentum conservation. An improvement in the thermodynamic consistency was realized in the free-energy approach with a pressure tensor $P_{\alpha\beta}$ (Swift, Osborn & Yeomans 1995). The main merit of this model is that the fluid must reach the right thermodynamic equilibrium directly within the framework of the correct thermodynamic equation of state. In particular, the free-energy approach leads to significant reduction of the velocity fluctuations near the interface and ensures a satisfactory isotropy of the surface tension. This second advantage is particularly useful for the modelling of the rise of a bubble in a fluid. There are however criticisms related to the rigorous thermodynamic consistency as well as to the possible exposure to higher-order lattice artefacts, but these shortcomings are likely to be problem-dependent. In the case of the rise of a bubble in a viscous Newtonian fluid, we did not experience such difficulties. To conserve the Galilean invariance, the LB scheme used in this work is for a two-component and binary system.

In the present study, air bubbles are assimilated as drops of fluid A in a viscous liquid B. The densities of components A and B of the binary fluid are respectively ρ_A and ρ_B; $\rho = \rho_A + \rho_B$ is the total density and $\Delta\rho = \rho_A - \rho_B$ the density difference. Macroscopic fields, ρ, $\Delta\rho$ and $\boldsymbol{u}$, are expressed as functions of $f_i(\boldsymbol{r}, t)$ and $g_i(\boldsymbol{r}, t)$ by

$$\rho = \sum_i f_i, \quad \rho u_\alpha = \sum_i f_i c_{i\alpha}, \quad \Delta\rho = \sum_i g_i. \tag{1.1a–c}$$

A quantity τ_f is linked to spatial step δx, time step δt, fluid viscosity η and fluid density ρ_F by $\eta = \tau_f \rho_F \delta t c_s^2 c^2$ (Nourgaliev *et al.* 2003), where $c = \delta x/\delta t$ and c_s is the pseudo-sound speed in lattice units. τ_g is another dimensionless time parameter equal to 1 here. With such definitions, we can then compute the time step:

$$\delta t = \frac{\rho_F \tau_f c_s^2 \delta x^2}{\eta}. \tag{1.2}$$

Velocities in real units are deduced from the lattice units via $U_\alpha = cu_\alpha$. As the vector $\boldsymbol{a}(\boldsymbol{r}, t)$ is an external acceleration, distributions f_i and g_i obey the so-called lattice Bhatnagar–Gross–Krook (LBGK) equation

$$f_i(\boldsymbol{r} + \boldsymbol{c}_i, t+1) - f_i(\boldsymbol{r}, t) = -\frac{1}{\tau_f}\left(f_i - f_i^{eq}\right) + \frac{\boldsymbol{a}\cdot(\boldsymbol{c}_i - \boldsymbol{u})}{c_s^2} f_i^{eq}, \tag{1.3a}$$

$$g_i(\boldsymbol{r} + \boldsymbol{c}_i, t+1) - g_i(\boldsymbol{r}, t) = -\frac{1}{\tau_g}\left(g_i - g_i^{eq}\right). \tag{1.3b}$$

Equilibrium values of the PPDF are deduced from macroscopic quantities:

$$\sum_i f_i^{eq} = \rho, \quad \sum_i f_i^{eq} c_{i\alpha} = \rho u_\alpha, \quad \sum_i f_i^{eq} c_{i\alpha} c_{i\beta} = \rho u_\alpha u_\beta + P_{\alpha\beta}, \tag{1.4a–c}$$

$$\sum_i g_i^{eq} = \Delta\rho, \quad \sum_i g_i^{eq} c_{i\alpha} = \Delta\rho u_\alpha, \quad \sum_i g_i^{eq} c_{i\alpha} c_{i\beta} = \Delta\rho u_\alpha u_\eta + \Delta\mu\delta_{\alpha\beta}. \tag{1.4d–f}$$

The chemical potential difference $\Delta\mu$ and the pressure tensor $P_{\alpha\beta}$ are defined by the well-known expressions

$$P_{\alpha\beta} = P\delta_{\alpha\beta} + \kappa(\partial_\alpha\rho\partial_\beta\rho + \partial_\alpha\Delta\rho\partial_\beta\Delta\rho), \tag{1.5a}$$

$$P = \rho c_s^2 - \kappa(\rho\,\partial_\alpha\partial_\alpha\rho + \Delta\rho\,\partial_\alpha\partial_\alpha\Delta\rho) - \tfrac{1}{2}\kappa(|\partial_\alpha\rho|^2 + |\partial_\alpha\Delta\rho|^2), \tag{1.5b}$$

$$\Delta\mu = \tfrac{1}{2}c_s^2 \ln\left(\frac{\rho + \Delta\rho}{\rho - \Delta\rho}\right) - \tfrac{1}{2}\lambda\frac{\Delta\rho}{\rho} - \kappa\,\partial_\alpha\partial_\alpha\Delta\rho. \tag{1.5c}$$

For the phase interaction parameter $\lambda > 2c_s^2$, the above scheme leads to spontaneous phase segregation (Swift *et al.* 1995). As a consequence, the interface does not require specific numerical tracking. Within the framework of the free-energy scheme, the parameter κ is closely linked to the surface tension. However, a shortcoming, is that there is still no rigorous physical understanding to allow its theoretical prediction for various gas–liquid systems. In the case of air bubbles rising in glycerol, we have made LB simulations with various values of κ to compare with the simplest visual parameter, which is the bubble's shape. For quite different bubble volumes ranging from spherical to spherical cap shape, a constant and fixed value $\kappa = 0.02$ was found to be the best for describing the bubble's shape. From a physical point of view, this requires further investigation both theoretically and experimentally.

The external force $\boldsymbol{a}$ depends mainly on $\Delta\rho$: $\boldsymbol{a} = -\boldsymbol{g}$ in gas, and $\boldsymbol{a} = \boldsymbol{0}$ in liquid, the $\boldsymbol{g}$ vector being gravity in dimensionless form.

To initiate the simulation, spherical bubbles of different volumes are placed at the bottom of a box 200 nodes wide and 400 nodes high and representing a liquid column of 7 cm large and 14 cm height. This is the compromise that we found between a satisfactory comparison with experimental data and acceptable computation time on a PC for the considered range of bubble volumes. To isolate the bubble, at the left and right boundaries solid wall boundary conditions are applied as in the experimental case, as well as at the top and bottom. The simulation section covered by the LB nodes is high

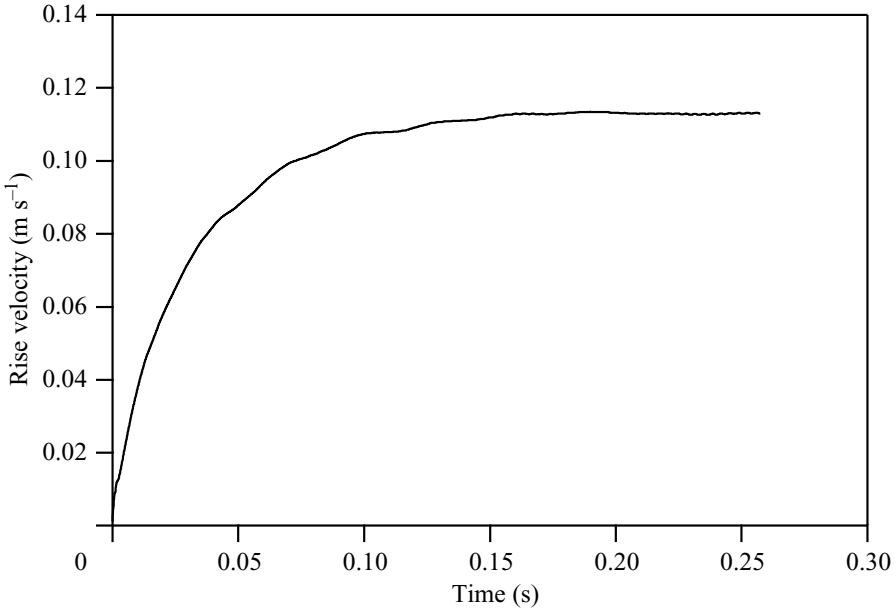

FIGURE 1. LB simulation: variation of the rise velocity towards an asymptotic terminal value for a bubble of $V_0 = 1100\,\mathrm{mm}^3$.

enough for a bubble to reach a stationary rise regime before approaching the top and sufficiently wide to avoid possible wall effects under deformable interface conditions.

After thermodynamic equilibrium is obtained, iterations with buoyancy are performed and useful data (velocity field, bubble shape) are stored. For each simulation, the stationary rise regime is effectively reached. In figure 1, the evolution of the rise velocity is illustrated for a bubble of volume $V_0 = 1100\,\mathrm{mm}^3$ and the terminal rise velocity can be easily determined. Another example is shown in figure 2 for the variation of the bubble shape from an initial sphere to a stationary shape with a flattened bottom. This is accompanied by the modification of the flow field around the bubble.

3. Experimental setup

The experiments were conducted in a Plexiglas cylindrical tank (0.24 m diameter and 1 m height), enclosed by a square duct (0.33 m) to eliminate optical distortions for visualization as well as to keep the liquid temperature inside the cylindrical tank at 293 K. Air bubble generation was through an orifice of 1 mm diameter, submerged in the liquid in the centre of the bottom section of the tank. An electronic valve of rapid response controlled by a PC allowed injection of individual bubbles of a desired volume by varying the open duration of the valve or the air pressure inside a $4 \times 10^{-3}\,\mathrm{m}^3$ reservoir. The bubble rise velocity was measured by both optical laser and photodiodes probes placed at different heights and a particle image velocimetry (PIV, Dantec Dynamics) device and bubble shapes were extracted from video recording and digitization.

The viscous Newtonian fluid used in this work was 99.5 % glycerol (Dow Europe) with some water trace due to humidity. Its density was $1261\,\mathrm{kg\,m}^{-3}$. A Rheometrics Fluid Spectrometer RFS II (Rheometric Scientific) was employed to measure the fluid viscosity, which was 1.20 Pa s, and the air–glycerol surface tension measured on a Krüss Tensiometer K100 was $62\,\mathrm{mN\,m}^{-1}$.

The flow field was measured by means of a PIV device composed of two YAG laser, a camera, a cross-correlator and a computer. In the viscous glycerol solution,

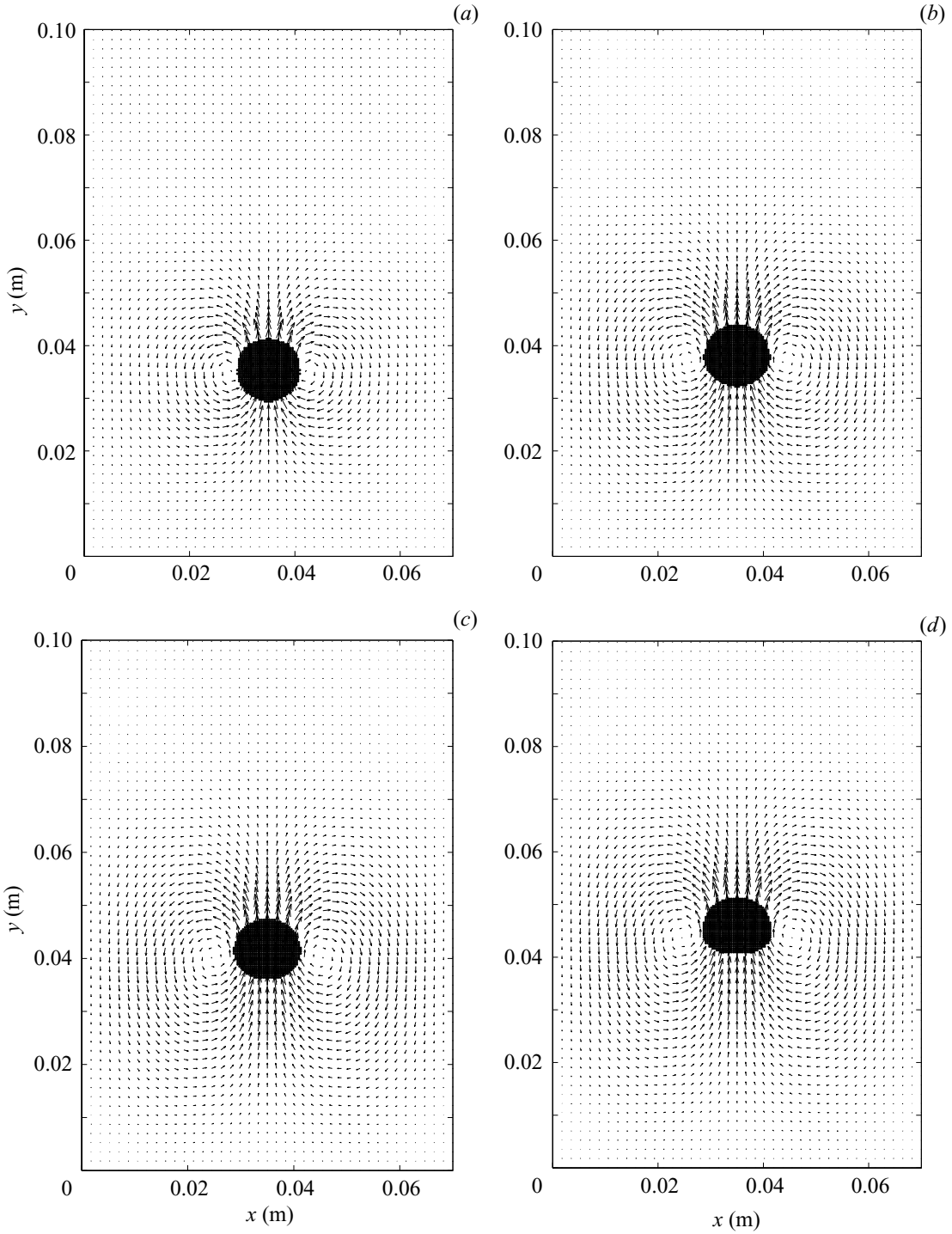

FIGURE 2. LB simulation of the transient rise of a bubble of volume $V_0 = 900\,\mathrm{mm}^3$ initially spherical at rest. (*a*) $t = 0.021$ s, (*b*) $t = 0.065$ s, (*c*) $t = 0.108$ s, (*d*) $t = 0.151$ s in the terminal rise regime.

bubbles were perfectly axisymmetric, and displayed neither shape nor trajectory oscillations within the range of bubble volumes studied. The flow field was also found to be axisymmetric. Hence, two-dimensional measurements in a plane crossing the symmetry axis of a rising bubble lead to a complete knowledge of the flow field around the bubble. The fluid was injected with fluorescent polymer beads of 75 μm diameter and comparable density as seeding particles. An orange filter placed in front of the camera eliminated the reflections of the lasers on the bubbles and allowed only the passage of the fluorescent light from the seeding particles. The two laser sheets

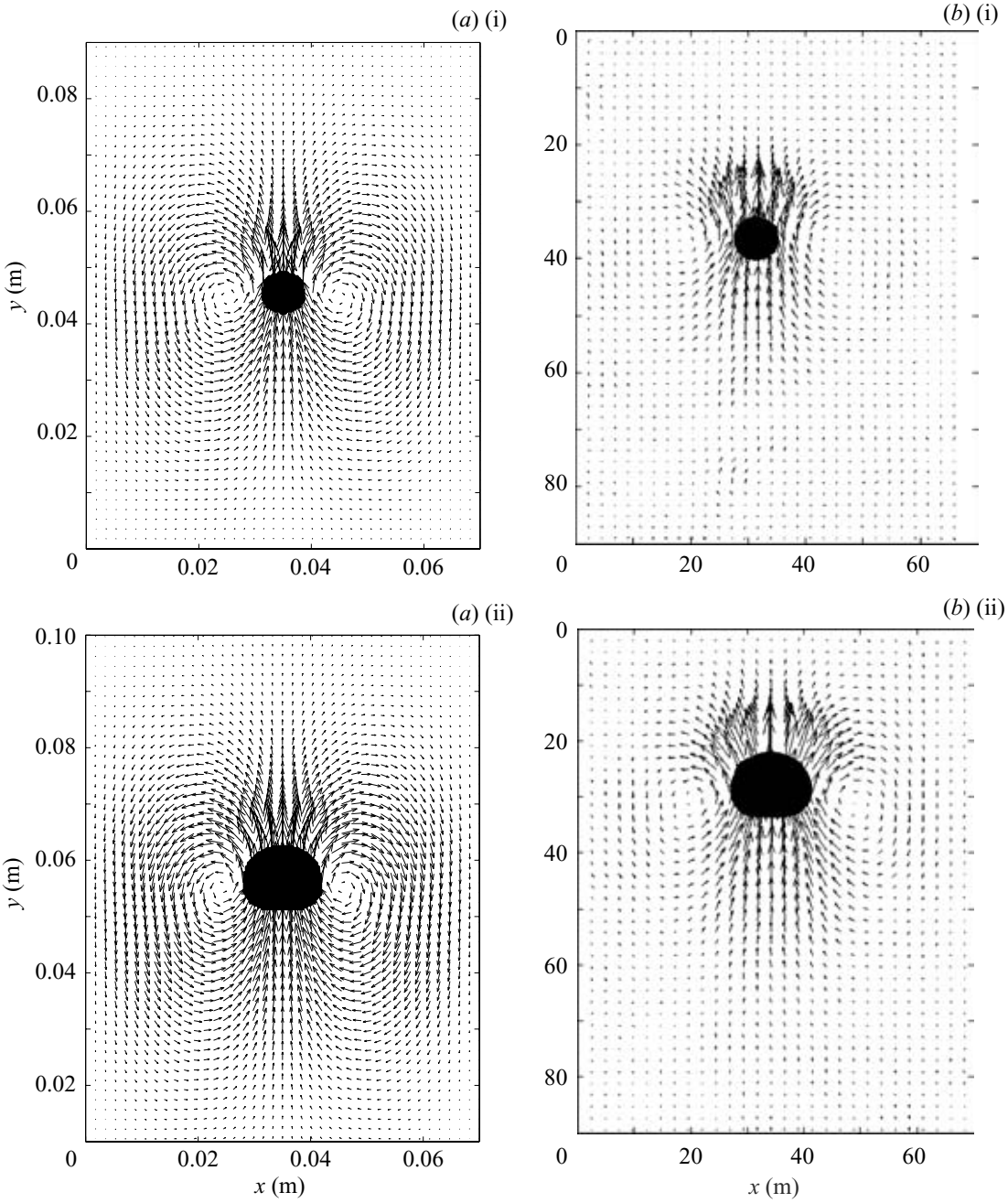

FIGURE 3. Flow field in glycerol around a bubble of volume (i) $V_0 = 200\,\mathrm{mm}^3$ and (ii) $V_0 = 1100\,\mathrm{mm}^3$. (*a*) LB simulations with the computed bubble shape. (*b*) PIV measurements with the real bubble shape.

crossed the vertical symmetry axis of the bubble. The camera, placed perpendicular to the laser sheets, took two successive images, each at the maximum intensity of the laser impulse. These images were divided into several thousand small interrogation areas of 32×32 pixels. A cross-correlation was then performed on the two corresponding interrogation areas to give the instantaneous flow field.

4. Results

As shown in figure 3 and figure 4, experimental flow fields are in qualitative agreement with the LB simulations for a small and large bubble. Note that the magnitude of the velocity fields of the experiments and the LB simulation is comparable. Both exhibit an upward flow at the top and bottom of the bubble,

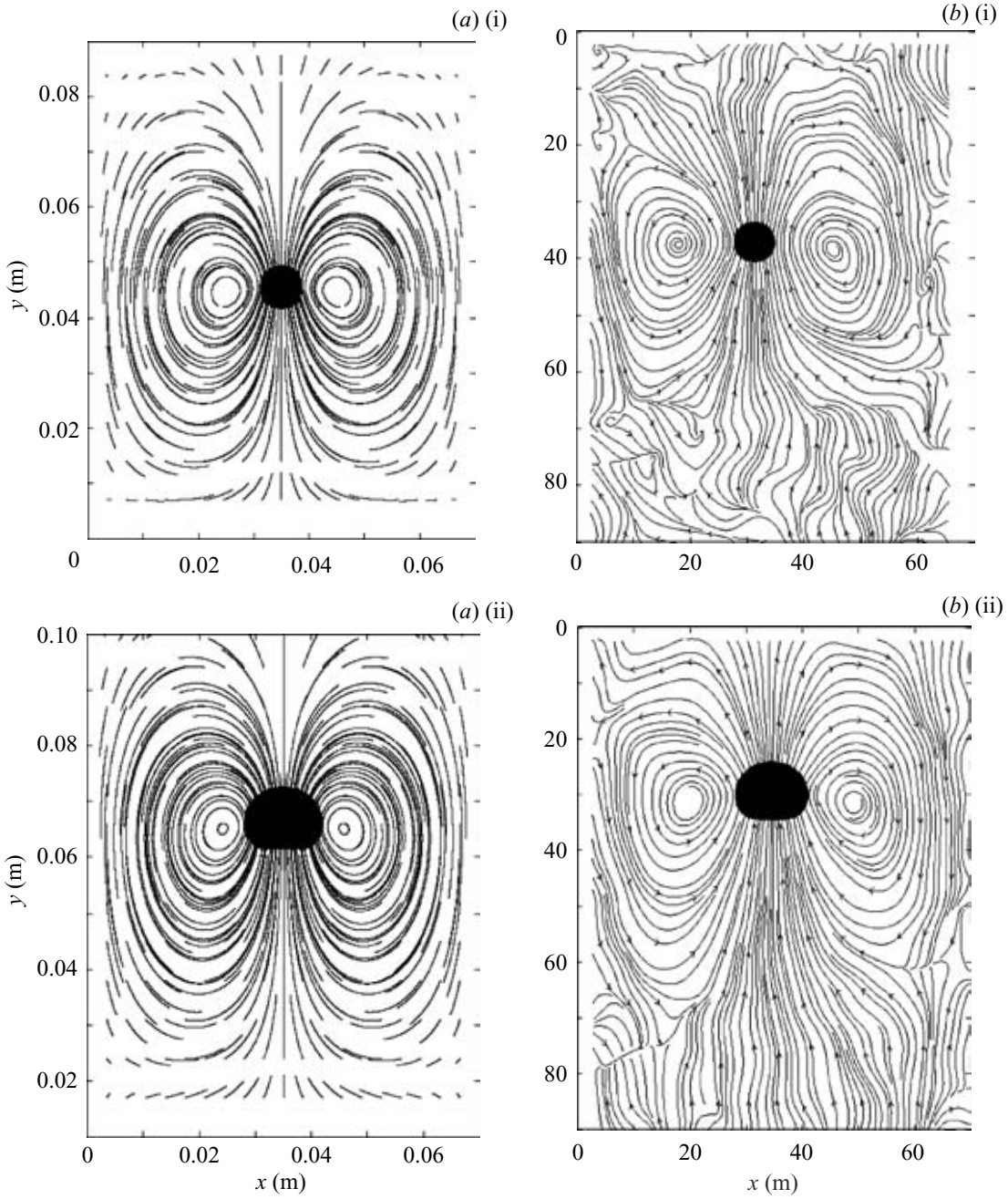

FIGURE 4. Streamlines in glycerol around a bubble of volume (i) $V_0 = 200\,\mathrm{mm}^3$ and (ii) $V_0 = 1100\,\mathrm{mm}^3$. (*a*) LB simulations with the computed bubble shape. (*b*) PIV measurements with the real bubble shape.

downward flow occurring at the edge of the column due to mass conservation. Streamlines of the flow around a rising bubble confirm the recirculation between the upward flow in the front of bubbles and that in the wake at the side of the bubble. This recirculation region expands space with an increase of the bubble volume.

These flow features can be closely linked to the results on the bubble shape (figure 5) where the experimental visualization compares well with the LB simulations. The experimental Reynolds, Eötvös and Weber numbers as well as the simulation Reynolds number are also indicated in figure 5. In spite of its relationship with the classical surface tension, the parameter κ in the LB scheme cannot allow a straightforward estimation for the Eötvös and Weber numbers. For small bubbles, the shape is spherical, and for larger bubbles the bottom is progressively flattened

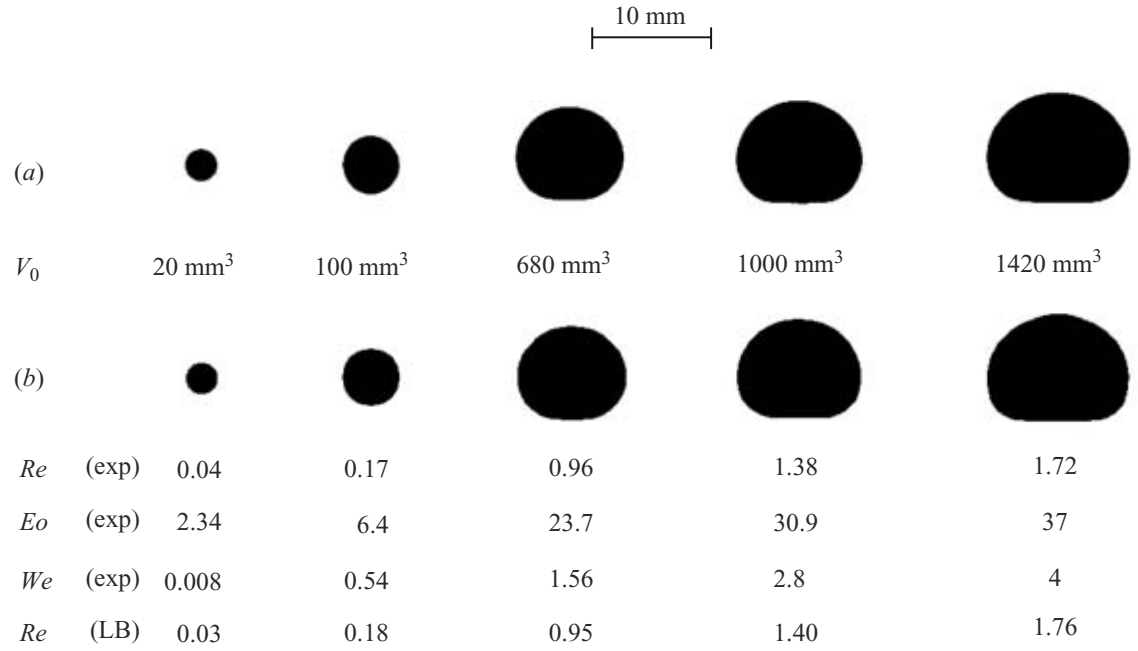

FIGURE 5. Some examples of the variation of bubble shape in glycerol with the bubble volume V_0, Re, Eo and We from experiments, and Re from LB simulations; (a) experimental visualization; (b) LB computation.

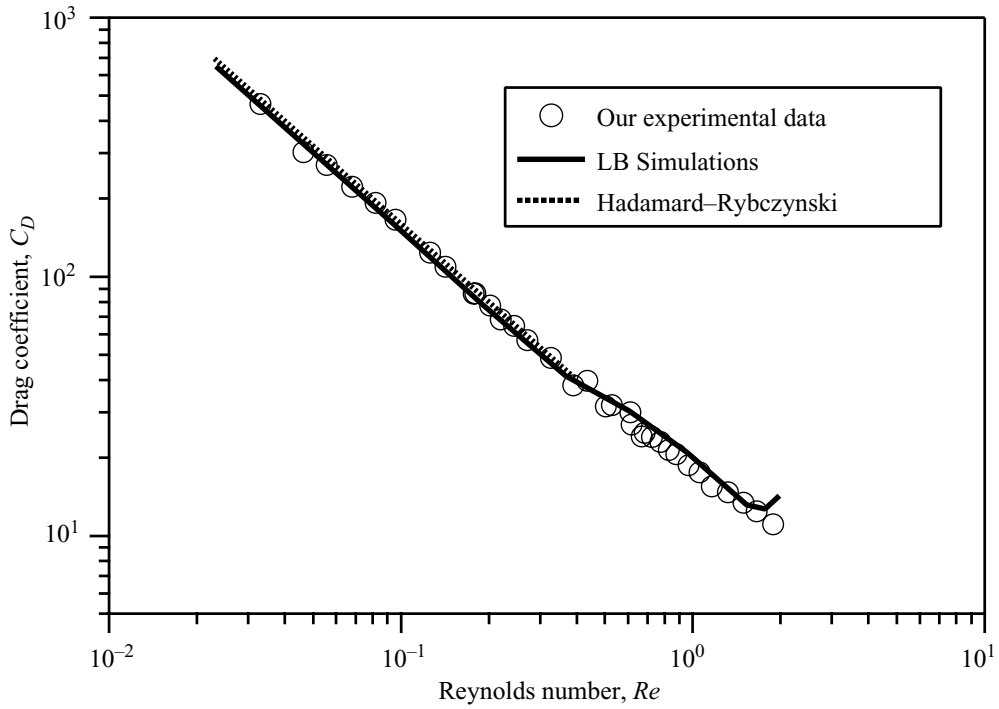

FIGURE 6. Variation of the drag coefficient C_D with the Reynolds number Re in glycerol.

whereas the top remains spherical, as found by other workers. The bubble's shape deformation can be regarded as a natural consequence of the fluid flow fields as the upward flow in the wake and the recirculation at the side are both increased with an increase of the bubble volume and flatten the bubble bottom towards a spherical cap shape. The effect of the shape deformation on the rise velocity of bubbles can be established by comparing the drag coefficient predicted by the LB approach with our experimental data obtained in the viscous glycerol fluid (figure 6). The theoretical

drag coefficient was directly determined from the rise velocity computed by the LB simulation. For $Re \leqslant 0.40$ corresponding to a bubble volume of $V_0 \leqslant 200\,\mathrm{mm}^3$ where the Hadamard–Rybczynskis drag expression is valid for a spherical bubble, the LB simulations compare satisfactorily with the experimental results. Above this critical value, accompanying the beginning of the shape deformation, the LB simulations are still in reasonable agreement with the experimental data but with increasing deviation.

As numerous multiphase flow situations exist where the fluid dynamics can be approximated as axisymmetric (Eggers 1997; Sussman & Smereka 1996), a two-dimensional approach is clearly a good approximation for three-dimensional phenomena. In particular, the working fluid in this study is very viscous with a Morton number of 67.7, and the two-dimensional LB simulation compares satisfactorily with the experiments, especially for the drag coefficient, which is a mean description, and for the bubble shape, which is not far from spherical. However, local differences exists between the simulation and experiments in both flow field and streamlines as shown in figure 3 and figure 4: the simulated flow structure is more extended than the two-dimensional measurements by the PIV device. This can be attributed to the macroscopic conservation laws such as for mass and momentum within the two-dimensional framework. Even for the drag coefficient, a deviation occurs for $Re > 1.8$ as the axisymmetric assumption is no longer valid (figure 6). In this case, a three-dimensional LB approach with parallel computation should be employed. In particular, a three-dimensional approach is essential for a study on the interactions and coalescence between bubbles with noticeable shape evolution and non-symmetric wake structure. This is an avenue we are currently exploring both experimentally by PIV measurements and numerically by the LB approach.

5. Conclusion

In summary, the lattice Boltzmann simulation captures the main features of the flow field, shape and rise velocity of bubbles in a viscous Newtonian fluid. These results are validated by a PIV device for the flow fields, camera visualization for the bubble shape and terminal velocity measurements. However, the two-dimensional LB simulations are limited to bubbles of a terminal rise Reynolds number under 1.8 to maintain the axisymmetric flow conditions. The apparent inadequacy of a two-dimensional approach is also obvious in the detailed quantitative comparison with experimental flow fields around a bubble. We are currently conducting fully three-dimensional studies for large bubbles and in particular for in-line interactions and coalescence between bubbles. For physical scales, we are also performing experiments in other fluids of varying viscosity and surface tension.

REFERENCES

Bhaga, D. & Weber, M. E. 1981 Bubbles in viscous liquids: shapes, wakes and velocities. *J. Fluid Mech.* **105**, 61–85.

Clift, R., Grace, J. R. & Weber, M. E. 1978 *Bubbles, Drops and Particles.* Academic.

Cui, Z. F., Chang, S. & Fane, A. G. 2003 The use of gas bubbling to enhance membrane processes. *J. Membrane Sci.* **221**, 1–35.

Eggers, J. 1997 Nonlinear dynamics and breakup of free-surface flows. *Rev. Mod. Phys.* **69**, 865–929.

Frank, X. & Li, H. Z. 2005 Complex flow around a bubble rising in a non-Newtonian fluid. *Phys. Rev.* E **71**, 036309.

Hnat, J. G. & Buckmaster, J. D. 1976 Spherical cap bubbles and skirt formation. *Phys. Fluids* **19**, 182–194.

Kilonzo, P. M. & Margaritis, A. 2004 The effects of non-Newtonian fermentation broth viscosity and small bubble segregation on oxygen mass transfer in gas-lift bioreactors: a critical review. *Biochem. Engng J.* **17**, 27–40.

Martys, N. S. & Douglas, J. F. 2001 Critical properties and phase separation in lattice Boltzmann fluid mixtures. *Phys. Rev.* E **63**, 031205.

Maxworthy, T., Gnann, C., Krten, M. & Durst, F. 1996 Experiments on the rise of air bubbles in clean viscous liquids. *J. Fluid Mech.* **321**, 421–441.

Moore, D. W. 1959 The rise of a gas bubble in a viscous liquid. *J. Fluid Mech.* **6**, 113–130.

Morrissey, M. M. & Chouet, B. A. 1997 Burst Conditions of explosive volcanic eruptions recorded on microbarographs. *Science* **275**, 1290–1293.

Nourgaliev, R. P., Dinh, T. N., Theofanous, T. G. & Joseph, D. 2003 The lattice Boltzmann equation method: theoretical interpretation, numerics and implications. *Intl J. Multiphase Flow* **29**, 117–169.

Rodrigue, D. 2001 Generalized correlation for bubble motion. *AIChE J.* **47**, 39–44.

Rust, A. C., Manga, M. & Cashman, K. V. 2003 Determining flow type, shear rate and shear stress in magmas from bubble shapes and orientations. *J. Volcan. Geotherm. Res.* **122**, 111–132.

Sadhal, S. S., Ayyaswamy, P. S. & Chung, J. N. 1997 *Transport Phenomena with Drops and Bubbles.* Springer.

Sankaranarayanan, K., Shan, X., Kevrekidis, I. G. & Sundaresan, S. 2002 Analysis of drag and virtual mass forces in bubbly suspensions using an implicit formulation of the lattice Boltzmann method. *J. Fluid Mech.* **452**, 61–96.

Shan, X. & Chen, H. 1994 Simulation of nonideal gases and liquid-gas phase transitions by the lattice Boltzmann equation. *Phys. Rev.* E **49**, 2941–2948.

Sussman, M. & Smereka, P. 1996 Axisymmetric free boundary problems. *J. Fluid Mech.* **341**, 269–294.

Swift, M. R., Osborn, W. R. & Yeomans, J. M. 1995 Lattice Boltzmann simulation of nonideal fluids. *Phys. Rev. Lett.* **75**, 830–833.

Taylor, T. D. & Acrivos, A. 1964 On the deformation and drag of a falling viscous drop at low Reynolds number. *J. Fluid Mech.* **18**, 466–476.

Xie, Y. & Oeters, F. 1994 Measurements of bubble plume behaviour and flow velocity in gas stirred liquid Woods metal with an eccentric nozzle position. *Steel Res.* **65**, 315–319.

Yang, Z. L., Palm, B. & Sehgal, B. R. 2002 Numerical simulation of bubbly two-phase flow in a narrow channel. *Intl J. Heat Mass Transfer* **45** 631–639.

International Journal of Multiphase Flow 36 (2010) 599–607

Contents lists available at ScienceDirect

International Journal of Multiphase Flow

journal homepage: www.elsevier.com/locate/ijmulflow

Multiphase flow in the vascular system of wood: From microscopic exploration to 3-D Lattice Boltzmann experiments

X. Frank [a,*], G. Almeida [b], P. Perré [c]

[a] INRA, UMR 1092 LERFOB, F-54042 Nancy cedex, France
[b] USP, ESALQ (Luiz de Queiroz College of Agriculture), Brazil
[c] AgroParisTech, UMR 1092 LERFOB, ENGREF 14, rue Girardet F-54042 Nancy cedex, France

ARTICLE INFO

Article history:
Received 16 February 2010
Received in revised form 22 April 2010
Accepted 24 April 2010
Available online 7 May 2010

Keywords:
Multiphase
Wood
3D modelling
Image processing
Lattice Boltzmann
Vascular
Morphology

ABSTRACT

This paper provides insights into liquid free water dynamics in wood vessels based on Lattice Boltzmann experiments. The anatomy of real wood samples was reconstructed from systematic 3-D analyses of the vessel contours derived from successive microscopic images. This virtual vascular system was then used to supply fluid–solid boundary conditions to a two-phase Lattice Boltzmann scheme and investigate capillary invasion of this hydrophilic porous medium. Behavior of the liquid phase was strongly dependent on anatomical features, especially vessel bifurcations and reconnections. Various parameters were examined in numerical experiments with ideal vessel bifurcations, to clarify our interpretation of these features.

1. Introduction

The xylem (wood) in trees is formed by the cambium. The role of this meristem is to enlarge each stem produced by the apical meristems. In living trees, the formation of wood provides mechanical support, allows reorientation and provides a vascular system, this latter differing between softwoods and hardwoods. In softwood, the vascular system consists of tracheids which are a few millimeters long and connected together by bordered pits. These pits serve as valves which limit the extension of undesired cavitation in the sap column. More precisely, the tracheids formed during spring have thin cell walls, wide radial diameters and hence a large lumen, and are more specifically involved in sap conduction. In hardwoods, the vascular system consists of tube-like vessels, varying in length from a few centimeters to several meters and formed by lines of cells known as vessel elements (Zimmermann, 1983). The ends of these vessel elements are perforated. Matching perforations between adjacent vessel elements provide an open passage for the upward movement of raw sap in the tree stem (Panshin and de Zeeuw, 1980). Hardwoods in which the vessels are fairly uniform in size and relatively evenly distributed throughout the growth ring are described as diffuse-porous woods. Vessels can account for 7–50% of the wood volume, depending on the species. In most diffuse-porous hardwoods of temperate zones, the vessel diameter varies from 20 μm to 100 μm. Air–water flow is crucial in the living tree, as bubbles trapped within the vascular system will have dramatic consequences on permeability and the efficiency of sap transport from roots to leaves. Wood is a hygroscopic porous medium, which means that within it water can exist in three different forms: bound water in the cell walls, free water and water vapor in the cell lumens. However, the diffusion of bound water occurs so slowly (Siau, 1984; Agoua et al., 2001) that fluid migration in wood can be considered as limited to mono- or multiphase flow in the vascular system.

As the anatomy of wood is highly complex, the fluid migration properties (permeability, capillary pressure, relative permeability) cannot be readily deduced from a simple geometrical representation of the vascular system. The situation is even more complex in softwoods, due to the presence of bordered pits between the tracheids. Although interesting models are available in the literature, they usually require considerable assumptions in order to be operational (Comstock, 1970; Perré and Turner, 2001; Aumann and Ford, 2002). The typical dual-scale mechanisms of fluid flow occurring in softwoods (tracheids and bordered pits) explains why some works have focused solely on fluid flow inside a single bordered pit (Hacke et al., 2004; Valli et al., 2002).

The situation in hardwoods is slightly less complex, due to the presence of specialized cells devoted to sap flow. At first sight, the vascular system of hardwood species can be simply repre-

* Corresponding author.
E-mail address: xfrank@nancy-engref.inra.fr (X. Frank).

0301-9322/$ - see front matter © 2010 Elsevier Ltd. All rights reserved.
doi:10.1016/j.ijmultiphaseflow.2010.04.006

sented as bundles of capillary tubes (Dullien, 1992). However, the measured permeability values are systematically overestimated by the theoretical permeability computed from anatomical images using the Hagen–Poiseuille equation (Zimmermann, 1983; Siau, 1984; Perré and Karimi, 2002). Early investigations by Zimmermann and collaborators (Zimmermann, 1983) in several hardwood species revealed that the vessels did not run in parallel but changed their relative positions in the axial direction. For example, it was shown that individual vessels in maple (*Acer rubrum* L.) and poplar (*Populus* spp.) moved from one vessel cluster to another and never really ended. They also observed that in many cases, two or more vessels could run side by side over considerable distances. This implies that the water conducting units do not have dead ends and water can pass from one vessel system into several others through the pits and perforations. It is thus obvious that the task of water-flow prediction is greatly complicated by the actual pore morphology, namely the tortuosity and change in section shape of the conductive elements, as well as the complex networks resulting from their connection. The situation in which multiphase flow occurs, such as cavitation during the tree's lifespan or in the drying of plant-derived material is even more complicated, requiring evaluation of the propagation dynamics of the air–water meniscus or, at the very least, partition of the liquid phase at equilibrium.

The purpose of this paper was to address different multiphase flow configurations by performing numerical experiments on reconstructed morphologies derived from real wood samples. To achieve this goal, two major difficulties were to be addressed: to reconstruct the wood vessel anatomy in three dimensions from a real wood sample, and to choose and implement a relevant numerical approach.

Impressive tools are currently available in the field of non-destructive testing. Micro-tomographic images obtained with a synchrotron provide a sub-micrometric spatial resolution (down to 200 nm). Such tools have been used to obtain a non-invasive insight into wood structure (Trtik et al., 2007; Steppe et al., 2004). One of the major drawbacks of micro-tomography, however, is the acquisition time. This is why NMR imaging provides a powerful complementary technique for non-invasive investigation of fluid flow dynamics in porous media. Indeed, 3D images of one or more fluid phase(s) are obtained in the case of NMR microscopy with a relatively short acquisition time and a spatial resolution in the order of 10 μm (Tyszka et al., 2005). Such a technique has been used, for example, to assess the behavior of bordered pits in early and late wood of Douglas fir during drainage (Almeida et al., 2008).

However, despite the existence of these amazing tools, to our knowledge a comprehensive approach, from the real sample to the simulation of multiphase flow in 3D morphology, has not yet been proposed for wood. In the present work, a relatively simple, low-cost experimental protocol was applied to reconstruct the 3D morphology of a real wood sample from images collected after successive slicing of a sample with a sledge microtome. This procedure, based on the construction of a 3D grid of points by vectorial image processing, could in future be applied to any data set obtained from NMR imaging or micro-tomography, despite its apparent simplicity.

To complete the sample-to-simulation chain, several conditions need to be satisfied when selecting an appropriate numerical method. Firstly, complex gas–liquid interfacial dynamics, including topological changes such as film ruptures and coalescence, will occur during computation. Secondly, the dynamic behavior of the system will emerge as a result of competition between wetting phenomena and viscous dissipation. In consequence, the fluid–solid interactions need to be correctly implemented, despite the complex geometrical features of wood vessels. Description of the fluid/solid and liquid/vapor interfaces is particularly challenging. Classical paradigms, such as front-tracking schemes (De Sousa et al., 2004), volume-of-fluid models (Štěpánek and Rajniak, 2006) and level-set approaches (Tanguy and Berlemont, 2005), give rise to huge computation loads when the system is large or in the case of complex interfacial geometries. These difficulties might be circumvented by using the seemingly attractive meshless methods (Frank and Perré, 2010). Several alternative numerical methods are available. In off-lattice approaches, the fluid is described through moving point-like elements. For example, in the context of smooth particle hydrodynamics (SPH) (Tartakovsky et al., 2007), the Navier–Stokes equation is solved on Lagrangian particles carrying macroscopic fluid properties and fields. In other numerical methods, macroscopic features can emerge spontaneously from the initial assumptions. Dissipative particle dynamics (DPD), a coarse-grained molecular dynamics approach, is part of this elegant family (Henrich et al., 2007). The Lattice Boltzmann (LB) scheme is another quite recent emergence-based mesoscale numerical tool for fluid flow simulation (Succi, 2001). It can be considered as a special discretization of the well-known Boltzmann's equation, despite its later development, as compared to lattice gas cellular automata (LGCA) (Hardy et al., 1976). The Lattice Boltzmann method has already proved its ability to simulate multiphase flows in porous media (Hatiboglu and Babadagli, 2008). In the present work, the latter was chosen as a satisfactory compromise between the computational work and the size of the computed domain.

2. Wood sample anatomy

2.1. Image acquisition and processing

The study was carried out on a 8-year-old White birch (*Betula verrucosa*). The final cross section dimension of the chosen sample was 3 mm (tangential) × 5 mm (radial) and 20 mm in length (longitudinal). This sample was fixed on a sledge microtome. A modular microscope (Nachet MS 98) equipped with long-focus lens and a digital camera from Basler Vision Technologies (Fig. 1A) was fixed on a support. The microtome chosen for this work had the advantage of vertically displacing the sample between successive cuts, thereby facilitating exploration of the vessel network. A microtome section thickness of 20 μm (along the longitudinal direction) was chosen for sample exploration and a digital image was taken every 40 μm. The images were stored in color (RGB, 8 bits per color) with a spatial resolution of 1388 × 1038. The magnification lens used in this work results in a pixel size of 1.3 μm. In all, 100 images were analyzed resulting in a depth of vascular system exploration of 4000 μm.

The 2-D images were processed with *MeshPore*, a customized software specifically developed for processing vectorial images (Perré, 2005) from a specific data structure. This multi-purpose software is based on the concept of directed line segments and is designed to be able to handle any shape (including closed or open contours), change the number of nodes in each chain, distinguish contour structure and the location of geometrical points, merge or split chains, re-sample a chain to give a more refined or coarser spatial resolution and so on. The basic elements are points and nodes and a contour consists of a chain of nodes, each one pointing towards a specific geometrical point. Each point carries geometrical information whereas each node carries connection information. This results in a very flexible structure, as the point properties are clearly distinct from the node properties. A vessel contour is defined by a chain, which consists of a set of connected nodes. The first node of each chain is stored in a table, which therefore contains the complete chain list for the image. Each node in a chain "knows" the previous node (= 0 for the first node) and the next

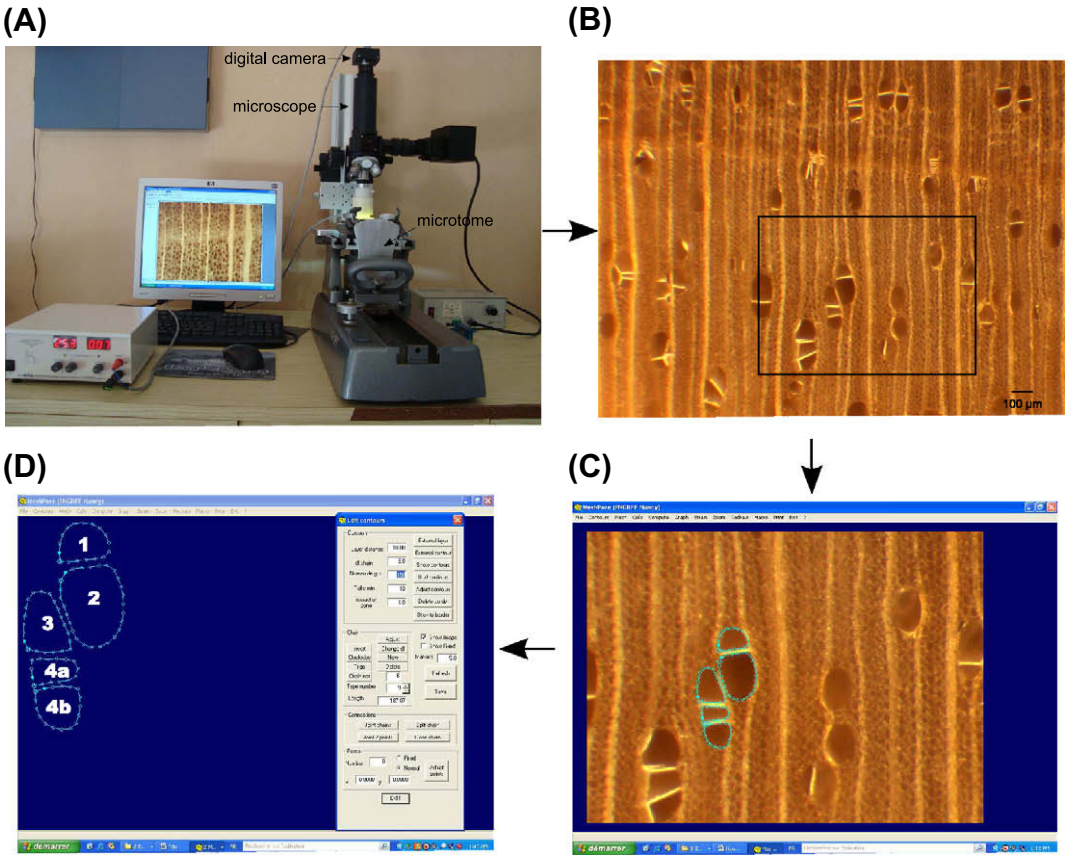

Fig. 1. Image acquisition and treatment. (1A) image acquisition system; (1B) initial image and delimitation of the region of interest (black square); (1C) vessel network demarcation using *MeshPore*; (1D) final 2D image.

node (= 0 for the last node). In the case of a closed chain, the first and last nodes point towards the same point.

As our image collection contained excessive number of vessels, a particular region of interest (ROI) was selected. The macro language available in *MeshPore* allowed easy selection of the same ROI on all images, as well as certain automatic instructions. The main steps of image acquisition and treatment are depicted in Fig. 1.

Due to minute sample movements during successive microtome cuts, a feature has been added to MeshPore to allow for small translations of all chains of an image, in order to align successive planes. Together with the pixel size and the definition of the vessel contour, the global accuracy of our procedure may be estimated at ±2 µm.

2.2. Reconstruction procedure

The LB scheme is based on generation of a 3D lattice with a distinction between pore and solid. As the LB lattice should remain cubic, a certain level of interpolation is required between two successive images, as a function of the desired spatial resolution in the *xy* plane. Note that the vectorial description of the contours provided by *MeshPore* permits a spatial resolution that is independent of the initial bitmap image resolution.

Constructing the true 3D morphology from the collection of *n* successive planes requires two crucial steps:

1. Finding the connectivities between the contours of successive planes
2. Choosing a method of interpolation between planes to generate a cubic lattice

For this purpose, a 3D version of *MeshPore*, which allows any number of slices to be loaded, has been developed. All the *MeshPore* 2D features were retained for each selected slice, so that the final data set consisted of a collection of planes, each one defined by a collection of chains. The graphical facilities implemented in *MeshPore* 3D used the concept of quaternions to compute the projections.

Numerous criteria can be imagined to find the connectivities between contours. Rather than a criterion based on the common surface area between two contours (Kwon et al., 2003), we chose to use a more demanding criterion i.e., that two contours would be considered as connected if the barycenter of one contour was included in the other. The reciprocity of the criterion is important, namely in the case of bifurcations (one vessel of a plane connected to two vessels of a neighboring plane (upper or lower). We took advantage of our vectorial data representation and made thorough use of integral contours in the data processing. For example, following Stokes's theorem, the barycenter of a closed chain was obtained from the contour integrals:

$$x_{bary} = \frac{1}{S}\oint_C x^2 \cdot dy \tag{1}$$

$$y_{bary} = -\frac{1}{S}\oint_C y^2 \cdot dx \tag{2}$$

Similarly, the Cauchy's residue theorem was used to determine if a specific point was inside a closed contour or not. This criterion was used both to generate the connectivities between contours and to allocate the solid or pore flag to each point of the lattice.

Once all the connectivities had been computed, all the chains were organized into clusters. These clusters (set of connected con-

tours) were built up step by step, until they spread throughout the whole domain.

In order to stay as close as possible to the real vessel morphology, the contours themselves were interpolated before lattice generation. For each couple of connected contours (initial contours) from two successive planes, one contour was built in each interpolation plane by creating a chain with the same number of nodes as the first initial chain. For each node i of the first initial chain, the *best* node of the other chain was chosen to form a generatrix of the vessel pathway. This node was indeed the one whose point was nearest to the plane formed by the two barycenters of the initial chains and the point of node i. The point of the current node of the interpolated chain is simply the intersection of the interpolation plane with this generatrix (Fig. 2).

An example of this interpolation procedure is shown in Fig. 3. This simple configuration depicts the interpolation obtained in two common cases:

- One single contour, slightly deformed and shifted from one plane to the other.
- Two contours connected to a single and larger contour on the upper plane.

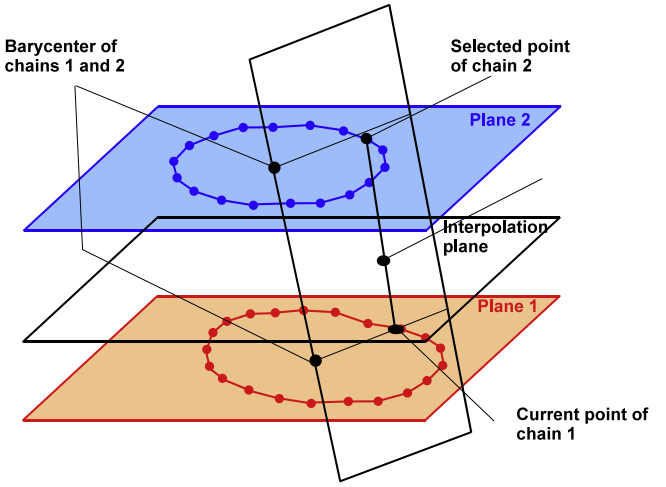

Fig. 2. Strategy used to interpolate 3-D morphology from connected chains of two successive initial planes.

2.3. Example of morphology

A set of four vessels was chosen as case study for the modeling work. The interest of the selected zone was based on two major features:

- The presence of vessel lines of different and variable sections,
- The existence of two bifurcations: one vessel line diverging into two sub-lines, which then merge again into a single vessel

The resulting morphology is depicted in Fig. 4. To ensure easy analysis and discussion of the capillary invasion simulated with this morphology, the vessels were numbered and vessels 4a and 4b indicate the bifurcation of vessel 4.

3. Shan–Chen Lattice Boltzmann approach

In the LB context, the Navier–Stokes equation is not implemented directly, as the fluid is described at the particle kinetics level. Particle presence probability density functions (PPDF) f_i are defined, where $f_i(\vec{r},t)$ is the probability of finding a particle exhibiting velocity $\vec{c}_i$ at point $\vec{r}$ and date t. A lattice is defined from the discrete velocity set $\{\vec{c}_i\}$, where $\vec{c}_i$ velocities are tuned to allow a particle to jump from one node of the lattice to a neighboring node. We chose a three-dimensional lattice which exhibited 19 velocities: the D3Q19 lattice (Table 1).

Fluid density ρ and velocity $\vec{u}$ are provided in a relatively simple way by equations:

$$\rho = \sum_i f_i \tag{3}$$

$$\rho\vec{u} = \sum_i f_i\vec{c}_i \tag{4}$$

The main idea of the Lattice Boltzmann approach is to implement both collisions between particles and free streaming from one collision to the next. To do this we chose the so-called LBGK model in which the f_i fuctions obey a linear approximation of the general lattice Boltzmann equation:

$$f_i(\vec{r}+\delta t\vec{c}_i, t+\delta t) - f_i(\vec{r},t) = -\frac{1}{\tau}\left(f_i - f_i^{eq}\right) \tag{5}$$

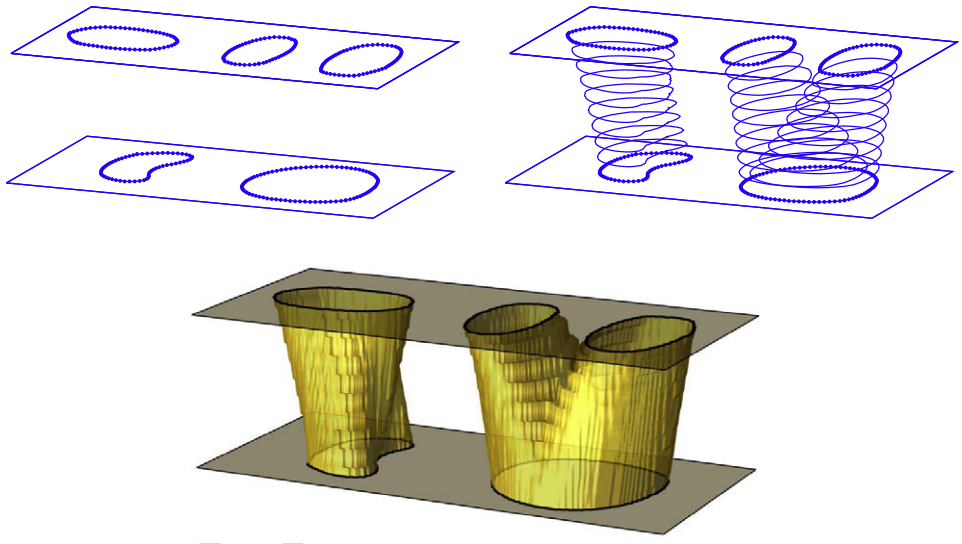

Fig. 3. Example of interpolation between two initial planes: two clusters with one bifurcation (top, left), calculated chains of nine interpolation planes between these two initial planes (top, right) and the 3D morphology obtained after grid generation (bottom).

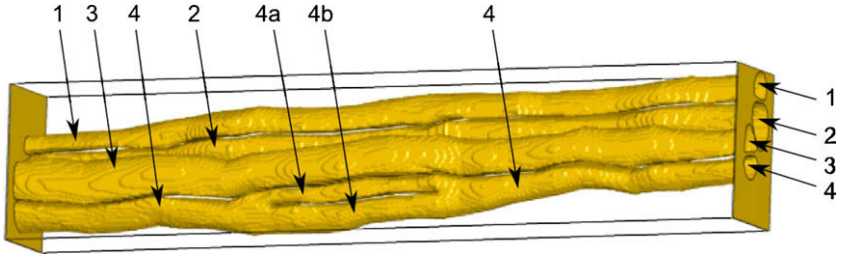

Fig. 4. Re-building of birch anatomy. Numbers are attributed to the vessels. Note that vessel 4 exhibits two bifurcations (divergent and convergent) and the resulting sub-vessels are termed vessel 4a and 4b.

Table 1
The D3Q19 lattice velocities.

i	0	1	2	3	4	5	6	7	8	9	10	11	12	13	14	15	16	17	18
$\vec{c}_i$	0	1	−1	0	0	0	0	1	1	−1	−1	1	1	−1	−1	0	0	0	0
	0	0	0	1	−1	0	0	1	−1	1	−1	0	0	0	0	1	1	−1	−1
	0	0	0	0	0	1	−1	0	0	0	0	1	−1	1	−1	1	−1	1	−1

The left member is implemented through a streaming step and the right member is a relaxation term, where τ is the relaxation time: inter-particle collisions drive f_i towards an equilibrium value f_i^{eq}, which is deduced from macroscopic quantities:

$$\sum_i f_i^{eq} = \rho \tag{6}$$

$$\sum_i f_i^{eq}\vec{c}_i = \rho\vec{u} \tag{7}$$

$$\sum_i f_i^{eq} c_{i\alpha}c_{i\beta} = \rho u_\alpha u_\beta + \rho c_s^2\delta_{\alpha\beta} \tag{8}$$

$$\sum_i f_i^{eq} c_{i\alpha}c_{i\beta}c_{i\gamma} = \rho c_s^2(u_\gamma\delta_{\alpha\beta} + u_\alpha\delta_{\gamma\beta} + u_\beta\delta_{\alpha\gamma}) \tag{9}$$

The value of τ is fixed at $\tau = 1$. Dirichlet boundary conditions were imposed by applying the well-known bounce-back boundary conditions: particles reaching a solid wall are simply reflected in the direction from which they came.

Fluid–fluid interactions are required when performing multiphase flow simulations. Several Lattice Boltzmann models for multiphase flow simulations have been proposed. These include the Gunstensen chromodynamic model (Gunstensen et al., 1991), the free energy-based approach for both liquid/vapor systems (Swift et al., 1995) and binary fluids (Swift et al., 1996), proposed by Swift et *al*, intermolecular interaction-based model of He et al. (1999), the Inamuro approach (Inamuro et al., 2004) and the Lee and Lin scheme (Lee and Lin, 2005). We chose the pseudo-potential approach (Shan and Chen, 1993)for the present work. A modified fluid velocity is computed in which fluid–fluid forces $\vec{F}_{FF}$ occur:

$$\rho\vec{u}' = \rho\vec{u} + \tau\vec{F}_{FF} \tag{10}$$

The modified velocity $\vec{u}'$, provided by Eq. (10), replaces $\vec{u}$ in Eqs. (7)–(9). The interaction forces are deduced from interactions taking place between neighboring particles:

$$\vec{F}_{FF}(\vec{r}) = \psi(\vec{r})\sum_i G_i^{FF}\psi(\vec{r} + \delta t\vec{c}_i) \tag{11}$$

The function $\psi = 1 - e^{-\rho}$ can be interpreted as an effective density. Parameter G_i^{FF} is an interaction parameter, the value of which depends on the direction, following:

$$G_i^{FF} = \begin{cases} 2G^{FF} & \|\vec{c}_i\| = 1 \\ G^{FF} & \|\vec{c}_i\| = \sqrt{2} \end{cases} \tag{12}$$

The scalar parameter G^{FF} must be adjusted to produce a liquid–vapor phase transition.

We implemented this model in a parallel code (FORTRAN and MPI routines) called *FlowPore* (Frank and Perré, 2010). We validated this tool by performing simulations in a cubic box to compute maximum and minimum values ρ_{min} and ρ_{max} of equilibrium ρ fields for various values of G^{FF}.

As can be seen in Fig. 5, our results match well-known results in the literature (Shan and Chen, 1993; Yuan and Schaefer, 2006). To ease the definition of the initial state in practical cases, we tuned the fitting expressions for ρ_{min} and ρ_{max} as a function of G^{FF}. These expressions were provided by equation:

$$\rho_{min/max} = \begin{cases} \rho_c & G^{FF} < G_c^{FF} \\ \rho_c + A(G^{FF} - G_c^{FF})^\alpha & G^{FF} \geqslant G_c^{FF} \end{cases} \tag{13}$$

The critical point is identified as $\rho_c = 0.708$ and $G_c^{FF} = 0.111$ and the parameters are $A = -1.2289$ and $\alpha = 0.234627$ for ρ_{min} and $A = 14.9537$ and $\alpha = 0.68383$ for ρ_{max}.

The value of surface tension σ was deduced from numerical experiments. The numerical setup was defined as follows: a drop was placed at the center of a cubic box, assuming periodic boundary conditions for each direction. Various drop diameters and values of G^{FF} were used. As indicated previously (Shan and Chen, 1993), the pressure difference across a liquid–vapor interface obeys the Laplace law. For a given value of G^{FF}, the value of σ is deduced from the slope of the linear fit of ΔP as a function of $\frac{1}{R}$, where R is the radius of the drop. We tuned following expression for σ as a function of G^{FF}:

$$\sigma = 3.059G^{FF} - 0.368 \tag{14}$$

In the same way, fluid–solid interactions are introduced when solid nodes are present, through a force term $\vec{F}_{FS}$ (Martys and Chen, 1996; Raiskinmäki et al., 2002) which leads to the final expression of the modified velocity:

$$\rho\vec{u}' = \rho\vec{u} + \tau(\vec{F}_{FF} + \vec{F}_{FS}) \tag{15}$$

Vector $\vec{F}_{FS}$ is expressed as:

$$\vec{F}_{FS}(\vec{r}) = \psi(\vec{r})\sum_i G_i^{FS}S(\vec{r} + \delta t\vec{c}_i) \tag{16}$$

The value of parameter $S(\vec{r})$ is 1 if the point $\vec{r}$ is within the solid phase, and 0 otherwise. The fluid–solid interaction parameter G_i^{FS} depends on the direction according to:

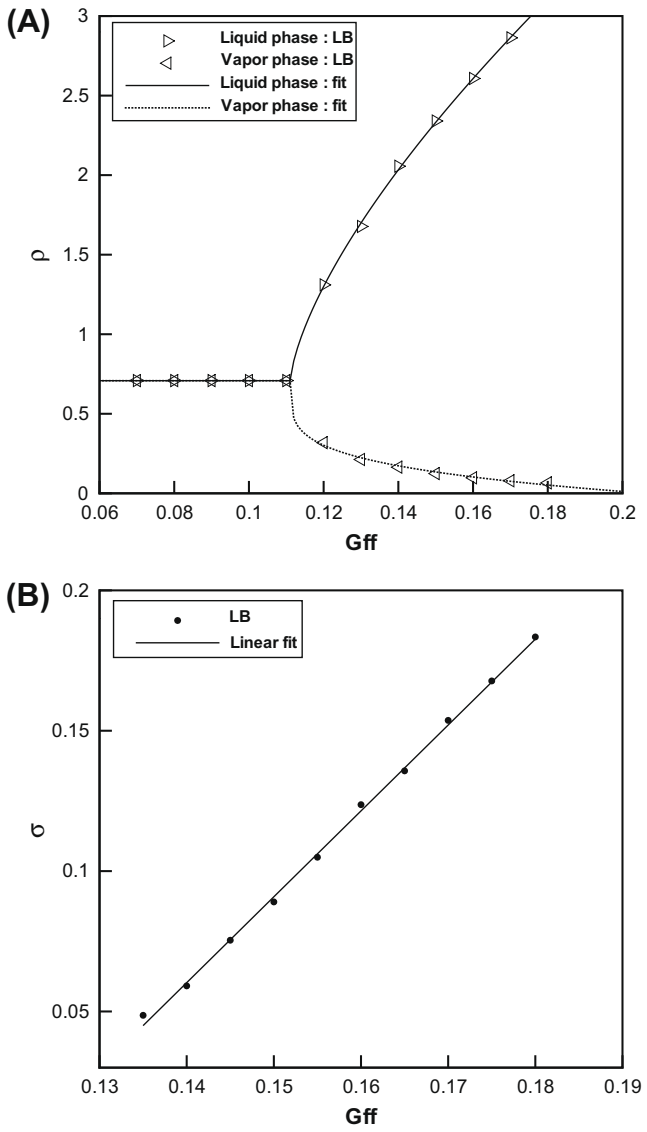

Fig. 5. A: Values of ρ_{min} and ρ_{max} for various values of G^{FF}. Points are from LB simulations and curves are from the expression (13). B: Values of surface tension σ as a function of G^{FF}. Points are from LB simulations and curves are from the expression (14).

$$G_i^{FS} = \begin{cases} 2G^{FS} & \|\vec{c}_i\| = 1 \\ G^{FS} & \|\vec{c}_i\| = \sqrt{2} \end{cases} \tag{17}$$

The value of the static contact angle at the solid–liquid–vapor contact line is dependent both on G^{FF} and G^{FS}, as it emerges from competition between the fluid–solid and fluid–fluid interactions. We estimated the value of the static contact angle by performing systematic 3D simulations for various (G^{FF}, G^{FS}) pairs (Fig. 6). As indicated in the Fig. 6 (inset), we defined a 3D box and placed two solid walls on opposite sides of $\vec{e_x}$ direction, assuming periodic boundary conditions in both other directions $\vec{e_y}$ and $\vec{e_z}$. A liquid layer is placed between two $y = cste$ planes, and the simulation is carried out until equilibrium is reached. The value of the contact angle can then be evaluated.

As can be seen in Fig. 6, a wide range of θ_c values is available. However, both G^{FS} and G^{FF} have to be tuned if a fixed value of θ_c is required.

Despite their extreme simplicity, pseudo-potential-based models have been successfully applied to numerous concrete cases, especially multiphase flow in porous media (Vogel et al., 2005; Sukop and Or, 2004; Sukop et al., 2008; Hatiboglu and Babadagli, 2008) and microfluidics (Yu et al., 2007; Sbragaglia et al., 2006). Such approaches can be easily and efficiently implemented, especially with a parallel computer (Pan et al., 2004). Thus the pseudo-potential Lattice Boltzmann approach seems, to date, to be the most convenient method for performing multiphase flow simulations in virtual wood samples.

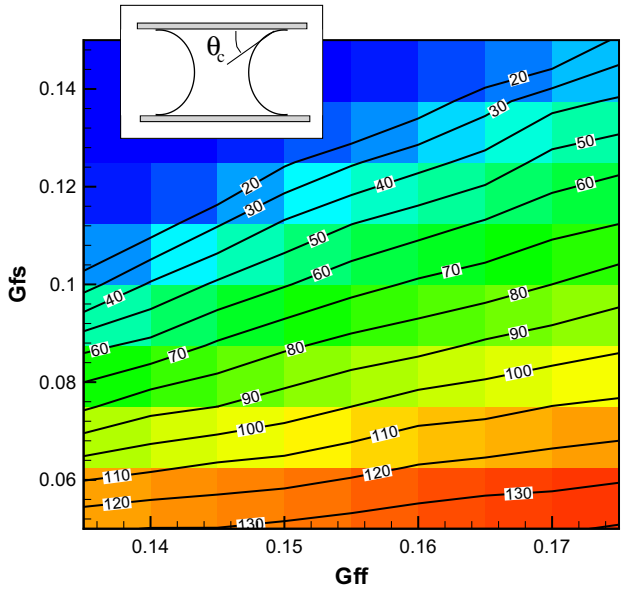

Fig. 6. Values of contact angle θ_c as a function of both G^{FF} (abscissa) and G^{FS} (ordinate).

4. Capillary invasion of a wood sample

4.1. Numerical setup

The purpose of the present work was to study the purely capillary invasion of a wood sample. It was therefore crucial to eliminate artificial effects on imbibition phenomena, especially within the liquid bath. We did this by following the method proposed by Chibbaro et al. (2009) to simulate an infinite liquid bath. We defined $\vec{e_z}$ as the imbibition direction, and n_z as the size, in $\vec{e_z}$ direction, of the grid which defined the sample anatomy. We assumed that $n_z' = 2n_z$ was the size of the effective simulation box in the $\vec{e_z}$ direction. The wood sample was placed between planes $z = n_z + 1$ and $z = n_z'$, and the nodes between planes $z = 1$ and $z = n_z$ were assumed to be fluid nodes. Periodic boundary conditions were assumed throughout. First, a liquid layer was placed in the simulation box without any solid node. This initial layer was placed between planes $z = 20$ and $z = n_z + 20$, the initial value of $\vec{u}$ was fixed at $\vec{u} = \vec{0}$, the initial values of f_i^{eq} were deduced from fields ρ and $\vec{u}$, and the initial values of f_i were set at f_i^{eq}.

At this point, the system is simulated through 20,000 iterations to ensure equilibrium. In a second step, the solid nodes are introduced, and the capillary imbibition starts and is computed until 250,000 iterations. The numerical setup is summarized in Fig. 7.

Both distances and time are expressed in lattice units, as grid step and time step are fixed to the unit. Therefore, in LB, the effect of time step cannot be analysed separately from the grid space. If the grid space is modified, a scaling in space and in time should be performed to compare the results. This point was checked on a simple configuration: we performed a simulation of capillary imbibition of an ideal bifurcation and two grid sizes ($n_x = 35$, $n_y = 35$ and $n_z = 350$ and $n_x = 50$, $n_y = 50$ and $n_z = 500$). From the

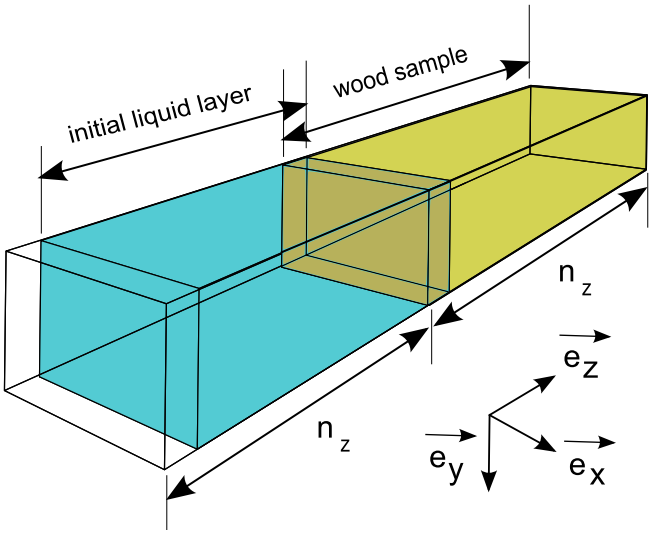

Fig. 7. Numerical setup for purely capillary imbibition of a porous medium.

computed results, we extracted rising curves in both sub-vessel 1 and sub-vessel 2 just in the same way. We observed the same behavior in the smaller grid and in the larger one. A curve crossing point at height z_c could be identified, and z_c/n_z has the same value in both cases. As a conclusion, we can say that results are grid-independent, provided the change in grid size is not sufficient to significantly change the grid Reynolds's number.

4.2. Results

Numerical experiments on capillary imbibition were carried out on the virtual birch sample anatomy described earlier (Fig. 4). The previously described simulation process was followed. We used the values $G^{FF} = 0.14$ and $G^{FS} = 0.08$ to impose a wetting solid phase. System dimensions were $n_x = 71$, $n_y = 133$, $n_z = 717$ and $n_{z'} = 1434$ which produces a numerical box with more than 6×10^6 lattices nodes. Using 64 processor cores of our Infiniband-based cluster, a typical run requires approximately 40 h to perform 250,000 iterations.

As can be seen in Fig. 8, the liquid/vapor interfaces exhibit menisci and, as expected, the liquid phase invades the vascular system, driven by wetting forces. Whereas imbibition within vessels 1–3 is a relatively common phenomenon as it occurs in channels close to cylindrical tubes, the case of vessel 4 is very interesting. When the liquid phase reaches the first bifurcation, the propagation interface is split into two menisci (Fig. 8:$t = 90{,}000$). After this step, the imbibition velocities within vessels 4a and 4b are different. Capillary invasion is slower in the larger vessel (4b) than in the narrower one (4a) (Fig. 8: $t = 140{,}000$). Then, when the liquid phase in vessel (4a) reaches the second bifurcation, its further propagation is stopped until vessel (4b) has been fully invaded. At this step, the 4a and 4b menisci coalesce and imbibition of the

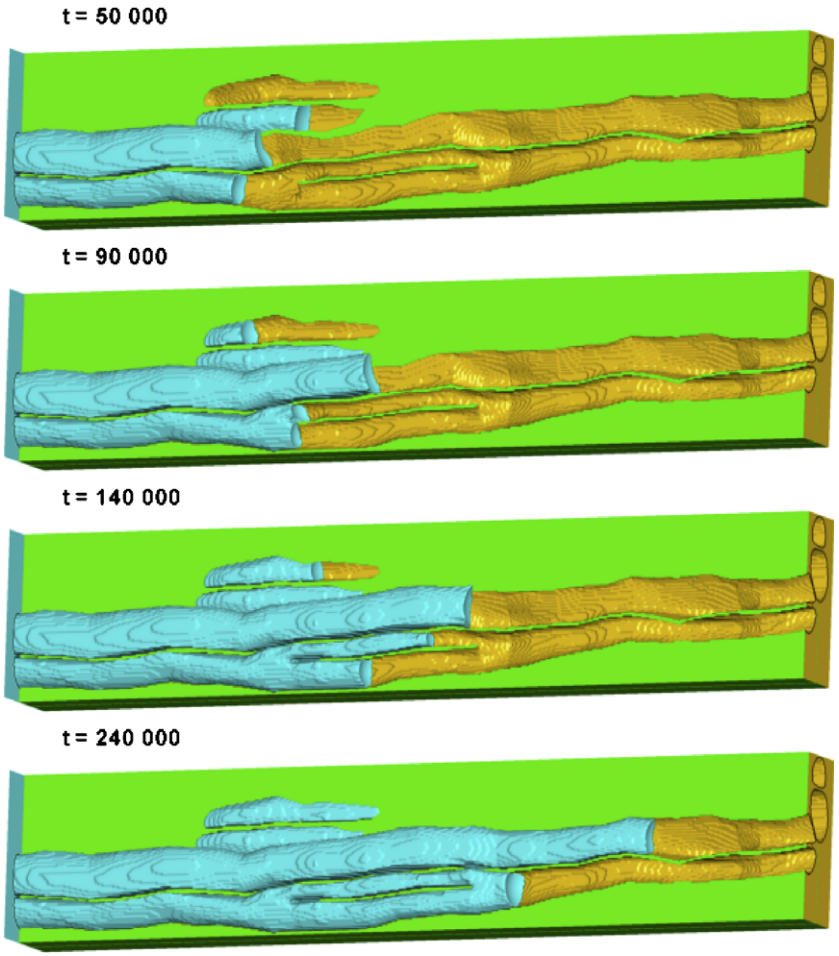

Fig. 8. Capillary invasion of the birch sample for different time values (lattice units). The dates were chosen to emphasize splitting of the meniscus in vessel 4 ($t = 90{,}000$) and coalescence of the resulting liquid columns ($t = 240{,}000$).

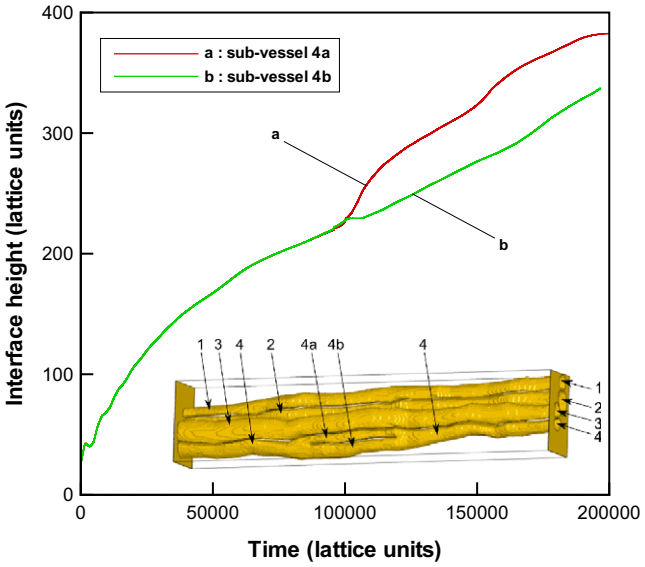

Fig. 9. Height of menisci in both 4a and 4b vessels as a function of time. A view of vascular anatomy (Fig. 4) is included.

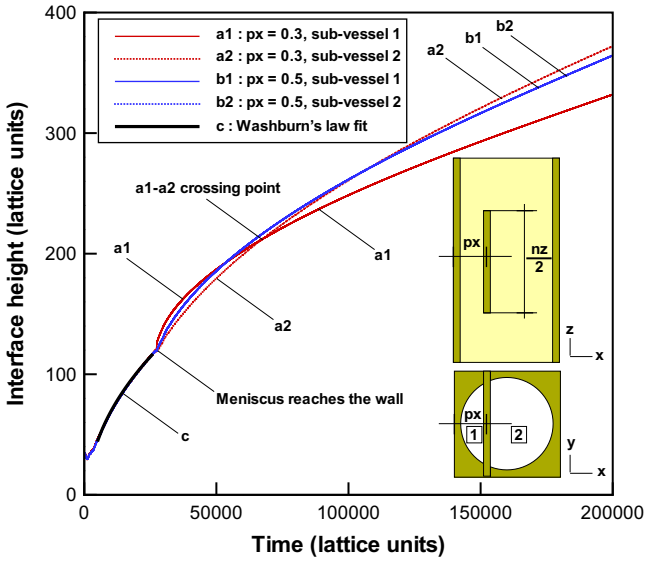

Fig. 10. Ideal bifurcation within a cylindrical tube: results.

upper part of vessel 4 can continue in the same way as in the other vessels (Fig. 8:$t = 240{,}000$). To confirm these phenomena, we tracked the liquid–vapor interface throughout the simulation:

The interface was traced inside both the $4 - 4a - 4$ vessel path and the $4 - 4b - 4$ vessel path. The density value ρ was extracted along a polyline defined by contour barycenters, as computed by *MeshPore* 3D, and the meniscus position was defined by curvilinear abscissa where the value $\rho = \frac{(\rho_L+\rho_V)}{2}$. As can be seen in Fig. 9, when the first bifurcation is reached, capillary invasion in the 4a sub-vessel becomes faster than in the 4b sub-vessel.

5. Discussion

It is well-known that, in the absence of gravity, capillary imbibition of a tube is dominated by a mechanism of competition between capillary forces and viscous forces (Chibbaro et al., 2009). In the simple case of a cylindrical tube, the assumption that inertia is negligible after a very short transitory period leads to Washburn's law (Washburn, 1921):

$$h^2 = \frac{\sigma d \cos\theta_c}{4\eta} t \tag{18}$$

where h is the height of the liquid phase inside the tube, d is the tube diameter, η is the viscosity of the fluid, and θ_c is the contact angle at the liquid/solid/gas triple line. Queries arise when the Eq. (18) is compared with the simulation results. According to Washburn's law, the speed of capillary invasion should increase with tube diameter. However, in our simulation, the behavior of the liquid phase after the bifurcation (Fig. 8) was in contradiction with this law.

We addressed this point by performing numerical experiments with an ideal bifurcation. We defined the solid phase as a cylindrical tube in which a flat longitudinal wall was inserted (Fig. 10: inset). The wall was inserted in a yz plane, the position of the wall was defined as p_x and the width was $n_x/10$. The fluid–fluid interaction parameters were fixed at $G^{FF} = 0.14$, and the wetting properties of the wall were exactly the same as for the tube, the interaction parameters being $G^{FS} = 0.08$ for each solid node. The same approach, as before, was applied to define the system dimensions and simulation procedure, (Fig. 7) and to set the following parameters at $n_x = 50$, $n_y = 50$, $n_z = 500$, and, as a consequence, $n'_z = 1000$. Two different cases were tested: case a:$p_x = n_x/3$ and case b:$p_x = n_x/2$. The height of the liquid–vapor interface within sub-vessels 1 and 2 was recorded and the computed results are shown in following figure:

The first stage of imbibition involves the classical capillary invasion of a cylindrical tube, and obeys Washburn's law (Fig. 10: curve c). All the curves are superimposed at this stage, as the tube diameter is the same for both numerical simulations. When the meniscus reaches the wall (Fig. 10: first annotation), the subsequent behavior depends on p_x. In the case of equal-sized sub-vessels ($p_x = n_x/2$), the curves of sub-vessel 1 and sub-vessel 2 remain superimposed until the last iteration (Fig. 10: curves $b1$ and $b2$) because the imbibition velocity is the same in both sub-vessels. It can be seen that imbibition briefly accelerates just after splitting of the meniscus. It is clear that new solid nodes increase the driving forces whereas narrower vessels increase viscous dissipation. Washbrun's law is a consequence of the competition between these contradictory effects. However, when the initial meniscus reaches the transverse wall, a transitory regime takes over, in which the meniscus (capillary forces) is of small hydraulic diameter while the flow (viscous forces) still occurs in a large diameter. The other test case ($p_x = n_x/3$) provides information about the influence of the relative widths of the sub-vessels. As can be seen on curves $a1$ and $a2$ in Fig. 10, the imbibition velocities are identical until the meniscus reaches the wall, but exhibit different patterns after this step. As explained previously, the acceleration is greater in the narrow sub-vessels than in the larger single vessel. During this transient stage, in the same way as in the real bifurcation within the virtual birch sample (Fig. 8: $t = 140{,}000$), Washbrun's law no longer holds. Later in the simulation, the height of sub-vessel 2 exceeds the height of sub-vessel 1 (Fig. 10: second annotation): the viscous forces and the capillary forces are again expressed in the same diameter, so that Washburn's law applies again.

These results provide a clear interpretation of the counter-intuitive evolution previously observed in the virtual birch sample. When the liquid phase reaches the first bifurcation of the 4th vessel, the velocity inside the 4th (a) sub-vessel increases strongly as the transitory regime takes place. However, the long-term behavior is not observed in this case, as the liquid column in the 4th (b) sub-vessel coalesces with the liquid column in the 4th (a) sub-vessel before this long-term behavior can occur. Consequently, only the transitory regime would be observed in our case of wood morphology.

6. Conclusion

In this paper, we have proposed a systematic approach for simulating multiphase flows in the vascular system of wood. Sample anatomy was determined from successive microtome sections and microscope images. The *Meshpore* software was applied to generate the contours of vessels in a vectorial way, suitable for 3D interpolation and lattice generation of any resolution. Intermediate slices were generated between real sections using an interpolation scheme to improve resolution in the longitudinal direction and 2D grids of points were deduced from the final set of slices. The resulting anatomy was a 3D cubic lattice, which provided solid boundaries for a Shan–Chen type Lattice Boltzmann scheme.

This framework was then used to simulate capillary invasion by means of a customized parallel numeric code, *FlowPore*. Special attention was given to phenomena occurring when a meniscus reached a bifurcation, i.e. where a vessel split into two sub-vessels. The observed imbibition in the narrower vessel was faster than in the larger one, and in contradiction with Washburn's law. Numerical experiments, involving an ideal bifurcation in a cylindrical tube, clearly proved that this behavior was transitory, and that it occurred near the bifurcation where the capillary forces and viscous forces were not expressed in the same hydraulic diameter.

In the future, this chain of tools could be applied to study the vascular system of different plants. For this purpose, micro-tomography is certainly a better solution than our tedious method to collect the 3-D morphology. The experimental validation is also a crucial concern. The challenge here is the ability of a 3-D imaging system to be fast enough to follow the water menisci during capillary invasion: NMR imaging or ultra-fast tomography are possible candidates.

Acknowledgements

The authors gratefully acknowledge the financial support of the CPER 2007–2013 "Structuration du Pole de Competitivite Fibres Grand Est" (Competitiveness Fibre Cluster), through local (Conseil General des Vosges), regional (Region Lorraine), national (DRRT and FNADT) and European (FEDER) funds.

References

Agoua, E., Zohoun, S., Perré, P., 2001. Utilisation d'une double enceinte pour déterminer la diffusivité massique du bois en régime transitoire: recours à la simulation numérique pour valider la méthode d'identification. Int. J. Heat Mass Transfer 44, 3731–3744.

Almeida, G., Leclerc, S., Perré, P., 2008. NMR imaging of fluid pathways during drainage of softwood in a pressure membrane chamber. Int. J. Multiphase Flow 34, 312–321.

Aumann, A., Ford, E.D., 2002. Parameterizing a model of douglas fir water flow using a tracheid-level model. J. Theor. Biol. 219, 431–462.

Chibbaro, S., Biferale, L., Diotallevi, F., Succi, S., 2009. Capillary filling for multicomponent fluid using the pseudo-potential lattice Boltzmann method. Proceedings for DSFD 2007. Eur. Phys. J. Special Topics 171, 223–228.

Comstock, G.L., 1970. Directional permeability of softwoods. Wood Fiber Sci. 1, 283–289.

De Sousa, F.S., Mangiavacch, N., Nonato, L.G., Castelo, A., Tomé, M.F., Ferreira, V.G., Cuminato, J.A., Mc Kee, S., 2004. A front-tracking/front-capturing method for the simulation of 3D multi-fluid flows with free surfaces. J. Comput. Phys. 198, 469–499.

Dullien, F., 1992. Porous Media: Fluid Transport and Pore Structure. Academic Press, San Diego.

Frank, X., Perré, P., 2010. The potential of meshless methods to address physical and mechanical phenomena involved during drying at the pore level. Drying Technol. J. 28, in press.

Gunstensen, A.K., Rothman, D.H., Zaleski, S., Zanetti, G., 1991. Lattice Boltzmann model of immiscible fluids. Phys. Rev. A 43, 4320–4327.

Hacke, U., Sperry, J., Pitterman, J., 2004. Analysis of circular bordered pit function – II. Gymnosperm tracheids with torus-margo pit membranes. Am. J. Botany 91, 386–400.

Hardy, J., de Pazzis, O., Pomeau, Y., 1976. Molecular dynamics of a lattice gas: transport properties and time correlation functions. Phys. Rev. A 13, 1949–1961.

Hatiboglu, C.U., Babadagli, T., 2008. Pore-scale studies of spontaneous imbibition into oil-saturated porous media. Phys. Rev. E 77, 066311.

He, X., Chen, S., Zhang, R., 1999. A lattice Boltzmann scheme for incompressible multiphase flow and its application in simulation of Rayleigh–Taylor instability. J. Comput. Phys. 152, 642–663.

Henrich, B., Cupelli, C., Moseler, M., Santer, M., 2007. An adhesive DPD wall model for dynamic wetting. Europhys. Lett. 80, 60004.

Inamuro, T., Ogata, T., Tajima, S., Konishi, N., 2004. A lattice Boltzmann method for incompressible two-phase flows with large density differences. J. Comput. Phys. 198, 628–644.

Kwon, G.H., Chae, S.W., Lee, K.J., 2003. Automatic generation of tetrahedral meshes from medical images. Comput. Struct. 81, 765–775.

Lee, T., Lin, C.L., 2005. A stable discretization of the lattice Boltzmann equation for simulation of incompressible two-phase flows at high density ratio. J. Comput. Phys. 206, 16–47.

Martys, N.S., Chen, H., 1996. Simulation of multicomponent fluids in complex three dimensional geometries by the lattice Boltzmann method. Phys. Rev. E 53, 743–750.

Pan, C., Prins, J.F., Miller, C.T., 2004. A high-performance lattice Boltzmann implementation to model flow in porous media. Comput. Phys. Commun. 158, 89–105.

Panshin, A., de Zeeuw, C., 1980. Textbook of Wood Technology: Structure, Identification, Properties and Uses of the Commercial Woods of the United States and Canada, forth ed. McGraw-Hill, New York.

Perré, P., Turner, I., 2001. Determination of the material property variations across the growth ring of softwood for use in a heterogeneous drying model. Part I: capillary pressure, tracheid model and absolute permeability. Holzforchung 55, 318–323.

Perré, P., Karimi, A., 2002. Fluid migration in two species of beech (Fagus silvatica and Fagus orientalis): a percolation model able to account for macroscopic measurements and anatomical observations. Maderas. Cienc. y tecnol. 4, 50–68.

Perré, P., 2005. MeshPore: a software able to apply image-based meshing techniques to anisotropic and heterogeneous porous media. Drying Technol. J. 23, 1993–2006.

Raiskinmäki, P., Shakib-Manesh, A., Jäsberg, A., Koponen, A., Merikoski, J., Timonen, J., 2002. Lattice-Boltzmann simulation of capillary rise dynamics. J. Stat. Phys. 107, 143–158.

Sbragaglia, M., Benzi, R., Biferale, L., Succi, S., Toschi, F., 2006. Surface roughness-hydrophobicity coupling in microchannel and nanochannel flows. Phys. Rev. Lett. 97, 204503.

Shan, X., Chen, H., 1993. Lattice Boltzmann model for simulating flows with multiple phases and components. Phys. Rev. E 47, 1815–1820.

Siau, J.F., 1984. Transport Processes in Wood. Springer-Verlag, Berlin.

Štěpánek, F., Rajniak, P., 2006. Droplet morphologies on particles with macroscopic surface roughness. Langmuir 22, 917–923.

Steppe, K., Cnudde, V., Girard, C., Lemeur, R., Cnudde, J., Jacobs, P., 2004. Use of X-ray computed microtomography for non-invasive determination of wood anatomical characteristics. J. Struct. Biol. 148, 11–21.

Succi, S., 2001. The Lattice Boltzmann Equation for Fluid Dynamics and Beyond. Clarendon Press, Oxford.

Sukop, M.C., Or, D., 2004. Lattice Boltzmann method for modeling liquid–vapor interface configurations in porous media. Water Resour. Res. 40, W01509.

Sukop, M.C., Huang, H., Lin, C.L., Deo, M.D., Oh, K., Miller, J.D., 2008. Distribution of multiphase fluids in porous media: comparison between lattice Boltzmann modeling and micro-X-ray tomography. Phys. Rev. E 77, 026710.

Swift, M.R., Osborn, W.R., Yeomans, J.M., 1995. Lattice Boltzmann simulation of nonideal fluid. Phys. Rev. Lett. 75, 830–833.

Swift, M.R., Orlandini, E., Osborn, W.R., Yeomans, J.M., 1996. Lattice Boltzmann simulations of liquid–gas and binary fluid systems. Phys. Rev. E 54, 5041–5052.

Tanguy, S., Berlemont, A., 2005. Application of a level set method for simulation of droplet collisions. Int. J. Multiphase Flow 31, 1015–1035.

Tartakovsky, A.M., Ward, A.L., Meakin, P., 2007. Pore-scale simulations of drainage of heterogeneous and anisotropic porous media. Phys. Fluids 19, 103301.

Trtik, P., Dual, J., Keunecke, D., Mannes, D., Niemz, P., Stähli, P., Groso, A., Stampanoni, M., 2007. 3D imaging of microstructure of spruce wood. J. Struct. Biol. 159, 45–55.

Tyszka, J.M., Fraser, S.E., Jacobs, R.E., 2005. Magnetic resonance microscopy: recent advances and applications. Current Opin. Biotech. 16, 93–99.

Valli, A., Koponen, A., Vesala, T., Timonen, J., 2002. Simulations of water flow through bordered pits of conifer xylem. J. Statist. Phys. 107, 121–142.

Vogel, H.J., Tölke, J., Schulz, V.P., Krafczyk, M., Roth, K., 2005. Comparison of a lattice-Boltzmann model, a full-morphology model, and a pore network model for determining capillary pressure–saturation relationships. Vadose Zone J. 4, 380–388.

Washburn, E.W., 1921. The dynamics of capillary flow. Phys. Rev. E 17, 273–283.

Yu, Z., Hemminger, O., Fan, L.S., 2007. Experiment and lattice Boltzmann simulation of two-phase gas–liquid flows in microchannels. Chem. Eng. Sci. 62, 7172–7183.

Yuan, P., Schaefer, L., 2006. A thermal lattice Boltzmann two-phase flow model and its application to heat transfer problems, part 1. Theoretical foundation. J. Fluids Eng. 128, 142–150.

Zimmermann, M.H., 1983. The Ascent of Sap in Trees. Springer-Verlag, Berlin.

I&EC research
Industrial & Engineering Chemistry Research

ARTICLE

pubs.acs.org/IECR

A Multiscale Approach for Modeling Bubbles Rising in Non-Newtonian Fluids

Xavier Frank,[†] Jean-Claude Charpentier,[†] Youguang Ma,[‡] Noël Midoux,[†] and Huai Z. Li[†,*]

[†]Laboratory of Reactions and Process Engineering, Nancy-University, CNRS 1 rue Grandville, BP 20451, 54001 Nancy Cedex, France

[‡]School of Chemical Engineering and Technology, State Key Laboratory of Chemical Engineering, Tianjin University, Tianjin 300072, P. R. China

ABSTRACT: The present work reports a multiscale approach to describe the dynamics of a chain of bubbles rising in non-Newtonian fluids. By means of the particle image velocimetry (PIV) and the lattice Boltzmann (LB) simulation, a deep understanding of the complex flow pattern around a single bubble is gained at microscale. The interactions and coalescences between bubbles rising in non-Newtonian fluids are experimentally investigated by the PIV measurements, birefringence, and rheological characterization for both an isolated bubble and a chain of bubbles formed from a submerged orifice. Two aspects are identified as central to interactions and coalescence: the stress creation by the passage of bubbles and their relaxation due to the fluid's memory. This competition between the creation and relaxation of stresses displays nonlinear complex dynamics. Along with the detailed knowledge around a single bubble, these fundamental mechanisms governing the bubbles' collective behavior in a train of bubbles at mesoscale leads to cognitive modeling on the basis of behavioral rules. By simulating bubbles as adaptive agents with the surrounding fluid via averaged residual stresses, model predictions for consecutive coalescence between a great number of bubbles compare very satisfactorily with the experimental investigation at macroscale.

1. INTRODUCTION

The bubble behaviors in non-Newtonian fluids play a key role in such diverse fields as decompression sickness, volcanic eruptions, glass manufacture, materials, metallurgy, and various chemical processes. In chemical engineering, typical examples of applications include wastewater treatment, handling and processing of fermentation broths, polymer devolatilisation, bubble column, mechanical stirrer with multiphase, enhanced oil and gas recovery, composites processing, plastic foam processing, etc. Naturally, the rates of heat and mass transfer processes and chemical or biological reactions are essentially governed by the collective behavior of numerous bubbles issued from a multihole distributor: flow field around a bubble, interactions and coalescence between bubbles, bubble size distribution in a column, etc. Also, there is a strong motivation from a theoretical standpoint toward developing a better understanding of the detailed influence of the fluid's rheology on the bubble flow patterns.

In comparison to the state-of-the-art of bubbles in Newtonian fluids,[1] much less is known about the bubble behaviors in non-Newtonian fluids.[2,3] Because of the inherent complex nature of bubble phenomena, a complete theoretical analysis is still impossible at present. An adequate understanding of the bubble hydrodynamics in such media is a prerequisite to studying other transport phenomena like heat and mass transfer with or without chemical reactions. Bubble behaviors can be subdivided into distinct processes: bubble formation from submerged orifices, interaction, and coalescence during the ascent. A somewhat simplified starting point has been the study of bubbles formed from a single submerged orifice. The first major work was reported by Astarita and Apuzzo[4] on the motion of single bubbles. The investigation in this field has been followed by numerous authors, for example, refs 5−9. The results available in the literature provid essentially experimental information on the rise velocity of a single bubble or on the global hydrodynamics and mixing in a bubble column. In particular, a more detailed review on the effects of the fluid's viscoelasticity on bubble shape and velocity can be found in the recent book of Chhabra.[5] Very few investigations on the interactions as well as coalescence between bubbles in such media have so far been reported in the literature.[10,11]

A common feature of the aforementioned phenomena is the existence of a wide range of spatial and temporal scales at which different physical mechanisms happen. Furthermore, these mechanisms of different scales usually interact each other in a nonlinear way to lead to a huge variety of phenomena that underlines the complexity of the subject. Thus, as for the so proposed "the molecular Processes−product−process Engineering (3PE) approach"[12] to describe multidisciplinary nonlinear and nonequilibrium phenomena occurring on different length and time scales in chemical engineering (Figure 1), the bubble behaviors in non-Newtonian fluids could be dealt with an integrated system approach of multiscale modeling. The main idea is to understand how physical, chemical, and interfacial phenomena at a fine scale relate to properties and behavior at a coarser scale, e.g., organizing levels of complexity.[13,14]

In this paper, we highlight a philosophical approach to model bubble behaviors in non-Newtonian fluids at different spatial and temporal scales: detailed information around a single bubble at

Special Issue: Nigam Issue

Received: April 1, 2011
Accepted: July 12, 2011
Revised: July 8, 2011
Published: July 12, 2011

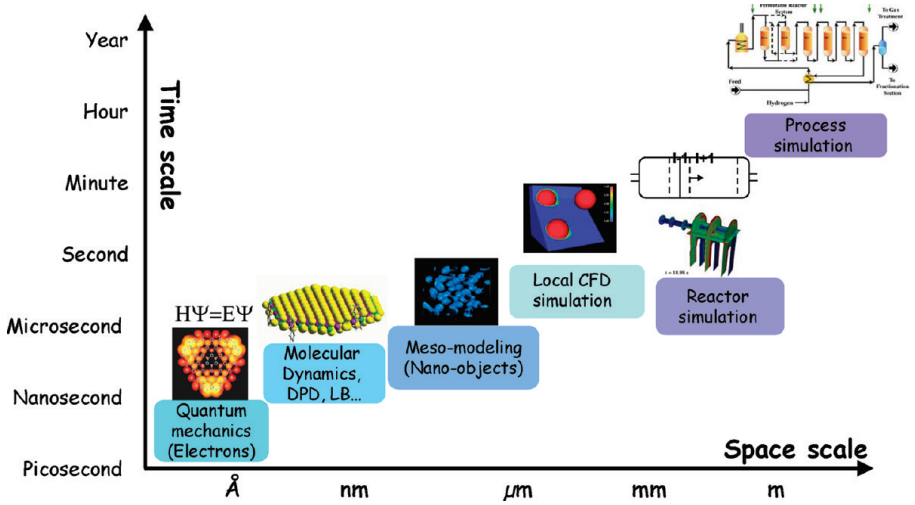

Figure 1. Illustrative view of a modern multiscale spatiotemporal approach in chemical engineering.

microscale by both the fine experiments and numerical simulation; at mesoscale, interactions, and coalescence laws issued from the detailed knowledge around a single bubble; and some illustrative prediction results of macroscopic properties such as the bubble size distribution and comparison with the relative experiments at macroscale. According to the logical order, this paper begins with the study of flow fields around a single bubble followed by the in-line interactions and coalescence between bubbles whose results are essential to global properties in such complex media.

2. EXPERIMENTAL SECTION

In the present study, the experimental setup consists mainly of Plexiglas cylindrical tanks surrounded by a square duct. The role of the square duct is to eliminate optical distortions for visualization as well as to control the liquid temperature inside the cylindrical tank. The diameters of the tanks ranges from 0.20 to 0.30 m, and their height varies from 0.30 to 1.50 m. Air and nitrogen bubble generation is through an orifice of varying diameters ($1-5 \times 10^{-3}$ m) submerged in the liquid in the center of the bottom section of the tanks. An electronic valve of rapid response controlled by a computer permits injection of bubbles of determined volume with the desired injection period T (spatial distance between bubbles). Otherwise, it is possible to inject bubbles under a continuous gas flow rate without the possibility to control the injection period between bubbles. The bubble rise velocity and the frequency of formation or passage are measured by laser probes at different heights. All experiments were carried out at constant temperature. The non-Newtonian fluids used in this work are different concentrations of polyacrylamide (PAAm) and of carboxymethylcellulose (CMC) in water or in water/glycerol mixtures. A rheometrics fluid spectrometer RFS II and an AR 2000 rheometer (TA Instruments) are employed to measure the rheological properties. These fluids behave as shear-thinning fluids and can be fitted for the whole range of the shear rates tested ($\dot{\gamma}$ = 0.01 to 1000 s^{-1}) by the Carreau model

$$\frac{\eta - \eta_\infty}{\eta_0 - \eta_\infty} = [1 + (\lambda\dot{\gamma})^2]^{(n-1)/2} \quad (1)$$

For example, 0.50% PAAm has the following data: η_0 = 38 Pa s, η_∞ = 0.005 Pa s, λ = 45.6 s, and n = 0.29.

Table 1. Rheological Characterization of the 6th Order Maxwell Model for 0.50% PAAm Solution

k	1	2	3	4	5	6
λ_k (s)	0.1	0.5	1	5	10	50
G_k (Pa)	2.81	0.72	1.51	0.66	0.47	0.37

Stress relaxation measurements show that at the same shear rate, the relaxation time ranges from 1 s for diluted CMC solutions to 30 s for concentrated PAAm solutions. Therefore, PAAm solutions may be considered as much more elastic than CMC solutions. To describe the viscoelastic properties of this fluid, a sixth order Maxwell model is developed on the base of rheological measurements

$$G(t) = \sum_{k=1}^{6} G_k \exp\left(-\frac{t}{\lambda_k}\right) \quad (2)$$

A typical example of the measured rheological values is given in Table 1 for the representative fluid of 0.50% PAAm.

Instantaneous velocity fields around a bubble are measured by means of a particle image velocimetry technique (PIV, Dantec Dynamics, Denmark) (Figure 2). Illumination sheets are generated with two pulsed Nd:YAG LASERS (SOLO-I-15 PIV New Wave Research, USA) arranged side-by-side and cross the vertical symmetry axis of the dispersed phase. The energy produced by this source is 2 mJ × 15 mJ. These lasers emit green light with a wavelength of 532 nm for a duration of 8−10 ns. The time between the flashes varies from less than one microsecond to a few milliseconds. The Nd:YAG lasers are also designed to ensure a sequence of illuminations at a frequency of 15 Hz. The laser beams first cross a cylindrical lens, which gave a laser sheet of strong light intensity and small thickness (2 mm maximum). They are focused and superimposed on one zone of measurement. The fluids are inseminated with fluorescent polymer beads (rhodamine B) of 50 μm as seeding particles. An orange filter placed in front of the camera eliminates the reflections of the lasers on the bubbles and lets only the fluorescent light of the particles pass. The size is determined to minimize both Brownian movement and seeding particle sedimentation. The camera, placed perpendicular to the laser sheets, takes two successive

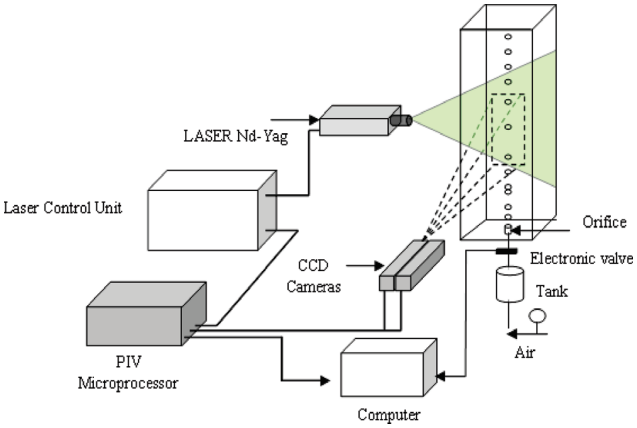

Figure 2. Experimental setup with the PIV and lightning devices.

images at the maximum intensity of the laser pulse. These images are divided into a few thousand small interrogation areas of 16 pixels × 16 pixels. A cross correlation is then performed between the corresponding interrogation areas. When the flow is correctly inseminated, the measurement errors on the velocities are less than 5%. The visualization is carried out by two high-speed digital cameras (VNR 950, Sysma Industrie, France; CamRecord600, Optronis GMBH, Germany) at a rate ranging from 100 to 5000 fps. The light is provided by a halogen light of 800 W, which enlightens the columns via indirect lighting on a white screen behind the bubble column.

3. MULTISCALE APPROACH AND RESULTS

3.1. Flow around a Single Bubble: A Microscopic Description. Direct simulation of flow around a bubble remains a challenging problem for computational fluid dynamics (CFD). The need to explicitly model the dynamics of the interface between different phases and the associated problems of adjusting the computational grid used to compute the flow within each phase present tremendous challenges for conventional fluid simulation approaches. The lattice Boltzmann method is a powerful technique for the computational modeling of a wide variety of complex fluid flow problems.[15] It is a discrete computational method based upon the Boltzmann equation. It considers a typical volume element of fluid to be composed of a collection of particles that are represented by a particle velocity distribution function for each fluid component at each grid point. The time is counted in discrete time steps, and the fluid particles can collide with each other as they move. The rules governing the collisions are designed such that the time-average motion of the particles is consistent with the Navier−Stokes equation.

Within the lattice Boltzmann (LB) framework, the fluid is described at the molecular level in a statistical way. Molecules are forced to move on a lattice that is a discretization of the phase space. We used here the so-called D2Q9 lattice, a bidimensional lattice, on which particles' velocity can have only nine values, including zero. Evolution of the system with the discrete time t consists in a streaming stage, where molecules move from their node and reach a neighboring node, and a collision stage, where molecules collide and velocities are consecutively modified. Molecules are not implemented directly but described in a statistical way by means of the particle probability distribution functions (PPDF)f_i, where $f_i(\vec{r},t)$ is the number of molecules having the velocity $\vec{c}_i$ at the point $\vec{r}$ and time t. Useful quantities are deduced from PPDF and molecules' velocities

$$\rho = \sum_i f_i \tag{3}$$

$$\rho\,\vec{u} = \sum_i f_i\,\vec{c}_i \tag{4}$$

The time evolution of PPDF obeys the LBGK (Lattice Bhatnagar−Gross−Krook) equation that is nothing but a simplification of the general lattice Boltzmann equation

$$f_i(\vec{r} + \delta t\,\vec{c}_i, t + \delta t) - f_i(\vec{r}, t) = -\frac{1}{\tau_r}(f_i - f_i^{eq}) + \frac{\vec{a}(\vec{c}_i - \vec{u})}{{c_s}^2} f_i^{eq}\delta t \tag{5}$$

Distributions f_i^{eq} are equilibrium polynomial expression and computed with the following conserved quantities

$$\sum_i f_i^{eq} = \rho$$

$$\sum_i f_i^{eq}\,\vec{c}_i = \rho\,\vec{u} \tag{6}$$

$$\sum_i f_i^{eq} c_{i\alpha} c_{i\beta} = \rho u_\alpha u_\beta + P_{\alpha,\beta} - \Gamma_{\alpha,\beta}$$

where $P_{\alpha,\beta}$ is the pressure tensor deduced from a free energy scheme[16−18] and $\Gamma_{\alpha,\beta}$ the viscoelastic stress tensor.

It is worth noting that the viscoelastic stress tensor $\Gamma_{\alpha,\beta}$ is computed with the help of a modified sixth order Maxwell model

$$\Gamma_{\alpha,\beta} = \sum_{k=1}^{6} \Gamma_{\alpha,\beta}^k$$

$$\frac{\partial \Gamma_{\alpha,\beta}^k}{\partial t} = G_k D_{\alpha,\beta} - \frac{1}{\lambda_k'}\Gamma_{\alpha,\beta}^k \tag{7}$$

$$D_{\alpha,\beta} = \partial_\alpha u_\beta + \partial_\beta u_\alpha$$

In order to take the shear thinning into account, λ_k' is modified relaxation time stemming from λ_k

$$\lambda_k' = \frac{\eta(\phi)}{\sum_{k'=1}^{6} \lambda_{k'} G_{k'}} \tag{8}$$

where the viscosity $\eta(\phi)$ is deduced from the Carreau model with the help of a phenomenological quantity $\phi(\vec{r},t)$ to describe its temporary evolution

$$\frac{\eta(\phi) - \eta_\infty}{\eta_0 - \eta_\infty} = [1 + (\lambda\phi)^2]^{(n-1)/2}$$

$$\frac{\partial \phi}{\partial t} = -\frac{\phi - \sqrt{|I_D^{(2)}|}}{t_r} \tag{9}$$

$$t_r = \frac{t_{r0}}{1 + \frac{\phi}{\phi_0}}$$

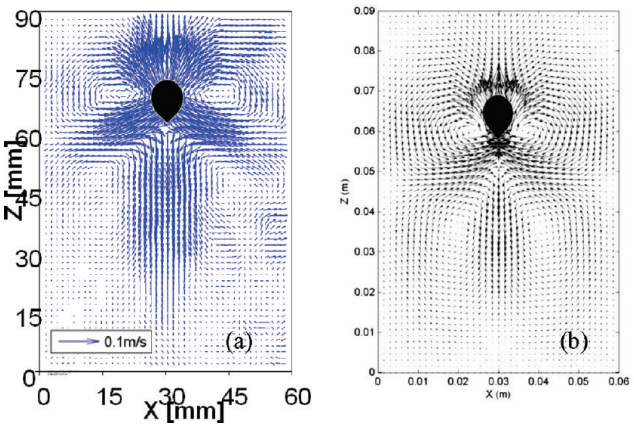

Figure 3. Flow field around a rising bubble of 190 × 10^{-9} m^3 in 1% (wt) PAAm solution: (a) experimental measurements by the PIV device and (b) LB simulation with computed bubble shape.

where $I_D^{(2)}$ is the second invariant of the tensor $D_{\alpha,\beta}$, and the reference values used in the present simulation are respectively t_{r0} = 12s, ϕ_0 = 0.5 s^{-1}.

This rheological approach was dynamically validated through successive relaxation experiments.[17,18]

To perform bubbly flow simulations at microscale, a gas−liquid model is required. The free energy-based model seems suitable to simulate bubbles in both Newtonian and non-Newtonian fluids.[16,17] To describe both hydrodynamics and multiphase patterns in binary fluids, two densities, ρ_A and ρ_B, are necessary with a total density $\rho = \rho_A + \rho_B$ and a density difference $\Delta\rho = \rho_A - \rho_B$. As ρ and $\vec{u}$ are implemented through PPDF f_i as in single phase flows, the density difference $\Delta\rho$ is computed from g_i, another PPDF function obeying a LBGK equation too

$$g_i(\vec{r} + \delta t\,\vec{c}_i, t + \delta t) - g_i(\vec{r}, t) = -\frac{1}{\tau_r}(g_i - g_i^{eq}) \quad (10)$$

Equilibrium distribution functions g_i^{eq} are then deduced to conserve the following quantities

$$\sum_i g_i^{qe} = \Delta\rho$$

$$\sum_i g_i^{eq}\,\vec{c}_i = \Delta\rho\,\vec{u} \quad (11)$$

$$\sum_i g_i^{eq} c_{i\alpha} c_{i\beta} = \Delta\rho u_\alpha u_\beta + \Delta\mu\delta_{\alpha,\beta}$$

The chemical potential difference $\Delta\mu$ is deduced from a free energy scheme.[16−18] The non-Newtonian properties, including viscoelastic ones, of the fluids were implemented in the LB scheme on the basis of a modified sixth order Maxwell fluid coupled to shear-thinning effects.

The flow fields around an individual bubble in these solutions have very peculiar features. The flow in front of the bubble is very similar to that in the Newtonian case. In the central wake, the movement of the fluid is surprisingly downward. Finally, a hollow cone of upward flow surrounds this negative wake. This conical upward flow zone begins on the sides of the bubble and is largely extended backward (Figure 3). The real typical shape of the bubble is also added in Figure 3 to locate the position of the bubble. Obviously, the bubble's shape in the non-Newtonian fluids differs much from that in Newtonian case. Small bubbles

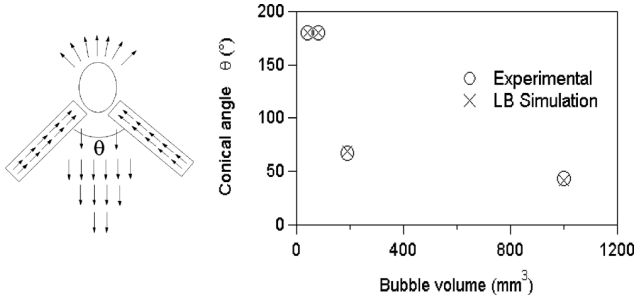

Figure 4. Schematic representation of the flow field around a bubble rising in viscoelastic fluids and variation of the conical angle with the bubble volume in 0.50% (wt) PAAm: experiments vs LB simulation.

are elongated vertically and have a teardrop shape. With a further increase in volume, bubbles take the flattened shape, however, with always a tail behind the bubble. In the past, the negative wake was initially investigated by both qualitative visualization[19] and the use of LDA[3,20] at a point in a non-Newtonian fluid; however, our results show clearly the global shape of the negative wake, in particular the conical upward flow zone around the negative wake. It is worth noting that the conical open angle θ decreases with the bubble's volume and tends to an asymptotic value in these fluids (Figure 4). These detailed flow patterns were extensively investigated by the PIV device in our group in function of the fluids' viscoelesticity.[21,22] The spatial distribution of stresses around a bubble between the conical ascension and the central negative wake was also quantified by the birefringence method. The fluid's viscoelasticity was identified as responsible for the origin of the negative wake.[23]

Figures 3 and 4 show the main features computed by the LB approach around a single bubble. The theoretical flow field exhibits effectively the negative wake, a conical positive flow around the negative wake with an open angle too. The comparison with the experimental measurements is quite satisfactory, including the bubble shape. The main advantage of the LB approach with respect to a direct numerical scheme is the possibility to explore very elastic fluids through the above-mentioned viscoelastic tensor. Moreover, the shape evolution of the bubble could also be computed as a direct consequence within the framework of a two-component and binary LB scheme.

Clearly, both the high resolution of about 50 μm of the PIV device and the microscopic equations used in the LB approach provide a solid foundation for understanding the various physical phenomena at microscale around a single bubble in non-Newtonian fluids.

3.2. In-Line Interactions and Coalescence between Bubbles: Mesoscopic Modeling. *3.2.1. In-Line Interactions between Bubbles: A Linear Competing Mechanism of Stresses.* With the help of the electronic valve controlled by the PC, it is possible to modulate the injection period T between two consecutive bubbles instead of the continuous injection of a gas flow rate. The evidence for in-line interactions between bubbles is clearly brought up in this work: the rise velocity decreases with the increase in the injection period T for a given bubble volume (Figure 5). A sufficiently long injection period is necessary to prevent the interactions between bubbles. When the injection period became short enough (<1 s), coalescence occurs. In particular, a significant factor differentiating bubble−bubble interactions in non-Newtonian fluids from that in water is the long field of action. So, we have the idea to simulate the passage of bubbles by imposing

dx.doi.org/10.1021/ie2006577 |Ind. Eng. Chem. Res. 2012, 51, 2084–2093

consecutive shear rates (pulses) to a fluid sample by means of the rheometer RFS II that measures the response of the sample in terms of shear stress. We call this original approach rheological simulation[24] that is performed in these fluids in the cone-and-plate geometry of the rheometer, taking especially into account the experimental values of rise velocity and injection period. There is a gradual accumulation of residual stresses tending asymptotically toward a stationary value. The magnitude of these residual stresses could be considered as both strongly dependent upon the injection period and proportional to the elasticity of the fluid.

To provide new evidence of the residual stresses after the passage of bubbles in non-Newtonian fluids, birefringence measurements are also carried out with a chain of bubbles rising in these fluids. In panel (a) of Figure 6, a typical example of the spatial stress distribution around two bubbles in 1% PAAm is presented. White zones illustrate the existence of axisymmetric stresses, in front of the bubble due to the fluid compression and especially behind the bubble because of the residual stresses, while black zones owing to the extinction of the polarized light characterize the absence or small magnitude of stress. It is clear that the trailing bubble can enter in the large field of residual stresses behind the leading one and provoke either interactions through pure acceleration of rise velocity or coalescence for closer intervals between bubbles. This illustrates visually the mechanism of in-line bubble interactions and coalescence.

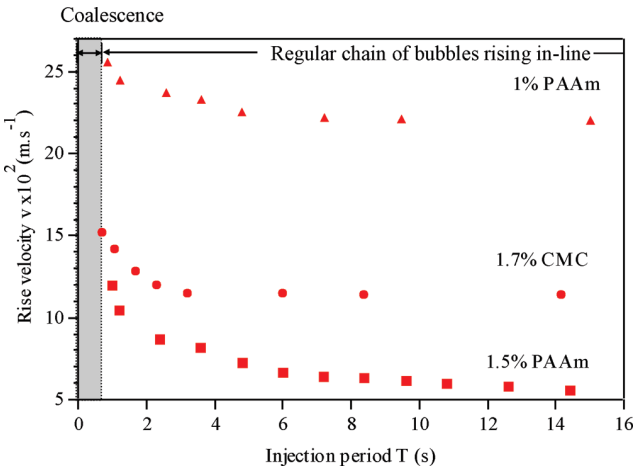

Figure 5. Linear in-line interactions between bubbles: decrease of the rise velocity with the injection period before reaching an asymptote after a characteristic period depending upon the fluid and bubble volume. Orifice diameter $d_0 = 2 \times 10^{-3}$ m, bubble volume $V_B = 1.37 \times 10^{-6}$ m^3.

Even if the flow field exhibits a negative wake behind a leading bubble as shown in panel (b) of Figure 6 by the PIV or panel (c) of Figure 6 by the LB simulation, the rise velocity increases for the whole train of bubbles as well. This flow configuration is totally different from that in Newtonian fluids. The wake hypothesis cannot explain the acceleration of bubbles because it tends to suggest that bubbles will decelerate. These results suggest clearly that another mechanism should be discovered for interactions in non-Newtonian fluids. In light of above findings, the following scenario can be proposed: after the passage of a leading bubble, the memory effect of the fluid holds the shear-thinning process during a certain time so that the local viscosity decreases and induces the acceleration of the rise velocity of the trailing bubble. Unambiguously, the mechanism governing the in-line bubble interactions is a dynamical competition between the creation and relaxation of stresses[25]

$$\frac{d\tau}{dt} + \alpha\tau = \beta\dot{\gamma} \qquad (12)$$

For example, typical values are $\alpha = 1$ s^{-1} and $\beta = 10$ Pa for 0.50% PAAM solution.

This memory effect of the residual stresses of preceding bubbles on the rise velocity of a bubble train is successfully modeled by means of the linear superposition principle to compute the acceleration of the rise velocity of a regular bubble train due to the temporary decrease of a local viscosity (Figure 7).

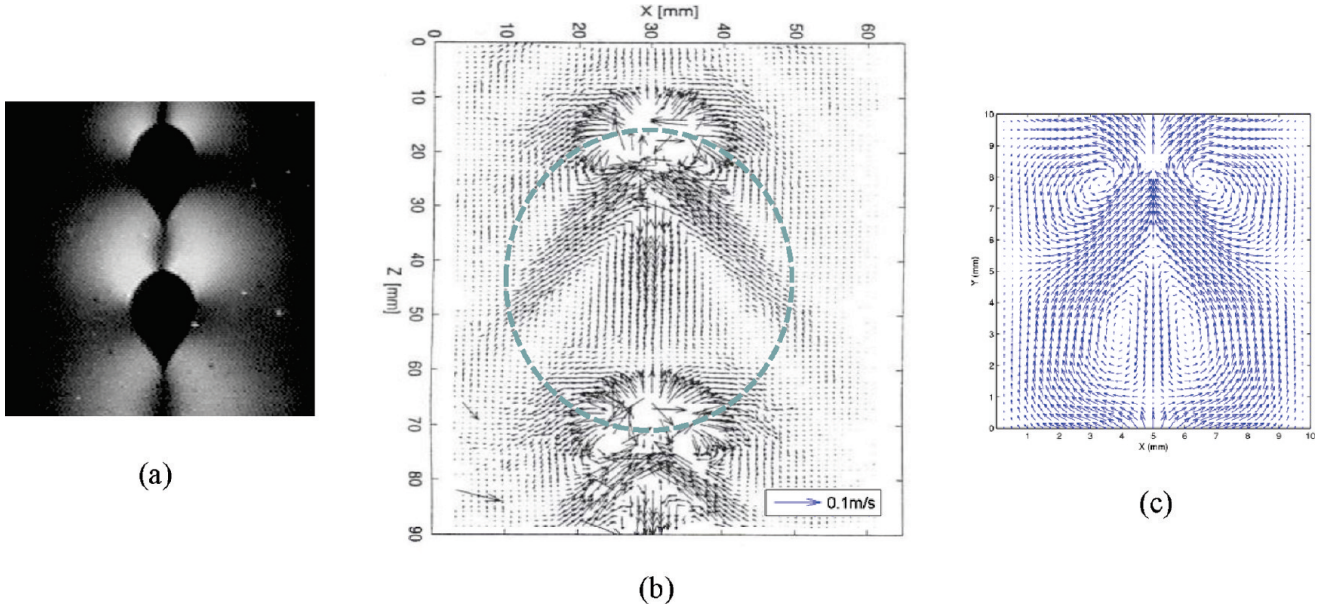

Figure 6. In-line interactions between a train of bubbles rising in 1% (wt) PAAm solutions: (a) birefringence visualization, (b) flow field measured by the PIV, and (c) LB simulation.

3.2.2. Nonlinear and Chaotic Coalescence between Bubbles: Cognitive Modeling. Above a threshold that depends on the nature of each fluid, especially the viscoelasticity, the interactions are no longer linear as the coalescence occurs (Figure 8): a regular bubble chain is broken up. The regularity of the bubble formation at the orifice[26] and the dynamical competition between the creation and relaxation of stresses lead naturally to the theory of chaos. In order to understand the coalescence nature, the time delay embedding method of reconstructing the phase−space diagram was applied to time series data (bubble passage) recorded at different heights in the bubble column. The calculation of several parameters, the largest Lyapunov exponent, the correlation dimension, the power spectrum and the phase portraits, indicates that the coalescence between bubbles is chaotic.[27,28] Experimentally, the chaos' appearance can also be described by the period-doubling sequences. It is worth noting that the variation of the correlation dimension with the embedding dimension shows that the chaos is deterministic with a limited number of degrees of freedom. As shown in Section 3.3, this is also confirmed by the macroscopic evolution of the bubble number at different heights in the column. In fact, the bubble number normalized by the total number of bubbles generated at the orifice for a fixed duration (typically about 3000 bubbles) levels off a plateau before falling due to the consecutive coalescence. The plateau corresponding to the constant bubble number in the inertial rise stage increases inversely with the fluid viscosity. The decrease in the bubble number in the higher column section is bounded by an asymptotic value due to the limited capacity of bubble generation at the orifice. This shows explicitly that the complexity of the in-line bubble coalescence in non-Newtonian fluids cannot degenerate into an arbitrary nature. Intuitively, the collective behaviors of bubbles in such media obey underlying fundamental laws.

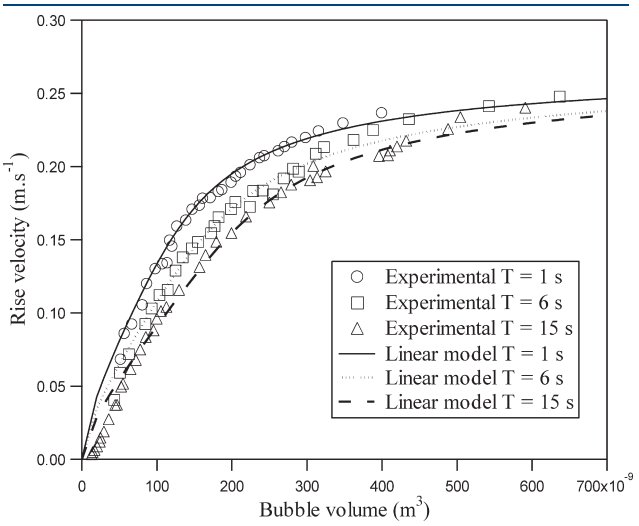

Figure 7. Comparison of the rise velocity of a bubble train between the theoretical linear modeling and experimental data in 0.5% PAAm with three injection periods.

Certainly, the LB simulation could be applied to simulate the complex interactions between bubbles as shown in panel (c) of Figure 6. However, it is worth noting that the LB is very CPU memory and time-consuming for the computation. Recently, some physicists and biologists[29,30] are trying to explore a new way to describe the complex evolving systems such as an anthill, a central nervous system, or ecosystems. Even though these complex systems differ in detail, the question of coherence under change is the central enigma for each. General principles usually rule the behavior of these *complex adaptive systems* (CAS), principles that point to ways of solving the attendant problems. The task of formulating theory for these systems is more than difficult as the collective behavior of such a system is not a simple juxtaposition of the behaviors of its parts. The main quest is to extract these general principles and to shape them into building blocks for a new scientific approach.

If we want to understand the interactions of large numbers of agents, we must be able to describe the capabilities of individual agents. It is quite logic to suppose that an agent's behavior is determined by some elementary rules. Stimulus−response rules are typical and simple: IF stimulus *S* occurs, THEN response *R* is given. In an anthill, the stimuli could be pheromones deposed by other ants in search of food; the response could be the moving direction according to the magnitude of pheromones. The collective behavior of the whole anthill would privilege the shortest way to go to the food source with progressive increase on the pheromones' intensity as each ant passing through this way would drop new pheromones. Therefore, we can establish qualitatively an ethnological analogy between bubbles and ants. They interact both between them through the interactions with their environment: pheromones for ants and residual stresses in fluid for bubbles (Figure 9). To some extent, there is a connection between an ant and a bubble as an individual agent as well as between the concentration of pheromones and the magnitude of stresses. This is experimentally confirmed by the injection of a sheared fluid through a syringe voluntarily displaced from the rise axe of the train of bubbles: because of the reduced viscosity in the sheared fluid, a rising bubble takes a bend to enter in the zone of reduced viscosity. The residual stresses left by this bubble guide the passage of trailing bubbles owing to the minimized drag, and the modified rise axe can be self-maintained as well as

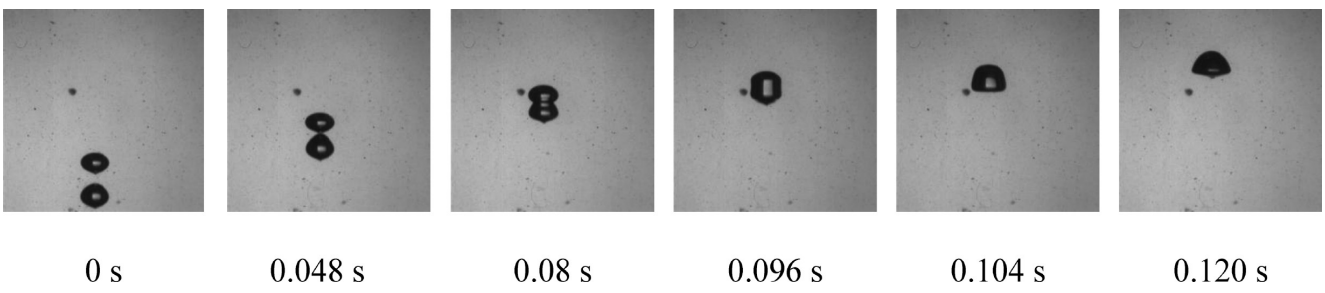

Figure 8. Coalescence between in-line rising bubbles.

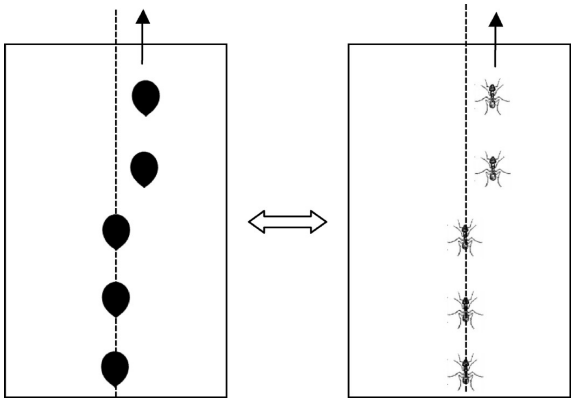

Figure 9. Communication similarity between agents: bubbles rising in non-Newtonian fluids through residual stresses (reduced drag) and an anthill through pheromones.

the displacement is not too large with respect to the initial vertical axe.

Our immediate objective is to find a simple syntax for IF/THEN rules that depend critically on the way an agent (a bubble) interacts with its environment (fluid) and other agents (bubbles). Starting from the knowledge of the interactions and coalescence between bubbles, we adopt the following strategy as the cognitive approach that specifies the bubble's capacities at a fixed point in fluid in time. The three basic elements of this approach are a set of detectors, a set of IF/THEN rules, and a set of effectors. The detectors represent the bubble's capacities for extracting information from its environment (residual stresses in fluid, presence of other bubbles). The IF/THEN rules describes its capacities for processing that information (accelerating or not the rise velocity, coalescence or not). The effectors are its ability to act on the environment (leaving its own residual stresses according to its size).

The total fluid height is divided into 20000 cells in which the stresses are continuously computed according to the passage of consecutive bubbles. Each cellule represents a height of 75 μm and is supposed to display homogeneous stresses whose evolution is estimated by the dynamical competition between the creation (passage of bubbles) and relaxation of stresses (memory effects) of the first order (eq 12).

As a first approximation, the bubble is considered as spherical with an equivalent diameter d_{eq}. With an added mass, the motion equation of a bubble is described by a classical balance of different forces: inertial, buoyancy, and drag

$$\left(\rho_G + \frac{11}{16}\rho_L\right)V_B\frac{dU}{dt} \approx \frac{11}{16}\rho_L V_B\frac{dU}{dt} = F_b - F_t \qquad (13)$$

where the buoyancy force is $F_b = (\rho_L - \rho_G)V_B g$, and the drag force is $F_t = (1/2)AC_D\rho_L U^2$ with $A = (\pi {d_{eq}}^2)/4$.

After the passage of a preceding bubble, the memory effect of the fluid holds the shear-thinning process during a certain time so that the local viscosity decreases and induces the acceleration of the rise velocity of the trailing bubble. The estimation of the local effective viscosity is made through a virtually additional shear rate corresponding to the residual stresses

$$\begin{cases} \tau = \eta_m\dot{\gamma}_m \\ \eta_m = \eta_\infty + (\eta_o - \eta_\infty)[1 + (\lambda\dot{\gamma}_m)^2]^{(n-1)/2} \end{cases} \qquad (14)$$

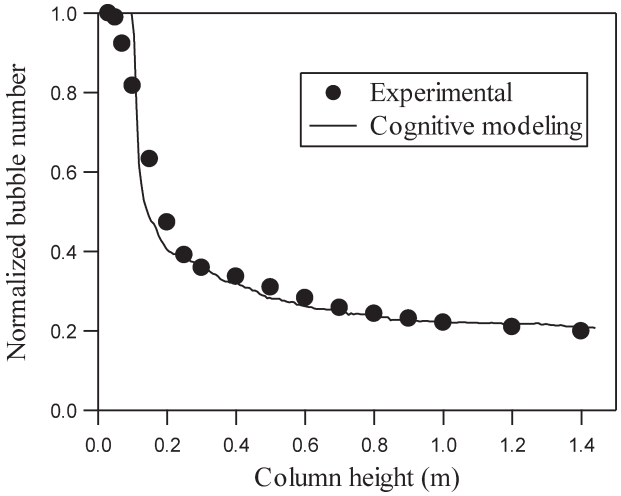

Figure 10. Comparison of the variation of the normalized bubble number with the column height in 0.5% PAAm solution between the experiments and cognitive modeling for 3000 bubbles.

In the present study, we use simply, as a first approximation, the characteristic shear rate

$$\dot{\gamma}_B = U/d_{eq} \qquad (15)$$

It is clear that the sum of these two shear rates leads to an effective viscosity

$$\eta_e = \eta_\infty + (\eta_o - \eta_\infty)\{1 + [\lambda(\dot{\gamma}_B + \dot{\gamma}_m)]^2\}^{(n-1)/2} \qquad (16)$$

For a bubble rising initially at U, the main rules have then the form:

- IF (there are residual stresses in a cellule τ), THEN (compute the new increased velocity U' viaη_e).
- IF (two bubbles enter in contact), THEN (coalescence takes place to form a new bigger bubble $V_B = V_{B1} + V_{B2}$ and compute the new rise velocity U').

These rules are based on the physical mechanisms understood at the mesoscopic level and could be hopefully expected to predict the interactions and coalescence between a great number of bubbles to come close to the industrial scale. In particular, the experimental results[27,28] show that the coalescence between bubbles rising in-line takes place easily in non-Newtonian fluids. The film drainage is mainly encountered in Newtonian fluids or for the lateral coalescence between bubbles in non-Newtonian fluids.

It is worth noting that the relaxation is a very complex procedure in polymer solutions. The cognitive approach employed in this study is to make use of averaged value of a temporarily relaxed local viscosity in the wake of a preceding bubble instead of complex and detailed local flow fields. Otherwise, the computation for the interactions and coalescence between a great number of bubbles will be excessively time consuming.

3.3. In-Line Interactions and Coalescence between Bubbles in a Bubble Column: Macroscopic Properties. Instead of dealing with the complexity of interactions and coalescence between a great number of bubbles rising in a bubble column at macroscopic scale, the mesoscopic interactions rules deduced from the understanding of the microscopic mechanisms are then

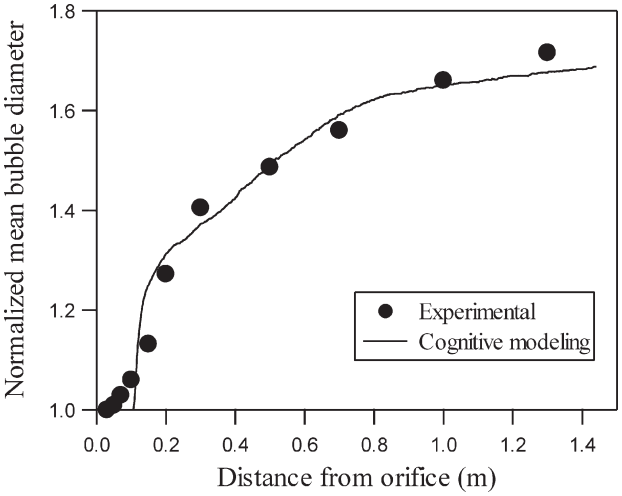

Figure 11. Comparison of the increase in the normalized bubble diameter with the column height in 0.5% PAAm solution between the experiments and cognitive modeling for 3000 bubbles.

applied to follow numerically the ascension of 3000 bubbles consecutively generated at the orifice in a bubble column filled up with a fluid of 1.50 m height. The total fluid height is represented by 20000 individual rectangular cellules as the simulation box. As the inlet condition, identical bubbles are regularly injected through an orifice at the bottom of the column with the experimental values of the period T. For the outlet condition, a bubble reaching the top of the column is eliminated for the following time step. A simple counter allows us to impose periodic bubbling in the numerical simulation. The coalescences takes place when two bubbles get in touch due to the acceleration of the rise velocity of a trailing bubble with the reduced drag. These two bubbles form then a bigger one, according to the mass conservation, and its new rise velocity is computed with the new coalesced size.

The computation is implemented on a classical PC, and several statistical quantities are stored at different heights in the column. Some illustrative results are given as follows in two PAAm solutions. Figure 10 shows a comparison of the local bubble number normalized by 3000 injected at total at different heights between the experiments and the computing from the mesoscopic cognitive approach. The global tendency is well described by this approach even though the local curve details are not perfect. The small difference results essentially in the mean values used of α and β for bubbles of different size instead of more accurate values for each size. With respect to the orifice, a minimum height that depends on the viscoelasticity is required to accumulate sufficient residual stresses to induce the first coalescence. With the increasing sequence of coalescences between bubbles, the number of bubbles decreases significantly with height. In contrary, the bubble size increases because of the consecutive coalescences. Figure 11 represents the evolution of the bubble diameter normalized by the initial one in function of the fluid height. It is interesting to note that both the bubble number and the bubble diameter tend to asymptotic values as stated before; this indicates indirectly a bounded complexity due to mainly a constant injection flow rate of gas at the orifice as a limited resource and then a signature of deterministic chaos. These macroscopic behaviors predicted by the mesoscopic cognitive approach are particularly noteworthy as they emerge naturally without special fitting. In addition, a close analysis reveals that the

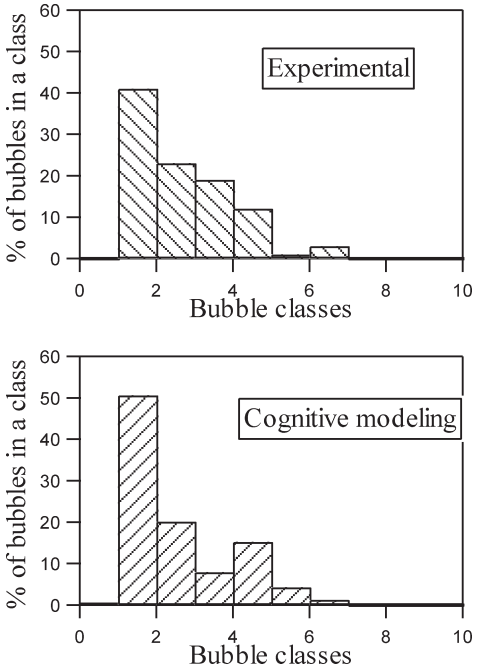

Figure 12. Bubble class distribution at a height of 0.40 m from the orifice in 0.75% PAAm solution, air flow rate $Q = 200 \times 10^{-9}$ m^3 s^{-1}. Comparison between the experimental results and cognitive modeling.

present mesoscopic modeling describes satisfactorily experimental details such as the intermediate distribution of bubble classes at different column heights (Figure 12). These macroscopic data are indispensable for the design, operation, and improvement of an industrial installation through the local knowledge of the bubble size distribution, gas holdup, specific interfacial area, etc. Detailed numerical intermediate values allow also signal treatments, for example, application of wavelets, bifurcation sequence analysis,and route to chaos. Obviously, this new approach captures important quantitative and qualitative features of the collective behaviors of bubbles at the macroscopic level from the knowledge of detailed physical and interfacial phenomena at microscopic and mesoscopic levels.

Certainly, the current approach is still limited to the dynamics of a single rising train of bubbles. In industrial reality, the multihole distributor injects numerous trains of bubbles, rising not only in line but also in parallel. The mutual interactions and eventual coalescences between lateral bubble trains should then be included in the multiscale approach. This is an avenue that we are currently exploring.

4. CONCLUSIONS

In this paper, the concept of a multiscale modeling approach is highlighted with which physical phenomena at different scales can be investigated. We have developed a comprehensive study on the collective behaviors of a chain of bubbles rising in non-Newtonian fluids in view of simulating an industrial bubble column one day. A coherent picture begins to emerge on the basis of fundamental physical understanding at different scales. By means of both the experimental PIV and the lattice Boltzmann simulation based on the particle dynamics, the detailed flow and stress features around a single bubble in different viscoelastic fluids are well understood at the microscale. The proposed LB scheme

interfaced with a viscoelastic model captures successfully the main flow features such as the complex negative wake, its physical origin, the bubble's teardrop shape, and the spatial stress distribution around a bubble rising in a non-Newtonian fluid. These various fine experimental tools such as the PIV device, rheological stimulus−response simulation, and birefringence visualization are also applied to the investigation of a train of bubbles at mesoscale with the main focus on the nature of interactions and coalescences between bubbles. The dynamical competition between the creation of stresses after the passage of bubbles and the relaxation of these stresses forming temporarily a corridor of reduced viscosity is clearly identified as the principal mechanism governing in-line interactions and coalescences. Along with the detailed information gained by both the experiments and theoretical LB simulation, this knowledge of an in-line train of bubbles is resumed as synthetic behavioral laws at mesoscale. An ethnological similitude can be drawn for the communicating agents between them through interactions with their environment: the evolution of the pheromone concentration deposed by ants on a favored passage in an anthill and the residual stresses left by the passed bubbles to guide trailing bubbles through a drag reduction in the fluid. Good agreement of the simulation results with experimental data is achieved for a train of numerous bubbles rising in a column at macroscale for various operating parameters at different heights such as the bubble number, mean bubble diameter, bubble class distribution, etc.

Our results elucidate then the nature of in-line interactions and coalescence between bubbles rising in line in viscoelastic non-Newtonian fluids. However, it is still far from an industrial bubble column where great populations of bubbles rise, interact, and coalesce not only in line but also in parallel. Further studies are then required to include this lateral spatial dimension in the multiscale modeling approach. It is envisaged that the present study could lay the foundation for a better comprehension of bubble dynamics in these complex media.

AUTHOR INFORMATION

Corresponding Author

*E-mail: Huai-Zhi.Li@ensic.inpl-nancy.fr.

ACKNOWLEDGMENT

The financial support provided by the French Ministry of Research, the National Centre for Scientific Research (CNRS), and the Program FSH with industrial companies (GDF, IFP-EN, Schlumberger) is gratefully acknowledged.

NOTATION

C_D = drag coefficient
$\vec{c}_i$ = lattice velocity
D_o = orifice diameter (m)
D_{max} = maximum bubble diameter (m)
DPD = Dissipative Particle Dynamics
F = force (N)
LB = Lattice Boltzmann
P = pressure (Pa)
$P_{\alpha,\beta}$ = pressure tensor
Q = gas flow rate ($m^3\ s^{-1}$)
$\vec{r}$ = lattice location
T = injection period between bubbles (s)
t = time (s)
U,U' = bubble rise velocity ($m\ s^{-1}$)
$\vec{u}$ = fluid velocity ($m\ s^{-1}$)
V_B = bubble volume (m^3)

Greek Letters

α = stress relaxation parameter (s^{-1})
β = stress creation parameter (Pa)
$\Gamma_{\alpha,\beta}$ = viscoelastic stress tensor
$\dot{\gamma}$ = shear rate (s^{-1})
$\Delta\mu$ = chemical potential difference
η = viscosity (Pa s)
κ = adiabatic coefficient
θ = angle between the normal to the bubble surface at any element and the vertical axis
λ = relaxation time in Carreau model (s)
λ_k = kth relaxation time in Maxwell model (s)
ρ_L = fluid density ($kg\ m^{-3}$)
ρ_G = gas density ($kg\ m^{-3}$)
σ = surface tension ($N\ m^{-1}$)
$\boldsymbol{\tau}$ = stress tensor
τ = stress (Pa)
τ_r = relaxation time (s)

REFERENCES

(1) Clift, R.; Grace, J. R. Weber, M. E. *Bubbles, Drops and Particles*; Academic Press: New York, 1978.

(2) Debregeas, G.; de Gennes, P. G.; Brochard-Wyart, F. The life and death of bare viscous bubbles. *Science* **1998**, *279*, 1704–1706.

(3) Hassager, O. Negative wake behind bubbles in non-Newtonian liquids. *Nature* **1979**, *279*, 402–403.

(4) Astarita, G.; Apuzzo, G. Motion of gas bubbles in non-Newtonian liquids. *AIChE J.* **1965**, *11*, 815–820.

(5) Chhabra, R. P. *Bubbles, Drops & Particles in Non-Newtonian Fluids*, 2nd ed.; CPC Press: Boca Raton, 2006.

(6) Rodrigue, D. A simple correlation for gas bubbles rising in power-law fluids. *Can. J. Chem. Eng.* **2002**, *80*, 289–292.

(7) Fan, W. Y.; Ma, Y. G.; Jiang, S. K.; Yang, K.; Li, H. Z. An experimental investigation for bubble rising in non-Newtonian fluids and empirical correlation of drag coefficient. *J. Fluids Eng.* **2010**, *132*, 021305.

(8) Haque, M. W.; Nigam, K. D. P.; Joshi, J. B.; Viswanathan, K. Studies on mixing time in bubble columns with pseudoplastic solutions. *Ind. Eng. Chem. Res.* **1987**, *26*, 82–86.

(9) Haque, M. W.; Nigam, K. D. P.; Joshi, J. B. Hydrodynamics and mixing in highly viscous pseudoplastic non-Newtonian solutions in large diameter bubble columns. *Chem. Eng. Sci.* **1986**, *41*, 2321–2331.

(10) Acharya, A.; Ulbrecht, J. Note on the influence of viscoelasticity on the coalescence rate of bubbles and drops. *AIChE J.* **1978**, *24*, 348–351.

(11) De Kee, D.; Chhabra, R. P.; Dajan, A. Motion and coalescence of gas bubbles in non-Newtonian polymer solutions. *J. Non-Newtonian Fluid Mech.* **1990**, *37*, 1–18.

(12) Charpentier, J. C. Among the trends for a modern chemical engineering, the third paradigm: The time and length multiscale approach as an efficient tool for process intensification and product design and engineering. *Chem. Eng. Res. Des.* **2010**, *88*, 248–254.

(13) Charpentier, J. C. The triplet "molecular processes-product-process" engineering: The future of chemical engineering? *Chem. Eng. Sci.* **2002**, *57*, 4667–4690.

(14) Luo, K. H.; Xia, J.; Monaco, E. Multiscale modelling of multiphase flow with complex interactions. *J. Multiscale Modell.* **2009**, *1*, 125–156.

(15) Succi, S. *The Lattice Boltzmann Equation for Fluid Dynamics and Beyond*; Clarendon Press: Oxford, 2001.

(16) Frank, X.; Funfschilling, D.; Midoux, N.; Li, H. Z. Bubbles in a viscous liquid: Lattice Boltzmann simulation and experimental validation. *J. Fluid Mech.* **2006**, *546*, 113–122.
(17) Frank, X.; Li, H. Z. Complex flow field around a bubble rising in non-Newtonian fluids. *Phys. Rev. E* **2005**, *71*, 036309.
(18) Frank, X.; Li, H. Z. Negative wake behind a sphere rising in viscoelastic fluids: A lattice Boltzmann investigation. *Phys. Rev. E* **2006**, *74*, 056307.
(19) Sigli, D.; Coutanceau, M. Effect of finite boundaries on the slow laminar isothermal flow of a viscoelastic fluid around a spherical obstacle. *J. Non-Newtonian Fluid Mech.* **1977**, *2*, 1–21.
(20) Bisgaard, C. Velocity fields around spheres and bubbles investigated by laser-Doppler anemometry. *J. Non-Newtonian Fluid Mech.* **1983**, *12*, 283–302.
(21) Funfschilling, D.; Li, H. Z. Flow of non-Newtonian fluids around bubbles: PIV measurements and birefringence visualisation. *Chem. Eng. Sci.* **2001**, *56*, 1137–1141.
(22) Frank, X.; Li, H. Z.; Funfschilling, D.; Burdin, F.; Ma, Y. Bubble motion in non-Newtonian fluids and suspensions. *Can. J. Chem. Eng.* **2003**, *81*, 483–490.
(23) Kemiha, M.; Frank, X.; Poncin, S.; Li, H. Z. Origin of the negative wake behind a bubble rising in non-Newtonian fluids. *Chem. Eng. Sci.* **2006**, *61*, 4041–4047.
(24) Li, H. Z.; Frank, X.; Funfschilling, D.; Diard, P. Bubbles' rising dynamics in polymeric solutions. *Phys. Lett. A* **2004**, *325*, 43–50.
(25) Frank, X.; Li, H. Z. An analytical approach to the rise velocity of periodic bubble chains in non-Newtonian fluids. *Europ. Phys. J. E* **2005**, *16*, 29–35.
(26) Li, H. Z.; Mouline, Y.; Midoux, N. Modelling the bubble formation dynamics in non-Newtonian fluids. *Chem. Eng. Sci.* **2002**, *57*, 339–346.
(27) Li, H. Z.; Mouline, Y.; Choplin, L.; Midoux, N. Chaotic bubble coalescence in non-Newtonian fluids. *Int. J. Multiphase Flow* **1997**, *23*, 713–723.
(28) Jiang, S. K.; Ma, Y. G.; Fan, W. Y.; Yang, K.; Li, H. Z. Fractal and chaotic behaviour of bubble coalescence in non-Newtonian fluids: A multiscale analysis. *Korean J. Chem. Eng.* **2011**, *28*, 56–63.
(29) Gell-Mann, M. *The Quark and the Jaguar: Adventures in the Simple and the Complex*; Wiley: Hoboken, NJ, 1994.
(30) Holland, J. H. *Adaptation in Natural and Artificial Systems: An Introductory Analysis with Applications to Biology, Control and Artificial Intelligence*, 2nd ed.; MIT Press: Cambridge, MA, 1992.

epl A Letters Journal Exploring the Frontiers of Physics

March 2014

EPL, **105** (2014) 54006
doi: 10.1209/0295-5075/105/54006

www.epljournal.org

A damping phenomenon in viscoelastic fluids

X. Frank[1,2(a)], N. Dietrich[2] and Huai Z. Li[2(b)]

[1] *IATE, INRA-CIRAD-UMII-Supagro - 2 place Pierre Viala, 34000 Montpellier, France*
[2] *Laboratory of Reactions and Process Engineering, University of Lorraine, CNRS 1 rue Grandville, BP 20451, 54001 Nancy Cedex, France*

received 11 December 2013; accepted in final form 5 March 2014
published online 24 March 2014

PACS 47.50.-d – Non-Newtonian fluid flows
PACS 83.60.Uv – Wave propagation, fracture, and crack healing

Abstract – Flow fields behind a sphere settling in polymeric fluids are investigated using a Particle Image Velocimetry (PIV) technique. Complex features including both a negative wake and a surrounding cone are quantified. In particular, an oscillation zone, which takes place behind the negative wake, is identified for the first time. A physical understanding of various phenomena involved in the wake is gained. The damping phenomenon can be attributed to the viscoelastic properties and the surrounding cone stems from a propagation front of lateral viscoelastic wave emitted by the settling sphere. The oscillation frequency and open angle of the surrounding cone are theoretically related to a viscoelastic Mach number. Satisfactory agreement with experiments is observed.

Introduction. – The classical description of the mechanical properties of fluids and materials at macroscopic scale is usually based on two distinct behaviors: the viscous fluid [1] and the elastic solid [2]. However, most natural materials are viscoelastic and exhibit both. For example, Maxwell was among the pioneers to combine both basic concepts for the description of real materials, such as the respective contribution of liquid and solid according to applied stresses [3]. A central parameter to be considered is then the relative time scale between deformation duration and materials' relaxation time. When imposed deformations are long enough to allow stresses to relax, materials display simple viscous properties. Otherwise, the application of deformations is shorter than stresses' relaxation, materials behave as an elastic solid [4]. Since the early linear model of Maxwell [3], viscoelastic fluids arose many intriguing questions. Moreover, the viscoelastic character of fluids plays the main role in such diverse fields as human tissues and polymers [5], swimming microorganisms [6,7], volcanic eruption [8], decompression sickness [9], besides numerous industrial applications [10].

Among peculiar phenomena due to the viscoelasticity, the negative wake behind a settling sphere was observed for the first time by Hassager [11]. As the main flow pattern around a sphere settling in a purely viscous Newtonian fluid is downward in the neighborhood of the settling axis, the flow behind a sphere settling in a viscoelastic fluid can be surprisingly upward to form a so-called negative wake [12]. More recently, a global view of such a wake was obtained by PIV measurements in the case of polymer solutions [13], suspensions [14] and gels [15]. In all cases, the negative wake is largely extended backward and is surrounded by a conical downward flow zone. The question of the physical origin of the negative wake gave rise to a controversial debate [12,16,17], the main role being successively attributed to various rheological features. Recently, a lattice Boltzmann model, coupled with a simple linear rheological model, was able to reproduce the main features of the flow [18], including the surrounding downward cone. This work clearly demonstrated that the negative wake stems from the fluid's viscoelasticity, as it appears when the Deborah number, which is the ratio between materials' relaxation time and deformation duration, reaches a threshold $De \geq 2$. When the negative wake does exist, the opening angle of the surrounding downward cone decreases with increasing sphere settling velocity, as observed in our previous experiments [13].

However, the long-range behavior in the negative wake remains unexplored yet. Such a point is crucial in many applications, as long-range interactions are responsible for bubble coalescences in chemical and biological

(a) E-mail: xavier.frank@supagro.inra.fr
(b) E-mail: Huai-Zhi.Li@univ-lorraine.fr

Table 1: Parameters of rheological models in SI units.

Fluid	η_0	η_∞	λ	n	m'	n'
0.25%	10.80	0.041	26.4	0.268	28.12	0.538
0.50%	12.05	0.045	38.9	0.291	38.10	0.529
1.00%	33.31	0.070	65.1	0.303	67.83	0.558

reactors [19] and eruption violence in volcanoes [8], and lead to the structuration of particle suspensions in viscoelastic fluids [20]. The present work aims at capturing a better understanding of the flow pattern far away from the settling sphere.

Experiments. – To investigate flow fields around a solid sphere settling in viscoelastic fluids, polyacrylamide (PAAm, AN 905 SH, SNF Floeger, France) solutions of three different concentrations, 0.25%, 0.5% and 1% (wt), were used. For a broad range of shear rates ($\dot\gamma = 0.01$ to $500\,\mathrm{s}^{-1}$), the Carreau model $\frac{\eta-\eta_\infty}{\eta_0-\eta_\infty} = [1+(\lambda\dot\gamma)^2]^{(n-1)/2}$ fits well the non-Newtonian viscosity η and a power-law model $N_1 = m'[\dot\gamma]^{n'}$ fits satisfactorily the first normal stress difference N_1. Rheological parameters are summarized in table 1.

Spheres of various diameters (5 to 20 mm) and materials (steel, glass and ceramic) were employed to reach a wide range of settling velocities in three square columns of various dimensions: 0.18 m large and 1 m high, 0.12 m large and 0.70 m high and 0.06 m large and 0.50 m high. Instantaneous velocity fields around a settling sphere were measured using a PIV (Dantec Dynamics, Denmark) device with the help of fluorescent seeding particles with a mean diameter of 15 μm. Numerous experimental investigations through both the PIV and drag coefficient in this work demonstrate that a ratio superior to 10 between the column size and the diameter of settling spheres is required to ensure negligible effects of the column walls. This is relevant compared to the reported results in the literature such as [21]. The experiments presented in this work were then based on an optimal compromise between the following factors: the measurement accuracy and measuring windows of the PIV; fluid's nature; column size; spheres' diameter and related flow fields. This approach was also validated and tested with flow around a gas bubble of different shapes rising in viscous Newtonian fluids with a maximum error of 4.7% [22]. The PIV device allowed also the determination of the instantaneous velocity of a sphere at different positions in the column as well as its terminal settling velocity v_s. Due to the relatively high value of the viscosity of fluids used, it was observed that the acceleration of a sphere was quickly absorbed by the fluids and the terminal settling regime was then reached after a travel of 0.1 m from the release point.

The flow fields around a sphere in the tested fluids have very peculiar features: the flow in the front of the sphere is very similar to that in the Newtonian case; in the central wake, the motion of the fluid is surprisingly upward in the opposite direction of the settling sphere; finally, a hollow cone of downward flow surrounds this negative wake. This conical downward flow zone begins on the sides of the sphere, and is largely extended backward (fig. 1(A), (B)). On the contrary, in the case of a Newtonian viscous fluid, the flow in the central wake is downward everywhere, as shown by a lattice Boltzmann simulation (fig. 1(C)) and experiments [14,23].

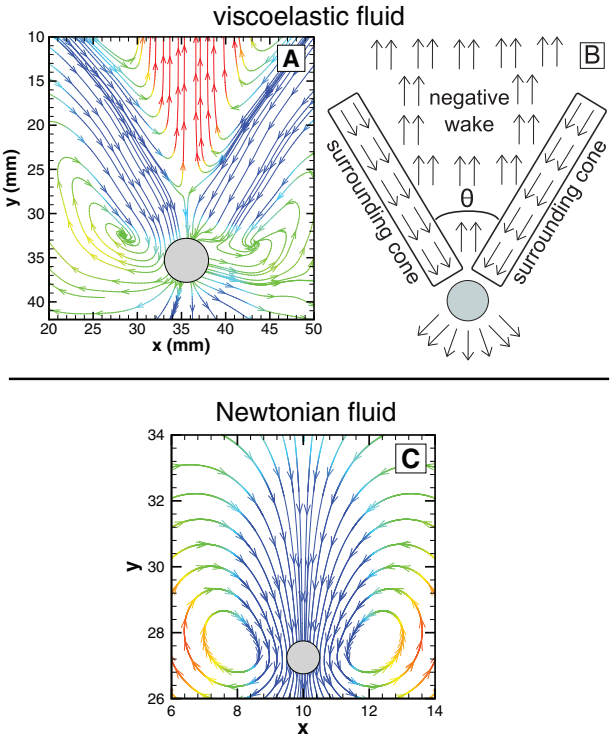

Fig. 1: (Color online) Streamlines of flow fields around a settling sphere. The sphere shape is added to guide the eye. Colors are related to the z component u_z of the fluid velocity $\vec{u}$: red for $u_z > 0$, blue for $u_z < 0$, green when u_z is close to 0. (A) Case of a viscoelastic fluid, from PIV measurement. The sphere diameter is $d_s = 5$ mm, the settling velocity is $v_s = 0.1\,\mathrm{m}\cdot\mathrm{s}^{-1}$, the sphere material is steel and the fluid is a 1% PAAm solution. (B) Schematic representation of the flow field around a sphere settling in a viscoelastic fluid. Negative wake, surrounding cone and cone's opening angle θ are drawn. (C) Case of a Newtonian fluid, from a lattice Boltzmann numerical simulation. The sphere diameter is $d_s = 1$, and the Reynolds number is set to $Re = 1$. Numerical results compare well with experimental data [14,23].

As the window size of the PIV is limited, we capture the long-range wake behind the settling sphere by continuously monitoring the flow fields after the leave of the sphere in an Eulerian framework. Besides the negative wake, another phenomenon not reported so far is observed: after the negative wake behind the sphere, a stagnant zone followed by another downward flow, and then again a stagnant zone followed by a new negative wake, and so on (fig. 2). This alternating pattern collapses progressively with increasing distance from the sphere.

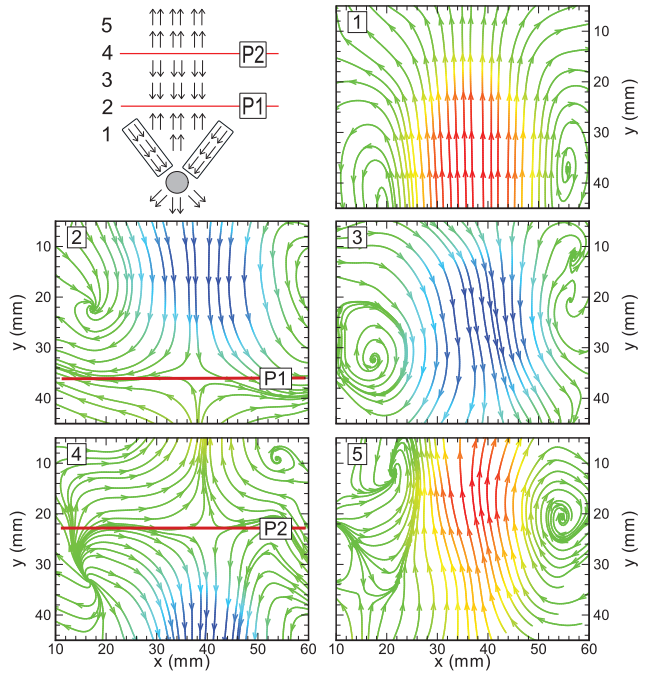

Fig. 2: (Color online) Successive captures of flow fields from PIV in a fixed window in the wake behind a 5 mm diameter steel sphere settling in a 1% PAAm solution. Colors are related to the z component of the fluid velocity $\vec{u}$: red for $u_z > 0\,\mathrm{m\cdot s^{-1}}$, blue for $u_z < 0\,\mathrm{m\cdot s^{-1}}$ and green when u_z is close to $0\,\mathrm{m\cdot s^{-1}}$. Top left: distribution of successive views in the wake. Planes $P1$ and $P2$, drawn as red lines, underline positions where $u_z = 0\,\mathrm{m\cdot s^{-1}}$.

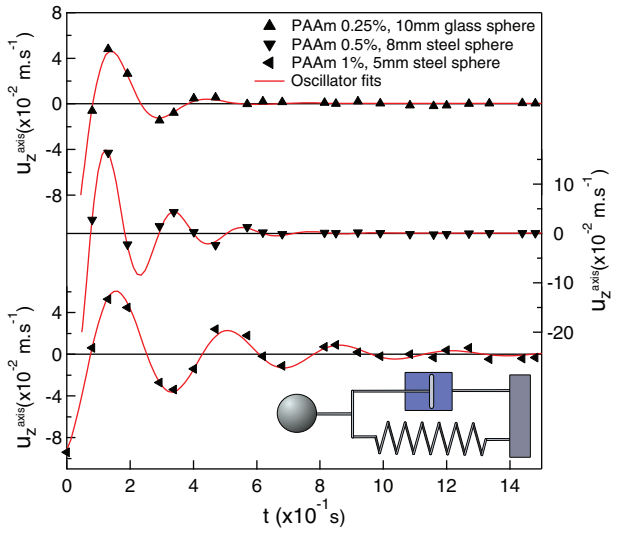

Fig. 3: (Color online) Examples of u_z oscillation at a fixed point on the settling axis after the sphere passage in a 0.25%, 0.5% and 1% PAAm solution, from top to bottom, respectively. The sphere diameter and the material vary with fluid and are included in each graph legend. Triangles are experimental data from PIV and curves are dissipative linear oscillator models $u_z\left(\vec{r}_0,t\right) = u_0 \sin\left(\sqrt{1-\sigma^2}\omega_0 t + \phi\right) e^{-\sigma\omega_0 t}$. The values of σ are 0.37, 0.21 and 0.16 for 0.25%, 0.5% and 1% PAAm, respectively.

The alternating pattern at the rear of the sphere can therefore be represented as a damped oscillation. To understand the physical origin of such an oscillator, a more quantitative approach is required. Clearly, only the axial component z of the velocity fields is relevant to characterize such an oscillator. According to an Eulerian description of the velocity fields, the temporary evolution of the z component is recorded in a fixed point behind the sphere's settling axis. The velocity variation exhibits a regular oscillation whose amplitude decreases with time and reaches zero as the settling sphere leaves away progressively from the measuring point (fig. 3). Obviously, observed damped oscillations are satisfactorily fitted by a linear Kelvin-Voigt model that is represented by a purely viscous damper and a purely elastic spring in parallel as shown (fig. 3). This implies that for the investigated range of viscoelastic fluids, a linear model can satisfactorily describe the damping phenomenon in the wake.

Discussion. – As shown in our earlier numerical experiments, the negative wake exists only in viscoelastic fluids [18]. An interpretation of such oscillations could be based on the consideration of fluid elasticity. Let us consider a local fluid strain as $\gamma \approx \frac{\delta}{r_s}$, where r_s is the sphere radius and δ a local fluid displacement. The resulting short-time viscoelastic stress can be deduced as $\approx G\gamma \approx G\frac{\delta}{r_s}$, where G is the fluid's elastic modulus, and the volume force is $\approx G\frac{\delta}{{r_s}^2}$. Assuming that ρ is the fluid density, the inertial force is $\approx \rho\frac{\mathrm{d}^2\delta}{\mathrm{d}t^2}$ and the local force balance leads to the following simple harmonic equation:

$$\frac{\mathrm{d}^2\delta}{\mathrm{d}t^2} + \frac{G}{\rho {r_s}^2}\delta = 0. \qquad (1)$$

A proper pulsation $\omega_0 = \sqrt{\frac{G}{\rho {r_s}^2}}$ can be deduced from eq. (1). Moreover, a shear wave propagation velocity $c = \sqrt{\frac{G}{\rho}}$ can easily be identified within this expression. The simplest dimensionless number that can be deduced from a wave propagation velocity is the well-known Mach number, which compares c and the translating source velocity v_s,

$$M = \frac{v_s}{c} = \frac{v_s}{\omega_0 r_s}. \qquad (2)$$

Recently, shear waves were identified around a sphere settling in a viscoelastic fluid and sphere oscillations were attributed to reflection of such waves on column walls [24]. By means of both the PIV and the settling velocity to ensure a negligible effect of the column's wall, wave reflections on walls can be excluded as a major parameter in the presented damping results. Thus, oscillations in the wake can be identified as an intrinsic manifestation of fluid viscoelasticity.

Shear waves are normally expected to propagate from the settling sphere towards column walls; however the fluid is viscous enough and the column width sufficiently large

to dissipate a significant amount of mechanical energy in possible reflected waves. The downward hollow cone could find the physical origin in the propagation of such elastic shear waves.

If such an assumption is justified, the opening angle θ should depend only upon M. To check this point, we perform Lattice Boltzmann (LB) numerical simulations [25–27]. In our previous work, a simple LB model, associated with a linear viscoelastic model for the fluid properties, is able to predict the apparition of a negative wake and a surrounding cone [18] as with a non-linear constitutive rheological model including shear-thinning behavior [13,28]. Along with the successful description of the damping velocity by the linear model (fig. 3), it is reasonable to argue that the main features of the fluid behaviour could be captured by a linear Maxwell equation. With a limited number of parameters, this approach aims at gaining the main contribution of elastic properties that seem to govern the damping phenomenon. This facilitates to some extent a straightforward comparison with experimental damping results that display linear behavior,

$$\frac{\partial \tau^{ve}_{i,j}}{\partial t} + \frac{1}{De}\left(\tau^{ve}_{i,j} - \frac{1}{Re}\dot{\gamma}_{i,j}\right) = 0. \qquad (3)$$

The Deborah number is defined as $De = \frac{t_r v_s}{d_s}$, where t_r is the fluid relaxation time, which should be distinguished from the characteristic time λ used in the Carreau model, The Reynolds number is defined as $Re = \frac{\rho d_s v_s}{\eta}$, where η is the fluid viscosity, $\tau^{ve}_{i,j}$, is the viscoelastic stress tensor, $\dot{\gamma}_{i,j}$ is the shear rate tensor and i, j are tensor indices. Our previous works reveal that both the Deborah number and the Reynolds number contribute to the negative wake in viscoelastic fluids. Instead of only the Deborah number, we make then use of a combination of both of them which is nothing but the Mach number easily deduced as $M = \sqrt{DeRe}$. As $\eta = t_r G$, this expression and the one from eq. (2) are clearly identical. Details of this model can be found in the original paper [18]. If the conical downward flow stems from the elastic wave propagation, its opening angle depends upon M and should not depend upon the Re-De couple when M is fixed. To adress such a point, two simulation sets with two fixed values of $M^2 = DeRe$ were carried out. Within each set, De is varied, the condition $De > 2$ being satisfied in order to give rise to a negative wake, and Re is easily deduced as $Re = M^2/De$.

Flow fields from the LB simulation (fig. 4(B)) exhibit both a negative wake and a surrounding cone, which compare favorably with PIV experiments (fig. 1(A)). Numerical simulations reveal that θ depends only upon M (fig. 4(A)) and corroborate the hypothesis that the surrounding cone is a viscoelastic wave front emitted by the settling sphere.

Experimental values of M range from ≈ 0.3 to ≈ 3, and conical shockwaves are expected in flow fields only for $M > 1$. A conical shockwave opening angle can then be deduced from a Mach number, using the relationship $\sin(\theta/2) = 1/M$ when $M > 1$. However, no

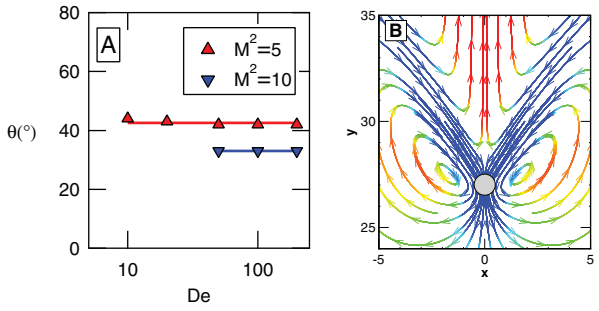

Fig. 4: (Color online) Results from LB simulations of a sphere settling in a viscoelastic fluid. (A) Opening angle of surrounding cone as a function of De for two values of $M^2 = DeRe$, horizontal lines are added to guide the eye. (B) Example of streamlines of the flow field from the LB simulation ($M = 2$), colors are related to the z component u_z of the fluid velocity $\vec{u}$: red for $u_z > 0$, blue for $u_z < 0$, green when u_z is close to 0. The flow pattern is presented by streamlines in satisfactory agreement with experimental results (fig. 1(A)).

qualitative difference appears in experimental results when the threshold occurs from $M < 1$ to $M > 1$. This confirms that a shockwave origin can be excluded. The hollow cone emerges from the propagation of elastic shear waves towards column walls, but cannot be identified as a shockwave. Shear rate at the surface of a sphere slowly translating in a fluid is not homogeneous. In the purely viscous fluid case, the maximum value of shear rate is mainly located at equatorial zones, according to the well-known potential flow theory. According to our experimental PIV measurements and the LB simulation, this flow pattern around the sphere's equatorial zone is quite similar between viscoelastic and Newtonian fluids. We can argue then that shear waves are essentially emitted from the sphere's equatorial zone. The fluid is sheared in vertical direction, and, consequently, transversal shear waves propagate in horizontal direction, orthogonally to its vertical translating axis. As the source is translating during wave emission, the wave front forms a conical shape, whose opening angle depends upon wave propagation velocity c and sphere settling velocity v_s through the viscoelastic Mach number M. If we consider a Δt time interval, the settling distance during such an interval is $v_s \Delta t$ and the wave propagation distance is $c\Delta t$. We can identify $v_s \Delta t$ as the cone height and $c\Delta t$ as the cone radius. The angle θ can be easily computed as

$$\tan\left(\frac{\theta}{2}\right) = \frac{1}{M}. \qquad (4)$$

According to our earlier experimental investigations, the opening angle of the cone θ depends upon the sphere's settling velocity, the cone is widely opened ($\theta \approx 180°$) for a slow settling sphere, and θ decreases as the sphere velocity increases [13]. Such results could be easily explained following eq. (4) as the viscoelastic Mach number M increases with the sphere's velocity v_s. Using eq. (2), a value of M can be deduced from experiments. Then,

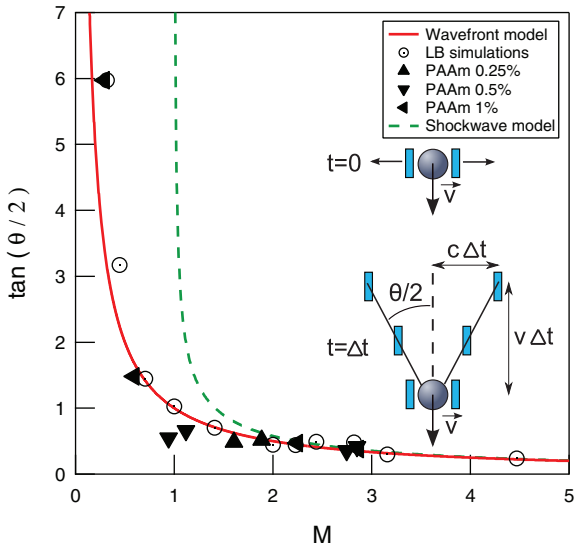

Fig. 5: (Color online) Downward flow cone opening angle θ as a function of Mach number M. Full symbols: data from experiments with 0.25%, 0.5% and 1% PAAm solutions and various sphere diameters and materials. Empty symbols: data from LB simulations. The determination of an angle for opening cones is not easy when the angle value is small. This is true for both the experimental flow fields measured by the PIV and the LB simulation. Small fluctuations observed can be attributed to this difficulty. The solid curve is the prediction from the lateral wave propagation theory (eq. (4)) and the dashed line is the prediction from shockwave theory: $\sin(\theta/2) = 1/M$ for $M > 1$. Inset: schematic representation of the lateral wave propagation theory. Two fictitious steps are drawn, at $t = 0$ and $t = \Delta t$ dates. Shear waves, schematically drawn as rectangles, are emitted from the sphere and propagate towards column walls while the sphere settles down. The half-angle $\frac{\theta}{2}$, shown in the inset, is the angle between the wave front and the settling axis.

experimental results can be satisfactorily described by this theory (fig. 5).

As illustrated in fig. 5, experimental data and LB simulations are in good agreement with the prediction of eq. (4). The opening angle value is close to $\theta \approx 180°$ for low values of M, and decreases with increasing M. It is worth distinguishing the lateral wave propagation from elastic shock transverse waves [29] or sonic boom [30]. In spite of an agreement when $M > 2$, the surrounding cone simply does not exist for $M < 1$ according to the shockwave theory. On the contrary, the lateral wave propagation theory describes satisfactorily the whole investigated range of M, in particular for $M < 1$.

As a consequence, a better understanding is gained for the complex wake behind a sphere settling in viscoelastic fluids. Spheres translating in these fluids induce a shear, whose propagation towards column walls provokes a hollow cone. As viscoelastic stresses created by the shear relax progressively in fluids, a damping phenomenon takes place in the wake through a slowly dissipated viscoelastic oscillation. There is no direct causal relationship between damped oscillations in the wake and the hollow cone. While both the damped oscillations in the wake and hollow cone emerge from the fluids' elasticity, a reliable correlation can be drawn between these phenomena. Concretely, the damped oscillations and the hollow cone are both related to the elastic shear wave velocity $c = \sqrt{\frac{G}{\rho}}$, through the proper pulsation ω_0 on the one hand, and the viscoelastic Mach number M on the other hand.

We have tried to assess quantitatively a possible analytical relationship between the damping frequency and experimental rheological data such as the relaxation modulus issued from a rheometer. The main difficulty arises from the length-scale–dependent rheology of polymer solutions that has yet to be fully described [31]. In a recent work reporting micro-macro-discrepancies in nonlinear rheology [32], it is recognised that the Lagrangian unsteady forcing experienced by material elements in response to the moving colloidal probe for active microrheology induces spatial inhomogeneity of the strain rate. The resulting microrheology reflecting the bulk microstructure differs qualitatively and quantitatively from the macroscopic rheology. The damping frequency is determined by local solicitations at microscale exerted by a solid sphere, similar to a colloidal probe employed in characterizing microrheology. However, our experimental data concerning the relaxation modulus is a macroscopic parameter, measured by means of a standard geometry like Couette's on the rheometer in an integral manner for the whole measuring sample. A modulus G at microscale would be required to allow a possible scaling as the rheological properties are sensitive to the length scales that determine both network structure and filament orientation of polymers in solution.

Conclusion. – In summary, we throw new insight into the long-range wake behind a sphere settling in viscoelastic fluids. Both negative wake, in which the fluid flows upward contrary to the settling sphere, and its surrounding cone taking place around the negative wake, were amply demonstrated. In particular, we identify for the first time a zone just behind the negative wake in which oscillations appear. A linear dissipative oscillator model fits well the vertical component of fluid velocity in this new zone. Clearly, we show that oscillations in the wake can be attributed to the viscoelasticity of the fluid, and deduce then a viscoelastic Mach number. Furthermore, we demonstrate that the surrounding cone arises from the lateral propagation of a shear wave with respect to the settling axis, the sphere being the translating source. The experiments validate this proposal. These results could provide a benchmark solution for both academic and industrial studies where viscoelastic fluids are involved.

REFERENCES

[1] Newton I. S., in *Philosophiae Naturalis Principia Mathematica*, edited by Pepys S. (Royal Society, London) 1686.

[2] Hooke R., *De Potentia Restitutiva*, edited by Martyn J. (Royal Society, London) 1678.
[3] Maxwell J. C., *Philos. Trans. R. Soc. Lond.*, **156** (1866) 249.
[4] Nosenko V., Goree J. and Piel A., *Phys. Rev. Lett.*, **97** (2006) 115001.
[5] Lakes R., *Viscoelastic Materials* (Cambridge University Press, Cambridge) 2009.
[6] Teran J., Fauci L. and Shelley M., *Phys. Rev. Lett.*, **104** (2010) 038101.
[7] Gagnon D. A., Shen N. and Arratia P. E., *EPL*, **104** (2013) 14004.
[8] Manga M. and Loewenberg M., *J. Volcanol. Geotherm. Res.*, **105** (2001) 19.
[9] Gault K. A., Tikuisis P. and Nishi R. Y., *Undersea Hyperbaric Med.*, **23** (1995) 249.
[10] Chhabra R. P., *Bubbles, Drops, and Particles in Non-Newtonian Fluids* (CRC Press, Boca Raton) 2006.
[11] Hassager O., *Nature*, **279** (1979) 402.
[12] Arigo M. T. and McKinley G. H., *Rheol. Acta*, **37** (1998) 4.
[13] Kemiha M., Frank X., Poncin S. and Li H. Z., *Chem. Eng. Sci.*, **61** (2006) 4041.
[14] Gueslin B., Talini L., Herzhaft B., Peysson Y. and Allain C., *Phys. Fluids*, **18** (2006) 103101.
[15] Mougin N., Magnin A. and Piau J. M., *J. Non-Newtonian Fluid Mech.*, **171-172** (2012) 42.
[16] Harlen O. G., *J. Non-Newtonian Fluid Mech.*, **108** (2002) 411.
[17] Dou H.-S. and Phan-Thien N., *Rheol. Acta*, **43** (2004) 203.
[18] Frank X. and Li H. Z., *Phys. Rev. E*, **74** (2006) 056307.
[19] Li H. Z., Frank X., Funfschilling D. and Mouline Y., *Chem. Eng. Sci.*, **56** (2001) 6419.
[20] Michele J., Pätzold R. and Donis R., *Rheol. Acta*, **16** (1977) 317.
[21] Chhabra R. P. and Uhlherr P. H. T., *Can. J. Chem. Eng.*, **66** (1988) 154.
[22] Frank X., Funfschilling D., Midoux N. and Li H. Z., *J. Fluid Mech.*, **546** (2006) 113.
[23] Tatum J. A., Finnis M. V., Lawson N. J. and Harrison G. M., *J. Non-Newtonian Fluid Mech.*, **127** (2005) 95.
[24] Tabuteau H., Sikorski D. and De Bruyn J. R., *Phys. Rev. E*, **75** (2007) 012201.
[25] Succi S., *The Lattice Boltzmann Equation for Fluid Dynamics and Beyond* (Clarendon Press, Oxford) 2001.
[26] Qian Y. H., d'Humieres D. and Lallemand P., *Europhys. Lett.*, **17** (1992) 479.
[27] Giraud L., d'Humieres D. and Lallemand P., *Europhys. Lett.*, **42** (1998) 625.
[28] Frank X. and Li H. Z., *Phys. Rev. E*, **71** (2005) 036309.
[29] Catheline S., Gennisson J.-L., Tanter M. and Fink M., *Phys. Rev. Lett.*, **91** (2003) 164301.
[30] Bercoff J. B., Tanter M. and Fink M., *Appl. Phys. Lett.*, **84** (2003) 2202.
[31] Liu J., Gardel M. L., Kroy K., Frey E., Hoffman B. D., Crocker J. C., Bausch A. R. and Weitz D. A., *Phys. Rev. Lett.*, **96** (2006) 118104.
[32] De Puit R. J. and Squires T. M., *J. Phys.: Condens. Matter*, **24** (2012) 464106.

Carbohydrate Polymers 127 (2015) 438–450

Contents lists available at ScienceDirect

Carbohydrate Polymers

journal homepage: www.elsevier.com/locate/carbpol

A coarse-grain force-field for xylan and its interaction with cellulose

Liang Li[a], Patrick Pérré[b], Xavier Frank[c], Karim Mazeau[d,e,*]

[a] LERFoB, AgroParisTech ENGREF, 14 Rue Girardet, 54000 Nancy, France
[b] LGPM, Ecole Centrale Paris, Grande Voie des Vignes, 92290 Châtenay-Malabry, France
[c] IATE INRA, CIRAD, Université Montpellier 2, Montpellier SupAgro, 2 Place Pierre Viala, 34000 Montpellier, France
[d] Univ. Grenoble Alpes, CERMAV, F-38000 Grenoble, France
[e] CNRS, CERMAV, F-38000 Grenoble, France

ARTICLE INFO

Article history:
Received 5 December 2014
Received in revised form 25 March 2015
Accepted 5 April 2015
Available online 10 April 2015

Keywords:
Xylan
Cellulose
Adsorption
Interaction
Composite
Molecular dynamics
Coarse grain

ABSTRACT

We have built a coarse-grain (CG) model describing xylan and its interaction with crystalline cellulose surfaces. Each xylosyl or glucosyl unit was represented by a single grain. Our calculations rely on force-field parameters adapted from the atomistic description of short xylan fragments and their adsorption on cellulose. This CG model was first validated for xylan chains both isolated and in the bulk where a good match was found with its atomistic counterpart as well as with experimental measurements. A similar agreement was also found when short xylan fragments were adsorbed on the (1 1 0) surface of crystalline cellulose. The CG model, which was extended to the (1 0 0) and (1 −1 0) surfaces, revealed that the adsorbed xylan, which was essentially extended in the atomistic situation, could also adopt coiled structures, especially when laying on the hydrophobic cellulose surfaces.

1. Introduction

In plants, the cell wall serves a variety of physical and biological purposes (Albersheim, Roberts, Seferoff, & Staehelin, 2010). Among these, one of its main functions is to provide support and mechanical strength to the plant and to ultimately organize its architectural design and diversity. The cell wall also possesses many biological and biophysical functions required for the plant development, ranging from the containment of the cell turgor pressure during the wall growth, the prevention of insect and pathogen invasion, the diffusion of signaling molecules, etc. All these roles rely on the unique nanocomposite ultrastructure of the wall that chiefly consists of slender crystalline cellulose microfibrils embedded in amorphous hemicelluloses, with or without lignin, depending on the class of the tissues (Carpita & McCann, 2002; Keegstra, 2010; Varner & Lin, 1989). An accepted scheme of this ultrastructure is that the hemicelluloses are laid along the cellulose microfibrils and when lignin is present, as in secondary walls, the hemicelluloses act as a "coupling agent" between cellulose and lignin (Page, 1976; Terashima et al., 2009).

Among the known hemicelluloses, xylan stands out as being by far the most abundant. On an industrial scale, the beneficial influence of xylan on cellulose fibers is well documented, either during the cooking of the wood pulp (Yllner & Enstrom, 1956), or its beating (Roberts & El-Karim, 1983). On the other hand, the presence of xylan in lignocellulosics is detrimental for the enzymatic digestion of the cellulose fibers prior to biofuel production (Ohgren, Bura, Saddler, & Zacchi, 2007). At the laboratory scale, the selective adsorption of xylan on cellulose microfibrils has been extensively studied (Kabel, van den Borne, Vincken, Voragen, & Schols, 2007; Koehnke, Oestlund, & Brelid, 2011; Mora, Ruel, Comtat, & Joseleau, 1986). In particular, this affinity is well exemplified when the addition of xylan to the culture medium of bacterial cellulose leads to a spontaneous xylan adsorption at the surface of the nascent cellulose microfibrils, which thus cannot get assembled into ribbons as in the xylan-less control case (Atalla, Hackney, Uhlin, & Thompson, 1993; Tokoh, Takabe, Sugiyama, & Fujita, 2002). The ultrastructural visualization of deposits of xylan on cellulose microfibrils has been illustrated in many micrographs obtained with a battery of high-resolution microscopy techniques (Henriksson & Gatenholm, 2001; Linder, Bergman, Bodin, & Gatenholm, 2003; Mora, Ruel, Comtat, & Joseleau, 1986).

* Corresponding author at: Univ. Grenoble Alpes, CERMAV, F-38000 Grenoble, France. Tel.: +33 0476037602; fax: +33 0476547203.
E-mail address: karim.mazeau@cermav.cnrs.fr (K. Mazeau).

http://dx.doi.org/10.1016/j.carbpol.2015.04.003
0144-8617/

Given its crucial role in the ultimate physical properties of the plant cell wall, the molecular description of the organization of xylan at the interface with cellulose is important. There are several spectroscopic studies that show that in wood cell wall, xylan as well as other hemicelluloses tend to be aligned, parallel to the cellulose microfibrillar direction (Liang, Bassett, McGinnes, & Marchessault, 1960; Marchessault & Liang, 1962; Olsson, Bjurhager, Gerber, Sundberg, & Salmen, 2011; Stevanic & Salmen, 2009). The co-crystallization of xylan on cellulose microfibrils was even described in one report (Marchessault, Settineri, & Winter, 1967), but this observation was criticized (Caulfield, 1968) and so far has not been reproduced.

In view of the difficulty of obtaining precise experimental data revealing the fine details of the interface of xylan and cellulose, modeling appears as a choice method to propose an energetically acceptable description of such an interface. In a previous report, we have simulated by molecular dynamics (MD) at the atomic scale, the adsorption of xylodextrins at the (1 1 0) surface of an Iβ crystal of cellulose (Mazeau & Charlier, 2012). This study showed that such xylan fragments could not only be adsorbed in a parallel or antiparallel fashion with respect to the cellulose molecular axis, but also that inclined situations were also possible. Counter-intuitively, the most populated adsorbed conformation of the xylodextrin backbone corresponded to the classical left handed 3_2 helices, suggesting that such helices could interact efficiently with a crystalline cellulose surface in spite of apparent conformational incompatibility. Adsorbed xylodextrins could also explore the 2_1 helicity as well as non-helical geometries. Atomistic simulations, restricted so far to several tenths of nanoseconds, have been performed, using a short fragment of xylan of five xylose units, adsorbed on a very small cellulose surface of 18 nm^2 made of only eight chains of eight glucosyl units each. In addition, only the (1 1 0) surface of cellulose was considered, based on results from ^{13}C solid-state NMR spectroscopy (Larsson, 2004; Larsson, Hult, Wickholm, Pettersson, & Iversen, 1999). However, recent WAXS data suggest that the (1 0 0) surface could also participate in the interaction of xylan on crystalline cellulose (Penttila et al., 2013).

Despite the interesting results obtained on rather small systems, an extensive characterization of the adsorption requires more realistic models including longer hemicellulose chains, wider cellulose surfaces, cellulose surfaces of different nature, and longer simulation times, which are beyond the reach of actual computing power.

To overcome such limitations, alternative methods have been developed for the simulation of biological systems as well as polymer in their various states. Among these new techniques, the coarse grain modeling has the capability of circumventing the limitations of atomistic simulations. The methods and applications of CG modeling in the field of biopolymers including polysaccharides have been reviewed at several occasions (Muller-Plathe, 2002; Noid, 2013; Saunders & Voth, 2013). Different CG models of cellulose were recently developed to answer critical problems that need to be solved for the use and processing of plant biomass. Along this line and referring to the cellulose component, one can quote (i) the determination of its intrinsic properties in both its crystalline and amorphous states (Glass, Moritsugu, Cheng, & Smith, 2012; Queyroy, Neyertz, Brown, & Mueller-Plathe, 2004; Shen & Gnanakaran, 2009; Srinivas, Cheng, & Smith, 2011; Wohlert & Berglund, 2011; Wu, Zhan, Wang, & Ju, 2012) (ii) its ability to interact with external agents such as cellulases (Asztalos et al., 2012; Bu et al., 2009; Bu, Himmel, & Nimlos, 2010; Lin, Beckham, Himmel, Crowley, & Chu, 2013), (iii) its dissolution into organic solvents (Gross, Bell, & Chu, 2013), (iv) its swelling with agents such as ammonia (Bellesia et al., 2012), etc.

The basic idea of the CG approach is to group a number of atoms into a single grain. In the field of carbohydrates, the number of grains that define a monosaccharide residue ranges from one to six. The choice of the CG scale depends on the desired level of structural information and on the desired scientific issue. CG models with many grains are able to describe the chemical specificity of carbohydrates, including the shapes of the pyranose ring, the accessible conformational states of the glycosidic bonds and even the rotation of the hydroxymethyl groups. Describing monosaccharides with a large number of grains requires however huge computational resources. At the opposite, CG models that scale glycosyl residues by a single grain are minimal models for the study of the structure and dynamics of large assemblies of polysaccharides. This scaling level is intuitively natural but presents some difficulties in its primitive form, as it is not able to distinguish different monosaccharides. In addition, it cannot handle the different shapes of the monosaccharides or the anisotropic interactions. Finally, reverse-scaling, i.e., deriving an atomistic description from the CG model, is difficult at this scaling level.

To our knowledge, only three CG models of the cellulose/hemicellulose interactions have been proposed. These models differ by the mapping level. A hyper-CG model, where cellulose was only represented by a flat surface and xyloglucan by beads having the Kuhn-length – i.e., 6 nm – has been developed to better understand the experimental extension forces between cellulose and xyloglucan measured by AFM (atomic force microscope) spectroscopy (Morris, Hanna, & Miles, 2004). In this system, the CG modeling was able to reproduce the observed plateaus when three chains of different lengths, with 40, 80 and 120 beads, were attached to the modeled tip. In another CG model, the cellulose microfibril is represented by a long stiff rod made of seven beads, whereas the xyloglucan is represented only by stretchable cross-links, placed at three points per rod (Manyuhina, Fasolino, & Katsnelson, 2007). This modeled system, which contained 288 rods, was generated to study the frustration effects induced by the xyloglucan particles on the co-orientation of the cellulose rods. Reorientation of these rods studied at different temperatures showed that the orientation correlation function presented a logarithmic time dependence, in agreement with the observed logarithmic creep motion in primary plant cell walls leading to the cell extension (Nieuwland et al., 2005). In the most precise CG model of the cellulose/hemicellulose complex developed so far, the beads of both polymers have a diameter of 1 nm, which is roughly the length of a disaccharide (Adler & Buehler, 2013). A generated cell wall model containing 10 cellulose microfibrils, each with 30 beads, and hemicelluloses made of 36 beads was developed. When stressed, this model was adapted to study the influence of the average orientation of the fibers on the mechanical response of the complex. In very good agreement with the experiments, it was found that a decrease in the microfibril angle had the effect of increasing the stiffness of the system. The CG mapping levels proposed so far of the association of hemicelluloses with cellulose are too coarse to address the question of the description of the adsorption, together with the interaction and organization of the hemicellulose at the exposed surfaces of the cellulose crystals.

In this report, which goes beyond our earlier atomistic study (Mazeau & Charlier, 2012), we present the development of a CG using a mapping scale where each bead has a diameter of 0.5 nm, corresponding to the size of a single anhydro sugar unit. Our new model is more accurate than the previous models that were capable of describing the cellulose–hemicellulose complexes. The model completes the existing ones and thus extends their possibilities in this particular field. Our long term objective is to integrate the description of non-spherical grains with anisotropic interactions (Zhu et al., 2013), to get rid of the limitations inherent to the scaling level. We feel that the tool that we are herewith developing will allow deeper investigation of the plant cell wall, but also the development advanced bio-sourced materials.

2. Materials and methods

The CG molecular was derived from molecular dynamics (MD) atomistic trajectories, which were mapped at the CG level by lumping an entire atomistic monomer into a single coarse grain bead (Fig. 1). Hence, a single CG bead represents a glucosyl or a xylosyl unit. The grain bead was defined at the mass center of the atom positions of the corresponding monomer.

The geometric statistical information such as the distributions of the grain distances, the bond angles and dihedral angles, extracted from the atomistic trajectories, were used to model the CG either by Boltzmann inversion (Li, Ma, Huang, & Liang, 2005; Reith, Meyer, & Mueller-Plathe, 2001; Reith, Puetz, & Mueller-Plathe, 2003) or by Force Matching methods (Ensing, Nielsen, Moore, Klein, & Parrinello, 2007; Izvekov & Voth, 2005; Shi, Izvekov, & Voth, 2006; Shi, Liu, & Voth, 2008).

2.1. Atomistic modeling

The Universal force field (UFF) (Rappe, Casewit, Colwell, Goddard, & Skiff, 1992) was applied in all the atomistic simulations. We have used this force field in order to describe various complexes involving a wide variety of polysaccharides (Henao & Mazeau, 2008, 2009; Mazeau & Charlier, 2012). This force field satisfactorily reproduces the specific conformational properties of carbohydrates, in particular the puckering of the pyranose rings and the exo-anomeric effect, but fails to well describe the conformational preferences of isolated cellobiose (Bazooyar, Momany, & Bolton, 2012). The charge equilibration method was used to calculate the charges for each atom (Rappé & Goddard, 1991). Molecular dynamics calculations were based on the canonical *NVT* ensemble (with constant number of particles, volume and temperature) at 400 K. The equations of motion were solved using the standard Verlet algorithm (Verlet, 1967), with a time step of 1 fs. The system was coupled to a bath at the desired temperature using Nose's algorithm (Evans & Holian, 1985). Typical dynamic simulations lasted 500 ps for the shortest one and up to 5 ns for the longest one. Under these conditions, equilibrium was quickly attained (see, for example, Fig. 2 in an earlier report (Mazeau & Charlier, 2012) showing the time evolution of the potential energy for xylan adsorbed on the cellulose surface (1 1 0), where the potential energy was constant after times beyond 100 ps). The geometric distributions were estimated using the final frames, where properties already converged.

The atomistic models of cellulose surfaces are derived from a previous study (Mazeau, 2011), where the surfaces were created from the super-crystalline models of cellulose Iβ allomorph (Mazeau, 2005) laterally cleaved along designated crystallographic planes. Three surfaces were considered, namely the (1 0 0), the (1 1 0) and the (1 −1 0) (see Fig. 1b-d). The surfaces (1 1 0) and (1 −1 0) possessed each three layers of eight chains, each chain being eight residues long, while the surface (1 0 0) consisted of five layers of six chains of eight residues. Typical dimensions of the periodic boxes parallel to the surfaces were around $5 \times 4\,nm^2$, while the perpendicular dimension was set to 10 nm. The surfaces were relaxed prior to the addition of the xylan fragment.

We have considered only unsubstituted fragments of linear xylan, of either 5 or 25 skeletal residues. Their initial conformations were taken from a previous conformational analysis, which included calculation of their adiabatic potential energy surface, coupled with the conformational statistics of the polymer chains using a Metropolis Monte Carlo approach (Mazeau, Moine, Krausz, & Gloaguen, 2005). In nature, the xylan molecules are branched by Ara*f*, GlucA (often methylated) and acetyl moieties (Ebringerova & Heinze, 2000). However, it was shown that the linear portions of the chains were responsible for the xylan adsorption on cellulose (Kabel, van den Borne, Vincken, Voragen, & Schols, 2007; Koehnke et al., 2011). Thus, we have concentrated our efforts only on the backbone of the xylan chains in this first version of the CG.

Various MD trajectories were performed, either on an isolated xylan chain of 25 residues, in order to capture its intrinsic conformational properties, or on an aggregate of two xylan chains of 25 residues, in order to study how they interact with each other. Models of the cellulose–xylan complex were also provided. A single fragment of xylan of five residues was inserted in the simulation box above the cellulose surface in a random orientation and the adsorption was then modeled using MD. Calculations were repeated three times on every surface model, modifying the initial orientation of the xylan chain with respect to the cellulose fiber axis. Trajectories involving the (1 1 0) surface were issued from a previous study (Mazeau & Charlier, 2012), those involving the (1 −1 0) and (1 0 0) planes were specifically calculated for this study.

2.2. Development of the CG

Our CG included intra-molecular interactions within the xylan chains, and inter-molecular counterparts of xylan to xylan and xylan to cellulose. The global structure of the CG was very similar to the traditional empirical atomistic force-fields, containing bonding and non-bonding energies (Li et al., 2005). The complete CG can be written as follows:

$$\begin{aligned} E_{\text{total}} &= E_{\text{bonds}} + E_{\text{angles}} + E_{\text{torsion}} + E_{\text{nonbond}} \\ E_{\text{nonbond}} &= E_{\text{inter-xylan}} + E_{\text{xylan-cellulose}} \end{aligned} \quad (1)$$

where the bonding energy comprises three terms: the stretching energy E_{bonds}, the angular deformational energy E_{angles} and the torsional energy E_{torsion}. The nonbonding term E_{nonbond} is composed of the inter-molecular energy between the xylan grains $E_{\text{inter-xylan}}$ and between xylan and cellulose grains $E_{\text{xylan–cellulose}}$.

2.3. Intra-molecular CG potentials of xylan

The CG bonding parameters were derived from the atomistic trajectories of a single xylan chain of DP (degree of polymerization) 25, which were mapped into CG trajectories. The distributions of the distances, bond angles and dihedral angles between two, three and four consecutive beads, respectively, were extracted and fitted into a Boltzmann-inverted empirical potential model. The Boltzmann inversion simply uses the common formula (Muller-Plathe, 2002) that relates a given potential E to the normed probability distribution P of a molecular system in equilibrium at temperature T through:

$$E = -k_B T \ \text{Ln}(P) \quad (2)$$

The probability distributions, P, for a bond distance r and a bending angle θ were normalized by their corresponding volume elements, r^2 and $\sin\theta$, respectively (Fritz, Harmandaris, Kremer, & van der Vegt, 2009).

The stretching energy was characterized by a harmonic potential:

$$E_{\text{bonds}}(r) = \frac{1}{2} k_{\text{stretching}} (r - r_0)^2 \quad (3)$$

where $k_{\text{stretching}}$ is the force constant and r_0 is the equilibrium bond distance between two consecutive beads. The parameters $k_{\text{stretching}}$ and r_0 were adjusted in order to minimize the difference between the distribution of the bond distance extracted from all atoms simulations and the normed probability distribution of inversed potential model in the sense of RMSD (root mean square deviation).

The bending energy was described by square cosines potential:

$$E_{\text{bending}}(\theta) = k_{\text{ang}} (\cos\theta - \cos\theta_0)^2 \quad (4)$$

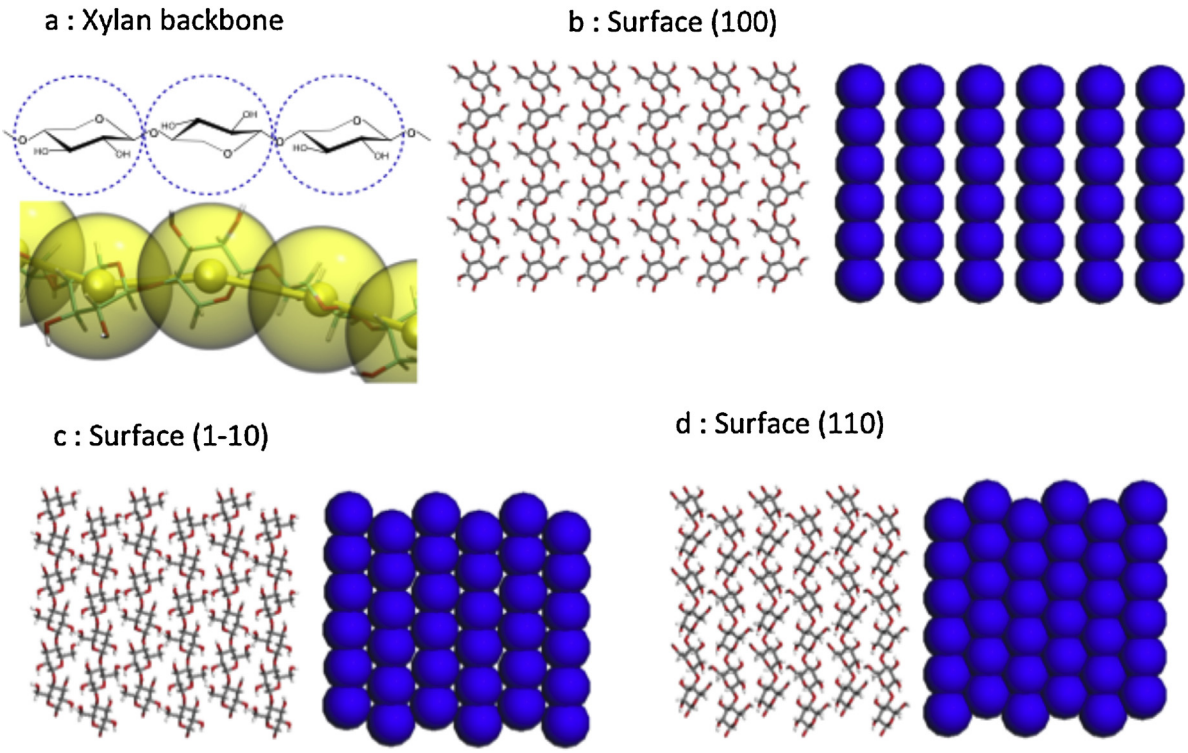

Fig. 1. a: Mapping a xylan chain at the CG level. b-d: Atomistic and coarse grain views of the various cellulose surfaces, for clarity, only six chains of six residues each are displayed.

where θ is the bond angle of three consecutive beads, k_{ang} the potential constant and θ_0 the equilibrium angle. Parameters k_{ang} and θ_0 were adjusted to accurately reproduce the probability distribution extracted from all-atom simulations.

A Fourier progression form described the dihedral energy:

$$E_{torsion}(\varphi) = \sum_{n=1}^{n=3} \frac{U_n}{2}(1 - \cos(n\varphi - \varphi n)) \quad (5)$$

where φ is the dihedral angle of four consecutive CG particles, φ_n is the phase angle, n the potential period and U_n the barrier energy. Parameters U_n and φ_n were iterated until the torsion angle probability distribution matched the Boltzmann-inverted potential model.

2.4. Inter-molecular CG potentials

2.4.1. Xylan–xylan potential

The inter-xylan potential at the CG level was derived from the atomistic trajectories of an aggregate of two xylan chains of DP 5 each, which were first mapped into CG trajectories. The distribution of shortest distances between two xylan chains was extracted and used as the reference distribution $f_0(r)$.

A Morse model described the inter-xylan beads potential:

$$E_{xylan-xylan}(r) = D_e(1 - e^{-\alpha(r-r_0)})^2 \quad (6)$$

where D_e is the depth of the potential well, r is the distance between non-bonding beads, r_0 is the equilibrium distance and α a parameter controlling the width of the potential energy curve.

The initial values of the parameters D_e, r_0 and α were derived from the Boltzmann-inverted distribution $f_0(r)$. These initial values were used to produce a CG MD trajectory of a molecular system containing two interacting CG xylan chains of DP 5 each, allowing an estimate of the corresponding distribution $f(r)$ of the shortest distance between two chains. The difference between the target distribution $f_0(r)$ and the actual one $f(r)$ was quantified using the following objective function:

$$f = \sum \exp\left(-\frac{|r - r_m|}{L}\right)(f(r) - f_0(r))^2 \quad (7)$$

where r_m and L correspond, respectively, to the position of the distribution peak and to the width of the reference distribution. In this equation, the exponential term is used to guarantee stronger deviations at small distances.

In the initial stage, the value of the objective function was far from minimal. The three parameters of the Morse model were iteratively optimized until a satisfactory concordance between $f_0(r)$ and $f(r)$ was achieved.

2.4.2. Xylan–cellulose potential

The xylan to cellulose potential at the CG level was derived from the atomistic trajectories of a xylan oligomer of five residues adsorbed on the (1 1 0) surface of cellulose (Mazeau & Charlier, 2012) and first mapped into CG trajectories. The distribution of the distance between the middle bead of the xylan chain and cellulose surface was extracted and used as the target distribution $g_0(r)$.

The xylan–cellulose potential is described by a Lennard–Jones (LJ) 12-6 model:

$$E_{xylan-cellulose}(r) = 4\varepsilon\left[\left(\frac{\sigma}{r}\right)^{12} - \left(\frac{\sigma}{r}\right)^{6}\right] \quad (8)$$

where ε is the depth of the potential well, σ is the distance at which the potential is minimal, r is the distance between the beads.

The initial values of the LJ parameters (ε and σ) were derived from the direct force matching of the atomistic trajectories. The first CG simulation, performed with the initial values of the LJ parameters, allowed producing $g(r)$, the distribution of the distances between the xylan beads and those of the cellulose surface. However, $g(r)$ was different from the target distribution $g_0(r)$. The optimization of the LJ parameters was thus performed until the

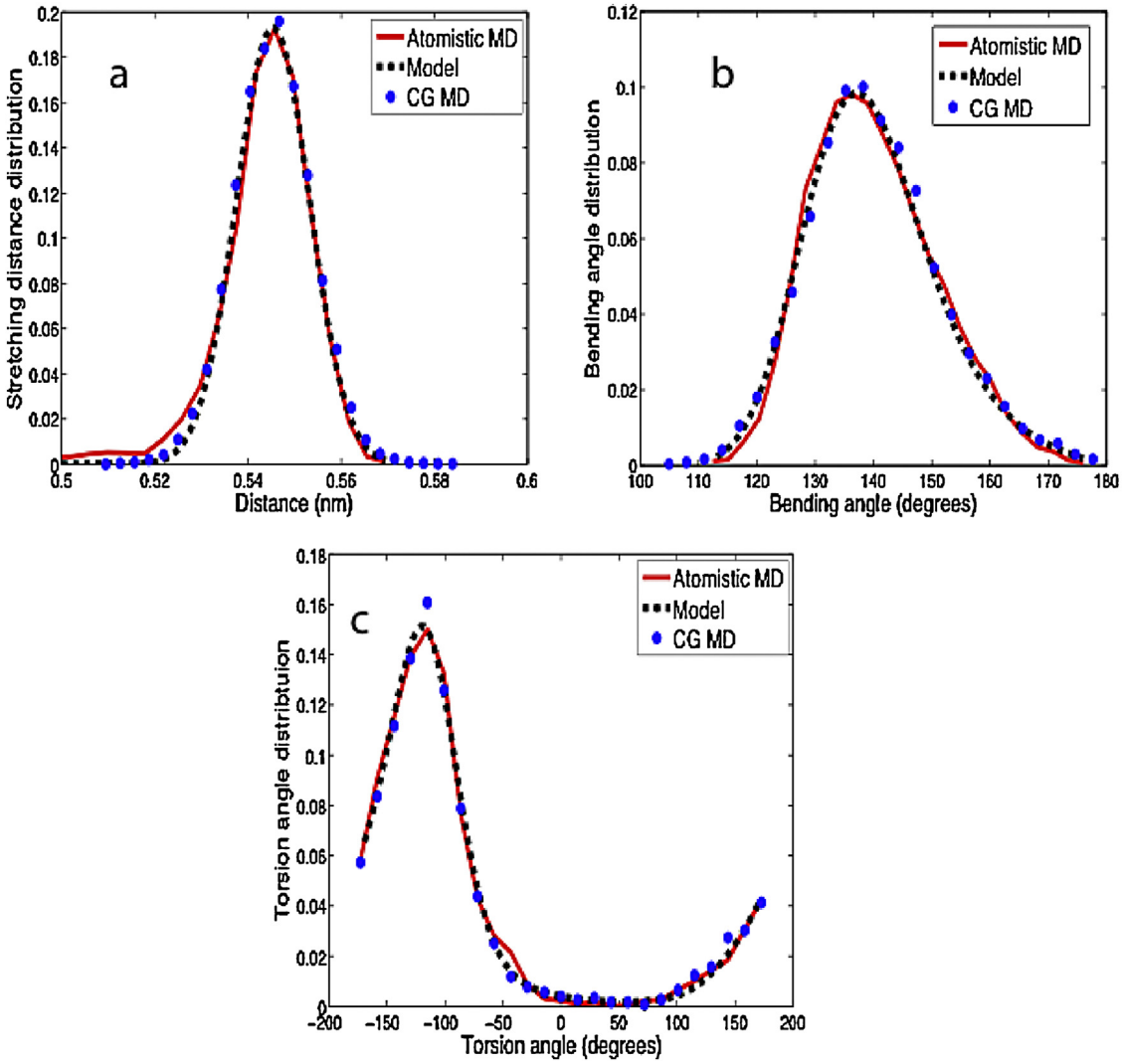

Fig. 2. Distributions of the bond length (a), bond angle (b) and torsional angle (c) in a single xylan chain. The red solid lines quoted "Atomistic MD" are obtained from atomistic molecular dynamic trajectories. The dotted lines quoted "Model" correspond to fits using the Boltzmann-inverted potential models. The blue dots quoted "CG MD" correspond to the distributions derived from CG simulation. (For interpretation of the references to color in this figure legend, the reader is referred to the web version of this article.)

objective function (which is similar to the Eq. 7), that compares the square of the difference between $g(r)$ and $g_0(r)$, was minimal.

2.5. Computational details

The presented work used an in-house CG molecular dynamic simulation software, which solved Newton equations using a Velocity Verlet integrator (Tuckerman, Berne, & Martyna, 1992), with Nosé–Hoover chains thermostat (Martyna, Klein, & Tuckerman, 1992) and Link-Cell Verlet neighbor list (Grest, Dünweg, & Kremer, 1989) construction.

All CG parameters were derived using the same simulation details. The initial CG molecular configurations were equilibrated for 1 ns with *NVT* or *NPT* ensemble. The systems were then simulated with *NVT* or *NPT* ensembles for 25 ns with time step $\Delta t = 25$ fs. A total of 10 000 time steps of CG dynamical trajectory were then sampled.

2.6. Application of the CG

2.6.1. Conformational statistics of a single xylan chain

Ten thousand xylan chains of 200 residues each have been generated according to a Monte-Carlo procedure. The xylan average size is related to the persistence length Lp as a function of DP. It is defined as the projection of the end-to-end distance vector on the first bond of the chain and represents an estimation of the length where the propagation of the chain in a given direction is preserved.

2.6.2. Xylan in the solid state

The initial configuration of amorphous xylan system consists of 200 xylan chains of DP 30 each. They were consecutively generated and inserted in a periodic simulation box of size $10 \times 10 \times 10\,\text{nm}^3$. The entire system was then equilibrated in the *NPT* ensemble for 500 ps, the production sampling was then carried out by a simulation under *NPT* ensemble. Both equilibration and production simulations were performed at 300 K and 1 atm with a time step of 25 fs; the total sampling duration was 25 ns. Fig. S1 in the supplementary material file gives the time evolution of the potential energy: it remained constant after about 4 ns, indicating that the system reached equilibrium.

2.6.3. Adsorption of xylan on cellulose

At first, we have studied at the CG level the adsorption of a single xylan chain on the different surfaces of cellulose. This xylan chain consisted of 36 skeletal beads; the (1 1 0), (1 0 0) and (1 −1 0) surfaces of the Iβ allomorph (Nishiyama, Langan, & Chanzy, 2002)

were mapped at the CG level (see Fig 1b-d to visualize the difference between the all-atom and CG descriptions of the various cellulose surfaces). In modeling the adsorption of xylan, each of these surfaces contained a single frozen layer of 40 cellulose chains of 40 beads each, their total sizes being of the order of $22 \times 22\ nm^2$. Periodic boundary conditions were applied in the directions parallel to the cellulose surface.

The modeling strategy was similar to the one used in the atomistic simulations (Mazeau & Charlier, 2012). In the initial stage, the xylan chain was inserted in the simulated medium above the cellulose surface, the model was then equilibrated for 20 ns, and simulated under the *NVT* ensemble at $T = 300$ K for 50 ns with time step of 25 fs (see Fig. S2 in the supplementary material). Six such CG-MD simulations were performed respectively for each cellulose surface, differing in the initial conformation, position and orientation of the xylan chain with respect to the cellulose surface to ensure reproducibility of the results and reasonable conformational sampling.

As a final application, we have studied still at the CG level the wrapping of a cellulose crystal by multiple xylan chains. The cellulose crystal of the Iβ allomorph contained 65 chains of 48 grains each (a total of 1248 glucosyl residues). Among these, the 26 surface chains were active for the interaction with xylan. The cellulose crystal had a hexagonal-like cross-section, exposing 2×8 chains of the (1 1 0) surface, 2×4 chains of the (1 −1 0) surface and 2×4 chains of the (1 0 0) surface. Periodic boundary conditions were applied along the *Z* direction (chain axis). Then 50 CG chains of xylan of 30 beads each were positioned randomly around the crystal and the system was relaxed by NVT molecular dynamics at 300 K for 8.37 ns (see Fig. S3 of the supplementary material). This procedure was repeated four times so that the final model contained 200 xylan chains of 30 beads each (a total of 6000 xylosyl residues). A final relaxation of 1.67 ns was performed.

3. Results and discussion

3.1. CG parameters

In this first version of the CG, we developed intra-molecular CG parameters exclusively for the xylan chains. Following our previous atomistic modeling (Mazeau & Charlier, 2012), the cellulose parameters were intentionally neglected due to the weak conformational response of cellulose during its interaction with xylan. In order to quantify this response, the average displacement of each CG grain away from its corresponding average coordinate position was measured and normalized by the average distance between two neighbor chains. This normalized value had an average of 0.0141%, ranging from a maximum of 0.024% to a minimum of 0.006%. In addition, we restricted the developments of the CG inter-molecular potentials to the xylan–xylan and xylan–cellulose interactions; the interactions between two cellulose fibers were not considered. In addition, since the two cellulose layers below the crystal surface were frozen in the atomistic trajectory, they were ignored during the development of the CG intermolecular potential between xylan and cellulose. However their interactions with xylan were naturally included in the interaction of the active cellulose surface with xylan in the CG potential. This strategy reduces the number of degrees of freedom in the CG model and decreases the computational effort of the CG MD simulation.

3.2. Intra-molecular potentials

All-atom molecular dynamics simulations of an isolated xylan chain were performed and mapped at the CG level. The distributions of bond distances, bond angles and dihedral angles between the mass centers of two, three and four consecutive xylan residues extracted from the atomistic trajectories are displayed in Fig. 2 as red solid lines quoted "Atomistic MD".

The Boltzmann-inversion procedure was then applied in order to get the optimal values of the CG parameters for E_{bonds}, E_{angles} and $E_{torsions}$, respectively. The optimal parameters for the bond stretching potential were: $k_{stretching} = 20246.54\ kJ/nm^2$, with $r_0 = 0.5451$ nm, and those for the angle bending were $k_{ang} = 74.75\ kJ/^{\circ 2}$ with $\theta_0 = 139.4^{\circ}$. For torsion potential, the optimized parameters were $U_1 = 5.3179$ kJ/mol, $U_2 = 0.2305$ kJ/mol, $U_3 = 0.4068$ kJ/mol, $\varphi_1 = 48.65^{\circ}$, $\varphi_2 = 170.74^{\circ}$, $\varphi_3 = 219.16^{\circ}$. The corresponding curves are also displayed in Fig. 2a–c as thin dashed lines. CG MD simulations were then performed for a single CG xylan chain of 25 beads using the derived bonding potentials. The resulted distributions of bond distances, bond angles and dihedral angles from CG simulations are indicated by the blue dots in Fig. 2a–c.

The good concordance of the three distributions curves suggests that the functional form of the CG function is appropriate and that the derived intra-molecular potential was able to precisely reproduce the conformational properties of the xylan chains as observed at the atomic level.

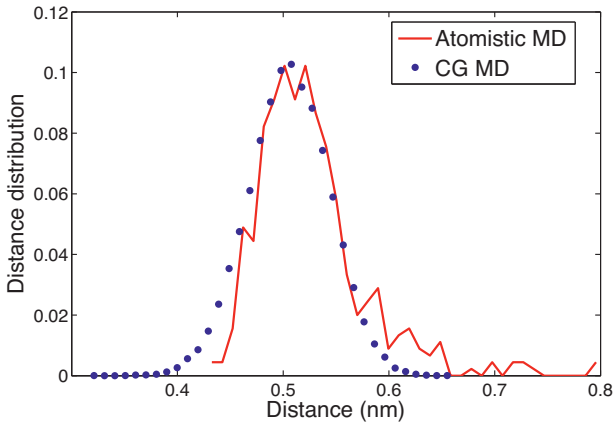

Fig. 3. Distributions of the inter-molecular distance between beads of two xylan chains. The red solid line quoted "Atomistic MD" is obtained from atomistic molecular dynamic trajectories. The blue dots quoted "CG MD" correspond to the distributions derived from CG simulation. (For interpretation of the references to color in this figure legend, the reader is referred to the web version of this article.)

3.3. Inter-molecular potentials

Unlike the derivation of the bonding CG potentials, which is performed by direct parameters adjustment method, the development of the non-bonding potentials requires parameters post-adjustment. Generally, this is achieved by iterating CG simulations while scanning the parameters of empirical potential model until the target distribution is well reproduced.

All-atom molecular dynamics simulations of two interacting xylan chains were performed and mapped at the CG level. The distribution of the shortest intermolecular distance between the mass centers of the xylan residues is displayed in Fig. 3 in red solid line. The initial figure of the merit function, which estimates the difference between the actual distribution of the bead distances and the reference distribution, was 0.081. The optimization process required only four iterations; the merit function took the minimal value of 0.0015. Further iterations did not improve the agreement. The final optimized parameters of the Morse function describing the xylan–xylan interaction at the CG level were $r_0 = 0.5731$ nm, $\alpha = 3.475\ nm^{-1}$, $D_e = 6.102$ kJ/mol. The distribution of the shortest distance obtained using CG simulation using the optimized parameters is shown in Fig. 3.

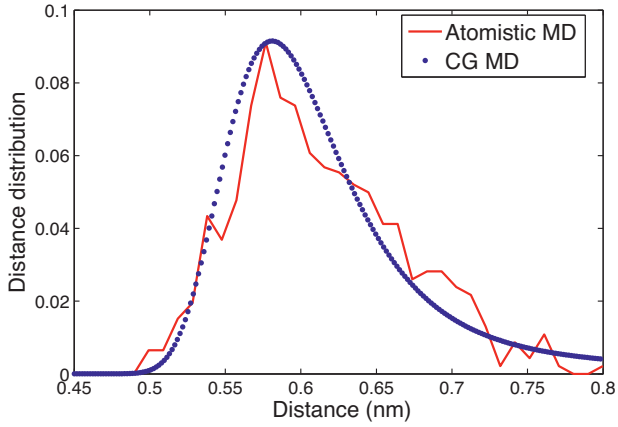

Fig. 4. Distributions of the shortest inter-molecular distance between beads of xylan and those of cellulose. The red solid line quoted "Atomistic MD" is obtained from atomistic molecular dynamic trajectories. The blue dots quoted "CG MD" correspond to the distributions derived from CG simulation. (For interpretation of the references to color in this figure legend, the reader is referred to the web version of this article.)

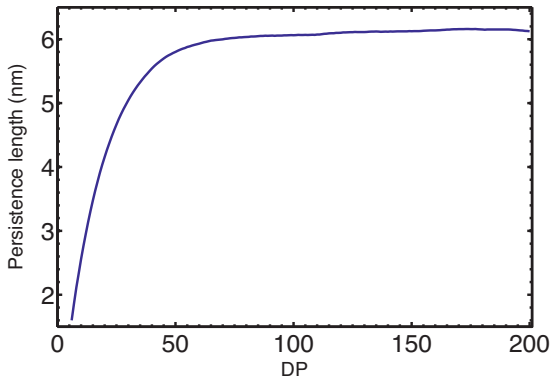

Fig. 5. Evolution of the predicted persistence length estimated at the CG level of xylan as a function of its degree of polymerization.

The distributions of the shortest intermolecular distances between the mass centers of the xylan residues and that of cellulose from all-atom molecular dynamics simulations of xylopentaose adsorbed on the (1 1 0) surface of cellulose (Mazeau & Charlier, 2012) are displayed in Fig. 4. The merit function has an initial value of 0.3631 and gets stabilized at 0.0024 at the end of the optimization process. The optimal parameters of the Lennard–Jones function describing the CG potential between xylan and cellulose were $\varepsilon = 2.13$ kJ/mol and $\sigma = 0.635$ nm. The distribution of the distance obtained using CG simulation with the optimized parameters is shown in Fig. 4.

For both systems, xylan–xylan and xylan–cellulose, there is a good concordance between the curves estimated from atomistic simulations and those derived from CG simulations, indicating that the generic macroscopic properties of the atomistic model have been translated into CG one.

The energies of interaction between xylan and the surfaces (1 1 0), (1 −1 0) and (1 0 0) of cellulose estimated from atomistic simulations were −32.175, −39.288 and −41.924 kJ/mol × monomer, respectively. In order to consider the surfaces (1 −1 0) and (1 0 0) of cellulose at the CG level, we scaled the potential energy density relative to the (1 1 0) surface. Setting the model of xylan and the surface (1 1 0) of cellulose as reference, the coefficients of energy density would be 1, 1.221 and 1.303 for the beads belonging to the (1 1 0), (1 −1 0) and (1 0 0) surfaces, respectively.

3.4. Applications of the CG

3.4.1. CG models of xylan

The developed CG was first applied to predict some fundamental properties of xylan in order to estimate the reliability of the CG approach.

We have performed simulation of isolated xylan chains differing in their degree of polymerization in order to predict their unperturbed dimensions. Fig. 5 gives the evolution of the predicted persistence length (Lp) with DP. As expected Lp increases rapidly at low DP and showed an asymptotic limit from DP 50. LP stabilized at the value of 6.25 nm, which is reasonably close to the span 6.6–9.2 nm obtained experimentally (Dervilly-Pinel, Thibault, & Saulnier, 2001).

We have also generated a CG bulk of xylan: its equilibrium density was 1.144 g cm^{-3}. The density of the crystal structures of xylan, estimated from the unit cell dimensions and content reaches 1.54 g cm^{-3} (Nieduszynski & Marchessault, 1971). On the other hand, the density of an atomistic model of xylan in the amorphous state is predicted to be 0.92 g cm^{-3}. The predicted density of the CG xylan model, which is in the good range, suggests that it contains disorganized domains mixed with organized ones. This result is consistent with the experimental observations:

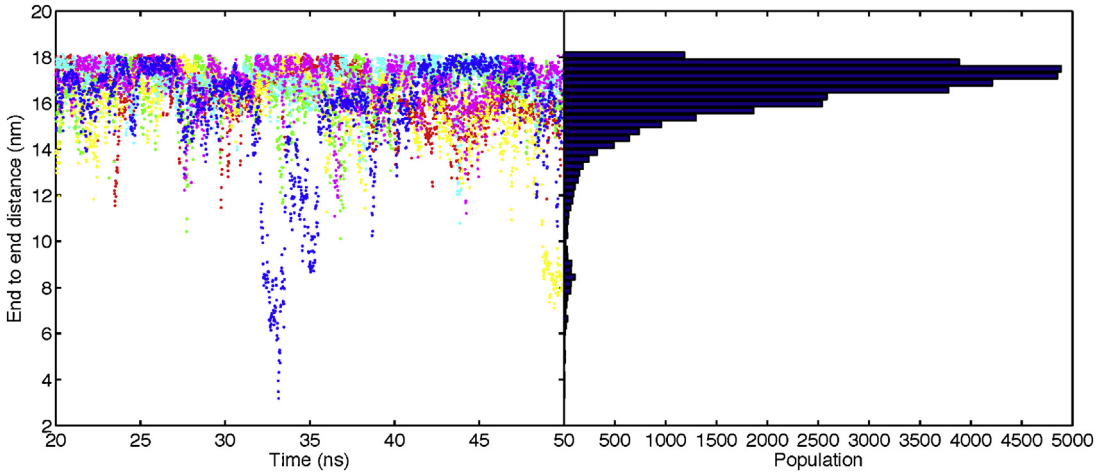

Fig. 6. Surface (1 1 0). Left: Evolution of the end-to-end distances with time for the xylan chains. The colors differentiate the six independent simulations. Right: Distribution histogram of the end-to-end distance. (For interpretation of the references to color in this figure legend, the reader is referred to the web version of this article.)

materials made of native branched xylan are essentially amorphous whereas those made of debranched xylan may contain up to 20% of crystalline phases (Heikkinen et al., 2013; Hoeije, Sternemalm, Heikkinen, Tenkanen, & Gatenholm, 2008; Mikkonen et al., 2012; Peng, Ren, Zhong, & Sun, 2011; Sternemalm, Hoeije, & Gatenholm, 2008; Stevanic et al., 2011). It is therefore not surprising that the density at equilibrium of our debranched xylan is between that of the two extreme organization states.

The overall similarity between the available data coming either from experiments or from atomistic modeling using well-established force-fields and the one from our newly developed CG suggests that our CG parameters were adequate.

3.4.2. Adsorption of a single xylan chain on the different cellulose surfaces

The developed CG was then applied to study the adsorption of a 36 grain single xylan chain on the (1 1 0), (1 −1 0) and (1 0 0) surfaces of the Iβ allomorph of cellulose. The surfaces considered in this section are infinite and planar. They are not designed to describe the real surfaces of cellulose crystals, which contain a limited number of chains. The choice of the surface models was motivated by the objective to further test the robustness of the CG approach and to reveal the variety of adsorption features depending on the cellulose surface nature. It is consequently required to use ideal conditions, where the xylan chain are only influenced by the surface and not perturbed by border effects, periodicity, curvature or even surface density. We analyzed the global conformation of the xylan backbone, which is described by its end-to-end distance, L_{xylan}, and its orientation with respect to the cellulose fiber axis, a parameter quantified by the variable DZ, the projection of L_{xylan} along the direction of cellulose axis (Mazeau & Charlier, 2012). The temporal evolution and population histogram of L_{xylan} for the (1 1 0), (1 −1 0) and (1 0 0) surfaces are given in Figs. 6, 8, and 10, respectively, while that of DZ are given in Figs. 7, 9, and 11, respectively.

Histograms of L_{xylan} show two populations: high values in the range 15–18 nm correspond to extended conformations (Fig. 12, right). The helical pitch of the xylan chains in the crystal state is about 0.5 nm per residue (Nieduszynski & Marchessault, 1971), a similar extension is observed here. Low values of L_{xylan} ranged from 2 to 8 nm. In this second population, the conformations of the adsorbed xylan chain are coiled. They are made of two extended segments kinked at the center of the chain. A typical example of a kinked xylan chain adsorbed on cellulose is given in Fig. 12 (left).

Similarly, histograms of the DZ parameter show two populations. Large values of +18 or −18 nm indicate that the xylan chain is aligned to the fiber axis, both in parallel and anti-parallel orientations, respectively. The second population has low values of DZ, ranging from −5 to +5 nm.

Interestingly, comparing the time evolution of the conformation and the orientation of xylan adsorbed on cellulose showed that DZ and L_{xylan} varied simultaneously, suggesting that these two parameters were highly correlated. In the simulations involving surface (1 1 0) for instance, this correlation is quite obvious in the blue trajectory (Figs. 6 and 7) in which a large fluctuation appeared at 33 ns and in the yellow one at around 50 ns. A similar phenomenon could also be observed in the simulations on surfaces (1 0 0) and (1 −1 0).

Consequently, xylan adsorbed on cellulose has two different states. It is mostly aligned along the fiber axis and either extended (called hereafter state A) or kinked (state B). The adsorption features of xylan depended strongly on the interacting surface. State A dominates with the surface (1 1 0), whereas states A and B are almost equally probable with surface (1 −1 0). This result was very surprising, considering that these two surfaces are very similar regarding surface roughness and degree of exposure of hydrophilic groups (Mazeau, 2011). Nevertheless in these two surfaces, some dissimilarity in dynamics of the surface chains has been found, using both MD and spin–lattice relaxations measured by NMR (Bergenstrahle, Wohlert, Larsson, Mazeau, & Berglund, 2008). State B dominates with surface (1 0 0). This surface, which is often quoted as hydrophobic and flat, has a character totally different from the two other surfaces. Thus, it is not surprising that the adsorption of xylan differs on this surface.

The adsorption of xylopentaose on the (1 1 0) surface has been modeled at the atomistic level (Mazeau & Charlier, 2012). Similar features are observed: xylan in the adsorbed state is extended and mostly aligned along the fiber axis. This similarity was unexpected, considering that no constraint was applied; it gives an additional support to the reliability of the CG developed here. The occurrence of coiled conformations, which is only occasional with the (1 1 0) surface but statistically significant with the other surfaces, occurring in the CG model is however a substantial difference. This feature is linked to the chain length. It could not be observed on a short oligomer of five residues. We have performed atomistic simulations similar to those published earlier (Mazeau & Charlier, 2012) but with xylan chains of increasing DP. Fig. S4 in the supplementary material gives a representation of the model of DP 25 at equilibrium. The adsorbed xylan showed two kinks, the first originates from re-puckering of a pyranose ring while the second is due to the exploration of the potential energy well by the glycosidic bond located at Φ, Ψ: 37° and 277°, respectively (Φ: O5-C1-O4-C4 and Ψ C1-O4-C4-C5). Similar to the atomistic description, the 36 beads CG xylan chain shows kinked or curved conformations. The correlation between L and DZ is another feature revealed specifically at the CG level.

3.4.3. Adsorption of multiple xylan chains on a cellulose crystal

There is a renewed considerable interest in materials made of xylan reinforced by cellulose (Gordobil, Egues, Urruzola, & Labidi, 2014; Koehnke, Lin, Elder, Theliander, & Ragauskas, 2012; Kohnke, Elder, Theliander, & Ragauskas, 2014; Saxena, Elder, Pan, & Ragauskas, 2009; Saxena, Foston, Kassaee, Elder, & Ragauskas, 2012; Sun et al., 2014). We have generated in this section a biomimetic model representing both, the basic element of the primary plant cell wall and a manufactured bio-sourced material. The model is based on a xylan phase consisting of 200 chains of 48 residues covering a single crystal of cellulose having a length of 24.47 nm and a width of about 3–5 nm (Fig. 13).

The distributions of the xylan beads above the different surfaces of cellulose as a function of the distance from these surfaces are given in Fig. 14. The probability peaks appearing at small distances indicate that xylan accumulates at the interface. In addition, large fluctuations of the amplitude of the peaks suggest that xylan is structured close to the surfaces. These features taper progressively with the distance from the surface and disappear at about 2 nm. Only three layers of organized xylan could be observed for each cellulose surface, and far from the surface, the xylan was amorphous. Interestingly, the position of the first peak and the thickness of the layers were found to depend on the surface type. It seems that these characteristics are more due to the interaction energies between xylan and the various surfaces of cellulose than to the alignment of the xylan chains to the cellulose axis. The larger the energy of interaction between xylan and the surface, the smaller is the distance at which the first peak occurs and the smallest is the thickness of the xylan layers.

For each surface, the normalized surface densities (NSD) for xylan beads correspond to the total number of xylan beads adsorbed on the surface divided by the area of the corresponding surface. To facilitate comparison, these quantities are normalized by the value obtained for surface (1 1 0). NSD for surface (1 1 0), (1 0 0) and (1 −1 0) are 1.0, 2.75 and 1.85, respectively. As expected, the key factor determining the local density of xylan at the interface

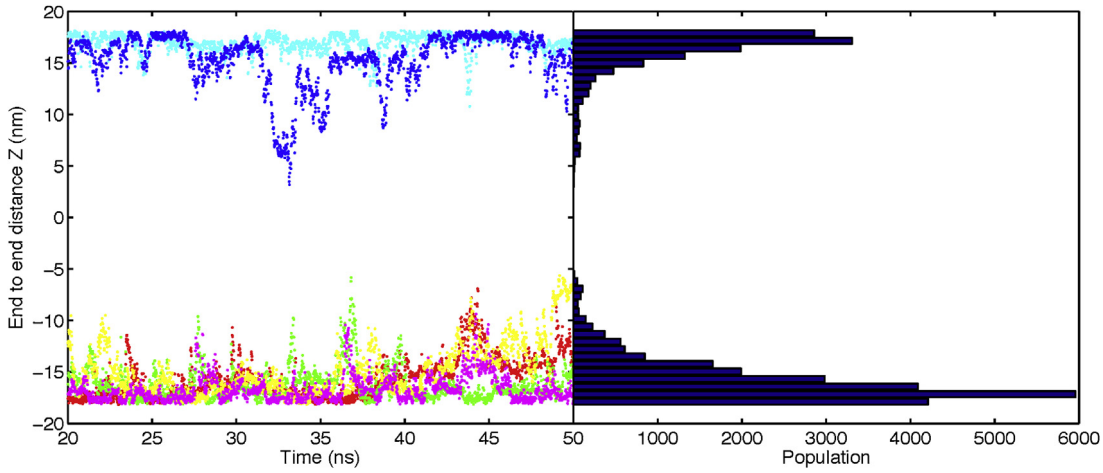

Fig. 7. Surface (1 1 0). Left: Evolution of the DZ distances with time. The colors differentiate six independent simulations. Right: Distribution histogram of the DZ distance. (For interpretation of the references to color in this figure legend, the reader is referred to the web version of this article.)

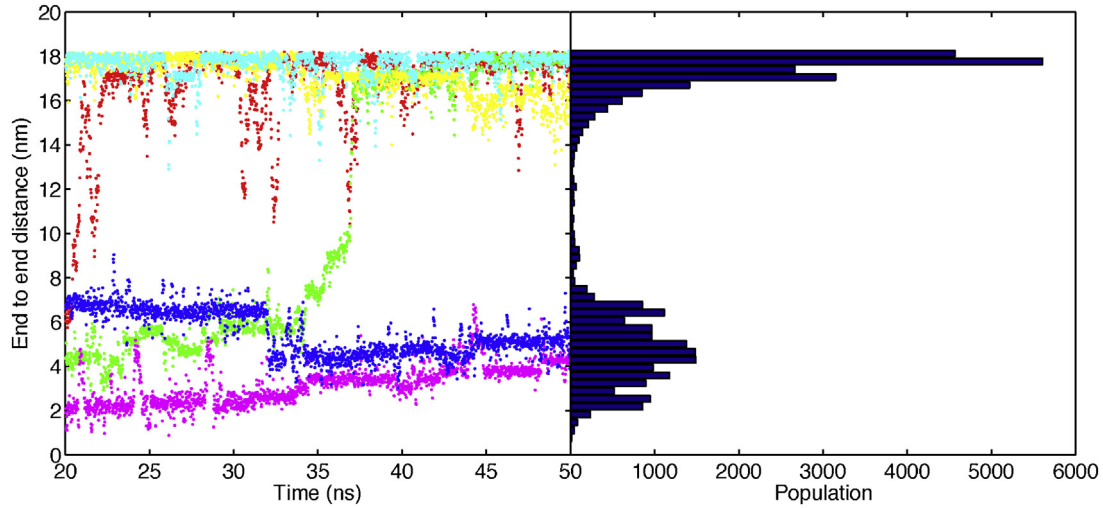

Fig. 8. Surface (1 −1 0). Left: Evolution of the end-to-end distances with time for the xylan chains. The colors differentiate the six independent simulations. Right: Distribution histogram of the end-to-end distance. (For interpretation of the references to color in this figure legend, the reader is referred to the web version of this article.)

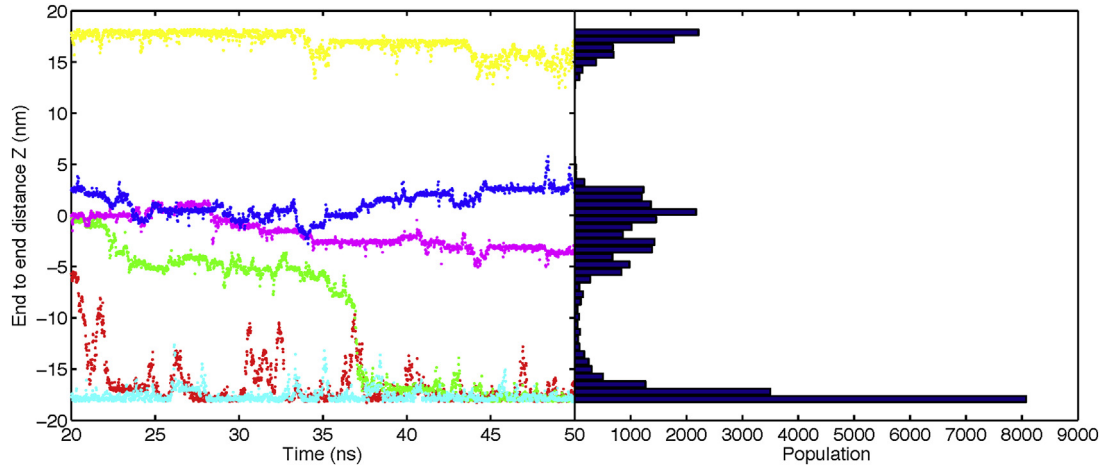

Fig. 9. Surface (1 −1 0). Left: Evolution of the DZ distances with time. The colors differentiate six independent simulations. Right: Distribution histogram of the DZ distance. (For interpretation of the references to color in this figure legend, the reader is referred to the web version of this article.)

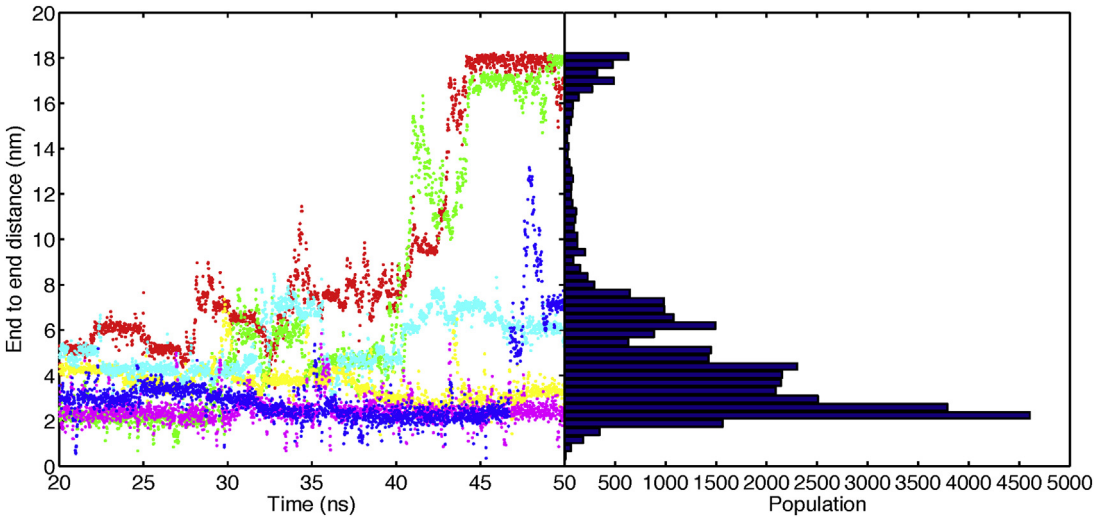

Fig. 10. Surface (1 0 0). Left: Evolution of the end-to-end distances with time for the xylan chains. The colors differentiate the six independent simulations. Right: Distribution histogram of the end-to-end distance. (For interpretation of the references to color in this figure legend, the reader is referred to the web version of this article.)

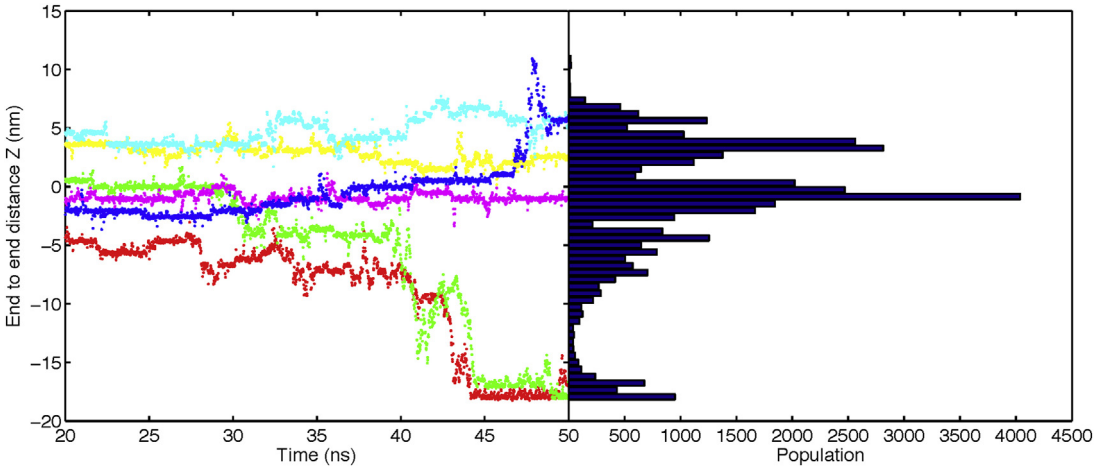

Fig. 11. Surface type (1 0 0). Left: Evolution of the DZ distances with time. The colors differentiate six independent simulations. Right: Distribution histogram of the DZ distance. (For interpretation of the references to color in this figure legend, the reader is referred to the web version of this article.)

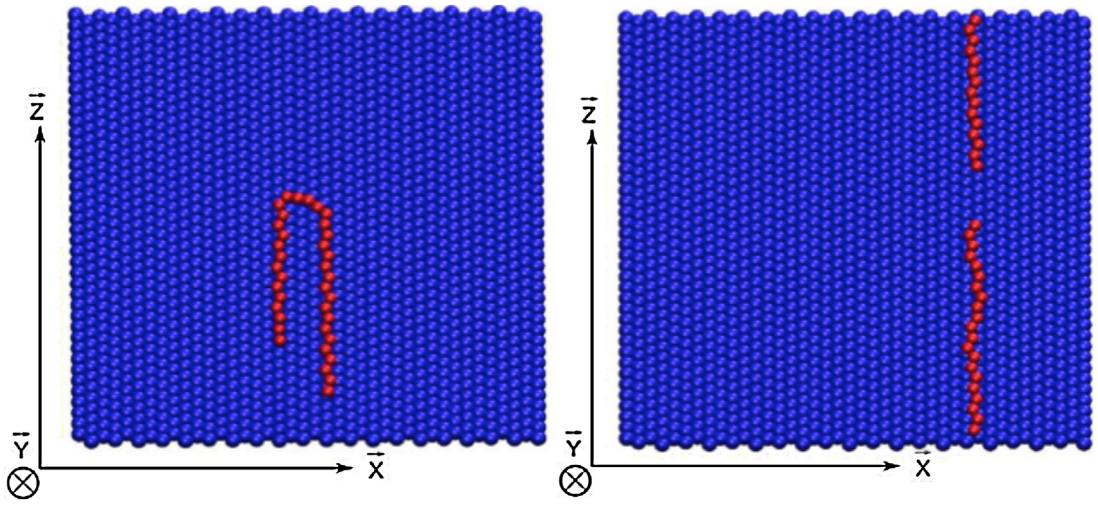

Fig. 12. Snapshots of the CG models of xylan adsorbed on the (1 1 0) surface of cellulose. Blue: cellulose beads, red: xylan beads. (For interpretation of the references to color in this figure legend, the reader is referred to the web version of this article.)

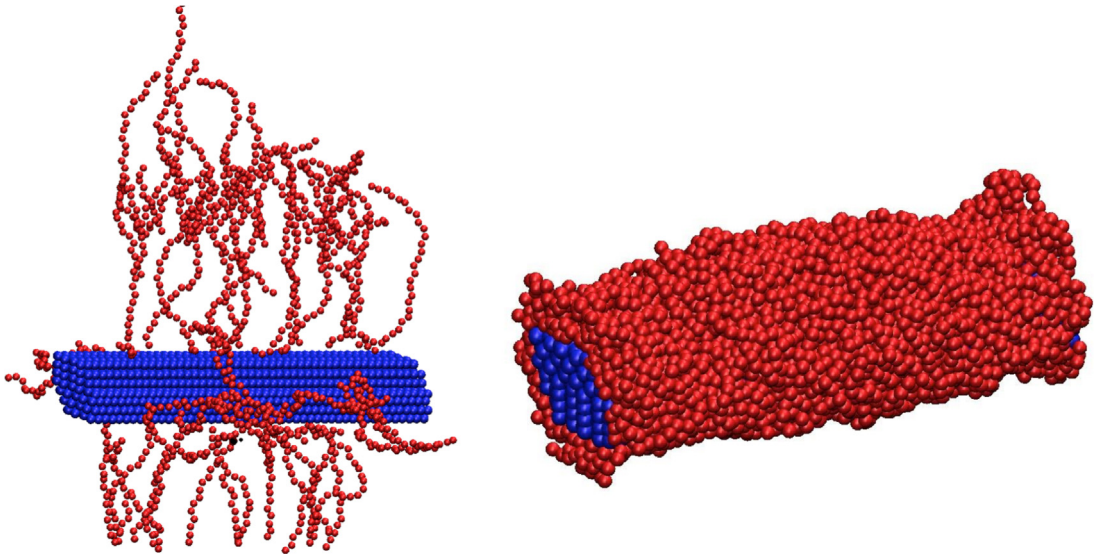

Fig. 13. Snapshots of the initial (left: a cellulose crystal surrounded by 50 chains of xylan) and equilibrated final (right: involving 200 xylan chains) model of cellulose–xylan complex. Cellulose beads are colored in blue, those of xylan in red. (For interpretation of the references to color in this figure legend, the reader is referred to the web version of this article.)

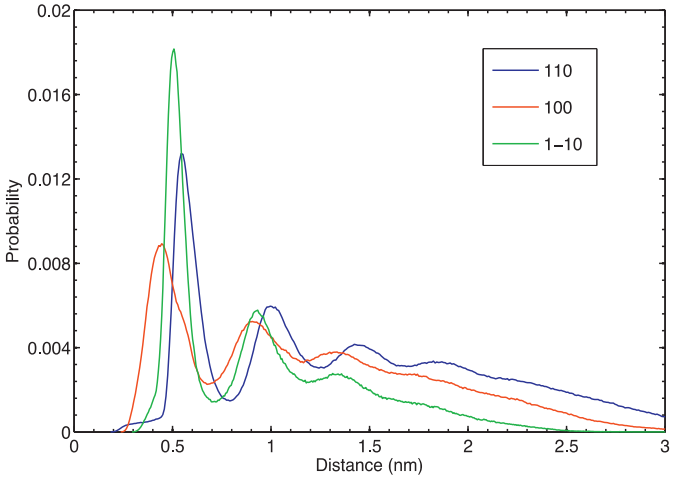

Fig. 14. Probability profiles of the xylan as a function of the distance from the cellulose surfaces. Blue: surface (1 1 0), green: surface (1 −1 0), red: surface (1 0 0) (For interpretation of the references to color in this figure legend, the reader is referred to the web version of this article.).

is the magnitude of the interaction energy between xylan and the cellulose surface. The alignment effect revealed in the previous section originates from kinetic effects.

Modeling the cellulose–xylan complex at the CG level instead of the atomistic one offers several benefits. Among these, the chain length is the first, although smaller than real chains, CG DP is however more realistic than that studied in the atomistic level modeling. CG modeling offers also the possibility to consider the (1 1 0), (1 −1 0) and (1 0 0) surfaces of the Iβ allomorph, which are the dominant surfaces in the external morphology of the native cellulose crystals (Mazeau, 2011). Last advantage with respect to the molecular modeling is the 9 μs total duration of the simulation; as opposed to the current maximum of several nanoseconds used in a typical atomistic modeling.

4. Conclusion and perspectives

We have developed a CG force field able to model unsubstituted xylan chains and their interactions with cellulose. This CG correctly reproduces the experimental unperturbed dimensions of single chains of xylan, their packing compactness in the bulk and their adsorption features on the (1 1 0) surface of cellulose modeled at the atomistic level. Remarkably, the CG model reveals that the skeletal extension of the xylan chain is correlated to its orientation with respect to the cellulose fiber axis and that the adsorption features depend strongly on the surface of cellulose. This force field may be further developed along various routes. Parameters for the side branches of xylan, namely Ara*f*, GlcA and Oac, can be implemented in order to provide structure to properties relationships. We can also consider non-spherical grains and anisotropic interactions (Zhu et al., 2013), in order to better account for the chemistry of the repeat units, while keeping the same CG mapping level. The interfacial effects in bio-sourced nano-composites made of xylan reinforced with cellulose nano-crystals will be explicitly presented in a future report.

Acknowledgements

This work was financed by the ANR grant ANALOGS ANR-BLAN08-3_310735. The authors acknowledge the help of Dr. H. Chanzy for valuable comments during the writing of this work.

Appendix A. Supplementary data

Supplementary data associated with this article can be found, in the online version, at http://dx.doi.org/10.1016/j.carbpol.2015.04.003

References

Adler, D. C., & Buehler, M. J. (2013). Mesoscale mechanics of wood cell walls under axial strain. *Soft Matter*, *9*(29), 7138–7144.

Albersheim, P. D. A., Roberts, K., Seferoff, R., & Staehelin, A. (2010). *Plant cell walls*. New York: Garland Science; Taylor and Francis Group; LLC.

Asztalos, A., Daniels, M., Sethi, A., Shen, T., Langan, P., Redondo, A., et al. (2012). A coarse-grained model for synergistic action of multiple enzymes on cellulose. *Biotechnology for Biofuels*, *5*, 55–70.

Atalla, R. H., Hackney, J. M., Uhlin, I., & Thompson, N. S. (1993). Hemicelluloses as structure regulators in the aggregation of native cellulose. *International Journal of Biological Macromolecules*, *15*(2), 109–112.

Bazooyar, F., Momany, F. A., & Bolton, K. (2012). Validating empirical force fields for molecular-level simulation of cellulose dissolution. *Computational and Theoretical Chemistry*, *984*, 119–127.

Bellesia, G., Chundawat, S. P. S., Langan, P., Redondo, A., Dale, B. E., & Gnanakaran, S. (2012). Coarse-grained model for the interconversion between native and liquid ammonia-treated crystalline cellulose. *The Journal of Physical Chemistry B*, *116*(28), 8031–8037.

Bergenstrahle, M., Wohlert, J., Larsson, P. T., Mazeau, K., & Berglund, L. A. (2008). Dynamics of cellulose–water interfaces: NMR spin–lattice relaxation times calculated from atomistic computer simulations. *The Journal of Physical Chemistry B*, *112*(9), 2590–2595.

Bu, L., Beckham, G. T., Crowley, M. F., Chang, C. H., Matthews, J. F., Bomble, Y. J., et al. (2009). The energy landscape for the interaction of the family 1 carbohydrate-binding module and the cellulose surface is altered by hydrolyzed glycosidic bonds. *The Journal of Physical Chemistry B*, *113*(31), 10994–11002.

Bu, L., Himmel, M. E., & Nimlos, M. R. (2010). Meso-scale modeling of polysaccharides in plant cell walls: An application to translation of CBMs on the cellulose surface. *ACS Symp. Ser.*, *1052*, 99–117 (Computational Modeling in Lignocellulosic Biofuel Production)

Carpita, N. C., & McCann, M. C. (2002). The functions of cell wall polysaccharides in composition and architecture revealed through mutations. *Plant Soil*, *247*(1), 71–80.

Caulfield, D. F. (1968). Questioning X-ray evidence of crystallizability of xylan in situ. *Tappi*, *51*(8), 371–372.

Dervilly-Pinel, G., Thibault, J. F., & Saulnier, L. (2001). Experimental evidence for a semi-flexible conformation for arabinoxylans. *Carbohydrate Research*, *330*(3), 365–372.

Ebringerova, A., & Heinze, T. (2000). Xylan and xylan derivatives – biopolymers with valuable properties. 1. Naturally occurring xylans structures, isolation procedures and properties. *Macromolecular Rapid Communications*, *21*, 542–556.

Ensing, B., Nielsen, S. O., Moore, P. B., Klein, M. L., & Parrinello, M. (2007). Energy conservation in adaptive hybrid atomistic/coarse-grain molecular dynamics. *Journal of Chemical Theory and Computation*, *3*, 1100–1105.

Evans, D. J., & Holian, B. L. (1985). The Nose–Hoover thermostat. *The Journal of Chemical Physics*, *83*(8), 4069–4074.

Fritz, D., Harmandaris, V. A., Kremer, K., & van der Vegt, N. F. A. (2009). Coarse-grained polymer melts based on isolated atomistic chains: Simulation of polystyrene of different tacticities. *Macromolecules*, *42*, 7579–7588.

Glass, D. C., Moritsugu, K., Cheng, X., & Smith, J. C. (2012). REACH coarse-grained simulation of a cellulose fiber. *Biomacromolecules*, *13*(9), 2634–2644.

Gordobil, O., Egues, I., Urruzola, I., & Labidi, J. (2014). Xylan–cellulose films: Improvement of hydrophobicity, thermal and mechanical properties. *Carbohydrate Polymers*, *112*, 56–62.

Grest, G. S., Dünweg, B., & Kremer, K. (1989). Vectorized link cell Fortran code for molecular dynamics simulations for a large number of particles. *Computer Physics Communications*, *55*(3), 269–285.

Gross, A. S., Bell, A. T., & Chu, J.-W. (2013). Preferential interactions between lithium chloride and glucan chains in N,N-dimethylacetamide drive cellulose dissolution. *The Journal of Physical Chemistry B*, *117*(12), 3280–3286.

Heikkinen, S. L., Mikkonen, K. S., Pirkkalainen, K., Serimaa, R., Joly, C., & Tenkanen, M. (2013). Specific enzymatic tailoring of wheat arabinoxylan reveals the role of substitution on xylan film properties. *Carbohydrate Polymers*, *92*, 733–740.

Henao, L., & Mazeau, K. (2008). The molecular basis of the adsorption of bacterial exopolysaccharides on montmorillonite mineral surface. *Molecular Simulation*, *34*, 1185–1195.

Henao, L. J., & Mazeau, K. (2009). Molecular modeling studies of clay-exopolysaccharide complexes: Soil aggregation and water retention phenomena. *Materials Science and Engineering C*, *29*, 2326–2332.

Henriksson, A., & Gatenholm, P. (2001). Controlled assembly of glucuronoxylans onto cellulose fibers. *Holzforschung*, *55*(5), 494–502.

Hoeije, A., Sternemalm, E., Heikkinen, S., Tenkanen, M., & Gatenholm, P. (2008). Material properties of films from enzymatically tailored arabinoxylans. *Biomacromolecules*, *9*, 2042–2047.

Izvekov, S., & Voth, G. A. (2005). A multiscale coarse-graining method for biomolecular systems. *The Journal of Physical Chemistry B*, *109*, 2469–2473.

Kabel, M. A., van den Borne, H., Vincken, J.-P., Voragen, A. G. J., & Schols, H. A. (2007). Structural differences of xylans affect their interaction with cellulose. *Carbohydrate Polymers*, *69*(1), 94–105.

Keegstra, K. (2010). Plant cell walls. *Plant Physiology*, *154*(2), 483–486.

Koehnke, T., Lin, A., Elder, T., Theliander, H., & Ragauskas, A. J. (2012). Nanoreinforced xylan–cellulose composite foams by freeze-casting. *Green Chemistry*, *14*, 1864–1869.

Koehnke, T., Oestlund, A., & Brelid, H. (2011). Adsorption of arabinoxylan on cellulosic surfaces: Influence of degree of substitution and substitution pattern on adsorption characteristics. *Biomacromolecules*, *12*(7), 2633–2641.

Kohnke, T., Elder, T., Theliander, H., & Ragauskas, A. J. (2014). Ice templated and cross-linked xylan/nanocrystalline cellulose hydrogels. *Carbohydrate Polymers*, *100*, 24–30.

Larsson, P. T. (2004). Interaction between cellulose I and hemicelluloses studied by spectral fitting of CP/MAS ^{13}C-NMR spectra. *ACS Symposium Series*, *864*, 254L 268 (Hemicelluloses).

Larsson, P. T., Hult, E. L., Wickholm, K., Pettersson, E., & Iversen, T. (1999). CP/MAS ^{13}C-NMR spectroscopy applied to structure and interaction studies on cellulose I. *Solid State Nuclear Magnetic Resonance*, *15*(1), 31–40.

Li, X., Ma, X., Huang, L., & Liang, H. (2005). Developing coarse-grained force fields for cis-poly(1,4-butadiene) from the atomistic simulation. *Polymer*, *46*, 6507–6512.

Liang, C. Y., Bassett, K. H., McGinnes, E. A., & Marchessault, R. H. (1960). Infrared spectra of crystalline polysaccharides. VII. Thin wood sections. *Tappi*, *43*, 1017–1024.

Lin, Y., Beckham, G. T., Himmel, M. E., Crowley, M. F., & Chu, J.-W. (2013). Endoglucanase peripheral loops facilitate complexation of glucan chains on cellulose via adaptive coupling to the emergent substrate structures. *The Journal of Physical Chemistry B*, *117*(37), 10750–10758.

Linder, A. P., Bergman, R., Bodin, A., & Gatenholm, P. (2003). Mechanism of assembly of xylan onto cellulose surfaces. *Langmuir*, *19*(12), 5072–5077.

Manyuhina, O. V., Fasolino, A., & Katsnelson, M. I. (2007). Slow dynamics in a model of the cellulose network. *Los Alamos Natl. Lab., Prepr. Arch., Condens. Matter*, *1–13*, arXiv:07060997v0701.

Marchessault, R. H., & Liang, C. Y. (1962). The infrared spectra of crystalline polysaccharides. VIII. Xylans. *Journal of Polymer Science*, *59*, 357–378.

Marchessault, R. H., Settineri, W. J., & Winter, W. (1967). Crystallization of xylan in the presence of cellulose. *Tappi*, *50*(2), 55–59.

Martyna, G. J., Klein, M. L., & Tuckerman, M. (1992). Nosé–Hoover chains: The canonical ensemble via continuous dynamics. *The Journal of Chemical Physics*, *97*, 2635–2643.

Mazeau, K. (2005). Structural micro-heterogeneities of crystalline Iβ-cellulose. *Cellulose*, *12*, 339–349.

Mazeau, K. (2011). On the external morphology of native cellulose microfibrils. *Carbohydrate Polymers*, *84*(1), 524–532.

Mazeau, K., & Charlier, L. (2012). The molecular basis of the adsorption of xylans on cellulose surface. *Cellulose*, *19*(2), 337–349.

Mazeau, K., Moine, C., Krausz, P., & Gloaguen, V. (2005). Conformational analysis of xylan chains. *Carbohydrate Research*, *340*(18), 2752–2760.

Mikkonen, K. S., Pitkaenen, L., Liljestroem, V., Mabasa Bergstroem, E., Serimaa, R., Salmen, L., et al. (2012). Arabinoxylan structure affects the reinforcement of films by microfibrillated cellulose. *Cellulose*, *19*, 467–480.

Mora, F., Ruel, K., Comtat, J., & Joseleau, J. P. (1986). Aspect of native and redeposited xylans at the surface of cellulose microfibrils. *Holzforschung*, *40*(2), 85–91.

Morris, S., Hanna, S., & Miles, M. J. (2004). The self-assembly of plant cell wall components by single-molecule force spectroscopy and Monte Carlo modelling. *Nanotechnology*, *15*(9), 1296–1301.

Muller-Plathe, F. (2002). Coarse-graining in polymer simulation: From the atomistic to the mesoscopic scale and back. *ChemPhysChem*, *3*(9), 755–769.

Nieduszynski, I., & Marchessault, R. H. (1971). Structure of β-D-(1 → 4) xylan hydrate. *Nature*, *232*(5305), 46–47.

Nieuwland, J., Feron, R., Huisman, B. A. H., Fasolino, A., Hilbers, C. W., Derksen, J., et al. (2005). Lipid transfer proteins enhance cell wall extension in tobacco. *Plant Cell*, *17*, 2009–2019.

Nishiyama, Y., Langan, P., & Chanzy, H. (2002). Crystal structure and hydrogen-bonding system in cellulose Iβ from synchrotron X-ray and neutron fiber diffraction. *Journal of the American Chemical Society*, *124*(31), 9074–9082.

Noid, W. G. (2013). Perspective: Coarse-grained models for biomolecular systems. *The Journal of Chemical Physics*, *139*(9), 090901/090901–090901/090925.

Ohgren, K., Bura, R., Saddler, J., & Zacchi, G. (2007). Effect of hemicellulose and lignin removal on enzymatic hydrolysis of steam pretreated corn stover. *Bioresource Technology*, *98*(13), 2503–2510.

Olsson, A.-M., Bjurhager, I., Gerber, L., Sundberg, B., & Salmen, L. (2011). Ultra-structural organisation of cell wall polymers in normal and tension wood of aspen revealed by polarisation FTIR microspectroscopy. *Planta*, *233*(6), 1277–1286.

Page, D. H. (1976). A note on the cell-wall structure of softwood tracheids. *Wood Fiber*, *7*(4), 246–248.

Peng, X.-W., Ren, J.-L., Zhong, L.-X., & Sun, R.-C. (2011). Nanocomposite films based on xylan-rich hemicelluloses and cellulose nanofibers with enhanced mechanical properties. *Biomacromolecules*, *12*, 3321–3329.

Penttila, P. A., Varnai, A., Pere, J., Tammelin, T., Salmen, L., Siika-aho, M., et al. (2013). Xylan as limiting factor in enzymatic hydrolysis of nanocellulose. *Bioresource Technology*, *129*, 135–141.

Queyroy, S., Neyertz, S., Brown, D., & Mueller-Plathe, F. (2004). Preparing relaxed systems of amorphous polymers by multiscale simulation: Application to cellulose. *Macromolecules*, *37*(19), 7338–7350.

Rappe, A. K., Casewit, C. J., Colwell, K. S., Goddard, W. A., III, & Skiff, W. M. (1992). UFF, a full periodic table force field for molecular mechanics and molecular dynamics simulations. *Journal of the American Chemical Society*, *114*, 10024–10035.

Rappé, A. K., & Goddard, W. A., III. (1991). Charge equilibration for molecular dynamics simulations. *The Journal of Physical Chemistry*, *95*(8), 3358–3363.

Reith, D., Meyer, H., & Mueller-Plathe, F. (2001). Mapping atomistic to coarse-grained polymer models using automatic simplex optimization to fit structural properties. *Macromolecules*, *34*, 2335–2345.

Reith, D., Puetz, M., & Mueller-Plathe, F. (2003). Deriving effective mesoscale potentials from atomistic simulations. *Journal of Computational Chemistry*, *24*, 1624–1636.

Roberts, J. C., & El-Karim, S. A. (1983). The behavior of surface adsorbed xylans during the beating of a bleached kraft pine pulp. *Cellulose Chemistry and Technology*, *17*(4), 379–386.

Saunders, M. G., & Voth, G. A. (2013). Coarse-graining methods for computational biology. *Annual Review of Biophysics*, *42*, 73–93.

Saxena, A., Elder, T. J., Pan, S., & Ragauskas, A. J. (2009). Novel nanocellulosic xylan composite film. *Composites Part B*, *40B*, 727–730.

Saxena, A., Foston, M., Kassaee, M., Elder, T. J., & Ragauskas, A. J. (2012). Biopolymer nanocomposite films reinforced with nanocellulose whiskers. *Journal of Nanoscience and Nanotechnology*, *12*, 218–226.

Shen, T., & Gnanakaran, S. (2009). The stability of cellulose: A statistical perspective from a coarse-grained model of hydrogen-bond networks. *Biophysics Journal*, *96*(8), 3032–3040.

Shi, Q., Izvekov, S., & Voth, G. A. (2006). Mixed atomistic and coarse-grained molecular dynamics: Simulation of a membrane-bound ion channel. *The Journal of Physical Chemistry B*, *110*, 15045–15048.
Shi, Q., Liu, P., & Voth, G. A. (2008). Coarse-graining in interaction space: An analytical approximation for the effective short-ranged electrostatics. *The Journal of Physical Chemistry B*, *112*, 16230–16237.
Srinivas, G., Cheng, X., & Smith, J. C. (2011). A solvent-free coarse grain model for crystalline and amorphous cellulose fibrils. *Journal of Chemical Theory and Computation*, *7*(8), 2539–2548.
Sternemalm, E., Hoeije, A., & Gatenholm, P. (2008). Effect of arabinose substitution on the material properties of arabinoxylan films. *Carbohydrate Research*, *343*, 753–757.
Stevanic, J. S., Joly, C., Mikkonen, K. S., Pirkkalainen, K., Serimaa, R., Remond, C., et al. (2011). Bacterial nanocellulose-reinforced arabinoxylan films. *Journal of Applied Polymer Science*, *122*, 1030–1039.
Stevanic, J. S., & Salmen, L. (2009). Orientation of the wood polymers in the cell wall of spruce wood fibers. *Holzforschung*, *63*(5), 497–503.
Sun, Q., Mandalika, A., Elder, T., Nair, S. S., Meng, X., Huang, F., et al. (2014). Nanocomposite film prepared by depositing xylan on cellulose nanowhiskers matrix. *Green Chemistry*, *16*, 3458–3462.
Terashima, N., Kitano, K., Kojima, M., Yoshida, M., Yamamoto, H., & Westermark, U. (2009). Nanostructural assembly of cellulose, hemicellulose, and lignin in the middle layer of secondary wall of ginkgo tracheid. *Journal of Wood Science*, *55*(6), 409–416.
Tokoh, C., Takabe, K., Sugiyama, J., & Fujita, M. (2002). Cellulose synthesized by *Acetobacter xylinum* in the presence of plant cell wall polysaccharides. *Cellulose*, *9*(1), 65–74.
Tuckerman, M., Berne, B. J., & Martyna, G. J. (1992). Reversible multiple time scale molecular dynamics. *The Journal of Chemical Physics*, *97*, 1990–2001.
Varner, J. E., & Lin, L. S. (1989). Plant cell wall architecture. *Cell*, *56*(2), 231–239.
Verlet, L. (1967). Computer experiments on classical fluids. I. Thermodynamical properties of Lennard–Jones molecules. *Physical Review*, *159*(1), 98–103.
Wohlert, J., & Berglund, L. A. (2011). A coarse-grained model for molecular dynamics simulations of native cellulose. *Journal of Chemical Theory and Computation*, *7*(3), 753–760.
Wu, S., Zhan, H.-y., Wang, H.-m., & Ju, Y. (2012). Secondary structure analysis of native cellulose by molecular dynamics simulations with coarse-grained model. *Chinese Journal of Chemical Physics*, *25*(2), 191–198.
Yllner, S., & Enstrom, B. (1956). Adsorption of xylan on cellulose fibers during the sulfate cook. *Svensk Papperstidning-Nordisk Cellulosa*, *59*, 229–232.
Zhu, Y.-L., Liu, H., Li, Z.-W., Qian, H.-J., Milano, G., & Lu, Z.-Y. (2013). GALAMOST: GPU-accelerated large-scale molecular simulation toolkit. *Journal of Computational Chemistry*, *34*, 2197–2211.

Lattice Boltzmann investigation of droplet inertial spreading on various porous surfaces

Xavier Frank*
IATE, INRA-CIRAD-UMII-SupAgro, 2 place Pierre Viala, 34060 Montpellier, France

Patrick Perré
École Centrale Paris, LGPM, Grande Voie des Vignes, 92290 Châtenay-Malabry, France

Huai-Zhi Li
Laboratoire Réactions et Génie des Procédés, Université de Lorraine, CNRS, 1 rue Grandville, BP 20451, 54001 Nancy Cedex, France
(Received 12 June 2014; published 26 May 2015)

The spreading of liquid drops on solid surfaces is a wide-spread phenomenon of both fundamental and industrial interest. In many applications, surfaces are porous and spreading patterns are very complex with respect to the case on smooth surfaces. Focusing on the inertial spreading just before the Tanner-like viscous regime, this work investigates the spreading of a low-viscosity droplet on a porous surface using lattice Boltzmann numerical simulations. The case of a flat surface is first considered, and it reveals a dependence on the solid equilibrium contact angle θ_s^{eq}, which is in good agreement with published experimental data. We conducted numerical experiments with various surfaces perforated by a regular pattern of holes of infinite length. The results show that the global spreading dynamics is independent of the porosity morphology. Through the assumption that, for wetting, the pores can be regarded as surface patches with a contact angle of $\theta_{\text{pore}}^{eq} = 180^\circ$, we deduce an effective equilibrium contact angle θ_{eff}^{eq} on the porous surface from the Cassie-Baxter law. A spreading model is then proposed to describe both a prefactor and an exponent that are similar to a flat surface whose equilibrium contact angle is θ_{eff}^{eq}. This model compares satisfactorily with a large number of numerical experiments under varying conditions.

DOI: 10.1103/PhysRevE.91.052405 PACS number(s): 68.08.−p, 47.55.dr, 47.55.nb, 47.56.+r

I. INTRODUCTION

The spreading of liquid drops on solid surfaces is of both fundamental and industrial interest. In many applications, surfaces are porous or covered with a thin porous layer. The presence of a porous layer modifies the wettability of the substrate and, hence, the spreading patterns [1,2]. The spreading of liquid drops on porous media is a wide-spread phenomenon [3] involved in natural and industrial processes such as ink jet printing [4], adhesion, coating [5,6], lubrication, detergency, plant treatment, composite manufacturing, painting, and oil recovery. This topic has received much attention from researchers [7–13]. To the best of our knowledge, the understanding of the underlying mechanisms of drop spreading on a porous surface remains limited, in particular with respect to spreading on a smooth surface. Earlier investigations were mainly devoted to viscous wetting, and most modeling and simulation approaches were performed within the framework of a continuous porous material, pore-scale approaches being quite rare [14–16]. Long-term spreading dynamics, arising from a competition between capillarity and viscosity both inside and outside the porous material, are preceded by an initially faster spreading. The spherical cap-shaped droplet approximation fails to describe this short-term spreading.

Recently, both the inertial spreading dynamics and capillary invasion of pores were investigated by means of numerical simulations [15]. However, the dependence of spreading dynamics on the porosity remains quite qualitative in this study. The present paper aims to address this point with the help of lattice Boltzmann (LB) numerical experiments. We will focus on simple porous substrate models, in which pore space is made of parallel holes of infinite length.

II. NUMERICAL METHOD

The LB method is a computational fluid dynamics approach derived from nonequilibrium statistical physics [17–20], and it has been successfully applied to multiphase flows and wetting problems since the early 1990s [21–25]. In the LB framework, the fluid is described at the particle kinetics level. Particle probability density functions (PPDFs) are defined, from which hydrodynamic quantities can be deduced. The Navier-Stokes equation can be recovered from the LB equation [18,26,27]. A no-slip boundary condition is imposed using the well-known bouncing-back method, in which incoming particles are reflected back toward the direction from which they came. Among multiphase LB approaches, pseudopotential methods are appealing due to their simplicity, and they have provided valuable results in various fields, such as droplet dynamics [28,29], capillary filling [25,30,31], porous media [32], microfluidics [33,34], colloidal fluids [35], contact line dynamics [36], complex fluid-fluid interfaces [37], and wetting phenomena [38–41].

In the present study, gas-liquid flows are simulated with the help of the well-known Shan-Chen pseudopotential approach [42]. The velocity used to compute equilibrium distributions is modified according to a local fluid-fluid force that emerges from interactions between neighboring fluid particles. A liquid phase and a vapor phase emerge spontaneously within this framework. Liquid density ρ_L, vapor density ρ_V, and surface tension σ depend on the magnitude of fluid attraction

*xavier.frank@supagro.inra.fr

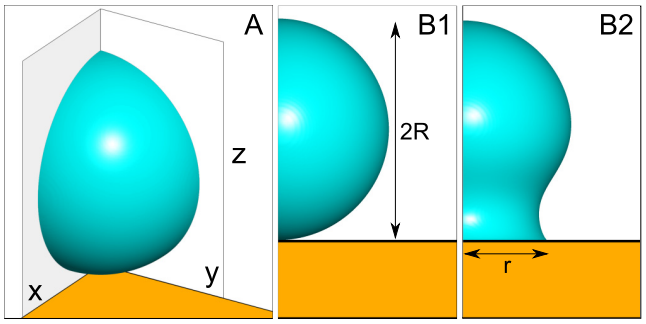

FIG. 1. (Color online) Scheme of a droplet spreading numerical experiment. A nonporous surface is used as an example. A: perspective view of the initial state. The solid surface is in the xy plane, and both the xz and yz symmetry planes are shown. B1: definition of the droplet radius R. B2: definition of the spreading radius r.

in the Chen-Shan model. An interface is located at the middle of the transition from ρ_G to ρ_L, where density ρ reaches the value $\rho_M = (\rho_G + \rho_L)/2$.

In this study, Martys and Chen's fluid-solid pseudopotential [43] describes interactions between fluid particles and the solid. The equilibrium contact angle θ_s^{eq} depends on the magnitude of both fluid-fluid and fluid-solid local interactions in the Chen-Shan model. Please see the previous works [24,42,43] for more details about the numerical approach.

III. NUMERICAL SETUP

We employ symmetries through the xz and yz planes to reduce the demand for numerical resources (Fig. 1, panel A). As a consequence, the initial position of the droplet center has to be placed on the z axis. The initial z position of the droplet center of mass is fixed to place the bottom of the liquid phase at the middle of z range. Simulation box dimensions are fixed to $180 \times 180 \times 450$, and the initial droplet diameter is set to 190. Simulations are conducted without gravity, and the wettability of the solid is defined using the solid equilibrium contact angle θ_s^{eq}. First, the droplet is equilibrated during 10 000 LB iterations without any solid node in the simulation box. The equilibrated droplet radius R, which is slightly different from the initial radius, has to be measured at the final state of this equilibrating phase (Fig. 1, panel B1). Then, the solid nodes are introduced in the simulation box, with a solid position adjusted in such a way that the droplet interface slightly touches the solid phase. To compute the radius of the droplet's footprint r (Fig. 1, panel B2), a density profile is extracted from a z,x = const. line, just above the solid surface. This specific position is chosen to extract the density profile only above the solid, and not above the pores. Wetting simulation runs during 15 000 iterations, and the spreading radius r is computed and saved at each time step.

IV. SPREADING ON FLAT SURFACES

First, numerical spreading experiments are conducted with flat surfaces. As spreading dynamics can depend significantly on liquid viscosity μ_L [44], it is crucial to compare the magnitude of inertial and capillary forces with that of viscous forces. In the present work, the value of the Laplace number $\mathrm{La} = \frac{\rho_L \sigma R}{\mu_L{}^2}$ is $\mathrm{La} = 135$ (in other words, the Ohnesorge number is $\mathrm{Oh} = 1/\sqrt{\mathrm{La}} = 8.6 \times 10^{-2}$), compared with the La values in the Bird *et al.* study [45], which ranged from 130 to 72 000. As $\mathrm{La} \gg 1$ we can then consider that the droplet is of low viscosity in our simulations. In such a case, the three following steps can be identified within droplet spreading dynamics [46]: a first step, independent of wettability, in which the spreading radius scales as $r \approx t^{1/2}$, a second step, in which the spreading dynamics depend on the solid equilibrium contact angle [45–47], and, finally, a slow viscous step [48]. The first step is not observed in our numerical simulations, as a consequence of grid resolution limits, and only the intermediate regime is studied in the present work. Under such conditions, the inertial dynamics of droplet spreading is dominated by the propagation of a capillary wave from the bottom to the top of the droplet interface [45]. As a consequence, the time scale τ of inertial spreading is $\tau = \sqrt{\rho_L R^3/\sigma}$. The normalized spreading radius r/R is deduced from r using R as the length scale, and it is plotted as a function of t/τ for 5 values of the equilibrium contact angle θ_s^{eq} (Fig. 2).

Strictly speaking, only the first inertial regime ($\frac{t}{\tau} \lesssim 0.04$) can be characterized by a power law [46], and the intermediate regime ($0.04 \lesssim \frac{t}{\tau} \lesssim 2$) is a crossover between the early inertial spreading and the viscous regime. However, as shown by Bird *et al.*, a power law is a good approximation for low viscosity

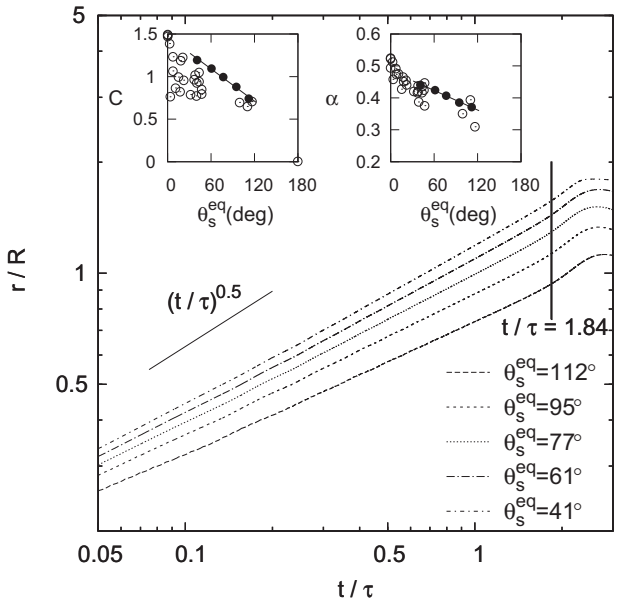

FIG. 2. Normalized spreading radius on a flat surface as a function of dimensionless time for various surface equilibrium contact angles. Each curve is fitted using a power law [Eq. (1)]. Insets are power law parameters as functions of the contact angle. Left inset: power law prefactor, right inset: power law exponent. In each inset, empty markers are experimental results from Bird *et al.* [45], full markers are values deduced from our numerical simulations, and lines are models of the power law prefactor and exponent, $C(\theta_s^{eq}) = 1.468 - 0.00631 \times \theta_s^{eq}$ and $\alpha(\theta_s^{eq}) = 0.485 - 0.00102 \times \theta_s^{eq}$, respectively. The theoretical duration of inertial spreading is underlined with a vertical line.

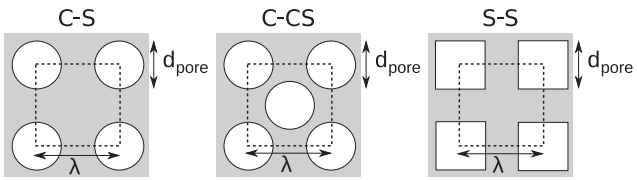

FIG. 3. Pore lattices used. C-S: square lattice of circle-sectioned pores, C-CS: centered square lattice of circle-sectioned pores, S-S: square lattice of square-sectioned pores. A unit cell is underlined with dashed lines. Both the pore period λ and pore size d_{pore} are shown for each case.

droplet spreading dynamics in this intermediate phase [45]. This power law approximation is expressed as

$$\frac{r}{R} = C\left(\frac{t}{\tau}\right)^{\alpha}, \tag{1}$$

where α is the power-law exponent and C is the prefactor, which is in good agreement with the experimental results [45]. The evolution of the power law prefactor $C(\theta_s^{eq})$ and exponent $\alpha(\theta_s^{eq})$ with θ_s^{eq}, shown in Fig. 2 as insets, has to be underlined and compared with earlier experimental results. Both decrease with θ_s^{eq}, which is in agreement with the experiments from Bird *et al.* [45]. The duration of inertial spreading [49] can be easily calculated from τ as $T \approx (\rho_L \sigma R/{\mu_L}^2)^{1/8}\tau$. Bird *et al.* showed that the duration of the inertial regime does not depend significantly on the equilibrium contact angle [45]. In the present study, the evaluation leads to $T \approx 1.84\tau$, which is in good agreement with our numerical simulations (Fig. 2).

V. SPREADING ON POROUS SURFACES

We consider now surfaces perforated by a regular pattern (square or centered square lattice) of holes of infinite length. Between neighboring cylindrical pores, solid walls are effective to avoid any liquid communication. Surface porosity is defined as $\epsilon = S_{\text{pores}}/\lambda^2$; S_{pores} is the sum of the transversal sections of all pores belonging to one lattice cell, and λ is the lattice period. The higher is the porosity, the lower is the driving force of spreading. As a consequence, the spreading dynamics are expected to slow down as ϵ increases. However, the porosity of a surface can be distributed in various ways: small pores with high numerical density or larger pores with lower numerical density, or various pore lattices and various pore section shapes. Do these details matter or not? If this is not the case, the spreading dynamics will depend only on ϵ regardless of the pore section shape, the pore lattice unit cell pattern, or the pore lattice period. To clarify this point, porous surfaces are built up using various geometrical parameters for both square and centered square lattices of circle-sectioned pores, and the square lattice of square-sectioned pores (Fig. 3).

For each kind of lattice, the geometry of the porous surface is completely defined by the pore size d_{pore} (diameter for circle-sectioned ones and side for square-sectioned ones) and spatial period λ. Porosity ϵ is easily computed from d_{pore} and λ. Surface parameters are summarized in Table I. As an example, a perspective view of one solid phase is shown in Fig. 4.

Numerical spreading experiments are conducted in the same way as for flat surfaces. The surface porosity leads to a greater complexity of the gas-liquid interface close to the solid surface: the solid-liquid-vapor triple line is no longer circular, but exhibits oscillations (Fig. 5). Liquid spreads on the solid surface and crosses the pores. Imbibition can start after the pore opening has been covered by the liquid interface. As expected, pores are invaded when $\theta_s^{eq} < 90°$, not when $\theta_s^{eq} > 90°$ (Fig. 6). Both droplet height evolution and droplet volume variation emerge from a competing mechanism between spreading on the solid phase of the surface and capillary imbibition inside the porous medium. Such a point was detailed in an earlier paper [15] and is not developed here.

The spreading dynamics are normalized as for flat surfaces, by means of R and τ (Fig. 7). Compared with the case of

TABLE I. Parameters of pore lattices: pore lattice type, pore size d_{pore}, and pore period λ, which is deduced the surface porosity ϵ. Both d_{pore} and λ in lattice units (l.u.).

Pore lattice	d_{pore}	λ	ϵ
C-S	10	20	0.20
C-S	10	30	0.087
C-S	10	40	0.049
C-S	20	30	0.35
C-S	20	40	0.20
C-S	30	40	0.44
C-CS	10	30	0.18
C-CS	20	40	0.39
S-S	10	20	0.25
S-S	20	40	0.25
S-S	20	30	0.44
S-S	30	40	0.56

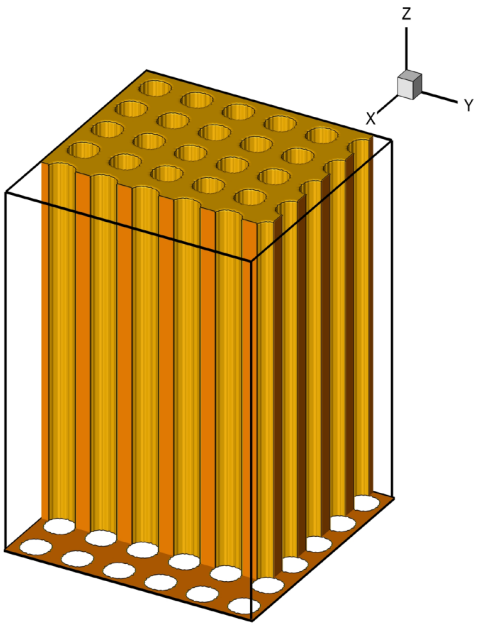

FIG. 4. (Color online) Perspective view of the solid phase. The square lattice of circular section pores; the pore diameter is $d_{\text{pore}} =$ 20 l.u., and the pore lattice spatial period is $\lambda = 30$ l.u. A small part of the solid phase is removed to facilitate the visualization.

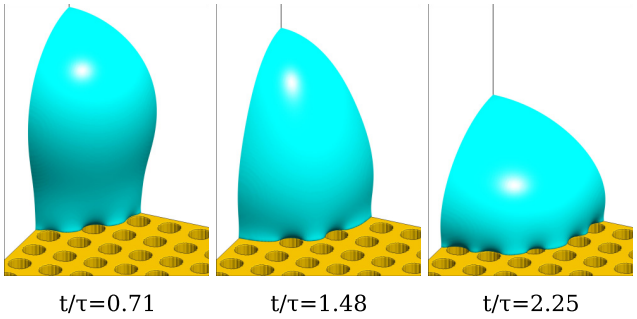

FIG. 5. (Color online) Snapshot of a droplet spreading simulation on a porous surface. The square lattice of circular section pores; the pore diameter is $d_{\text{pore}} = 20$ l.u., the pore lattice spatial period is $\lambda = 30$ l.u., and the intrinsic solid equilibrium contact angle is $\theta_s^{eq} = 77^\circ$.

a flat surface, successive accelerations and decelerations can be observed as the three-phase contact line crosses the pores. Clearly, the spreading radius dynamics are similar to a power law, despite these oscillating phenomena.

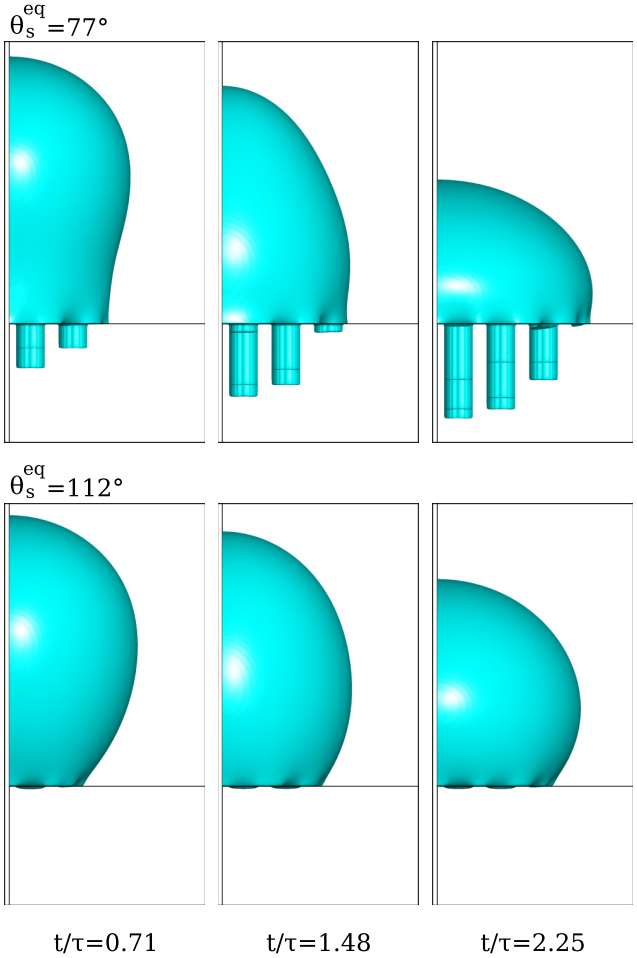

FIG. 6. (Color online) Snapshot of droplet spreading simulation on a porous surface with two values of the intrinsic solid equilibrium contact angle, the solid phase being removed. The square lattice of circular section pores; the pore diameter is $d_{\text{pore}} = 20$ l.u., and the pore lattice spatial period is $\lambda = 30$ l.u.

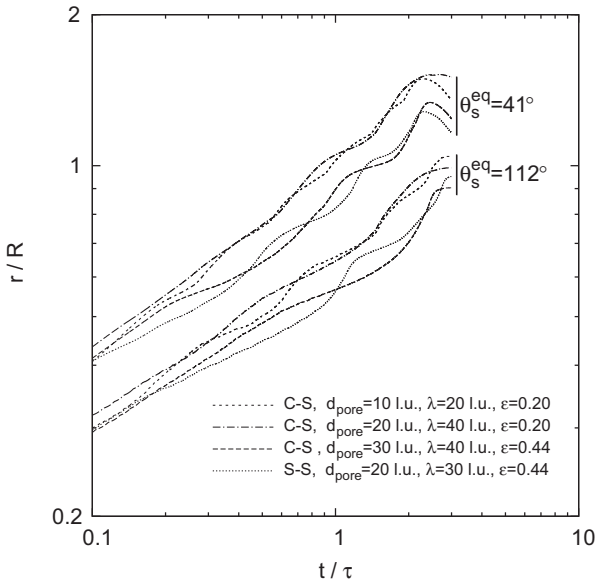

FIG. 7. Normalized radius of the wetted zone as a function of dimensionless time during droplet spreading on two porous surface pairs of porosity, $\epsilon = 0.20$ and $\epsilon = 0.44$, respectively, and with the solid equilibrium contact angles $\theta_s^{eq} = 41^\circ$ and $\theta_s^{eq} = 112^\circ$. Both d_{pore} and λ in lattice units (l.u.).

As expected, spreading slows down when θ_s^{eq} increases for a given porosity, or when porosity increases, θ_s^{eq} being fixed (Fig. 7). Surprisingly, the global spreading dynamics do not depend on how the porosity is distributed over the surface. Increases in θ_s^{eq} and ϵ induce similar evolutions of spreading dynamics, and a global model, including both parameters, should be attainable.

The simplest approach to consider both the contact angle and morphology of a complex surface in a single law is to assume that the surface behaves as an equivalent smooth surface. Such a description leads to the famous Cassie-Baxter law [50]. Considering a composite surface involving two materials with two different equilibrium contact angles, the surface is supposed to exhibit an effective homogeneous equilibrium contact angle θ_{eff}^{eq}, depending on both the intrinsic equilibrium contact angle and the proportion of basic materials. In the present case, we have a solid phase with an equilibrium contact angle θ_s^{eq} and a surface fraction $(1-\epsilon)$, and a pore phase with equilibrium contact angle $\theta_{\text{pore}}^{eq}$ and surface fraction ϵ. Using these assumptions, an effective equilibrium contact angle $\theta_{\text{eff}}^{eq}(\theta_s^{eq},\epsilon)$ could be deduced from the Cassie-Baxter law as follows:

$$\cos\theta_{\text{eff}}^{eq} = (1-\epsilon)\cos\theta_s^{eq} + \epsilon\cos\theta_{\text{pore}}^{eq}. \tag{2}$$

Effective power-law parameters can stem from the computed values of θ_{eff}^{eq}, as if the porous surface is an equivalent smooth solid surface with equilibrium contact angle θ_{eff}^{eq}:

$$C_{\text{eff}}\left(\theta_s^{eq},\epsilon\right) = C\left(\theta_{\text{eff}}^{eq}\right), \tag{3}$$

$$\alpha_{\text{eff}}\left(\theta_s^{eq},\epsilon\right) = \alpha\left(\theta_{\text{eff}}^{eq}\right). \tag{4}$$

The application of the Cassie-Baxter law to our case requires $\theta_{\text{pore}}^{eq}$ to be fixed. A simple hypothesis can then be proposed:

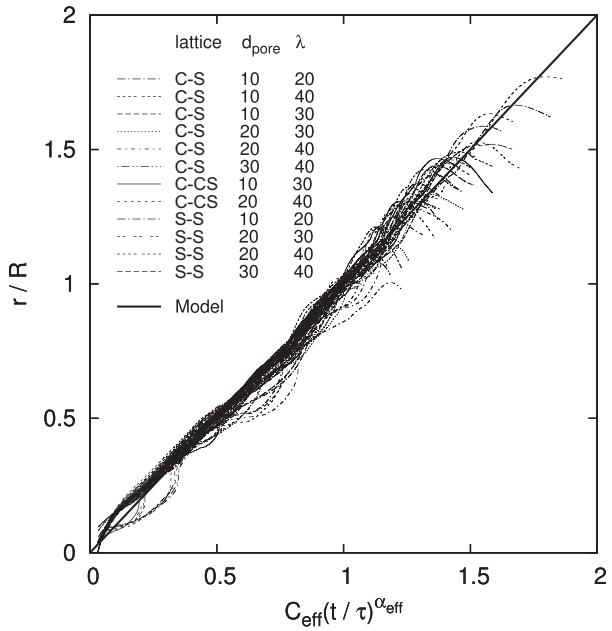

FIG. 8. Normalized spreading radius on various porous surfaces with various intrinsic solid equilibrium contact angles vs the prediction of the proposed effective spreading law with $\theta^{eq}_{\text{pore}} = 180^\circ$. Pore lattices are square lattice of circle-sectioned pores (C-S), centered square lattice of circle-sectioned pores (C-CS), and square lattice of square-sectioned pores (S-S). Both d_{pore} and λ in lattice units (l.u.). For each of the 12 pore lattices, 5 values of θ^{eq}_s were used (cf. Fig. 2), which means a total of 60 curves.

as long as a pore is not invaded by liquid, it remains an obstacle to global spreading. Thus, $\theta^{eq}_{\text{pore}} = 180^\circ$ seems to be a straightforward hypothesis.

To compare our effective law with the numerical results, we plot the ratio r/R as a function of $C_{\text{eff}}(t/\tau)^{\alpha_{\text{eff}}}$, t/τ being a curve parameter (Fig. 8). Concretely, for each simulation, θ^{eq}_{eff} is computed as a function of both θ^{eq}_s and ϵ, and effective power-law parameters C_{eff} and α_{eff} are deduced from linear fits of values extracted from the numerical simulation of droplet spreading on a smooth surface (Fig. 2). Despite oscillations, it is clear that the spreading radius dynamics from numerical simulations are similar to a power-law whose prefactor and exponent are predicted by the Cassie-Baxter law. Moreover, various curves fit this simple effective law well, although the proposed spreading law does not explicitly take into account the distributed pattern of porosity on the surface. Only the pore fraction matters whatever its distribution. The global behavior of the droplet is very close to that on an equivalent smooth surface.

Recently, Stapelbroek *et al.* conducted droplet spreading experiments with various complex solid surfaces, such as microtextured and chemically striped substrates [51]. In this study, the data collapse of the crossover time between the early inertial spreading and intermediate regime could be achieved using only a single parameter, the effective contact angle, regardless of the details of the substrate. Such result corroborates our findings. To overcome the energy barriers in the presence of topographic or chemical patterns that lead to a spatial variation of the local surface energy, an additional source of energy is required in the vicinity of the contact line. This energy must come from the kinetic energy of the flow inside the droplet. As a consequence, it could be reasonably argued that the balance between the kinetic energy of the spreading drop and the surface energies is a relevant mechanism, and that the details of a complex surface play a minor role in the inertial spreading global dynamics. Of course, such a picture is no longer valid in the viscous regime [47].

VI. CONCLUSIONS

In summary, we have proposed a droplet spreading law on porous surfaces, including both the intrinsic solid contact angle and surface porosity. Lattice Boltzmann numerical simulations were performed for smooth surfaces with various equilibrium contact angles and the predicted power law for spreading dynamics compares favorably with published experimental results. Simulations with various porous surfaces and solid equilibrium contact angles show that increasing porosity slows down spreading in the same way as increasing the equilibrium contact angle for smooth surfaces. Assuming that pores are perfectly nonwetting patches, we deduced an effective equilibrium contact angle of the surface, and both the power law prefactor and exponent from an effective equilibrium contact angle are in satisfactory agreement with the simulation.

[1] H. Koivula, M. Toivakka, and P. Gane, J. Colloid Interface Sci. **369**, 426 (2012).
[2] V. M. Starov, S. R. Kostvintsev, V. D. Sobolev, M. G. Velarde, and S. A. Zhdanov, J. Colloid Interface Sci. **252**, 397 (2002).
[3] D. Quéré, Annu. Rev. Mater. Res. **38**, 71 (2008).
[4] A. Määttänen, P. Ihalainen, R. Bollström, M. Toivakka, and J. Peltonen, Colloids Surf., A **367**, 76 (2010).
[5] A. Zadražil, F. Stepanek, and O. Matar, J. Fluid Mech. **562**, 1 (2006).
[6] P. Colombo, G. Mera, R. Riedel, and G. D. Sorarù, J. Am. Ceram. Soc. **93**, 1805 (2010).
[7] P. Neogi and C. A. Miller, J. Colloid Interface Sci. **92**, 338 (1983).
[8] M. Denesuk, B. J. J. Zelinski, N. J. Kreidl, and D. R. Uhlmann, J. Colloid Interface Sci. **168**, 142 (1994).
[9] S. H. Davis and L. M. Hocking, Phys. Fluids **11**, 48 (1999).
[10] S. H. Davis and L. M. Hocking, Phys. Fluids **12**, 1646 (2000).
[11] V. M. Starov, S. A. Zhdanov, S. R. Kosvintsev, V. D. Sobolev, and M. G. Velarde, Adv. Colloid Interface Sci. **104**, 123 (2003).
[12] L. Cueto-Felgueroso and R. Juanes, Phys. Rev. Lett. **101**, 244504 (2008).
[13] T. G. D'Onofrio, H. K. Navaz, B. Markicevic, B. A. Mantooth, and K. B. Sumpter, Langmuir **26**, 3317 (2010).

[14] J. C. R. Neyval, R. F. Griffiths, and J. M. Santos, Appl. Math. Model. **32**, 341 (2008).
[15] X. Frank and P. Perré, Phys. Fluids **24**, 042101 (2012).
[16] S. Meng, R. Yang, J. S. Wu, and H. Zhang, Int. J. Heat Mass Transf. **77**, 828 (2014).
[17] R. Benzi, S. Succi, and M. Vergassola, Phys. Rep. **222**, 0130008 (1992).
[18] S. Succi, *The Lattice Boltzmann Equation for Fluid Dynamics and Beyond* (Clarendon Press, Oxford, 2001).
[19] D. d'Humières, I. Ginzburg, M. Krafczyk, P. Lallemand, and L. S. Luo, Philos. Trans. R. Soc. London A **360**, 437 (2002).
[20] C. K. Aidun and J. R. Clausen, Annu. Rev. Fluid Mech. **42**, 439 (2010).
[21] M. Sbragaglia, R. Benzi, L. Biferale, S. Succi, and F. Toschi, Phys. Rev. Lett. **97**, 204503 (2006).
[22] M. L. Blow and J. M. Yeomans, Philos. Trans. R. Soc. A **369**, 2519 (2011).
[23] X. Frank and H.-Z. Li, Phys. Rev. E **71**, 036309 (2005).
[24] X. Frank, D. Funfschilling, N. Midoux, and H.-Z. Li, J. Fluid Mech. **546**, 113 (2006).
[25] X. Frank, G. Almeida, and P. Perré, Int. J. Multiphase Flow **36**, 599 (2010).
[26] Y. H. Qian, D. D'Humières, and P. Lallemand, Europhys. Lett. **17**, 479 (1992).
[27] H. Chen, S. Chen, and W. H. Matthaeus, Phys. Rev. A **45**, R5339 (1992).
[28] Q. Kang, D. Zhang, and S. Chen, J. Fluid Mech. **545**, 41 (2005).
[29] J. Hyväluoma, A. Koponen, P. Raiskinmäki, and J. Timonen, Eur. Phys. J. E **23**, 289 (2007).
[30] P. Raiskinmäki, A. Shakib-Manesh, A. Jäsberg, A. Koponen, J. Merikoski, and J. Timonen, J. Stat. Phys. **107**, 143 (2002).
[31] F. Diotallevi, L. Biferale, S. Chibbaro, A. Lamura, G. Pontrelli, M. Sbragaglia, S. Succi, and F. Toschi, Eur. Phys. J. Spec. Top. **166**, 111 (2009).
[32] A. Parmigiani, C. Huber, O. Bachmann, and B. Chopard, J. Fluid Mech. **686**, 40 (2011).
[33] Z. Yu, O. Hemminger, and L. S. Fan, Chem. Eng. Sci. **62**, 7172 (2007).
[34] L. Clime, D. Brassard, J. P. Pezacki, and T. Veres, Microfluid. Nanofluid. **12**, 371 (2012).
[35] A. S. Joshi and Y. Sun, Phys. Rev. E **82**, 041401 (2010).
[36] M. Sbragaglia, K. Sugiyama, and L. Biferale, J. Fluid Mech. **614**, 471 (2008).
[37] M. Sega, M. Sbragaglia, S. S. Kantorovich, and A. O. Ivanov, Soft Matter **9**, 10092 (2013).
[38] Q. Li, Z. Chai, B. Shi, and H. Liang, Phys. Rev. E **90**, 043015 (2014).
[39] M. Sbragaglia, L. Biferale, G. Amati, S. Varagnolo, D. Ferraro, G. Mistura, and M. Pierno, Phys. Rev. E **89**, 012406 (2014).
[40] H. Farhat, S. Kondaraju, S. K. Na, and J. S. Lee, Phys. Rev. E **88**, 013013 (2013).
[41] H. P. Jansen, K. Sotthewes, J. van Swigchem, H. J. W. Zandvliet, and E. S. Kooij, Phys. Rev. E **88**, 013008 (2013).
[42] X. Shan and H. Chen, Phys. Rev. E **47**, 1815 (1993).
[43] N. S. Martys and H. Chen, Phys. Rev. E **53**, 743 (1996).
[44] A. Eddi, K. G. Winkels, and J. H. Snoeijer, Phys. Fluids **25**, 013102 (2013).
[45] J. C. Bird, S. Mandre, and H. A. Stone, Phys. Rev. Lett. **100**, 234501 (2008).
[46] K. G. Winkels, J. H. Weijs, A. Eddi, and J. H. Snoeijer, Phys. Rev. E **85**, 055301 (2012).
[47] L. Courbin, J. C. Bird, M. Reyssat, and H. A. Stone, J. Phys.: Condens. Matter **21**, 464127 (2009).
[48] L. H. Tanner, J. Phys. D: Appl. Phys. **12**, 1473 (1979).
[49] A. L. Biance, C. Clanet, and D. Quéré, Phys. Rev. E **69**, 016301 (2004).
[50] A. B. D. Cassie and S. Baxter, Trans. Faraday Soc. **40**, 546 (1944).
[51] B. B. J. Stapelbroek, H. P. Jansen, E. S. Kooij, J. H. Snoeijer, and A. Eddi, Soft Matter **10**, 2641 (2014).

Tensile strength of granular aggregates: Stress chains across particle phase versus stress concentration by pores

Xavier Frank [1,*] Farhang Radjaï [2] Saied Nezamabadi [2,1] and Jean-Yves Delenne [1]
[1]*IATE, INRAE, Montpellier SupAgro, Université de Montpellier, F-34060, Montpellier, France*
[2]*LMGC, Université de Montpellier, CNRS, Montpellier, France*

(Received 12 May 2020; accepted 28 July 2020; published 20 August 2020)

We use the bond-based peridynamics approach to analyze the strength and fracture of dense granular aggregates with variable amount of a solid binding matrix, distributed according to a simple protocol in the interstitial space between particles. We show the versatility of the peridynamics approach in application to crack propagation and its scaling behavior in a homogeneous medium (in the absence of particles and pores). Then we apply this method to simulate the deformation and failure of aggregates as a function of the amount of the binding matrix under tensile loading. We find that the tensile strength is a strongly nonlinear function of the matrix volume fraction. It first increases slowly and levels off as the gap space in-between touching particles is gradually filled by the binding matrix, up to nearly 90% of the total pore volume, and then a rapid increase occurs to the maximum strength as the remaining interstitial space, composed of isolated pores between four or more particles, is filled. By analyzing the probability density functions of stresses in the particle and matrix phases, we show that the adhesion of the matrix to the particles and the thickening of stress chains (i.e., stresses distributed over larger cross sections) control the strength in the first case whereas the homogenizing effect of the matrix by filling the pores (hence reducing stress concentration) is at the origin of further increase of the strength in the second case. Interestingly, these two mechanisms contribute almost equally to the total strength.

DOI: 10.1103/PhysRevE.102.022906

I. INTRODUCTION

Porous materials are classically described as a homogeneous matrix hosting connected or disconnected (open) pores and associated with upscaling models essentially based on single-pore or single-crack analysis [1,2]. However, this description does not cover the class of porous materials in which porosity is an intrinsic property of their basic microstructure defined by a dense assembly of elementary constituents. Granular aggregates partially filled with a binding matrix belong to this broad class of *structured* porous materials. It includes concrete [3,4], sintered powders [5,6], sedimentary rocks [7], and wheat endosperm (composed of starch granules distributed in a protein matrix) [8]. Understanding the origins of their elastic and failure properties is of practical interest for the design of concretes [9–13], dense particle-filled composites [14], and other new materials [15–17], as well as for predicting rock fracture [18,19] and the influence of operating parameters on cereal milling [8,20].

Since these granular aggregates have a rich microstructure, their mechanical properties depend not only on the phase volume fractions but also on the geometrical and topological disorder (connectivity and interactions of the particles) of the particle phase [21]. For example, the strength and failure of cemented granular materials and particle-enriched composites have been shown to depend on the adhesion of the inclusions to the matrix [22,23], as well as the size [22] and shapes of the inclusions [24,25].

In this paper we use peridynamics simulations to quantify and distinguish two different mechanisms underlying the tensile strength of granular aggregates: (1) stress concentration by tensile stress chains encompassing the particles and the binding matrix filling the gap space in between particles, and (2) stress concentration by isolated pores enclosed between several particles. The first mechanism is well known for confined granular materials in which the stress is transmitted along compressive force chains [26]. The second mechanism is common to all porous materials in which stress concentration by the pores controls the strength and toughness of the material [27]. The peridynamics method allows us to discretize both the particles and the matrix, and to follow the evolution of the stress field throughout the samples. We also use a protocol for the distribution of the matrix inside our numerical granular samples so that the interparticle gaps are filled before the remaining isolated pores begin to be filled as the matrix volume fraction is gradually increased. As we shall see, this procedure provides a neat distinction between the two effects.

In the following we first describe the mathematical background of the bond-based peridynamics method and mesh convergence in Sec. II. In Sec. III we present the method used to build the samples. Then in Sec. IV we consider the tensile strength as a function of the matrix volume fraction. In Sec. V we investigate the stress transmission to analyze the two mechanisms underlying the tensile strength. We conclude with a brief discussion of the results and future lines of research.

*xavier.frank@inra.fr

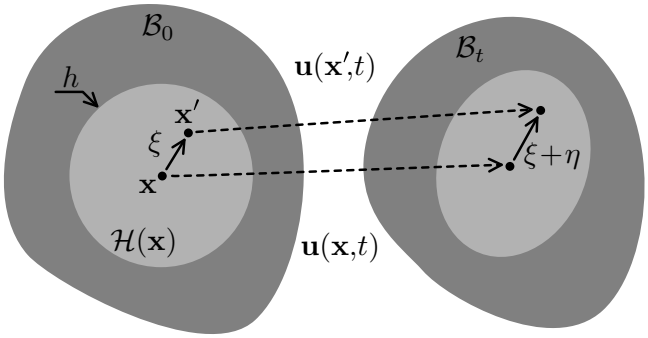

FIG. 1. Left: Reference configuration $\mathcal{B}_0$ of a bond $\boldsymbol{\xi}$ connected to a material point $\boldsymbol{x}$ and its horizon domain $\mathcal{H}(\boldsymbol{x})$. Right: Deformed configuration $\mathcal{B}_t$. Representation of displacement field $\boldsymbol{u}$ and relative displacement field $\boldsymbol{\eta}$.

II. NUMERICAL METHOD

The numerical simulation of the deformation and fracture of inhomogeneous materials is an active field of research [28,29]. We used the peridynamics method for its capacity of crack nucleation and computational performance [30,31]. In this method the material is represented as a network of interacting nodes governed by a nonlocal (integral) formulation of the equations of dynamics inside a given "horizon." Bond rupture events lead to damage or to fracture when a critical number of bonds is damaged. Before its application to granular aggregates, we provide in this section a brief description of its principles and show that for brittle materials considered in this paper, this method is accurate and consistent with fracture mechanics. These aspects are important for the validity and robustness of our results.

A. Bond-based peridynamics

The bond-based peridynamics method is a subset of general state-based peridynamics approaches [32]. This method has been successfully used in a wide range of applications such as the modeling of concrete failure [4], dynamic crack branching [33,34], polycrystal fracture [35], nanoscale rupture mechanics [36,37], microelectronics materials damage [38], and wood failure [39].

Let us consider a domain $\mathcal{B}_0$ in $\mathbb{R}^D$, where D is space dimension. This domain represents a body in the reference configuration at time $t = 0$. The equation of motion for a material point $\mathbf{x} \in \mathcal{B}_0$ is given by

$$\rho(\boldsymbol{x})\ddot{\boldsymbol{u}}(\boldsymbol{x},t) = \int_{\mathcal{H}(\boldsymbol{x})} \boldsymbol{f}[\boldsymbol{u}(\boldsymbol{x}',t)-\boldsymbol{u}(\boldsymbol{x},t),\boldsymbol{x}'-\boldsymbol{x},\boldsymbol{x}]dV_{\boldsymbol{x}'} + \boldsymbol{b}(\boldsymbol{x},t)\,, \tag{1}$$

where ρ, $\boldsymbol{u}$, and $\boldsymbol{b}$ denote the density, displacement field, and body force, respectively. All material points originally at $\boldsymbol{x}$ in $\mathcal{B}_0$ are at the position $\boldsymbol{x}+\boldsymbol{u}$ in $\mathcal{B}_t$ at time t. The pairwise force exerted between two material points $\boldsymbol{x}$ and $\boldsymbol{x}'$ is denoted by $\boldsymbol{f}$. The relative position vector, called *bond* here, is $\boldsymbol{\xi} = \boldsymbol{x}' - \boldsymbol{x}$. $\mathcal{H}(\boldsymbol{x})$ represents the set of bonds connected to $\boldsymbol{x}$ with lengths below a cutoff distance h called *horizon*: $\mathcal{H}(\boldsymbol{x}) = \{\boldsymbol{\xi} \in \mathbb{R}^D \mid \boldsymbol{x}+\boldsymbol{\xi} \in \mathcal{B}_0 \wedge \|\boldsymbol{\xi}\| < h\}$ (Fig. 1).

In the most general implementation of peridynamics, called nonordinary state-based models, the force density $\boldsymbol{f}[\boldsymbol{u}(\boldsymbol{x}',t)-\boldsymbol{u}(\boldsymbol{x},t),\boldsymbol{x}'-\boldsymbol{x},\boldsymbol{x}]$ exerted from $\boldsymbol{x}$ on $\boldsymbol{x}'$ and $\boldsymbol{f}[\boldsymbol{u}(\boldsymbol{x},t)-\boldsymbol{u}(\boldsymbol{x}',t),\boldsymbol{x}-\boldsymbol{x}',\boldsymbol{x}']$ exerted from $\boldsymbol{x}'$ on $\boldsymbol{x}$ can have different directions and magnitudes [32]. In ordinary state-based models, these two forces are supposed to be radial but may have different magnitudes. Here, we choose a bond-based peridynamics approach which neglects the local tangential and torque components: $\boldsymbol{f}[\boldsymbol{u}(\boldsymbol{x}',t)-\boldsymbol{u}(\boldsymbol{x},t),\boldsymbol{x}'-\boldsymbol{x},\boldsymbol{x}] = -\boldsymbol{f}[\boldsymbol{u}(\boldsymbol{x},t)-\boldsymbol{u}(\boldsymbol{x}',t),\boldsymbol{x}-\boldsymbol{x}',\boldsymbol{x}']$. Hence the equation of motion (1) can be simplified by assuming that each bond $\boldsymbol{\xi}$ evolves to a deformed state $\boldsymbol{\xi}+\boldsymbol{\eta}$, where $\boldsymbol{\eta} = \boldsymbol{u}(\boldsymbol{x}',t) - \boldsymbol{u}(\boldsymbol{x},t)$ is the relative displacement between the bond endpoints:

$$\rho(\boldsymbol{x})\,\ddot{\boldsymbol{u}}(\boldsymbol{x},t) = \int_{\mathcal{H}(\boldsymbol{x})} \boldsymbol{f}(\boldsymbol{\xi},\boldsymbol{\eta},\boldsymbol{x})\,dV_{\boldsymbol{x}'} + \boldsymbol{b}(\boldsymbol{x},t)\,. \tag{2}$$

Thus a pairwise force $\boldsymbol{f}$ can be defined from the bond initial state $\boldsymbol{\xi}$ and its relative displacement $\boldsymbol{\eta}$:

$$\boldsymbol{f}(\boldsymbol{\xi},\boldsymbol{\eta}) = f(\boldsymbol{\xi},\boldsymbol{\eta},\boldsymbol{x})\frac{\boldsymbol{\xi}+\boldsymbol{\eta}}{\|\boldsymbol{\xi}+\boldsymbol{\eta}\|}\,, \tag{3}$$

where $f(\boldsymbol{\xi},\boldsymbol{\eta},\boldsymbol{x})$ is a scalar representing the magnitude of the force in units of force per unit volume squared. Inserting (3) into the equation of motion (2) yields

$$\rho(\boldsymbol{x})\,\ddot{\boldsymbol{u}}(\boldsymbol{x},t) = \int_{\mathcal{H}(\boldsymbol{x})} f(\boldsymbol{\xi},\boldsymbol{\eta},\boldsymbol{x})\frac{\boldsymbol{\xi}+\boldsymbol{\eta}}{\|\boldsymbol{\xi}+\boldsymbol{\eta}\|}\,dV_{\boldsymbol{x}'} + \boldsymbol{b}(\boldsymbol{x},t)\,. \tag{4}$$

In this paper, inhomogeneous elastic materials are investigated where the force density $\boldsymbol{f}$ depends on different phases. Hence the elasticity of each bond $\boldsymbol{\xi}$ explicitly depends on both points $\boldsymbol{x}$ and $\boldsymbol{x}+\boldsymbol{\xi}$. We assume a harmonic potential energy for which the force function is given by

$$f(\boldsymbol{\xi},\boldsymbol{\eta},\boldsymbol{x}) = \begin{cases} c_{\boldsymbol{x},\boldsymbol{x}+\boldsymbol{\xi}}\; s(\boldsymbol{\xi},\;\boldsymbol{\eta}) & \|\boldsymbol{\xi}\| \leqslant h \\ 0 & \|\boldsymbol{\xi}\| > h \end{cases}, \tag{5}$$

where s is the bond elongation

$$s(\boldsymbol{\xi},\boldsymbol{\eta}) = \frac{\|\boldsymbol{\xi}+\boldsymbol{\eta}\| - \|\boldsymbol{\xi}\|}{\|\boldsymbol{\xi}\|} \tag{6}$$

and $c_{\boldsymbol{x},\boldsymbol{x}+\boldsymbol{\xi}}$ is the so-called "elastic micro-modulus" and $c_{\boldsymbol{x}+\boldsymbol{\xi},\boldsymbol{x}} = c_{\boldsymbol{x},\boldsymbol{x}+\boldsymbol{\xi}}$. For all points located in the pores or outside the domain we set $c = 0$. The effective Young's modulus of a homogeneous sample is given by [34]

$$E = \frac{c\pi h^3(1-\nu)}{6}\,, \tag{7}$$

which linearly depends on c. The Poisson's ratio is $\nu = 1/3$ for the bond-based peridynamic approach in two dimensions (2D) [4].

To take into account the possibility of fracture, we assume that a bond fails when it exceeds its critical elongation s_0, which depends on the phase (Fig. 2). The fracture energy G_c of a homogeneous material of elastic modulus E and critical elongation s_0 is given by [34]

$$G_c = \frac{9Ehs_0^2}{4\pi}\,. \tag{8}$$

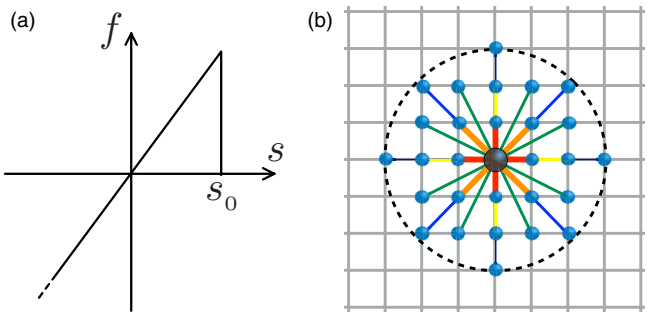

FIG. 2. (a) Schematic representation of the pairwise force f as a function of bond elongation s. Failure can occur only in tension for a critical elongation s_0. (b) Connectivity of bonds for a horizon of 3.

Furthermore, the toughness K of the material is related to G_c and E through $K = \sqrt{EG_c}$.

In peridynamics approaches, both cracks and interfaces between phases have a finite thickness depending upon $h/\delta x$. To overcome this blurring effect, higher spatial resolutions are needed. Another drawback of the bond-based peridynamic approach is that the mechanical behavior is brittle. An arbitrary mechanical behavior may be implemented by means of a state-based peridynamic approach, but it involves larger computing time. Despite the simplicity of the bond-based peridynamic approach, it has the advantage of allowing for complex material features to be implemented in this framework, such as anisotropic fabric or a fiber-reinforced matrix [40–42]. In this paper we focus on highly heterogeneous distributions of the phases.

Most studies using the peridynamics approach have concerned the dynamic propagation of cracks [31,33,34] and dynamic fragmentation [31]. In these studies an explicit time integration scheme is generally used. Much less attention has been paid to quasistatic conditions, which are of great interest for low-rate processes [43,44]. Several techniques have been reported in the literature for quasistatic simulations in the context of lattice approaches [23]. In most cases, the sample is loaded until one bond reaches a critical stress (or elongation). This critical bond is then removed and, after a full relaxation of the system, the load is incremented. The main disadvantage of this procedure is its high computational cost. For this reason, we choose here to allow several bonds to break during each load increment. See Appendix A for further details.

B. Discretization

The simulated domain is discretized into a two-dimensional $N_x \times N_y$ rectilinear grid of spatial resolution δx. Each material point i of position $\boldsymbol{x}_i$ has a mass $m_i = (\delta x)^2 \rho(\boldsymbol{x}_i)$. The system can be viewed as a mass-spring lattice in which each bond (linear spring) connects two points on the grid. The equation of motion (4) is discretized on the grid:

$$m_i \ddot{\boldsymbol{u}}_i(t) = \sum_{\boldsymbol{x}_j \in \mathcal{H}(\boldsymbol{x}_i)} k_{ij} s(\boldsymbol{\xi}_{ij}, \boldsymbol{\eta}_{ij}) \frac{\boldsymbol{\xi}_{ij} + \boldsymbol{\eta}_{ij}}{\|\boldsymbol{\xi}_{ij} + \boldsymbol{\eta}_{ij}\|} + \boldsymbol{b}_i(t) \,, \qquad (9)$$

where $\boldsymbol{u}_i(t) = \boldsymbol{u}(\boldsymbol{x}_i, t)$, $\boldsymbol{\xi}_{ij} = \boldsymbol{x}_j - \boldsymbol{x}_i$, $\boldsymbol{\eta}_{ij} = \boldsymbol{u}_j - \boldsymbol{u}_i$, $\boldsymbol{b}_i(t) = (\delta x)^2 \boldsymbol{b}(\boldsymbol{x}_i, t)$, and $k = c(\delta x)^4$. Since no excluded-volume constraints are imposed on the points, the strain should be kept small enough to avoid overlaps between neighboring bonds and ensure a macroscopic linear behavior.

The stress tensor at each node i is given by the following equation [45]:

$$\sigma_i(t) = \frac{1}{{\delta_x}^2} \sum_{\boldsymbol{x}_j \in \mathcal{H}(\boldsymbol{x}_i)} \boldsymbol{f}_{ij} \otimes (\boldsymbol{\xi}_{ij} + \boldsymbol{\eta}_{ij}) \,, \qquad (10)$$

where $\boldsymbol{f}_{ij}$ is the force exerted from material point i to material point j.

The number of bonds interacting with each grid point depends on h/δ_x. Figure 2(b) shows an example of bond connectivity for a horizon $h = 3\delta_x$. The node connectivity W_p increases with h/δ_x approximately as a power law of exponent 2. For example, for h/δ_x varying from 1 to 6, we have $W_p = 4$, 12, 28, 48, 80, and 112, respectively. Finally, it is interesting to note that, although the determination of the number of points on a regular lattice within a given distance is numerically straightforward, it is not fully resolved analytically. This problem is known as the Gauss circle problem and remains an open mathematical problem [46]. We developed a parallel implementation of the discretized bond-based peridynamics approach with the help of a message passing interface (MPI). The simulation domain was split into a regular grid of subdomains, each one being attributed to a single CPU core. See Appendix B for further details about the scaling behavior of the code.

C. Numerical accuracy

The accuracy of a mesh-based simulation depends on the numerical method, type of elements, and the way the simulated domain is discretized. One needs to find a tradeoff between numerical accuracy and computation time. As finer meshes generally lead to a more accurate solution but longer computation time, it is necessary to quantify the required accuracy for the problem at hand and the mesh effects with respect to the considered behavior, such as failure stress or toughness. Below, we will show that the global Griffith fracture approach is consistent with our simulations.

In peridynamics approaches, both the density of the mesh (which depends on the number of elements in x direction N_x) and the resolution of the horizon (which depends on $h/\delta x$) should be fixed. For an inhomogeneous material, the rectilinear mesh leads to the rasterization of the interfaces but also to a blurring effect due to the nonlocal interactions. This issue was extensively studied in [47,48], and the authors concluded that a horizon of 2 should be avoided, but a horizon of 3, which corresponds to 28 bonds per node, provides a good compromise between the accuracy of the solution and computational efficiency. We studied mesh convergence of elasticity properties, and our results confirmed their conclusion.

The failure stress or the strength σ_c of a homogeneous material can be deduced from the Young's modulus E and critical elongation s_0 as $\sigma_c = E s_0$. In multiphase or damaged materials, failure is triggered by stress concentration in the vicinity of defects, and the failure is described in terms of both the strength σ_c and toughness K of the material [49–51]. According to the classical fracture mechanics, for a single crack of length $2a$, the toughness in mode-I fracture is given

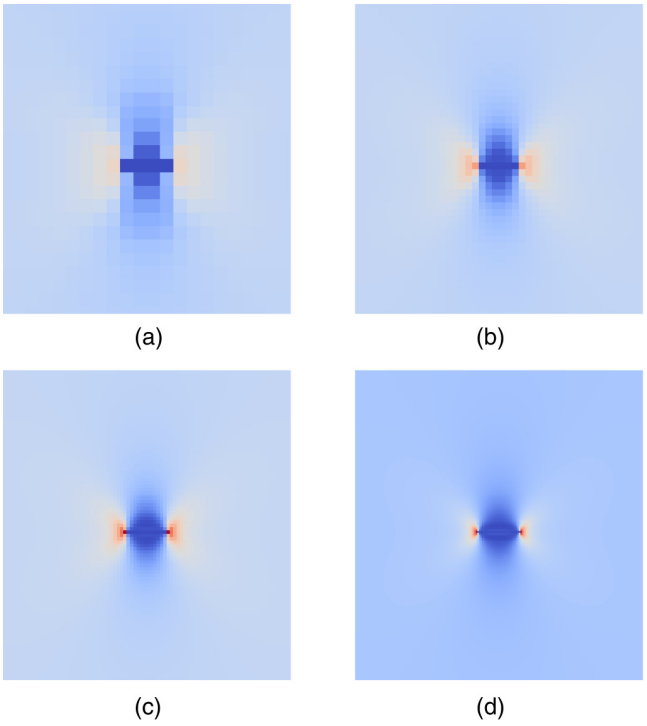

FIG. 3. Stress field around a crack before failure for $h/\delta_x = 6$, $a = 0.0125$ and (a) $N_x = 128$, (b) $N_x = 256$, (c) $N_x = 512$, and (d) $N_x = 1024$.

by

$$K = \sigma_c\sqrt{\pi a} = \sqrt{EG_c}\,, \tag{11}$$

where G_c is the critical energy release rate. Hence the ratio σ_c/K as a function of $1/\sqrt{\pi a}$ is expected to be a linear function of slope 1. In the same way, setting that the theoretical toughness is $K_{th} = \sqrt{EG_c}$, the ratio σ_c/K_{th} as a function of $1/\sqrt{\pi a}$ should be a linear function of slope K/K_{th}, where $K = \sigma_c\sqrt{\pi a}$ is the value of toughness measured from peridynamics simulations.

In the case of a sufficiently small defect, knowing that $\sigma_c = Es_0$, a length l_p can be defined from Eqs. (8) and (11):

$$l_p = \frac{2}{\pi}\left(\frac{K}{\sigma_c}\right)^2 = \frac{9}{2\pi^2}h\,. \tag{12}$$

This length represents that of the fracture process zone (FPZ), where the material undergoes damage ahead of the fracture tip. The above expression indicates that the horizon h is more than a purely numerical parameter and can be physically interpreted as the size of FPZ.

To investigate the evolution of K as a function of both spatial resolution and horizon and for different values of the crack length, we performed extensive simulations of a homogeneous sample containing a single central crack perpendicular to the direction of extension, as shown in Fig. 3. The sample is square-shaped and its side length is 1. The initial crack is a segment, and the bonds crossing it are broken at time $t = 0$. The simulations were carried out for a set of values of $h/\delta x = 2, 3, 4, 5, 6, 7, 8$ and $N_x = 128, 256, 512, 665, 1024$, and in each case the crack half-length was set to different values

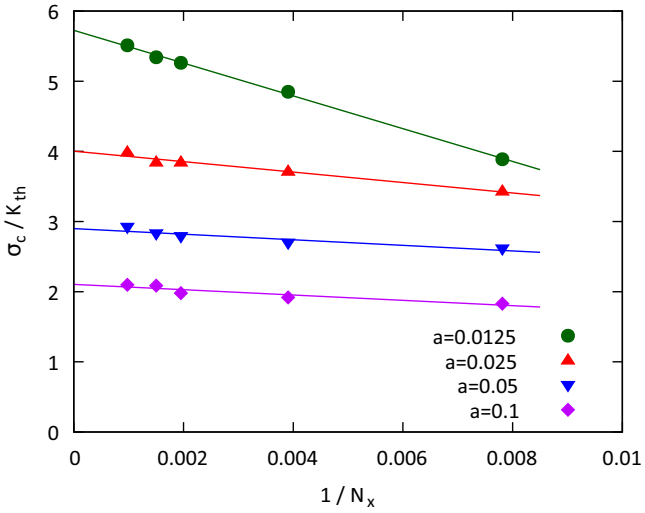

FIG. 4. Failure stress σ_c of a homogeneous material including a single crack of length $2a$ as a function of $1/N_x$ for $h/\delta x = 3$ and several values of a. σ_c is normalized by the theoretical toughness $K_{th} = \sqrt{EG_c}$. The straight lines are a linear regression to the data points.

$a = 0.1, 0.05, 0.025, 0.0125$. With these sets of parameters, 140 simulations were performed.

Let us first consider the spatial mesh convergence at a fixed value of $h/\delta x$. Figure 4 displays σ_c/K_{th} as a function of $1/N_x$ for different values of a in the case $h/\delta x = 3$. For all crack lengths, we observe a nearly linear increase of σ_c as N_x increases, with larger variations and larger strength for shorter crack lengths. The asymptotic value of the strength can be obtained by a linear extrapolation in the limit $1/N_x \to 0$ (limit of infinite precision). The finite spatial resolution leads to reduced elastic moduli and failure stress due to the insufficient number of elements or meshes to represent the continuum elasticity correctly [13,52,53]. This value depends on both a and the horizon $h/\delta x$. Its values are plotted as a function of $1/\sqrt{\pi a}$ for different values of $h/\delta x$ in Fig. 5. As expected, $[\sigma_c/K_{th}]_{N_x\to\infty}$ is a linear function of $1/\sqrt{\pi a}$, and the slope of the curve for a given $h/\delta x$ can be identified as $[K/K_{th}]_{N_x\to\infty}$, measured by peridynamics simulations. This slope is plotted in Fig. 6 as a function of $h/\delta x$. Its value is above 1 at small horizon and tends to 1 as the horizon increases.

The above results show how the accuracy of peridynamics simulations increases with h/δ_x. However, a large horizon such as $h/\delta_x = 8$ implies a larger number of interactions and thus long simulations. The choice $h/\delta_x = 3$ remains a good compromise between numerical efficiency and accuracy. This is consistent with earlier results [54]. Furthermore, the accuracy gained by a larger value of h/δ_x is too expensive and unnecessary to delineate the regime transition addressed in the following.

The examples presented and discussed in this section prove that the peridynamics method captures the continuum-scale quantities such as toughness despite its discrete nature, which removes stress singularities and does not necessarily meet the assumptions of scale separability as required by the continuum mechanics models of fracture. The bond-based

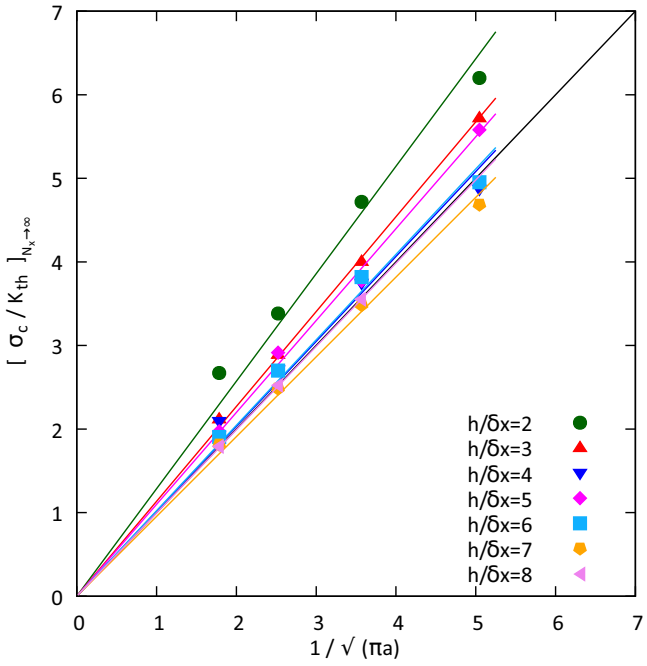

FIG. 5. Extrapolated value of normalized failure stress at infinite resolution in a homogeneous sample that contains a single crack of length $2a$ as a function of $1/\sqrt{\pi a}$ for several values of $h/\delta x$. Straight lines represent linear fits to the data. The slopes represent in each case the ratio $[K/K_{th}]_{N_x\to\infty}$ in the high-resolution limit.

peridynamics is used here for both its capacity of crack nucleation and propagation and its computational performance and versatility. In its basic formulation, the simulated mechanical behavior is brittle and Poisson's ratio is 1/3. Although this method can be extended for the simulation of other mechanical behaviors, it is fully suited in its basic form to multiphase materials in which the complexity of the mechanical behavior arises from the geometrical texture.

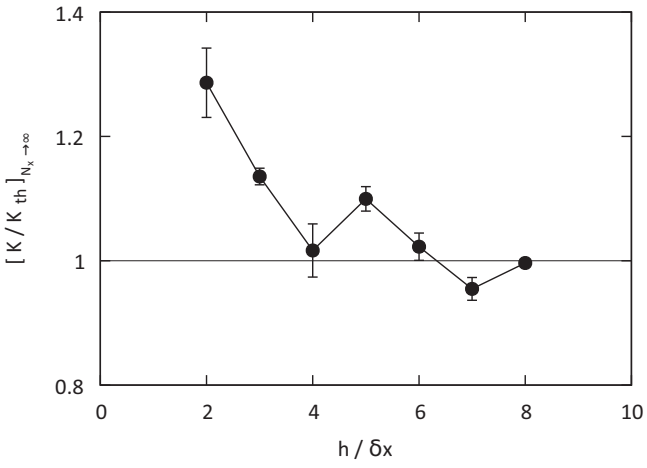

FIG. 6. Infinite-resolution normalized toughness $[K/K_{th}]_{N_x\to\infty}$ measured from peridynamics simulations as a function of $h/\delta x$. Error bars represent standard deviation.

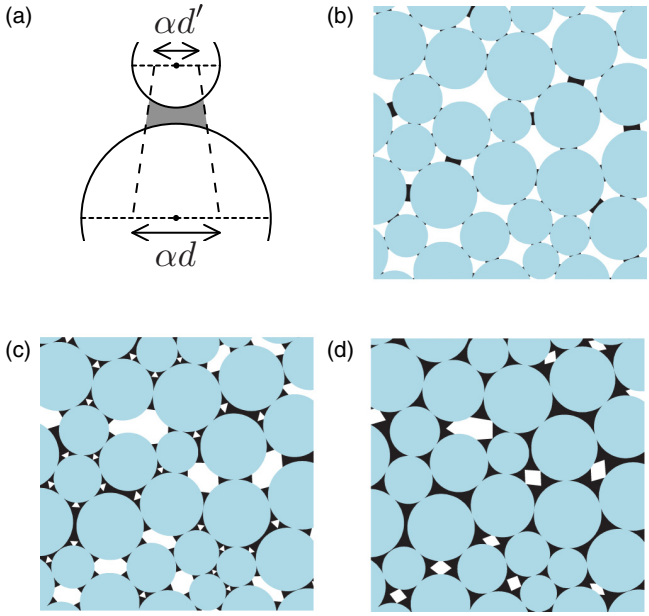

FIG. 7. (a) Algorithm for inserting the binding matrix in the form of pairwise trapezoidal bridges in the gap space in between pairs of neighboring particles. Snapshots for $\alpha = 0.25$ (b), $\alpha = 0.5$ (c), and $\alpha = 0.75$ (d).

III. SAMPLE BUILDING

To generate the microstructure with a distribution of nonoverlapping particles, we used the discrete element method (DEM). The particles are polydisperse disks placed initially inside a 2D simulation box of side lengths L_x and L_z. Then a weak confining pressure (compared to particle stiffness) is applied to the walls of the simulation box until a fully jammed state is reached with an aspect ratio $L_z \simeq 2L_x$ [45]. The particle volumes have a uniform distribution [55] with a size ratio of 2 between the largest and smallest particles. Due to isotropic compaction, the resulting packing has an isotropic texture in terms of contact orientations and forces. Ten independent samples of 400 particles were prepared using this procedure.

The binding matrix is then added to the interstitial space between particles according to the following protocol. A trapezoidal-shaped bridge of the matrix phase is added in the gap space between all pairs of particles for which the center-to-center distance is below $\beta(d + d')/2$, where d and d' are the diameters of the paired particles and β is a control parameter [8,56]. For $\beta = 1$, the eligible pairs include only the pairs of touching particles. As illustrated in Fig. 7, the thickness of the bridges is a fraction α of the particle diameters. For sufficiently low values of α, to which we will refer as a *gap-filling factor*, the binding matrix connects only adjacent pairs of particles [Fig. 7(b)]. When α increases, the thickness of the matrix bridge increases as shown in Fig. 7(c), and for $\alpha = 1$, the bridge fills nearly the whole gap between the two particles; see Fig. 7(d). At this point, some neighboring bridges overlap. In particular, all the pores enclosed between three particles are filled, and the remaining pore space is composed of isolated pores enclosed between four or more particles. To fill these

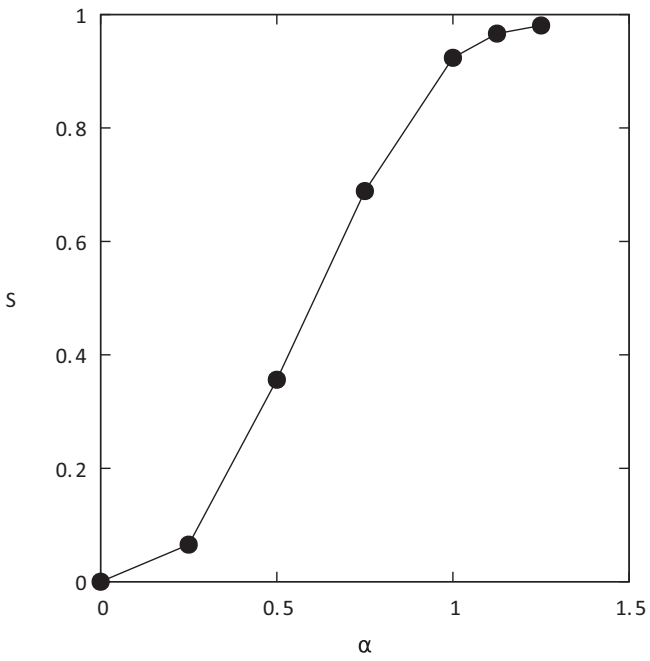

FIG. 8. Saturation factor S of the binding matrix as a function of the gap-filling factor α. The data points are averages over ten independent samples. Error bars are smaller than the symbols.

pores, α must further be increased beyond 1. In the following, we refer to the matrix for $\alpha < 1$ as a *gap-filling* matrix. Of course, other protocols for the distribution of the matrix phase are possible. The protocol used here has the advantage of allowing the gap-filling matrix to be clearly distinguished from the pores of higher order, i.e., pores that do not belong to a gap space in between a pair of particles.

In our simulations, we set $\beta = 1.1$ so that the solid bridges are attributed only to the touching and very close pairs of particles. The parameter α was varied from 0.25 to 1.25. Let Φ_m be the matrix volume fraction and Φ_v the volume fraction of the interstitial space between particles (called also void space). The *saturation factor* $S = \Phi_m/(\Phi_m + \Phi_v)$ represents the volume fraction of the void space filled by the matrix. The saturation factor increases with α, as shown in Fig. 8. Note that S is a nearly linear function of α for intermediate values of α. For $\alpha = 1$, 90% of the interstitial space is filled. This means that the isolated pores at this filling degree represent only 10% of the interstitial volume between particles. We also created a sample with $S = 1$ by simply filling the whole void space.

Figure 9 displays zoomed snapshots of the pore space for different values of the saturation factor S. Both the number and size of the pores decrease by orders of magnitude with increasing S. We used a flood fill algorithm to build the list of pores and their volumes in the samples. Figures 10 and 11 show the number and average volume (area in 2D) of the pores, respectively, as a function of S. We see that the number of pores declines continuously beyond $S = 0.34$, whereas the average pore volume declines significantly only at higher values of S close to 1, reflecting the filling of isolated pores. The largest pore volume, shown also in Fig. 11, follows a similar trend.

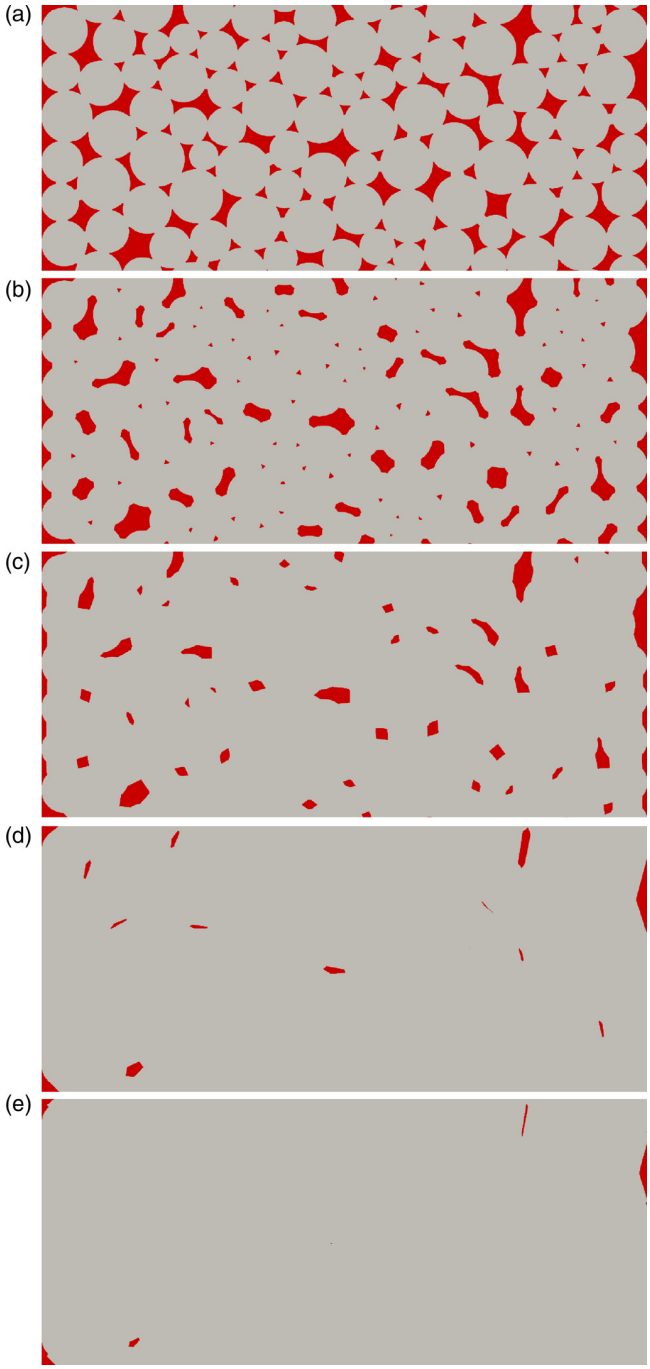

FIG. 9. Pores in cemented granular materials for (a) $S = 0.064$, (b) $S = 0.34$, (c) $S = 0.67$, (d) $S = 0.91$, and (e) $S = 0.97$.

IV. TENSILE STRENGTH

The samples created by the compaction of rigid particles in a box and filled with a given amount of matrix are discretized on a lattice. The lateral walls (along the x axis) are removed, and the top and bottom walls are assumed to have the same mechanical properties as the particles. The bottom wall is fixed, and the top wall is subjected to incremental quasistatic extension at constant rate along the z axis.

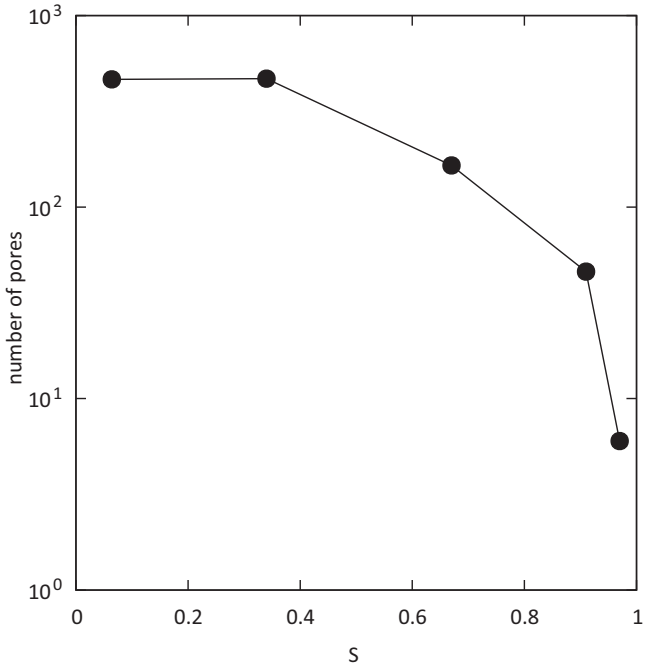

FIG. 10. Number of pores in a sample as a function of the saturation factor S.

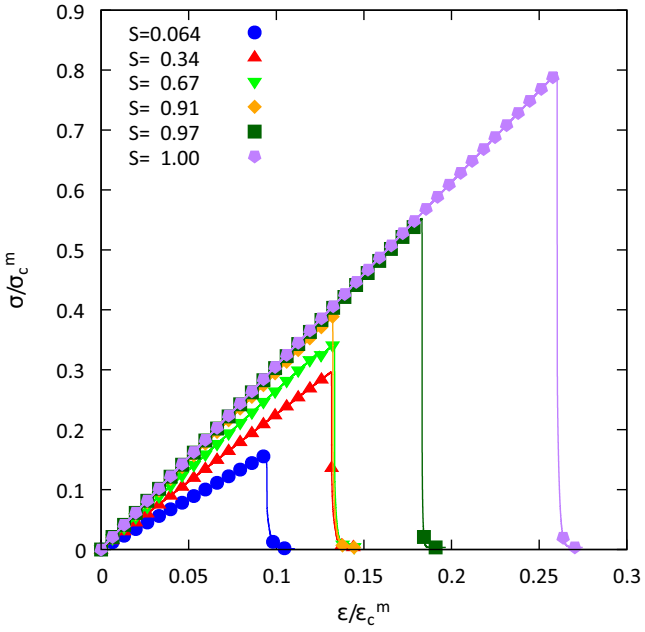

FIG. 12. Stress-strain relationships for different values of S. The stress is normalized by the matrix failure stress, and the strain is normalized by the matrix failure strain.

Each bond connecting two lattice points i and j (closer than the horizon h) has a stiffness k_{ij} depending on the phase in which the points are located. When i or j is in the pores, $k_{ij} = 0$; when i and j are in the matrix, $k_{ij} = k_{MM}$; and when i and j are in the same particle, $k_{ij} = k_{PP}$. Otherwise, $k_{ij} = k_{PM}$ when i and j are in different phases or in different particles.

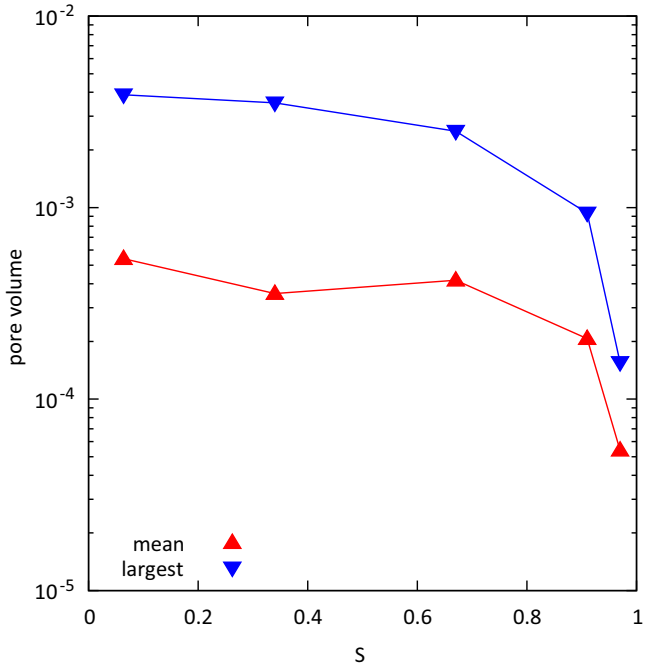

FIG. 11. The average volume of pores and the largest pore volume in a sample as a function of the saturation factor S.

The value of the critical elongation s_{0ij} follows the same assumptions: when i and j are in the matrix, $s_{0ij} = s_{0MM}$; when i and j are in the same particle, $s_{0ij} = s_{0PP}$; otherwise, $s_{0ij} = s_{0PM}$.

The ratio of Young's modulus E_{PP} of the particles to that of the matrix E_{MM} was set to $\psi = E_{PP}/E_{MM} = 4$. This choice implies that most of the deformation occurs in the matrix phase. In the same way, the ratio of the toughness of the particles to that of the matrix was set to $K_{PP}/K_{MM} = \psi = 4$. The particle-matrix interface is assumed to have the same properties as the matrix: $E_{PM} = E_{MM}$ and $K_{PM} = K_{MM}$. This choice of the mechanical parameters was motivated by the general observation that in most aggregates the matrix is the weakest phase and the properties of the interface are generally closer to those of the weaker phase. The focus of this paper is on the effect of the binding matrix. According to our earlier results [57], the value $\psi = 4$ is high enough to ensure that particles will not be damaged during tensile tests and the cracks propagate only inside the binding matrix. A similar analysis can be performed for other values of the phase material properties.

Figure 12 shows the vertical stress, normalized by the tensile strength σ_c^m of the matrix, as a function of vertical strain ε, normalized by the fracture strain $\varepsilon_c^m = \sigma_c^m/E_{MM}$, for different values of S. In all cases we observe a brittle linear elastic behavior with an increasing effective Young's modulus and fracture stress as S increases. The tensile strength of the aggregate is the fracture stress σ_c at the failure point. Up to the failure point, no breakage events are observed inside the sample, which continues to deform elastically. At failure, a crack nucleates and propagates instantly across the sample, leading to sudden stress drop. Figure 13 shows two examples of typical crack paths. The cracks are extended damaged

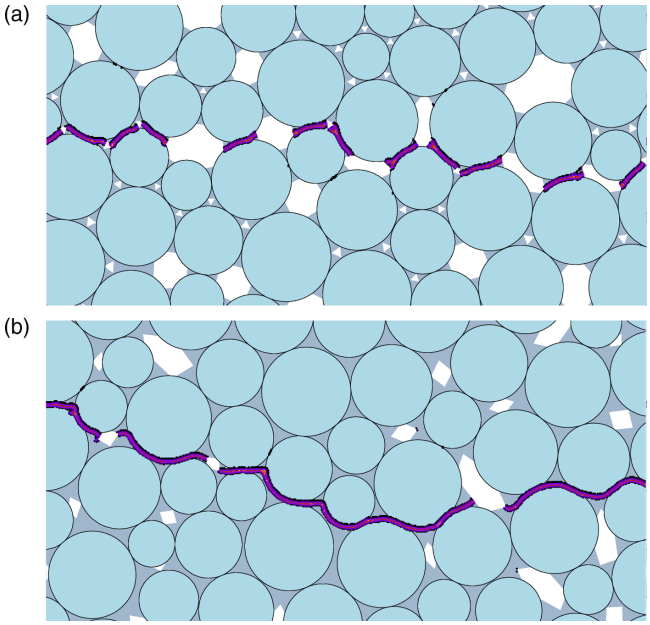

FIG. 13. Zoomed snapshots of crack paths for (a) $S = 0.34$ and (b) $S = 0.67$.

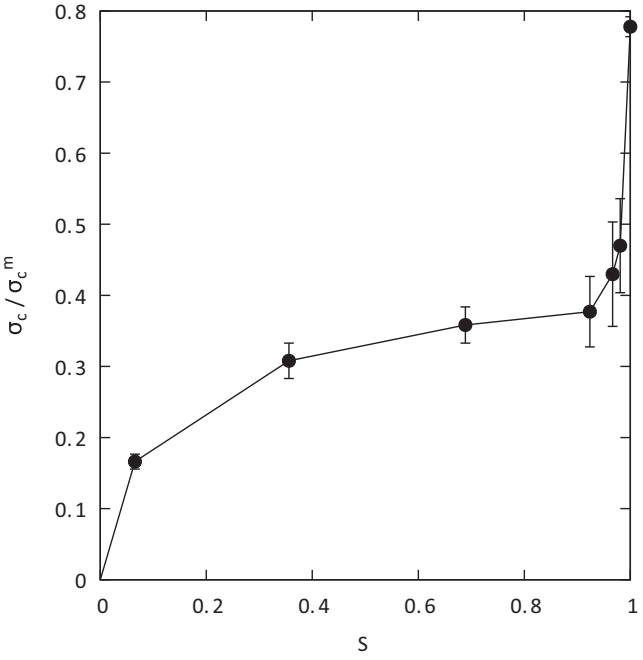

FIG. 14. Tensile strength σ_c normalized by the strength σ_c^m of the matrix phase as a function of the saturation factor S. The data points are averages over ten samples, and the error bars are the corresponding standard deviations.

zones with a constant thickness controlled by the size of the peridynamics horizon. As expected, they are initiated in the matrix and cannot penetrate the particles since the matrix has a lower toughness than the particles ($\psi = 4$). For this reason the tensile strength depends on the strength of the matrix phase and the arrangement of the particles, and may thus be quantified in terms of a tortuosity parameter [58].

Figure 14 shows the tensile strength σ_c as a function of the saturation factor S. The tensile strength first increases rapidly with S in the range from 0 to 0.4, then increases only slightly from 0.4 to 0.9 before rising strongly again as S increases from 0.9 to 1. The tensile strength is nearly doubled in this range, increasing from $\sigma_c \simeq 0.38\sigma_c^m$ to $\sigma_c \simeq 0.78\sigma_c^m$. This means that for $S = 1$, the matrix filling the isolated higher-order voids, representing only 10% of the total matrix volume, contributes as much to the strength of the aggregate as the gap-filling matrix, corresponding to 90% of the total matrix volume. This behavior reflects stress concentration by both the particle chains and the isolated pores that we analyze in detail below. In the fully saturated case $S = 1$, the ratio $\sigma_c/\sigma_c^m \simeq 0.78$ reflects the fact that the crack propagates only in the matrix phase following a tortuous path.

V. STRESS TRANSMISSION

The tensile stress in cemented aggregates is transmitted through both the particle phase and the matrix phase. As the amount of the matrix increases, we expect an increasingly homogeneous transmission of the stress, with the matrix playing two different roles depending on whether it fills the gaps in-between the particles or the remaining isolated pores when the gaps are filled. In other words, as long as the saturation factor S is below 0.9, we expect the matrix just to bridge the particles, allowing tensile stresses to be transmitted across the particle phase. For larger values of S the higher-order pores are filled by the matrix, and thus stress concentration by the pores is reduced. We would like to clarify the signature of these two different effects on the distribution of tensile and compressive stresses inside the material.

Figure 15 displays several zoomed maps of the vertical stress field σ_{zz} for different values of S for $\epsilon/\epsilon_c{}^m = 1.62 \times 10^{-2}$. At low values of S, the tensile (positive) stresses are concentrated at the contact points between particles, which define *stress chains* across the contacts and particles throughout the system, although they are blurred inside the particles, showing both large stresses close to the contact points and a large number of vanishing stress values. The stress chains thicken with increasing volume of the matrix, while losing their intensity. At larger values of S we still observe the stress chains, but the patterns of stress concentration are correlated both with the remaining pores and with the particle positions. This is consistent with a recent work showing that stress chains can be induced not only by the contact network but also by the presence of disordered pores inside a continuous matrix [27].

The compressive forces (not shown in Fig. 15) are by at least one order of magnitude lower than tensile forces. The mean values of the tensile (positive) and compressive (negative) vertical stress σ_{zz} for $\epsilon/\epsilon_c{}^m = 1.62 \times 10^{-2}$ are shown in Fig. 16 as a function of S. As expected, the average tensile stress increases with S. Moreover, its value is well above that in the matrix alone ($\langle\sigma_{zz}\rangle/\sigma^m > 1$). This reflects the fact that the particle phase carries the largest stresses due its largest volume fraction. The mean compressive stress is approximately 10 times lower than the tensile stress, and it declines with increasing S. In particular, its rapid decrease

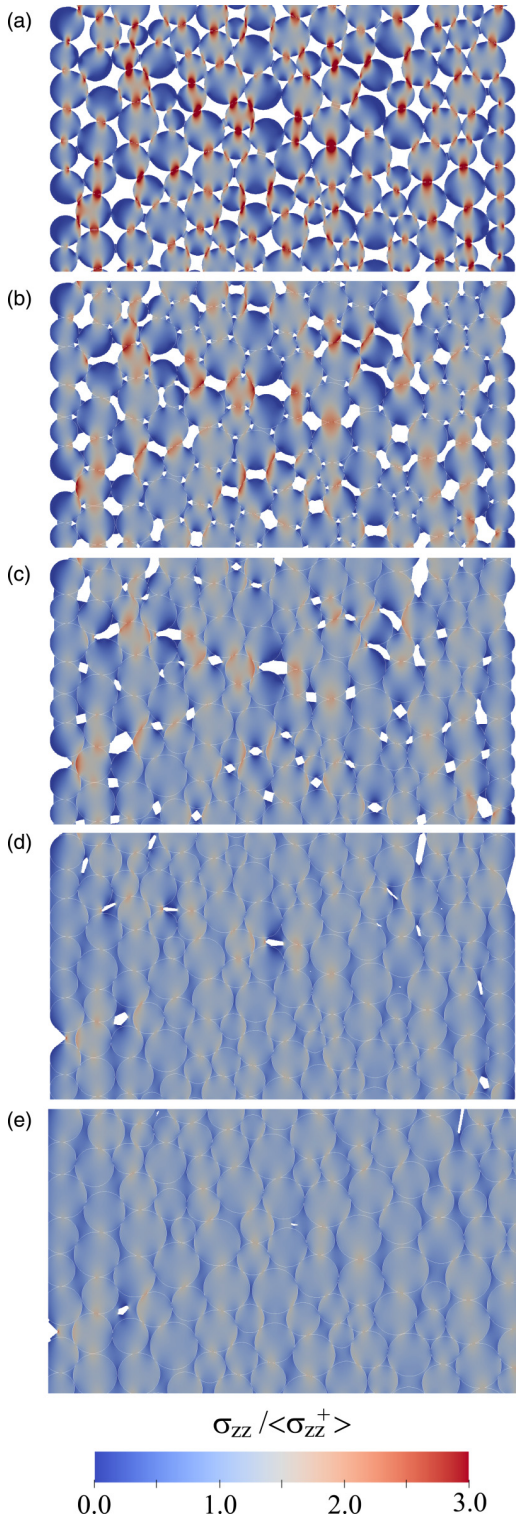

FIG. 15. Zooms in typical vertical stress maps in simulated aggregates for $\epsilon/\epsilon_c{}^m = 1.62 \times 10^{-2}$ and (a) $S = 0.064$, (b) $S = 0.34$, (c) $S = 0.67$, (d) $S = 0.91$, and (e) $S = 0.97$. The stress is normalized by the mean vertical tensile (positive) stress. The color scale ranges from heavy blue for zero stress to heavy red for strong stresses.

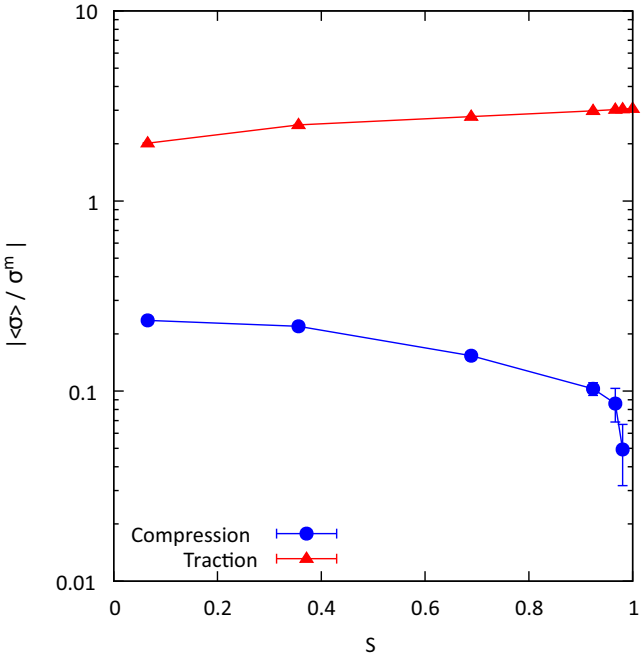

FIG. 16. Average value of tensile (positive) and compressive (negative) vertical stresses in the sample as a function of the matrix saturation factor S for $\epsilon/\epsilon_c{}^m = 1.62 \times 10^{-2}$. The stresses are normalized by the stress in pure matrix at the same strain. The data points are averages over ten samples and the vertical error bars are the corresponding values of the standard deviation.

towards zero for values of S close to 1 is a signature of load transfer from the particles to the matrix as the isolated voids are filled by the matrix.

The probability density functions (PDFs) of vertical stresses σ_{zz} are shown in Fig. 17 for different values of S. For small values of S we observe a broad distribution, with the largest tensile stresses extending to several times the average tensile stress of the sample. As S increases the PDF shrinks, reflecting larger homogeneity of stress transmission. For all values of S we observe a pronounced peak centered on the average tensile stress. Its increasing value with S is another signature of the increasing homogeneity due to the pore-filling role of the matrix. The number of compressive stresses also declines and vanishes as $S \to 1$. The PDFs are also characterized by a peak or kink at zero stress. This peak is clearly a signature of the inhomogeneous stress distributions inside the particles. The strongest stresses are located at the contact zones between particles, but the stresses in the outer layers or rims of the particles that are not covered by the matrix are induced by the small deformations of the particles, and thus they are vanishingly small. These small stresses are also induced by the arching effect, i.e., deviation of stress lines due to local archlike structures, giving rise to low-stress regions [26].

A common feature of the stress PDFs is the exponential falloff at large tensile stresses:

$$P(\sigma) \propto e^{-\theta \sigma_{zz}/\langle \sigma_{zz}^{+} \rangle}. \tag{13}$$

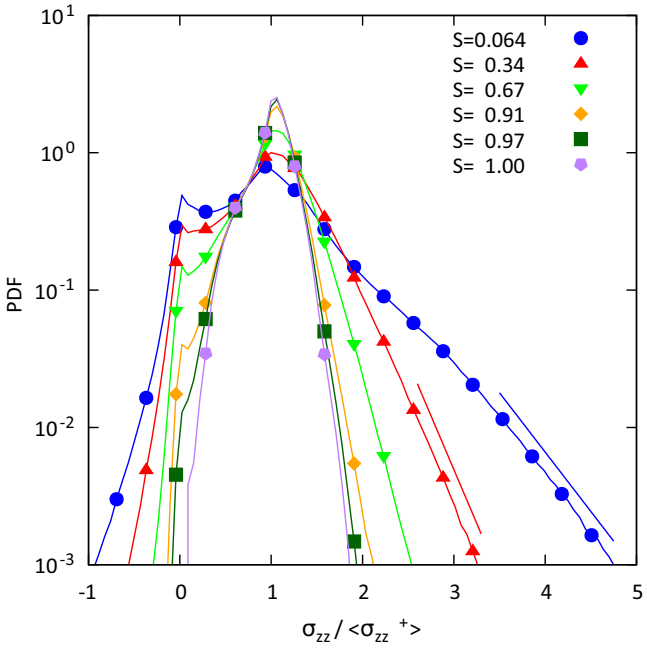

FIG. 17. Probability density function (PDF) of vertical stresses in granular aggregates for different values of S. The stresses are normalized by the average tensile stress (positive) σ_{zz}^{+} in each sample. On each curve, a symbol is drawn every five points. The straight lines represent exponential functions that are added here as a guide to the eyes.

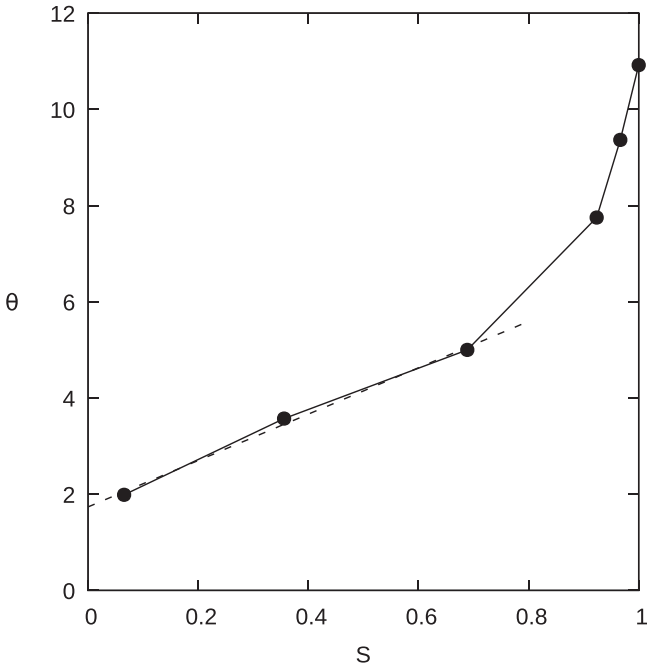

FIG. 18. The coefficient θ of the exponential falloff of tensile stresses as a function of the saturation factor S. The dashed line is plotted as a guide to the eyes.

This feature is a hallmark of force transmission in granular materials [26,59–62]. It is generally associated with the force chains, i.e., long-range correlations of strong forces across the contact network. Since we observe tensile stress chains (Fig. 15) in our aggregates, we may conclude that the exponential tails represent a signature of the contact network, connecting the particle phase at least in the gap-filling stage ($S < 0.9$). For larger values of S, the exponential tails can be attributed to disorder in the distribution of isolated pores [27]. This distinction between the two origins of the exponential tails is best quantified in Fig. 18, where the coefficient θ is plotted as a function of S. We observe a nearly linear increase of θ with S, followed by a rapid increase for the largest values of S. This sudden change is consistent with the rapid increase of the tensile strength in Fig. 14. This change can be described as a transition from stress concentration by the particle chains to stress concentration by pores.

VI. CONCLUSION

The central idea of this work was to investigate the origins of the tensile strength in granular aggregates for a varying amounts of the binding matrix. The bond-based peridynamics model was used for its versatile nature, allowing for the discretization of both particle and matrix phases on the same underlying lattice and crack nucleation based on a local stress criterion. We showed that the Griffith model is in full agreement with peridynamics simulations for crack propagation, and we investigated the mesh effects and the choice of numerical parameters such as lattice step and the peridynamics horizon, identified here as the size of the fracture process zone.

The sample building procedure was designed to allow filling the gap space between pairs of particles by the binding matrix in the first stage. This procedure leads to a fraction $S = 0.9$ of the interstitial space between particles to be filled. The remaining fraction is composed of isolated pores that are filled in a second stage. By subjecting the samples to tensile loading, we found that the contributions of the gap-filling matrix and pore-filling matrix to the tensile strength of the aggregates are nearly equal. The underlying physical effects are, respectively, tensile stress chains in the presence of a gap-filling matrix in the first stage and reduced stress concentration by the pores as they are filled by the matrix in the second stage.

The granular samples used in this work were dense packings created by compaction. Hence the number and volumes of isolated (higher-order) pores is small once all the gaps between pairs of particles are filled. For a lower packing fraction we expect this fraction to increase. It would therefore be interesting to consider in a future work samples of different packing fractions and evaluate the effect of the binding matrix. Further simulations can also be performed to analyze the shear strength of the aggregates by subjecting them to simple shear. A similar work in three dimensions (3D) requires much more computation time and memory. Although the pore structure in 3D packings is different, we still may distinguish the interparticle gap space from higher-order pores. For this reason, we expect similar results in 3D. Finally, the peridynamics approach can be used to investigate other classes of structured porous materials such as cellular solids where both porosity and stress correlations should underlie their strength and failure properties.

ACKNOWLEDGMENTS

We are grateful to the INRAE MIGALE bioinformatics facility [63] and to the Genotoul Bioinformatics platform Toulouse Occitanie [64] for providing computing and storage resources.

APPENDIX A: QUASISTATIC LOADING

In order to enforce quasistatic loading, we damp elastic waves by adding a viscous force $-\nu\dot{\boldsymbol{u}}_i(t)$ to all material points [43]. The viscosity ν should be below the critical viscosity $\min\{\sqrt{2m_i k}\}$ to avoid supercritical damping.

Upon failure, the stored elastic energy is released. Under stress-controlled conditions, this may lead to unstable crack propagation and bifurcations. To remain in quasistatic regime, one may decrease the loading rate at incipient breakage. Following the idea of the snap-back method [9], we use a regulation procedure which consists of applying the strain ε at a rate $\Gamma(t)$ which depends on the cumulative damage energy ω:

$$\dot{\omega} = -\frac{1}{\tau}\omega + \sum_i \delta(t - i\delta t)\Delta\omega_i\,, \tag{A1}$$

$$\dot{\Gamma} = -\frac{1}{\tau}(\Gamma - \Gamma_0\, e^{-\frac{\omega}{\omega_0}})\,, \tag{A2}$$

where τ is a relaxation time, Γ_0 is the imposed strain rate, δ is the Dirac function, and $\Delta\omega_i$ represents the total damage energy of all bonds broken during the ith time step. ω_0 is the energy required to open a crack of length $\Delta\ell$ in mode I in the weakest phase. A value of $\Delta\ell$ below 1% of the system characteristic size is sufficiently small to ensure quasistatic loading with a reasonable CPU time. This value was used in all the simulations reported in this paper.

APPENDIX B: PARALLEL IMPLEMENTATION

Mechanical simulation of natural materials generally requires: (1) highly resolved samples accounting for their complex microstructures, and (2) a large statistical set of tests to fully capture the mean behaviors and their variability. For these reasons and due to the CPU cost of the simulations, parallel computing is necessary.

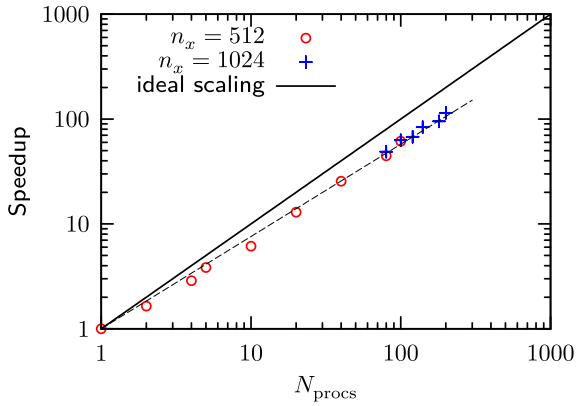

FIG. 19. Speedup of the developed peridynamics code (for $h/\delta x = 3$) as a function of the number of processes for two resolutions: 512 × 1024 and 1024 × 2048.

We developed a parallel bond-based peridynamic computer code relying on the message-passing interface (MPI), which provides efficient routines to exchange data between a set of processes. In this code the spatial domain is split in equal-size subdomains which is attributed to a single process. The scalability of the code was tested on the French national cluster "Genotoul Bioinformatics." In this cluster, each computer node involves two IvyBridge 10 cores hyperthreaded microprocessors of frequency 2.5 GHz interconnected through a Quad Data Rate (QDR) infiniband network for both MPI and input/output communications.

Figure 19 shows the speedup as a function of the number P of processes involving up to 200 cores. The global trend shows a good scalability of the parallel algorithm. However, the speedup is not linear due to the nonlocal third-order neighborhood employed in the computation, which increases the exchange of data during the communication steps.

[1] H. J. Herrmann and S. Roux, *Statistical Models for the Fracture of Disordered Media* (Elsevier, New York, 2014).

[2] L. Dormieux, D. Kondo, and F.-J. Ulm, *Microporomechanics* (John Wiley & Sons, New York, 2006).

[3] O. Buyukozturk and B. Hearing, Int. J. Solids Struct. **35**, 4055 (1998).

[4] W. Gerstle, N. Sau, and S. A. Silling, Nucl. Eng. Des. **237**, 1250 (2007).

[5] A. Manoylov, F. Borodich, and H. Evans, Proc. R. Soc. A **469**, 20120689 (2013).

[6] L. Reig, C. Tojal, D. Busquets, and V. Amigó, Materials **6**, 4868 (2013).

[7] R. Holtzman, Int. J. Numer. Anal. Methods Geomech. **36**, 944 (2012).

[8] V. Topin, F. Radjai, J.-Y. Delenne, A. Sadoudi, and F. Mabille, J. Cereal Sci. **47**, 347 (2008).

[9] E. Schlangen and J. van Mier, Cem. Concr. Compos. **14**, 105 (1992).

[10] B. Chiaia, J. van Mier, and A. Vervuurt, Cem. Concr. Res. **28**, 103 (1998).

[11] I. Merchant, D. Macphee, H. Chandler, and R. Henderson, Cem. Concr. Res. **31**, 1873 (2001).

[12] M. A. Issa, M. A. Issa, M. S. Islam, and A. Chudnovsky, Eng. Fract. Mech. **70**, 125 (2003).

[13] R. Affès, J.-Y. Delenne, Y. Monerie, F. Radjaï, and V. Topin, Eur. Phys. J. E **35**, 117 (2012).

[14] R. Eckner, M. Krampf, C. Segel, and L. Krüger, Mech. Comp. Mater. **51**, 707 (2016).

[15] J. Bauer, S. Hengsbach, I. Tesari, R. Schwaiger, and O. Kraft, Proc. Nat. Acad. Sci. **111**, 2453 (2014).

[16] I.-H. Oh, N. Nomura, N. Masahashi, and S. Hanada, Scr. Mater. **49**, 1197 (2003).

[17] C. Zou, E. Zhang, M. Li, and S. Zeng, J. Mater. Sci. - Mater. Med. **19**, 401 (2008).

[18] A. Fakhimi and A. Tarokh, Int. J. Rock Mech. Min. Sci. **60**, 95 (2013).

[19] H. Laubie, F. Radjai, R. Pellenq, and F.-J. Ulm, J. Mech. Phys. Solids **105**, 116 (2017).

[20] V. Topin, F. Radjai, J.-Y. Delenne, and F. Mabille, Powder Technol. **190**, 215 (2009).

[21] S. Torquato, *Random Heterogeneous Materials: Microstructure and Macroscopic Properties* (Springer-Verlag, New York, 2002).

[22] S.-Y. Fu, X.-Q. Feng, B. Lauke, and Y.-W. Mai, Composites, Part B **39**, 933 (2008).

[23] V. Topin, J.-Y. Delenne, F. Radjai, L. Brendel, and F. Mabille, Eur. Phys. J. E **23**, 413 (2007).

[24] T. T. Wu, Int. J. Solids Struct. **2**, 1 (1966).

[25] F. Saadat, V. Birman, S. Thomopoulos, and G. M. Genin, J. Mech. Phys. Solids **82**, 367 (2015).

[26] F. Radjai, D. E. Wolf, M. Jean, and J.-J. Moreau, Phys. Rev. Lett. **80**, 61 (1998).

[27] H. Laubie, F. Radjai, R. Pellenq, and F.-J. Ulm, Phys. Rev. Lett. **119**, 075501 (2017).

[28] T. Nguyen, J. Yvonnet, Q.-Z. Zhu, M. Bornert, and C. Chateau, Eng. Fract. Mech. **139**, 18 (2015).

[29] K. Matouš, M. G. Geers, V. G. Kouznetsova, and A. Gillman, J. Comput. Phys. **330**, 192 (2017).

[30] S. A. Silling, J. Mech. Phys. Solids **48**, 175 (2000).

[31] S. A. Silling and E. Askari, Comput. Struct. **83**, 1526 (2005).

[32] S. A. Silling, M. J. Epton, O. Weckner, J. Xu, and E. Askari, J. Elasticity **88**, 151 (2007).

[33] Y. D. Ha and F. Bobaru, Int. J. Fract. **162**, 229 (2010).

[34] Y. D. Ha and F. Bobaru, Eng. Fract. Mech. **78**, 1156 (2011).

[35] E. Askari, F. Bobaru, R. B. Lehoucq, M. L. Parks, S. A. Silling, and O. Weckner, J. Phys.: Conf. Ser. **125**, 012078 (2008).

[36] F. Bobaru, Model. Simul. Mater. Sci. Eng. **15**, 397 (2007).

[37] E. Celik, I. Guven, and E. Madenci, Theor. Appl. Fract. Mech. **55**, 185 (2011).

[38] A. Agwai, I. Guven, and E. Madenci, Microelectron. Reliab. **51**, 2298 (2011).

[39] P. Perré, G. Almeida, M. Ayouz, and X. Frank, Ann. Forest Sci. **73**, 147 (2016).

[40] J. Xu, A. Askari, and S. Silling, J. Aerosp. Eng. **21**, 187 (2008).

[41] W. Hu, Y. Ha, and F. Bobaru, Int. J. Multiscale Comp. Eng. **9**, 707 (2011).

[42] E. Oterkus and E. Madenci, J. Mech. Mater. Struct. **7**, 45 (2012).

[43] B. Kilic and E. Madenci, Theor. Appl. Fract. Mech. **53**, 194 (2010).

[44] S. Sun and V. Sundararaghavan, Int. J. Solids Struct. **51**, 3350 (2014).

[45] F. Radjai and F. Dubois, *Discrete Numerical Modeling of Granular Materials* (Wiley ISTE, London, 2011).

[46] N. Sloane, *A Handbook of Integer Sequences* (Academic Press, New York, 1973).

[47] A. Freimanis and A. Paeglitis, Procedia Eng. **172**, 284 (2017).

[48] A. Yaghoobi and M. G. Chorzepa, Comput. Struct. **161**, 43 (2015).

[49] T. L. Anderson, *Fracture Mechanics: Fundamentals and Applications* (CRC Press, Boca Raton, FL, 2017).

[50] G. Irwin, *Fracture Dynamics, Fracturing of Metals* (American Society of Metals, Metals Park, OH, 1948).

[51] G. Irwin, J. Appl. Mech. **24**, 351 (1957).

[52] A. P. Roberts and M. Teubner, Phys. Rev. E **51**, 4141 (1995).

[53] J.-M. Gatt, Y. Monerie, D. Laux, and D. Baron, J. Nucl. Mater. **336**, 145 (2005).

[54] P. Diehl, F. Franzelin, D. Pflüger, and G. Ganzenmüller, Int. J. Fract. **201**, 157 (2016).

[55] C. Voivret, F. Radjai, J.-Y. Delenne, and M. S. El Youssoufi, Phys. Rev. E **76**, 021301 (2007).

[56] E. Chichti, V. Lullien-Pellerin, M. George, F. Radjai, R. Affès, and J.-Y. Delenne, J. Food Eng. **190**, 40 (2016).

[57] X. Frank, J.-Y. Delenne, and F. Radjai, EPJ Web Conf. **140**, 02029 (2017).

[58] M. A. Issa, A. M. Hammad, and A. Chudnovsky, Int. J. Fract. **60**, 97 (1993).

[59] N. Estrada, A. Taboada, and F. Radjai, Phys. Rev. E **78**, 021301 (2008).

[60] F. Radjai, C. R. Phys. **16**, 3 (2015).

[61] D. M. Mueth, H. M. Jaeger, and S. R. Nagel, Phys. Rev. E **57**, 3164 (1998).

[62] T. S. Majmudar and R. P. Behringer, Nature (London) **435**, 1079 (2005).

[63] MIGALE, INRAE, 2018. Migale Bioinformatics Facility, https://doi.org/10.15454/1.5572390655343293E12.

[64] GenoToul Bioinfo, INRAE, 2018. GenoToul Bioinformatics Facility, https://doi.org/10.15454/1.5572369328961167E12.

Computational Particle Mechanics
https://doi.org/10.1007/s40571-021-00390-5

Breakage of flawed particles by peridynamic simulations

Nicolas Blanc[1] · Xavier Frank[1] · Farhang Radjai[2] · Claire Mayer-Laigle[1] · Jean-Yves Delenne[1]

Received: 13 January 2020 / Revised: 22 December 2020 / Accepted: 1 February 2021

Abstract
In this paper, we use a 2D bond-based peridynamic model to investigate the strength of disk-shaped particles including pre-cracks. We use a diametral (or Brazilian) test to break the particles. For the flawless particles, we find that the stress distribution compares well with an analytical model accounting for the size of the contact zone, and the particle stiffness tends linearly to a well-defined value for increasingly resolved meshing. We then introduce cracks, which are numerically defined by reducing the Young modulus of the bonds crossing linear segments. We consider in detail the effect of a single vertical crack on the yield stress as a function of its position. We also consider a randomly distributed population of cracks with sizes generated from a Gaussian size distribution. For a parametric study with a hundred particles, we found a probability of failure that is well fit by a Weibull law. Finally, using an image analysis algorithm, we investigate the statistics of cracks and the resulting fragments.

Keywords Particle breakage · Flaws · Peridynamics · Crack patterns

1 Introduction

In chemical engineering, the powder particles can be the result of various down-sizing or up-sizing processes such as grinding, micronization, erosion, agglomeration, atomization, and RESS (Rapid Expansion of Supercritical Solutions). These particles may present a wide range of bulk or interface properties, and they are most often broadly distributed with various shapes.

An important issue is to evaluate the strength of these particles depending on the material and mechanical loading. This strength plays a key role in many practical problems such as the minimization of energy to achieve a given size reduction or the reduction in fine particles resulting from powder processing. In the same vein, it is well known that the strength highly depends on the internal microstructure of the particles. For example, the strength of compacted powders depends on the porosity [1,2] or in cohesive granular aggregates it also depends on the amount of gluing matrix [3]. Although homogenization methods have been used to account for the effect of heterogeneities [4], they usually fail in predicting the influence of singularities such as cracks or bare contacts on the onset and propagation of cracks.

For practical reasons, the diametral compression, which consists in crushing a grain in compression between two plates, is frequently used for the evaluation of the strength of particles [5,6]. This test gives an indirect but easy-to-handle measurement of the tensile strength. Both disk (or cylindrical)- [7] and sphere-shaped [8] particles were tested but also non-spherical grains [9]. This test has been successfully employed in many practical issues in civil engineering, pharmaceutical tableting, strength of ore granules, as well as in more fundamental studies of the influence of the microstructure on fracture and fragmentation [10,11].

Numerical simulations based on the Discrete Element Method (DEM) have been used for the investigation of particle crushing by modeling each grain as a cohesive agglomerate of smaller (primary) particles [12–15]. Although these approaches fundamentally consider the material as a discrete medium with potential pre-existing fragments, the evolution of cracks and complex geometries of fragments in 2D [16–18] and 3D are reproduced with rather good accuracy [19–22].

However, in DEM-type approaches, such as cohesive DEM [16] or bonded-cell [17,23] methods, the crack path

We thank BPI France for their financial support.

Jean-Yves Delenne
jean-yves.delenne@inrae.fr

[1] IATE, Univ Montpellier, INRAE, Institut Agro, Montpellier, France

[2] LMGC, Univ Montpellier, CNRS, Montpellier, France

Published online: 24 February 2021

is strongly guided by the characteristic size of the DEM elements or by an underlying tessellation of the particles at the microscale. Due to the non-local character of peridynamics the crack propagation is less affected by the local ordering induced by the angular distribution of the bond orientations [24–26]. In this paper, we use such a method applied to particles that can break into fragments of arbitrary sizes and shapes (up to the discretization limit) in the presence of microcracks. Peridynamics has been successfully used for modeling the fracture of materials such as concrete [27], nickel nanowires [28], and wood [29]. It was introduced by Silling [30] as an alternative method to continuum mechanics based on integro-differential equations instead of differential equations. This framework allows one to include discontinuities such as pores, cracks or stiffness, and damage gradients without involving any particular case-sensitive processing for each problem [30]. Although it can be CPU time consuming, peridynamics exhibits a weaker dependence with respect to the discretization grid contrary to other lattice methods that consider only the nearest neighbors such as the Fuse Models [24], the Lattice Element Method (LEM) [25], or peridynamics approaches computed for $h = 1\delta x$ [26].

In this paper, we use a bond-based implementation of peridynamics to investigate the crack patterns of 2D disk-shaped particles embedding flaws. The population of flaws is randomly distributed with a controlled density. The particles are loaded in compression between two horizontal plates. We are interested in the probability distribution of yield stresses and fragments for a large number of particles.

2 Bond-based peridynamics

In our model, we consider that the domain is discretized using material points located on a $N_x \times N_y$ grid with a spatial resolution δx (Fig. 1). In the following, we assume $N_y = N_x$. A volume V_i and a mass $m_i = \rho V_i$ (where ρ is the density of the material) are associated with each point i of position $\boldsymbol{x}_i$. The point i interacts with its surrounding nodes j of position $\boldsymbol{x}_j$ within a distance called the horizon h. Hence, this horizon contains all nodes j belonging to the set

$$\mathcal{H}_i = \{j, ||\boldsymbol{x}_j - \boldsymbol{x}_i|| < h\} \tag{1}$$

The vector $\boldsymbol{\xi}_{ij} = \boldsymbol{x}_j - \boldsymbol{x}_i$ is the relative position between the two nodes defined at the *initial state*, and we denote by $\boldsymbol{\eta}_{ij}$ their relative displacement after deformation.

In bond-based peridynamics, the 1D elements called "bonds" connecting the material points only transmit independent pair-wise forces. We assume in this paper a linear relationship

$$\boldsymbol{f} = cs\boldsymbol{n} \tag{2}$$

where $s = (\|\boldsymbol{\xi} + \boldsymbol{\eta}\| - \|\boldsymbol{\xi}\|)/\|\boldsymbol{\xi}\|$ is the bond elongation, $\boldsymbol{n} = (\boldsymbol{\xi} + \boldsymbol{\eta})/\|\boldsymbol{\xi} + \boldsymbol{\eta}\|$ an orientated unitary vector and c the so-called micromodulus. For elastic materials described in plane stress, $c = 6E/(\pi h^3(1-\nu))$ [31], where E is the Young modulus and ν is the Poisson coefficient. Note, however, that for theoretical reasons [30,32] and similar to other lattice approaches [25,33] ν is fixed in the bond-based model (value is 1/3 in 2D and 1/4 in 3D). A more in-deep discussion on the way Poisson's ratio is related to the connectivity of the lattice bonds can be found in [34]. It is also possible to overcome this limitation using enriched models [35,36]. However, as 1/3 is a reasonable value for many materials such as many polymers (PPMS 0.34, polystyrene 0.35, PMMA 0.36…) [37], metals (copper 0.33, aluminum 0.32…) [38], or geopolymers [39], in this study, we focus on the effect of inhomogeneities which play a dominant role on the failure mechanisms.

The material can be viewed as a mass–spring system where material points interact through harmonic bonds. The time evolution of such systems can be computed using the velocity-Verlet algorithm [40] with a time step δt. To dissipate the elastic waves, a damping force $\boldsymbol{F}_i^d = \eta \dot{\boldsymbol{x}}_i$ is applied on each node, where $\dot{\boldsymbol{x}}_i$ is the velocity of the material point i and η a viscosity coefficient. This latter should be chosen below the minimal critical damping value η_c. In the same vein as other dynamic models based on mass-spring systems, the critical damping η_c is the value of the viscosity above which the bond between two neighbors is overdamped. The value of the damping was chosen to damp the elastic waves during the quasi-static loading phase without influencing the crack propagation at breakage. Note, however, that the yield stress, investigated in details in this study, is almost not influenced by the damping which was fixed to $\eta = \eta_c/10$ for all simulations.

The occurrence of fracture in the material can be taken into account by introducing a critical elongation s_0 above which the bonds fail. For plain stress [31]

$$s_0 = \sqrt{4\pi G/(9Eh)} \tag{3}$$

where G is the macroscopic fracture energy of the material. Due to the non-local description of peridynamics, it is usually convenient to consider a damage parameter. Assuming that the cell volumes do not vary significantly, this damage can be evaluated at each node as the ratio between the number of broken bonds and the initial number of bonds connected to the node.

A horizon $h = 3\delta x$ is used in the following, corresponding to 28 connections for bulk nodes (which are at a distance greater than $3\delta x$ from the boundaries). According to several authors who investigated the sensitivity of macroscopic elastic properties to the horizon size in discrete peridynamics approaches [41,42], this value is a good compromise

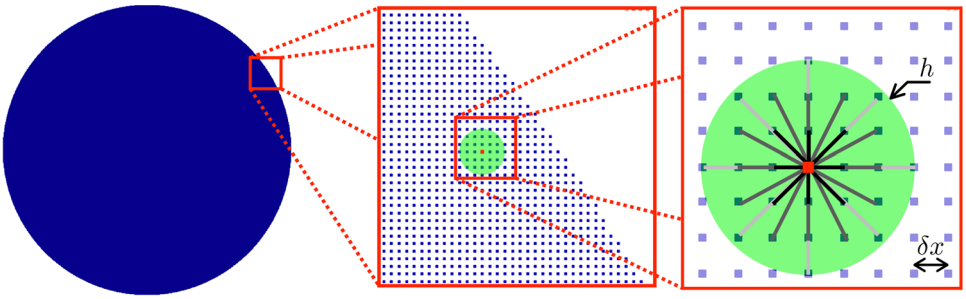

Fig. 1 A disk particle discretized by a rectilinear grid of nodes (512 nodes per diameter) with two successive zoom-ins on the boundary of the disk and a node with all its bonds within a peridynamic horizon $h = 3\delta_x$

between the accuracy of the solution (in the sense of continuum mechanics prediction and real experimental values), which increases with the size of the horizon, and the computational efficiency, which declines as the size of the horizon increases. The material parameters E and G are kept constant for all simulations mentioned in our study.

3 Diametral compression test

The diametral compression test is frequently used for the experimental evaluation of the strength of particles. For different practical problems, it has been simulated using many numerical approaches, for example, the Finite Element Method [43], the Discrete Element Method [44,45], Contact Dynamics [46], peridynamics [47,48], Material Point Method [49], Phase Field simulations [50]…

In this study, we performed diametral compression tests of disk-shaped particles of diameter $D = 2R$ between two plates. These particles are discretized on a rectilinear grid of 512×512 nodes using a simple cutoff procedure. They are then subjected to a diametral compression between two plates (Fig. 2). The plates, initially separated by a distance $\ell_0 = D$, are moved inward. The macroscopic vertical strain is defined by

$$\varepsilon = -\frac{\ell - \ell_0}{\ell_0} \tag{4}$$

where ℓ is the distance between the two plates. The top plateau is connected via bonds of a given stiffness k_w (wall stiffness), which is 100 times that of particle bonds, to the nodes belonging to the periphery of the particle. The plateau is moved downward at constant speed. With a linear elastic behavior, a normal force $k_w(\delta - \delta_0)$ is added to each node at a distance δ from the wall, where δ_0 is the reference length of the bond. For each wall, the total resulting vertical force F exerted on the particle is equal to the total force acting on the wall, obtained by summing all the contributions of the boundary nodes. For the particle–plate friction, we considered a regularized Coulomb friction law [51] with a coefficient of friction $\mu = 0.5$.

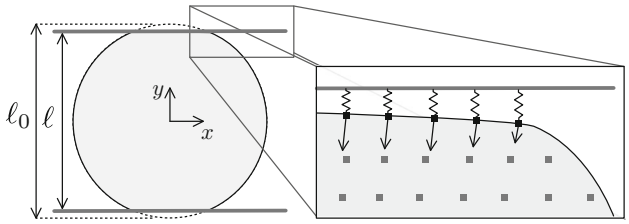

Fig. 2 Diametral compression test on a particle between two rigid plates. Schematic representation of the contact area

3.1 Stress–strain curve

The applied strain rate should be a compromise between the simulation time and the propagation time of the elastic waves in the lattice mass–spring system. In the following, it is fixed to a value equal to 0.07 % of the lattice speed to reduce the inertial effects. Figure 3 shows a typical stress-strain curve where the average stress $\sigma = F/D$ is normalized by the theoretical stress at failure

$$\sigma_t^Y = \frac{F^Y}{\pi R} \tag{5}$$

for a rupture force equal to F^Y [52]. The curve is nonlinear, the change in slope being due to the rasterization of the particle. This effect tends to vanish at increasingly higher resolution. We see that rupture occurs for $\sigma^Y \simeq 1.4\sigma_t^Y$. This is because we have set here $\sigma = F/(2R)$, and failure occurs for $F = F^Y$. Hence, according to Eq. (5), we have $\sigma^Y/\sigma_t^Y = \pi/2$ at failure. After breakage, the plates are stopped to avoid additional breakage of fragments. We define the damage rate $\lambda(\varepsilon)$ as the ratio of the number of broken bonds for a deformation of 1% to the initial number of bonds. An example of cumulative damage $100 \int \lambda(\varepsilon)\mathrm{d}\varepsilon$ is shown in Fig. 3 as a function of cumulative deformation. The damage rate begins to increase rapidly at $\varepsilon \simeq 1.9\%$ as the stress is approaching its peak value. Then, it vanishes rapidly with stress drop. To allow a full crack pattern development, the simulation was allowed to run until the damage rate is below $\lambda = 0.002$.

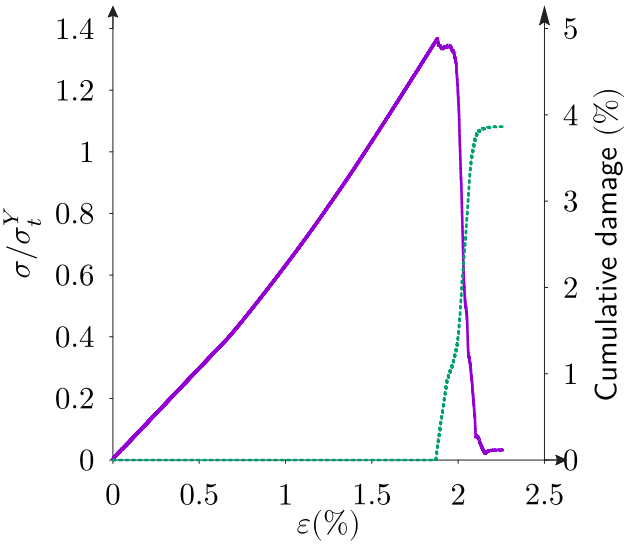

Fig. 3 Vertical stress (purple curve, solid line) and cumulative damage (green curve, dashed line) as a function of cumulative vertical strain for a particle meshed with $N_x = 512$. The stress is normalized by the theoretical failure stress σ_t^Y

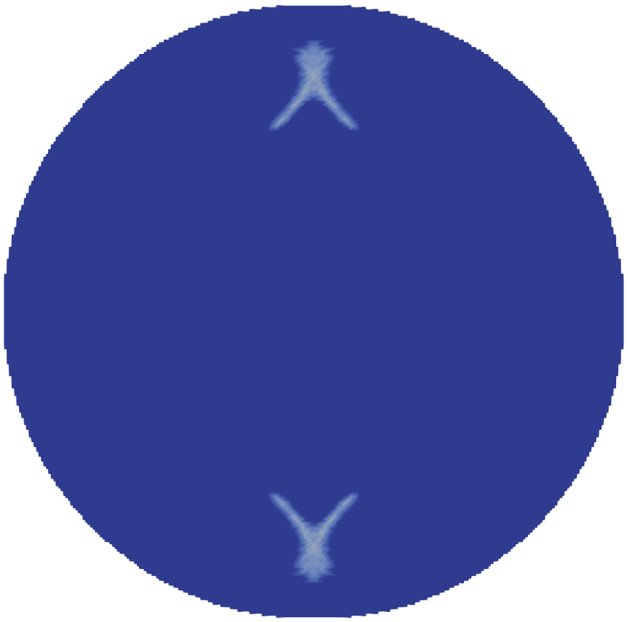

Fig. 4 Damage zone (in light blue) showing the onset of fracture

Interestingly, as observed in Fig. 4, the onset of fracture is not located at the maximum tensile stress but at $y/D = \pm 0.375$ corresponding to points where the Tresca equivalent stress $\max(\sigma_{\mathrm{I}} - \sigma_{\mathrm{II}})$, where σ_{I} and σ_{II} are the principal stresses, is maximum. The slip plane is nearly at 45° to the compression axis, as expected for an amorphous material. This indicates that the particle does not break in pure tension but in shear, as it was also observed in FEM tests [53]. The damaged zone is symmetrical, which is consistent with the fact that no defects are present in the particle. We note also a bifurcation of the crack path showing a dynamic propagation after the onset of failure. Indeed, prior to fracture the stress concentration zone is large and the elastic energy stored is suddenly released leading to branching cracks.

3.2 Stress transmission

The stress tensor at each node i can be computed by summing all contributions of connected bonds j using [54]

$$\sigma_i = \frac{1}{2V_i} \sum_{j \in \mathcal{H}_i} \boldsymbol{\xi}_{ij} \otimes \boldsymbol{F}_{ij} \tag{6}$$

where $\boldsymbol{F}_{ij}$ is the force exerted on node i by node j. Figure 5 shows the horizontal σ_{xx} and vertical σ_{yy} components of the stress fields. The maximum absolute values of these fields are located on the vertical symmetry axis of the particle. In compression, this maximum occurs in the vicinity of the contacts with the plates and in tension at the center of the particle.

Figure 6 shows peridynamics computed values, represented by circles together with two theoretical models. The horizontal and vertical stresses are normalized by the theoretical tensile stress at the center of the particle $\sigma_t = \frac{1}{\pi}\frac{F}{R}$ as a function of y/R (for $x = 0$). σ_{yy} is always in compression (negative values) and is maximal at the contact with the plate and minimal at the center. The horizontal stress σ_{xx} can be either negative or positive and reaches its maximum in traction close to the center. The first theoretical model assumes that the contact forces are applied on two points at the bottom and top of the particle [55]. Figure 6 shows this model where

$$\sigma_{xx} = \sigma_t = \frac{1}{\pi}\frac{F}{R} \tag{7}$$

and

$$\sigma_{yy} = -\frac{1}{\pi}\frac{F}{R}\left(\frac{4}{1-(y/R)^2} - 1\right) \tag{8}$$

plotted as dotted lines for all points $(x = 0, y)$ on the vertical axis. In the center of the particle, we note a rather good agreement with peridynamics while the discrepancy increases with distance to the center of the particle. The second model, introduced by Hondros [56], takes into account the extension of the contact zone (solid lines in Fig. 6). For each contact, the force is assumed to be uniformly distributed on an arc of size 2α on both sides of the contact. This model valid for small values of α leads to

$$\sigma_{xx} = \frac{1}{\pi}\frac{F}{R}(u - v)/\alpha \tag{9}$$

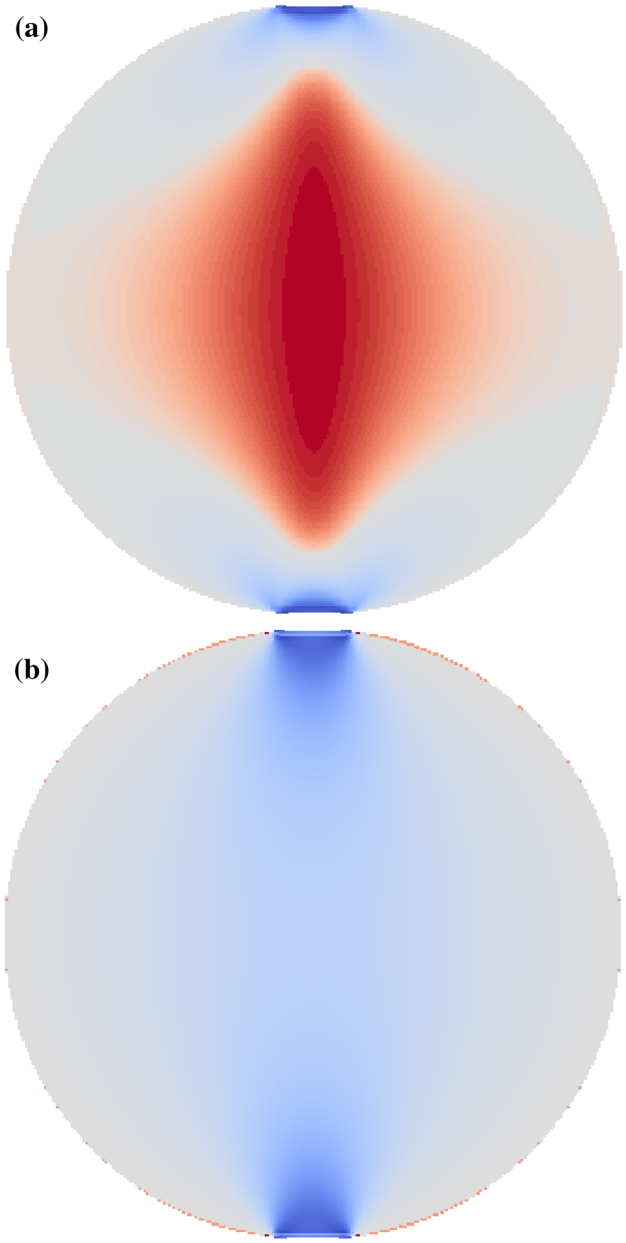

Fig. 5 Components **a** σ_{xx} and **b** σ_{yy} of the stress field for a particle submitted to diametral compression between two plates. The color gradient ranges from blue for maximal compression to red for maximal tensile stress and the mesh resolution is $N_x = 512$

and

$$\sigma_{yy} = -\frac{1}{\pi}\frac{F}{R}(u+v)\,/\alpha \tag{10}$$

where

$$u = \frac{1-(y/R)^2}{1-2(y/R)^2\cos 2\alpha + (y/R)^4}\sin 2\alpha \tag{11}$$

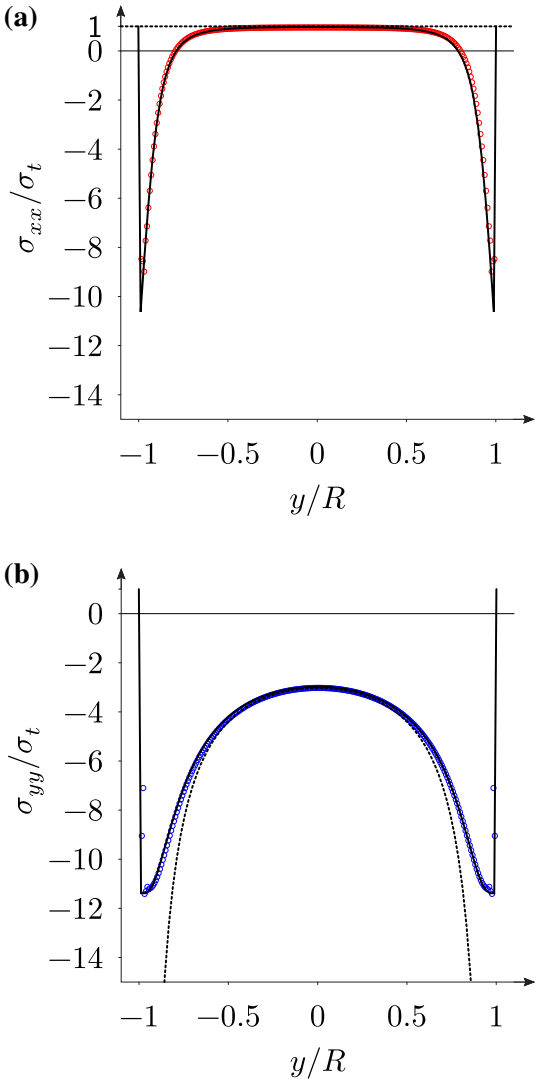

Fig. 6 Stress components σ_{xx} (red circles) (**a**) and σ_{yy} (blue circles) (**b**) normalized by σ_t as a function vertical position along the vertical axis y/R. The solid lines and dotted lines correspond to distributed-loading model with an adjusted value of the angle $\alpha \simeq 8°$ [see Eqs. (9), (10)] and point loading model (Eqs. 7, 8), respectively

and

$$v = \tan^{-1}\left(\frac{1+(y/R)^2}{1-(y/R)^2}\tan\alpha\right) \tag{12}$$

.

We get a nice fit of the stress profiles σ_{xx} and σ_{yy} as shown in Fig. 6 by adjusting the value of α. We also evaluated its value directly from the simulations for a particle with $N_x = 256$ by considering the nodes in contact with the top plateau. The value that we get in this way is by 13% below the adjusted value. This can be explained by the fact that, despite the difference between the model and simulations in the way the wall force is applied, in both cases we have a diametral compression with free boundaries and strong stress concen-

tration along the central axis. For this reason, the stress fields are similar up to a small adjustment of the model parameter α.

3.3 Discretization effects on Young's modulus

In the literature, the sensitivity of macroscopic behavior to spatial discretization has been studied for various numerical methods and mesh conditions. For example, it has been shown that the elastic modulus converges toward a theoretical value when the spatial resolution tends to zero in the case of foam using Finite Elements Method [57], of the compaction of deformable particles using Material Point Method [58] or for pores and particle-embedded composites using Lattice Elements Method [3]. For peridynamics, this issue was addressed as a function of h and δx for homogeneous materials [41] and for a single-notched sample [59].

Eight diametral compression tests were performed for the same size of the particle $D = 2R$ with resolutions ranged from $N_x = 256$ to $N_x = 704$ nodes. In all simulations, the horizon was $h = 3\,\delta x$ and the stiffness K was derived from the stress–strain curves $\sigma = K\varepsilon$ by considering the maximum slope before failure. Figure 7 shows K normalized by the Young modulus E as a function of $1/N_x$. For elastic particles, the Hertz formula gives the relationship between the applied force F and the elastic deflection δ at contact. For a 2D disk in contact with a rigid plate, $F = \frac{\pi}{4} E\delta$. As we consider, a grain compressed between two plates, $\delta = \Delta\ell/2$ for each contact, where $\Delta\ell$ is the cumulated macroscopic displacement. Thus, dividing Hertz expression by D we get $\sigma = K^{\text{th}}\varepsilon$ where $\frac{K^{\text{th}}}{E} = \frac{\pi}{8} \simeq 0.393$. Interestingly, in Fig. 7, when $1/N_X$ tends to zero, K/E can be linearly extrapolated to $\simeq 0.388$ independently of mesh size. This value which can be extrapolated with reasonable accuracy from a limited number of tests is slightly lower than K^{th}/E.

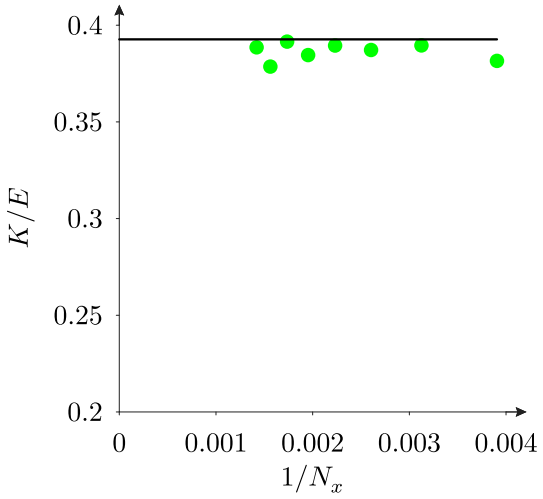

Fig. 7 Evolution of K/E as a function of $1/N_x$

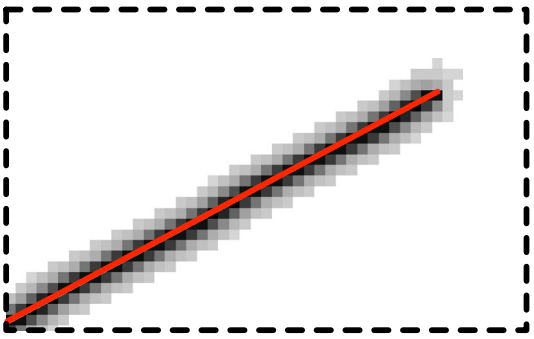

Fig. 8 Magnification of a defect in red. The material points are represented in gray levels, showing the total number of bonds per node which cross the defect. The scale ranges from white to black

4 Fracture of particles embedding defects

In this section, we consider a particle in which 1D cracks are introduced by modifying the elastic properties of the bonds crossing a predefined flaw. The cracks act as inclusions with a lower stiffness than the original material. An interesting feature is the possibility to vary this stiffness from 0 to that of the matrix, where 0 corresponds to a perfect crack, and a value between 0 and the stiffness of the matrix to a partially detached crack. Figure 8 shows in gray level the density of bonds affected by this procedure. The ratio between the Young modulus of bonds crossing the defects and that of the matrix is set to 0.2. We keep the same value of the critical elongation s_0 for all cracks independently of their positions although it has recently been suggested that its value may be different at the edges [60]. In a similar vein, as a first-order approximation, the micromodulus c was kept constant over the whole domain. Corrections regarding surface effects on both elasticity and fracture properties may be found in [61]. In our case, the cracks are essentially initiated in the bulk where the flaws are distributed.

4.1 Breakage of particles including a single vertical defect

The presence of a defect and its position play an important role in the breakage of particles. Figure 9 shows an example of stress fields σ_{xx} and σ_{yy} in a particle with a vertical defect of length $0.1\,D$ located at its center. We observe strong stress concentrations in compression in the vicinity of contacts and in tension at the tips of the flaw. We also see that the stresses spread over a large zone between the two tips.

In order to quantify the influence of the position of this defect on the yield stress of the particle, we performed a parametric study with more than 100 compression tests until rupture for a resolution $N_x = 256$. The weakening effect of

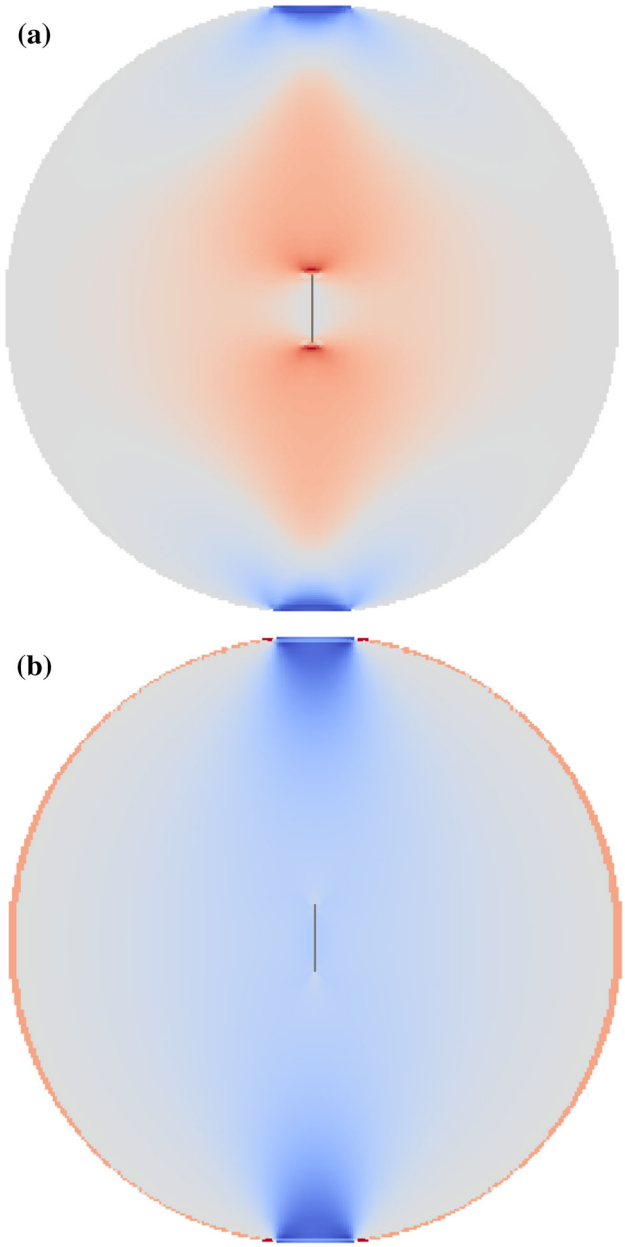

Fig. 9 Components **a** σ_{xx} and **b** σ_{yy} of the stress field for a particle under diametral compression embodying a single vertical defect at its center. The color scale ranges from blue (compression) to red (in tension)

defects on the particle is quantified using the parameter

$$\zeta = \frac{\sigma^Y}{\sigma_0^Y}, \tag{13}$$

where σ_0^Y is the failure stress for a material without defect (with the same meshing conditions). We have $\zeta \in [0, 1]$ with $\zeta = 1$ if the defect has no influence on the failure stress of the particle.

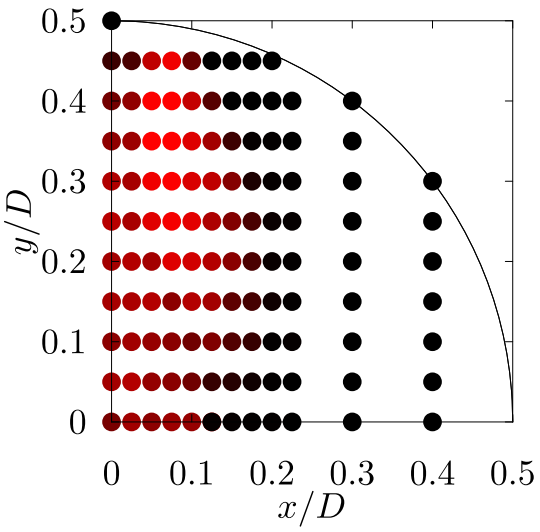

Fig. 10 Map of the influence of the position of a vertical defect on the yield stress of particles. The dots show the locations of the centers of the defects. The weakening effect of the defect is represented in red levels from black for no effect to red for maximum effect ($\zeta = 0.55$)

Figure 10 shows a map of ζ values for various locations of defects in the particle. Due to axial symmetry, only a quarter of particle is considered. This map reveals two interesting features: (1) The critical zone is neither at the center of the particle nor on the vertical axis, and the maximal influence of the defect is around ($x/D = 0.075$,$y/D = 0.35$); (2) For a distance on the x-axis above $x/D \simeq 0.2$, the defect has a negligible impact on σ^Y ($\zeta = 1$). This means that the flaws and surface irregularities occurring at such distances from the vertical axis are not relevant to the fracture behavior of particles, whereas the same flaws along the axis are critical for the strength of the particle.

4.2 Rupture of particles embedding a population of defects

In this section, we consider particles of diameter $D = 1$ embedding a population of defects of number density $\bar{n} = 100\pi/4$ with random orientation and length. The coordinates of the crack centers are randomly drawn in $[-D/2, D/2]$ following a multivariate uniform distribution. The length of defects follows a well-peaked normal distribution $d \sim \mathcal{N}(\mu_d/D = 0.035, \varsigma_d/D = 0.005)$, where μ_d is the mean defect size and ς_d is its standard deviation. By well peaked, we mean a small ratio $\varsigma_d/\mu_d \simeq 0.14$. Figure 11a shows an example of these particles and Fig. 11b its horizontal stress component σ_{xx} before failure for a particle subjected to compression between two plates. Compared to the horizontal stress field plotted in Fig. 5a, the population of defects generates fluctuations which may either concentrate or decrease the magnitude of the stress in the vicinity of defects. Note

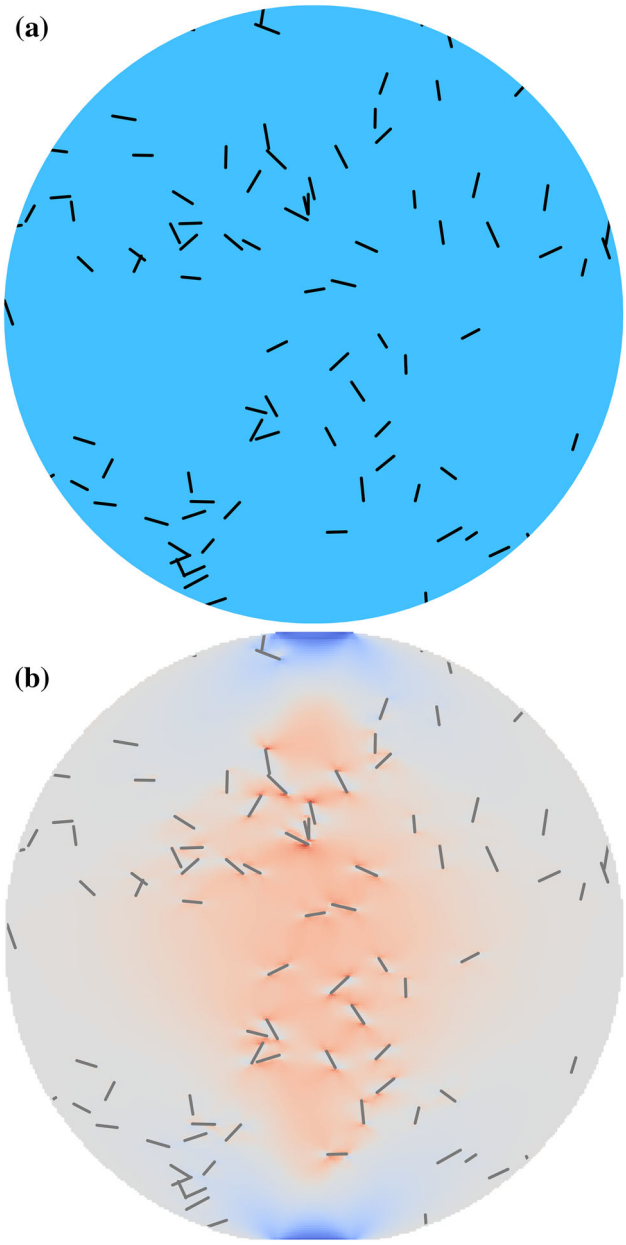

Fig. 11 Particle embedding a defect population. **a** Position of defects in the particle and **b** horizontal stress σ_{xx}

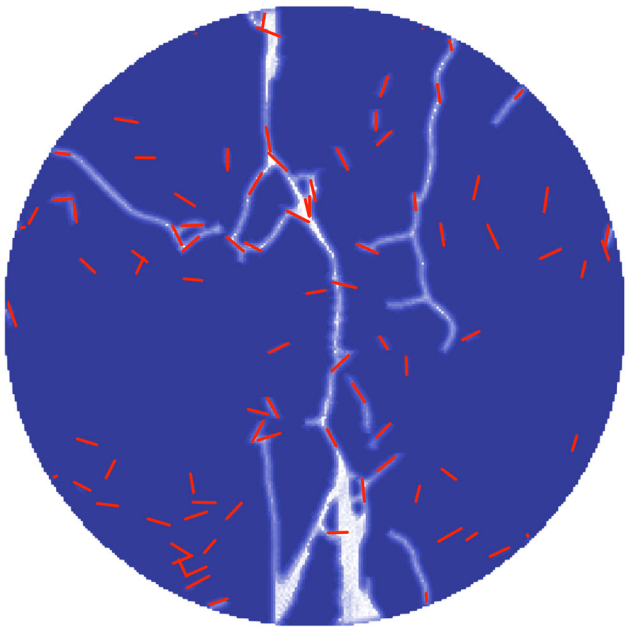

Fig. 12 Damage field after breakage (from blue for 0 damage to white for 100%). In red, the initial position of defects is shown

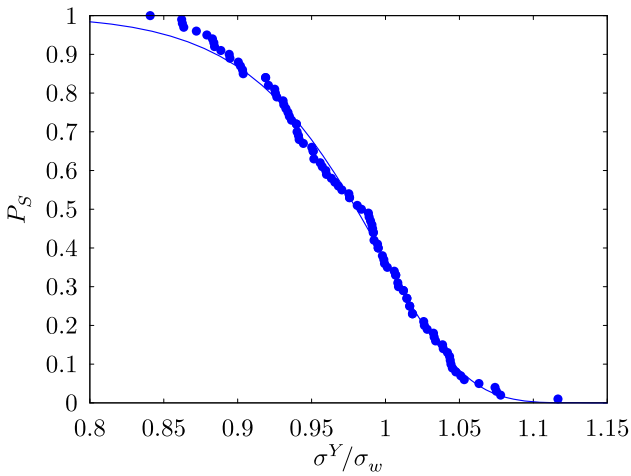

Fig. 13 Survival probability of particles as a function of the applied stress. The solid line represents Weibull fits to the data

that crack propagation strongly depends on spatial stress resolution around the cracks, and therefore, the thickness and lengths of the cracks should be larger than the value of horizon used in the simulations. This is the case in our simulations and, as shown in Fig. 11b, the stress field is rather smooth even in the vicinity of the cracks.

When rupture occurs, these fluctuations are at the origin of an asymmetrical crack propagation (Fig. 12) which mainly split particles in two parts. We note also in this image that some cracks are at the origin of secondary fractures which do not fully propagate.

In order to study the dispersion of the values of the yield stress, we consider the probability for a particle to survive to a specific loading stress. For N particles, the probability $P_S(i) = 1 - \frac{i}{N}$ is assigned to the ith smallest yield stress value. Figure 13 shows this distribution and a fit by the Weibull law

$$P_S = e^{-(\sigma^Y/\sigma_w)^m} \tag{14}$$

In this expression, σ_w corresponds to the stress for which 63% of particles are broken and m is the Weibull modulus characterizing the width of the distribution. Using Least Square

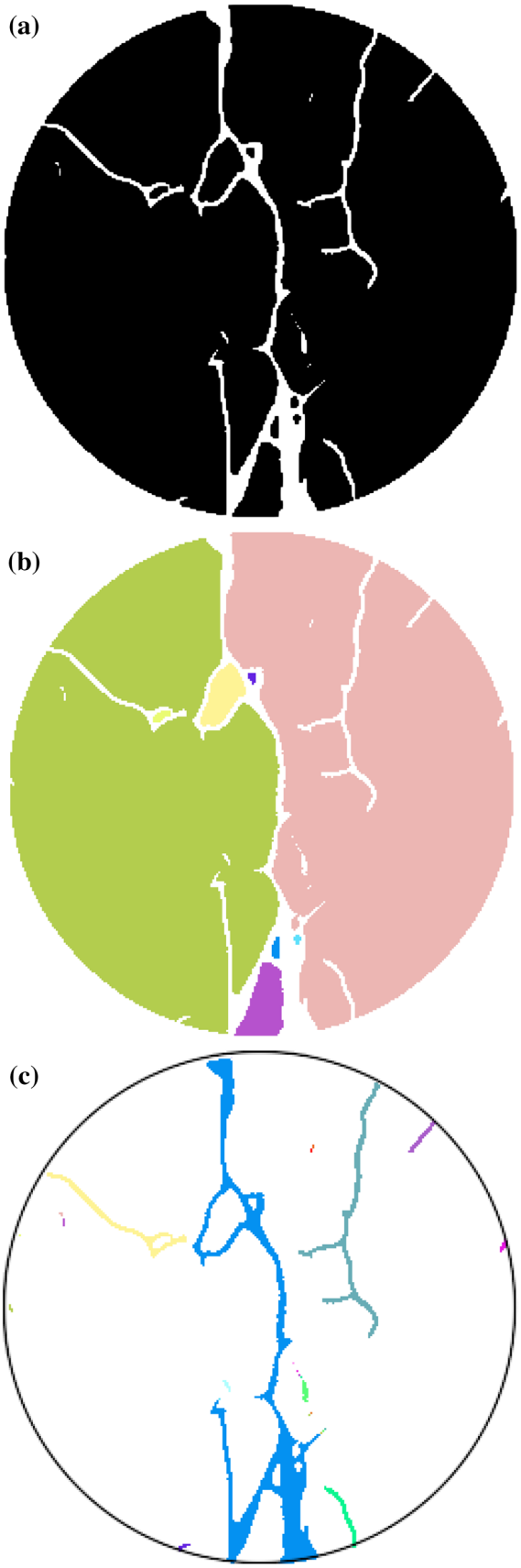

Fig. 14 **a** Binarized thresholded image based on the damage level (Fig. 12). Floodfill identification (colors indicates independent regions) of the fragments (**b**) and of cracks (**c**)

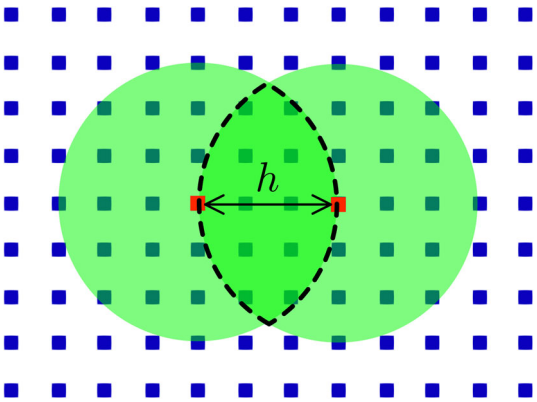

Fig. 15 Two nodes at a distance equal to the horizon h and their respective horizons. The nodes linked to the two nodes belong to the intersection area

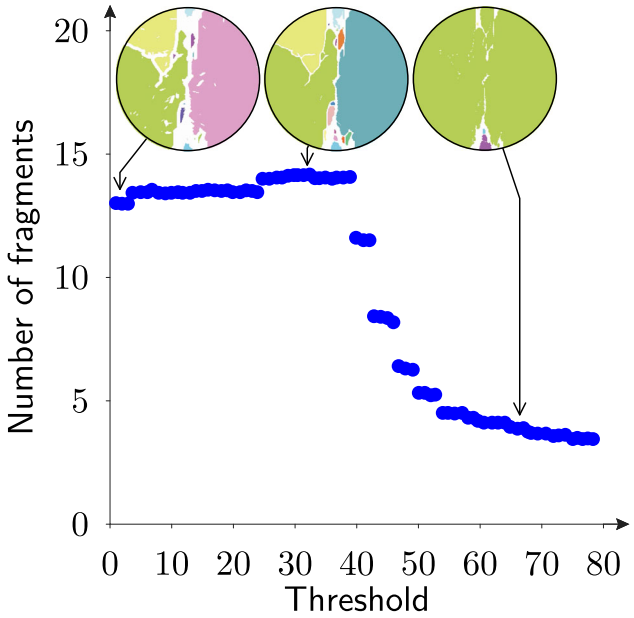

Fig. 16 Number of fragments as a function of damage threshold. Three examples of the fragment maps are displayed for three different values of damage threshold

Method, m was found to be equal to 18.5 which is in the range of ceramics materials [62].

4.3 Statistical analysis of fragments and cracks

A "floodfill" algorithm [63,64] is used to create maps of fragments where each fragment is labeled by a unique color number (Fig. 14b). From a computational point of view, this color map is a 2D table `map[x][y]` initialized with a binarized image (Fig. 14a) obtained from the damage levels (Fig. 12).

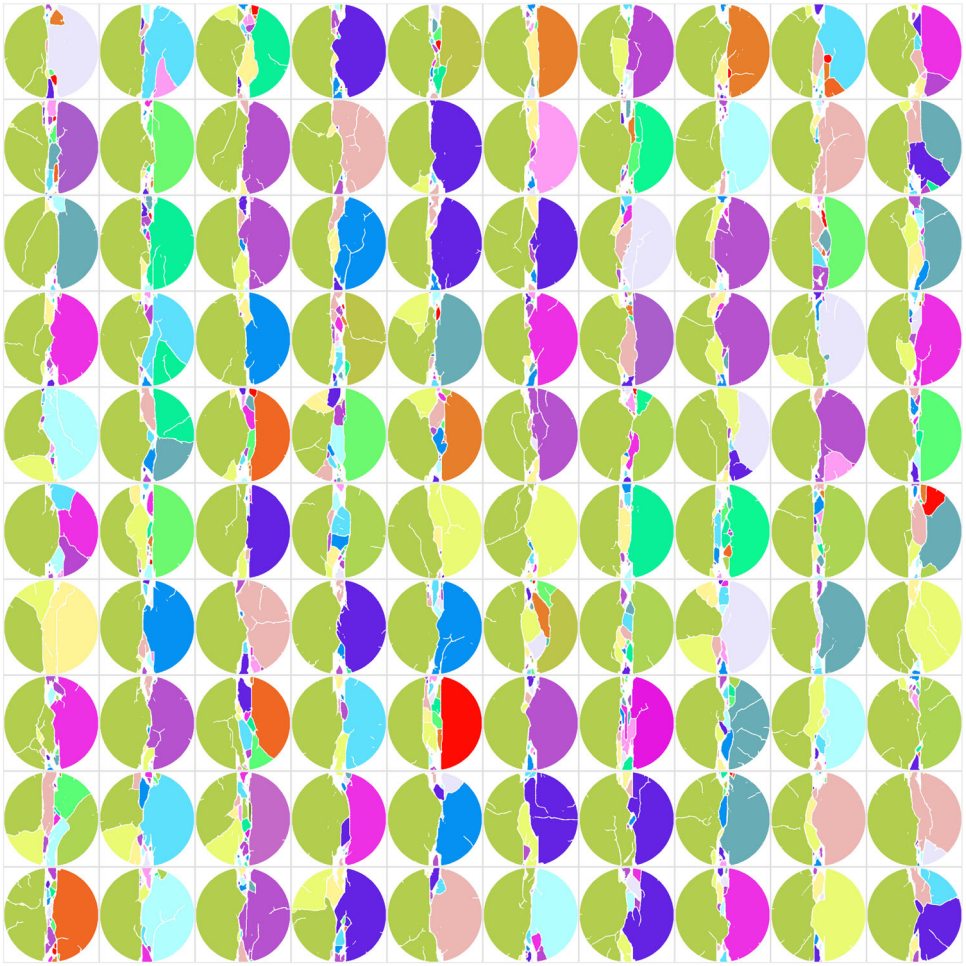

Fig. 17 Colored fragments of all tested particles. Colors are chosen randomly

In our simulations, we attributed the black color for all material points with a damage below a threshold of 30% corresponding to fragments and white otherwise, corresponding to crack pattern. This choice is based on the fact that the interactions between nodes and thus the threshold for breakage should be consistent with the length scale of mechanical interactions, which in Peridynamics is governed by the horizon h. Two nodes separated by a distance h interact through a direct link but also through all others nodes that are linked to the two nodes. As illustrated in Fig. 15, these mediating nodes belong to the intersection area of the horizons of the two nodes, and thus, they represent a fraction

$$P_d = \frac{2}{3} - \frac{\sqrt{3}}{2\pi} \simeq 0.39 \tag{15}$$

of the total area of all bonds inside the horizon of a bond. This implies that for two nodes separated at a distance h, at least 39% of bonds should be removed in order to avoid the transmission of information between the two nodes through a neighboring node. In practice, we used the slightly lower value of 30% for the analysis of the fragments. With this choice, the sizes of the fragments are expected to be larger than h. The crack patterns are practically similar for the fractions of 30% and 39%. Figure 16 shows an example of the number of fragments as a function of the threshold. We see that, as because of an increasingly finer resolution, the number of fragments slightly increases as the threshold is increased from zero, but beyond 39% the number of fragments declines rapidly with threshold since there are less cracks.

In the floodfill algorithm, the connected nodes are identified as fragments. Hence, each fragment is surrounded by cracks, and two different fragments have no common node. The method consists in flooding the connected black regions with a new color "`color`" according to the following routine:

```
floodfill(x,y,color)
    if map[x][y] == BLACK do
        map[x][y] = color
        floodfill(x+1,y,color)
        floodfill(x-1,y,color)
        floodfill(x,y+1,color)
        floodfill(x,y-1,color)
```

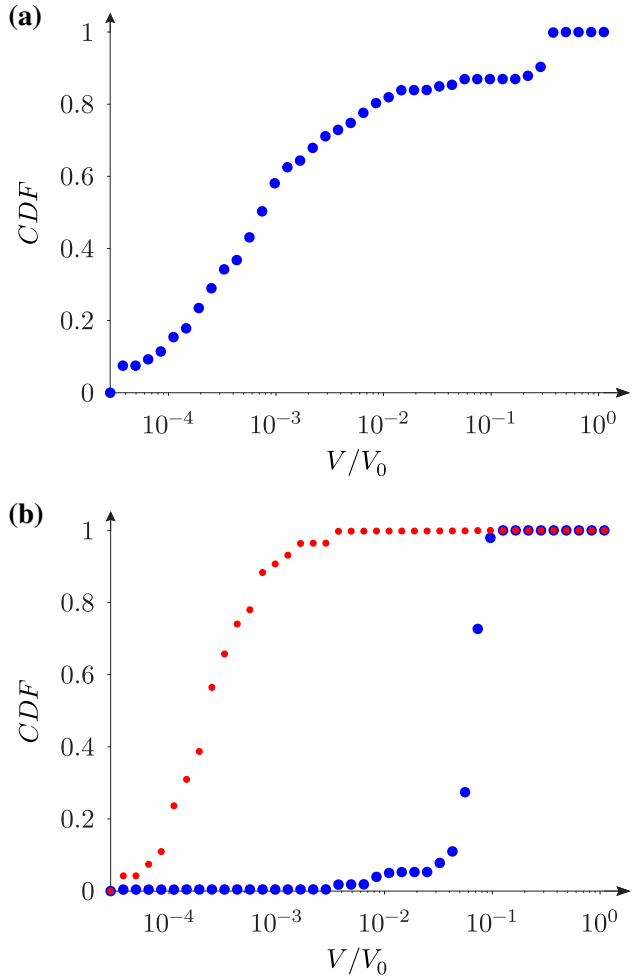

Fig. 18 **a** Cumulative distribution function of fragment sizes. **b** Cumulative distribution function of crack sizes in red and of the cracks at the origin of fragments in blue. (Color figure online)

```
    end if
end floodfill
```

In this procedure, all (x, y) are called with a new color id `color`. Note that the order the pixels are called does not change the result. The same procedure is used to identify the cracks (Fig. 14c). Figure 17 shows the fragment identification performed on 100 flawed particles the same statistical distribution of the pre-cracks.

The cumulative distribution function (CDF) of the volumes V of the fragments, normalized by the initial volume of the particle V_0, is plotted in Fig. 18a. We see two different populations of fragments: a broad distribution of smallest pieces, representing nearly 7% of the initial particle volume and a narrowly distributed zone centered on 40%. This distribution includes fragments of all sizes and a few very large fragments.

Figure 18b (blue curve) displays the CDF of crack volumes. We distinguish two types of cracks: (a) cracks that are located inside a fragment and (b) cracks that are at the interface between fragments. The latter are the cracks that created the fragments by their propagation. We see that the fragments are mostly related to the main crack splitting the particle into two parts. In most cases, the smallest fragments are located in this central zone as observed in Fig. 17. The cracks of the first kind can be found also near the central crack, but also far from it. They represent the cracks that did not propagate long enough to create fragments. They are often quite small with an average volume of 0.03% of the particle volume. We clearly see the difference between the cumulative volumes of the two kinds of cracks in Fig. 18b.

These results show that, despite the presence of defects, a particle breaks mainly due to the propagation of a crack along the central axis, as expected from a classical analysis. However, we also see that defects and disorder lead to diffuse crack patterns that can create many more fragments of different sizes.

5 Conclusions

In this paper, we used a 2D bond-based peridynamics method to investigate the breakage of particles containing defects. In the case of particles without defects, we showed that, even if the rectilinear meshing of the particle may lead to a poor description of the curvature at the contact scale, the horizontal and vertical stress fields are well predicted. Furthermore, for an increasingly resolved meshing, the particle stiffness converges linearly to a well-defined value close to the theoretical value obtained using Hertz equation for the contact between a disk and a plate in plan strain. A model of defect was introduced, based on a weakening of the elastic modulus of elements crossing a 1D linear notch. More than 100 compression tests were performed to investigate the influence of the location of a vertical defect in the upper right quadrant of a disk-particle. Interestingly, we show that the lowest yield stress does not occur for a position of the defect at the center of the particle.

We also characterized the evolution of yield stress for 100 particles with the same statistical population of defects and different random draws. We found that the yield stress follows a Weibull distribution whose exponent $m \simeq 18$ is consistent with that of ceramic's materials. A floodfill procedure was then employed to determine the volumes occupied by fragment and cracks and aggregated data allowed us to plot the corresponding probability distributions for the whole set of particles.

In future work, we would like to analyze more deeply the link between the parameters controlling the population of defects at local scale and the global probability of survivals

of particles. A key feature of the peridynamics method is its ability to simulate highly dynamical problems as breakage under impact. Another perspective is the effect of the deformation rate on the fragmentation of particles.

Acknowledgements We are grateful to the INRAE MIGALE bioinformatics facility (MIGALE, INRAE, 2020. Migale bioinformatics Facility, doi: 10.15454/1.5572390655343293E12) and to the genotoul bioinformatics platform Toulouse Occitanie (Bioinfo Genotoul, doi: 10.15454/1.5572369328961167E12) for providing computing and storage resources.

Compliance with ethical standards

Conflict of interest The authors report no conflict of interest in this study.

References

1. Song B, Rough S, Wilson D (2007) Effects of drying technique on extrusion-spheronisation granules and tablet properties. Int J Pharm 332(1–2):38
2. Fichtner F, Rasmuson Å, Alderborn G (2005) Particle size distribution and evolution in tablet structure during and after compaction. Int J Pharm 292(1–2):211
3. Affes R, Delenne JY, Monerie Y, Radjai F, Topin V (2012) Tensile strength and fracture of cemented granular aggregates. Eur Phys J E 35(11):117
4. Torquato S (2002) Random heterogeneous materials. Springer, Berlin
5. Aliha M, Ayatollahi M (2014) Rock fracture toughness study using cracked chevron notched Brazilian disc specimen under pure modes I and II loading-A statistical approach. Theor Appl Fract Mech 69:17
6. Guo H, Aziz N, Schmidt L (1993) Rock fracture-toughness determination by the Brazilian test. Eng Geol 33(3):177
7. Zhou XP, Wang YT (2016) Numerical simulation of crack propagation and coalescence in pre-cracked rock-like Brazilian disks using the non-ordinary state-based peridynamics. Int J Rock Mech Min Sci 89:235
8. Khanal M, Schubert W, Tomas J (2005) Experiment and simulation of breakage of particle compounds under compressive loading. Part Sci Technol 23(4):387
9. Xiao Y, Sun Z, Desai CS, Meng M (2019) Strength and surviving probability in grain crushing under acidic erosion and compression. Int J Geomech 19(11):04019123
10. Dan DQ, Konietzky H, Herbst M (2013) Brazilian tensile strength tests on some anisotropic rocks. Int J Rock Mech Min Sci 58:1
11. Tavallali A, Vervoort A (2013) Behaviour of layered sandstone under Brazilian test conditions: layer orientation and shape effects. J Rock Mech Geotech Eng 5:366
12. Zubelewicz A, Bažant ZP (1987) Interface element modeling of fracture in aggregate composites. J Eng Mech 113(11):1619
13. Kun F, Herrmann HJ (1996) A study of fragmentation processes using a discrete element method. Comput Methods Appl Mech Eng 138(1–4):3
14. Åström JA, Herrmann HJ (1998) Fragmentation of grains in a two-dimensional packing. Eur Phys J B Condens Matter Complex Syst 5(3):551
15. Tsoungui O, Vallet D, Charmet JC (1999) Numerical model of crushing of grains inside two-dimensional granular materials. Powder Technol 105(1–3):190
16. Nguyen DH, Sornay P, Azéma E, Radjai F (2015) Evolution of particle size distributions in crushable granular materials. Geomech Micro Macro 1:275
17. Nguyen DH, Azéma E, Sornay P, Radjai F (2015) Bonded-cell model for particle fracture. Phys Rev E 91(2):022203
18. Orozco LF, Nguyen DH, Delenne JY, Sornay P, Radjai F (2019) Discrete-element simulations of comminution in rotating drums: effects of grinding media. Powder Technol 362:157–167
19. Ciantia M, de Toledo M, Alvarez Arroyo, Calvetti F, Gens Solé A (2015) An approach to enhance efficiency of DEM modelling of soils with crushable grains. Géotechnique 65(2):91
20. Zhou W, Yang L, Ma G, Chang X, Cheng Y, Li D (2015) Macro-micro responses of crushable granular materials in simulated true triaxial tests. Granul Matter 17(4):497
21. Galindo-Torres S, Pedroso D, Williams D, Li L (2012) Breaking processes in three-dimensional bonded granular materials with general shapes. Comput Phys Commun 183(2):266
22. Orozco LF, Delenne JY, Sornay P, Radjai F (2019) Discrete-element model for dynamic fracture of a single particle. Int J Solids Struct 166:47
23. Radi K, Jauffrès D, Deville S, Martin CL (2019) Elasticity and fracture of brick and mortar materials using discrete element simulations. J Mech Phys Solids 126:101
24. Kertész J (1990) 8 - Dielectric breakdown and single crack models. In: Herrmann HJ, Roux S (eds) Statistical models for the fracture of disordered media. Random materials and processes. North-Holland, Amsterdam, pp 261–290
25. Topin V, Delenne JY, Radjaı F, Brendel L, Mabille F (2007) Strength and failure of cemented granular matter. Eur Phys J E 23(4):413
26. Nikravesh S, Gerstle W (2018) Improved state-based peridynamic lattice model including elasticity, plasticity and damage. Comput Model Eng Sci 116(3):323
27. Gerstle W, Sau N, Silling S (2007) Peridynamic modeling of concrete structures. Nucl Eng Des 237(12–13):1250
28. Celik E, Guven I, Madenci E (2011) Simulations of nanowire bend tests for extracting mechanical properties. Theor Appl Fract Mech 55(3):185
29. Perré P, Almeida G, Ayouz M, Frank X (2016) New modelling approaches to predict wood properties from its cellular structure: image-based representation and meshless methods. Ann For Sci 73(1):147
30. Silling SA (2000) Reformulation of elasticity theory for discontinuities and long-range forces. J Mech Phys Solids 48(1):175
31. Ha YD, Bobaru F (2011) Characteristics of dynamic brittle fracture captured with peridynamics. Eng Fract Mech 78(6):1156
32. Love AEH (1944) A treatise on the mathematical theory of elasticity. Dover Publications, Mineola
33. Herrmann HJ, Roux S (1990) Statistical models for the fracture of disordered media. Elsevier, Amsterdam
34. Laubie H, Monfared S, Radjaï F, Pellenq R, Ulm FJ (2017) Effective potentials and elastic properties in the lattice-element method: isotropy and transverse isotropy. J Nanomech Micromech 7(3):04017007
35. Sarego G, Le QV, Bobaru F, Zaccariotto M, Galvanetto U (2016) Linearized state-based peridynamics for 2-D problems. Int J Numer Methods Eng 108(10):1174
36. Zhu Q, Ni T (2017) Peridynamic formulations enriched with bond rotation effects. Int J Eng Sci 121:118
37. Brandrup J, Immergut EH, Grulke EA, Abe A, Bloch DR (1999) Polymer handbook, vol 89. Wiley, New York
38. Comte C, von Stebut J (2002) Microprobe-type measurement of Young's modulus and Poisson coefficient by means of depth

sensing indentation and acoustic microscopy. Surf Coat Technol 154(1):42
39. Ridha S, Hamid AIA, Halim AHA, Zamzuri NA (2018) Elasticity and expansion test performance of geopolymer as oil well cement. IOP Conf Ser Earth Environ Sci 140:012147. https://doi.org/10.1088/1755-1315/140/1/012147
40. Allen M, Tildesley D (1986) Computer simulation of liquids. Oxford University Press, Oxford
41. Freimanis A, Paeglitis A (2017) Mesh sensitivity in peridynamic quasi-static simulations. Procedia Eng 172:284
42. Yaghoobi A (2015) Meshless modeling framework for fiber reinforced concrete structures. Comput Struct 161:43
43. Indriyantho BR (2014) Finite element modeling of concrete fracture in tension with the Brazilian splitting test on the case of plane-stress and plane-strain. Procedia Eng 95:252
44. Vo TT, Mutabaruka P, Nezamabadi S, Delenne JY, Izard E, Pellenq R, Radjai F (2018) Mechanical strength of wet particle agglomerates. Mech Res Commun 92:1
45. Wu S, Ma J, Cheng Y, Xu M, Huang X (2018) Numerical analysis of the flattened Brazilian test: failure process, recommended geometric parameters and loading conditions. Eng Fract Mech 204:288
46. Nguyen DH, Azéma E, Sornay P, Radjai F (2015) Bonded-cell model for particle fracture. Phys Rev E 91:022203
47. Wu L, Huang D, Xu Y, Wang L (2019) A non-ordinary state-based peridynamic formulation for failure of concrete subjected to impacting loads. Comput Model Eng Sci 118(3):561
48. Wang Y, Han F, Lubineau G (2019) A hybrid local/nonlocal continuum mechanics modeling and simulation of fracture in brittle materials. Comput Model Eng Sci 121:399–423
49. Raymond SJ, Jones BD, Williams JR (2019) Modeling damage and plasticity in aggregates with the material point method (MPM). Comput Part Mech 6(3):371
50. Bilgen C, Homberger S, Weinberg K (2019) Phase-field fracture simulations of the Brazilian splitting test. Int J Fract 220(1):85
51. Luding S (2008) Cohesive, frictional powders: contact models for tension. Granul Matter 10(4):235
52. Timoshenko S, Goodier J (1969) Theory of elasticity. McGraw-Hill, New York
53. Lin H, Xiong W, Zhong W, Xia C (2014) Location of the crack initiation points in the Brazilian disc test. Geotech Geol Eng 32(5):1339
54. Laubie H, Monfared S, Radjai F, Pellenq R, Ulm FJ (2017) Disorder-induced stiffness degradation of highly disordered porous materials. J Mech Phys Solids 106:207
55. Jianhong Y, Wu F, Sun J (2009) Estimation of the tensile elastic modulus using Brazilian disc by applying diametrically opposed concentrated loads. Int J Rock Mech Min Sci 46(3):568
56. Hondros G (1959) The evaluation of Poisson's ratio and the modulus of materials of a low tensile resistance by the Brazilian (indirect tensile) test with particular reference to concrete. Aust J Appl Sci 10(3):243
57. Roberts AP, Garboczi EJ (2016) Elastic properties of model random three-dimensional open- cell solid. J Mech Phys Solids 50:33
58. Nezamabadi S, Radjai F, Averseng J, Delenne JY (2015) Implicit frictional-contact model for soft particle systems. J Mech Phys Solids 83:72
59. Frank X, Radjaï F, Nezamabadi S, Delenne JY (2020) Tensile strength of granular aggregates: stress chains across particle phase versus stress concentration by pores. Phys Rev E 102:022906
60. Yu H, Li S (2020) On energy release rates in peridynamics. J Mech Phys Solids 142:104024
61. Le QV, Bobaru F (2018) Surface corrections for peridynamic models in elasticity and fracture. Comput Mech 61(4):499
62. Stoyan D, Gloaguen R (2011) Nucleation and growth of geological faults. Nonlinear Process Geophys 18(4):529
63. Haig TD, Attikiouzel Y, Alder M (1992) Border following new definition gives improved borders. IEE Proc I (Commun Speech Vis) 139(2):206
64. Delenne JY, Richefeu V, Radjai F (2015) Liquid clustering and capillary pressure in granular media. J Fluid Mech 762:R5